Implementation and Numerical Exploration of Advanced Aqueous Carbon Dioxide Corrosion Models

By

Michael Peter Jones

Submitted in accordance with the requirements for the degree of

Doctor of Philosophy

The University of Leeds
Institute of Functional Surfaces, iFS
School of Mechanical Engineering

December 2024

Publication Statement

The candidate confirms that the work submitted is his/her own, except where work which has formed part of jointly-authored publications has been included. The contribution of the candidate and the other authors to this work has been explicitly indicated below. The candidate confirms that appropriate credit has been given within the thesis where reference has been made to the work of others.

In all papers listed below, the primary author completed all experimental studies, evaluation of data and preparation of publications. All authors contributed to proof reading of the articles prior to publication.

Papers contributing to this thesis:

- Jones, M., Owen, J., de Boer, G., Woollam, R.C., Folena, M.C., Farhat, H. and Barker, R. Numerical Exploration of a Fully Mechanistic Mathematical Model of Aqueous CO_2 Corrosion in Steel Pipelines. *Corrosion science.* 2024, **236**, pp.1-15.
- Jones, M., Owen, J., de Boer, G., Woollam, R.C. and Barker, R. Numerical Exploration of a Comprehensive Mechanistic CO_2 Corrosion Model Part I: Influence of Temperature, Pressure and Bulk pH. In: *AMPP 2022*, *Denver, CO*. AMPP, 2023, pp.1-12.
- Jones, M., Owen, J., de Boer, G., Woollam, R.C. and Barker, R. Numerical Exploration Of A Comprehensive Mechanistic CO_2 Corrosion Model Part II: Influence Of Hydrodynamics And Bulk pH. In: *AMPP Annual Conference + Expo 2023*, *Denver, Colorado*. AMPP, 2023, pp.1-9.
- Jones, M., de Boer, G., Woollam, R., Owen, J., Folena, M.C., Farhat, H. and Barker, R. Assessing Comprehensive Mechanistic CO_2 Corrosion Modeling Methods and their Impact on Predicted Corrosion Behavior. In: *AMPP*, *New Orleans, LA*. AMPP, 2024, pp.1-15.
- Jones, M., de Boer, G., Woollam, R., Owen, J., Folena, M.C., Farhat, H. and Barker, R. Advancement of a Comprehensive Mechanistic CO_2 Corrosion Model to Incorporate Simulated Hydrodynamics via a Turbulent Flow Model In: *AMPP*, *New Orleans, LA*. AMPP, 2024, pp.1-12.

Acknowledgements

Firstly, I'd like to thank my primary supervisor Professor Richard Barker for the unbelievable amount of support he has provided throughout my academic journey. Both academically and personally he has been an incredible mentor, and I'm honoured to have had the opportunity to work with him. I'd also like to thank my secondary supervisors, Dr Gregory de Boer and Dr Joshua Owen, for always making time for me when I needed it most. Greg's vast knowledge of numerical modelling techniques and Josh's pragmatic approach to experimental work have help me through every barrier I've faced along the way. A special thanks must also go to Richard Woollam for meeting with me every week to guide me through the complexities of academic literature.

I'd like to thank all my colleagues in the School of Mechanical Engineering and in particular all my friends in office 3.32a. Being around such an amazing group of people has made it a joy to come work every day and made the entire PhD experience one that I will always remember. In this regard I'd also like to thank the iFS technicians, Jordan Thomas, Michael Huggan, Paul Kilburn, and Dec Isaac, not only for being so generous with your time and technical expertise, but also for lifting my spirits at every opportunity.

I'd of course like to thank my family for giving me their constant and ongoing support in everything I do. In particular I'd like to thank my brother Alex for always being there when I've needed him and for being so accommodating in rearranging our plans to fit with my often-hectic schedule.

I'd also like to thank the entire LUU Pool & Snooker Society for giving so many happy memories since I joined in my first year. Through the society I have had the opportunity to meet so many amazing people and made so many great friends, and I will always be grateful for that.

Lastly, I would like to thank the University of Leeds for being my home for the last 9 years. I couldn't imagine studying anywhere else.

Abstract

When carbon dioxide (CO_2) is dissolved in an aqueous solution, it forms carbonic acid (H_2CO_3) which can cause steel surfaces to corrode. This is a serious issue in many industrial pipelines which are often used to transport CO_2 saturated solutions. Understanding exactly how the internal surface of a pipe is going to corrode is vital in effective corrosion control. In this work, the potential for simulating the corrosive environment via finite element modelling is explored. Comprehensive mechanistic models of CO_2 corrosion have previously been developed, but not extensively interrogated. As a result, the associated limitations of these models, as well as their potential for further advancement, is not fully understood. It is therefore the intent of this thesis to conduct a thorough investigation into the current state of the CO_2 modelling and explore pathways to their continued advancement via computational modelling, numerical exploration, and experimental testing.

Two one-dimensional (1-D) models of CO_2 corrosion have been developed within the COMSOL Multiphysics® software. The models focus on the hydrodynamic boundary layer in the near-wall region and incorporate both chemical and electrochemical reactions throughout the boundary, as well as at the surface, and in the bulk flow. Extensive numerical exploration of these two models is conducted to investigate how changes in the environmental and hydrodynamic conditions influence important outputs, such as the corrosion rate, surface pH, and the likelihood of protective films forming. Significant differences in the response were identified based upon the controlling mechanism for the corrosion reactions; whether it is the rate of charge-transfer at the surface or the rate at which electro-active species are transported to the surface.

Computational fluid dynamics (CFD) is used to model common flow scenarios and then integrated into the corrosion models. A novel methodology is explored to expand the application of the models to higher dimensions and more complex flow fields. Rotating cylinder electrode (RCE) experiments are conducted alongside the simulations to assess the accuracy of the corrosion models and explore their various strengths and weaknesses. In doing so, it was found that the specific mechanisms CO_2 corrosion included in the model, as well as the temperature dependencies, and the method by which flow effects are accounted for can all have a significant difference on the accuracy of the simulation.

Throughout the thesis, many avenues for improvement and further development are identified. These ideas have been collated and explored to lay the groundwork for future modelling projects based on the fundamental approaches

detailed here. Approaches are summarised and preliminary work has been completed to clearly identify how the current models can be built upon, as well as the potential pitfalls and areas of complexity.

Table of Contents

List of Tables

List of Figures

Table of Notation

Notation	Definition
[a]	Concentration of arbitrary species a (M)
$\|\boldsymbol{a}\|$	Absolute magnitude of arbitrary variable $\boldsymbol{a}$
$\boldsymbol{a}^*$	Modified arbitrary constant $\boldsymbol{a}$
$\boldsymbol{a}(\boldsymbol{x})$	Arbitrary variable $\boldsymbol{a}$ as a function of a secondary variable $\boldsymbol{x}$
$\boldsymbol{\nabla a}$	Gradient of arbitrary scalar field $\boldsymbol{a}$
$\boldsymbol{\nabla \cdot a}$	Divergence of arbitrary vector field $\boldsymbol{a}$
$\boldsymbol{\nabla \times a}$	Curl of arbitrary vector field $\boldsymbol{a}$
$\boldsymbol{a_n}$	Numbered constant $\boldsymbol{a}$ where $\boldsymbol{n}$ is an integer value
a_{eq}	Value of arbitrary property a under equilibrium conditions
$\boldsymbol{a_{ref}}$	Reference value relating to arbitrary variable $\boldsymbol{a}$
$\vec{\boldsymbol{a}}$	Forward component of arbitrary reversible reaction $\boldsymbol{a}$
$\overleftarrow{\boldsymbol{a}}$	Backward component of arbitrary reversible reaction $\boldsymbol{a}$
$\boldsymbol{k_{f,a}}$	Forward reaction rate constant for reversible reaction $\boldsymbol{a}$
$\boldsymbol{k_{b,a}}$	Backward reaction rate constant for reversible reaction $\boldsymbol{a}$
$\boldsymbol{a_j}$	Constant or variable $\boldsymbol{a}$ relating to arbitrary species $\boldsymbol{j}$
$\overline{\boldsymbol{a}}$	Mean value of variable $\boldsymbol{a}$
$\boldsymbol{a'}$	Fluctuating component of variable $\boldsymbol{a}$
$\frac{\boldsymbol{da}}{\boldsymbol{dx}}$	Derivative of arbitrary variable $\boldsymbol{a}$ with respect to arbitrary variable $\boldsymbol{x}$
$\frac{\boldsymbol{\partial a}}{\boldsymbol{\partial x}}$	Partial derivative of arbitrary variable $\boldsymbol{a}$ with respect to arbitrary variable $\boldsymbol{x}$

List of Units, Chemicals, Symbols, and Abbreviations

All units provided in the table below represent the standard units used throughout the thesis, unless otherwise stated.

$[A]$	Matrix of coefficients
$[C]$	Matrix of unknown variables
$[S]$	Matrix of known values
ΔS	Mass reaction rate (kg/m^2·s)
∇	Del operator
A	Area (m^2)
a_i	Effective ion diameter (Å)
a_j	Activity of species j
a_p	Activity of products
a_r	Activity of reactants
A_0	Pre-exponent constant
Ag	Silver
AgCl	Silver Chloride
b	Truesdell-Jones equation constant (dm^3/mol)
A	Debye-Hückel constant (mol$^{-0.5}$·dm$^{0.5}$)
B	Debye-Hückel constant (mol$^{-0.5}$·dm$^{0.5}$)
b_a	Anodic Tafel constant (mV/decade)
b_c	Cathodic Tafel constant (mV/decade)
c_j	Concentration of species j (M)
Cl^-	Chloride ion
CLAR	Corrosion layer accumulation rate
CO_2	Carbon dioxide
CO_3^{2-}	Carbonate ion
CR	Corrosion rate (mm/year)
D	Diameter (m)

D_M	Molecular diffusion rate (m^2/s)
D_T	Turbulent diffusivity (m^2/s)
DI	De-ionised
DNN	Deep neural network
DNS	Direct numerical simulation
E	Potential (V)
e^-	Electron
E_a	Activation energy ($kJ \cdot mol^{-1}$)
E_{app}	Applied potential (V)
E_0	Amplitude of applied potential (V)
E^o	Standard electrode potential (V)
E_{rev}	Reversible potential (V)
E_T	Total energy (J)
EIS	Electrochemical impedance spectroscopy
F	Faraday constant ($C \cdot mol^{-1}$)
f_{CO_2}	Fugacity of carbon dioxide
F_T	Transition function
F_1	Blending function
F_2	Blending function
FDM	Finite difference method
f_e	External volume forces
Fe	Iron
Fe^{2+}	Iron ion
$FeCO_3$	Iron carbonate
FEM	Finite element method
FVM	Finite volume method
GUI	Graphical user interface
$H^*_{CO_2}$	Modified Henry's law constant

H^+	Hydrogen ion
H_2	Hydrogen
H_2CO_3	Carbonic acid
H_2O	Water
H_2S	Hydrogen sulphide
HCO_3^-	Bicarbonate
I	Ionic strength (M)
i_0	Exchange current density under standard conditions (A/m^2)
I_{corr}	Corrosion current (A)
i_{corr}	Corrosion current density (A/m^2)
i_{Fe}	Iron dissolution reaction current density (A/m^2)
i_H	Hydrogen evolution reaction current density (A/m^2)
$i_{H_2CO_3}$	Carbonic acid reaction current density (A/m^2)
i_{loc}	Local current density (A/m^2)
i_{net}	Net current density (A/m^2)
i_{tot}	Total current density (A/m^2)
I_{tot}	Total current (A)
j	Arbitrary species
K_{ca}	Carbonic acid dissociation equilibrium constant (M)
K_{bi}	Bicarbonate dissociation equilibrium constant (M)
K_{eq}	Arbitrary equilibrium constant
K_H	Henry's law constant (bar/M)
K_θ	Transition function constant
K_w	Water dissociation equilibrium constant (M^2)
K_{hyd}	Hydration constant
K_r	Arrhenius rate constant
K_{sp}	Solubility limit (M^2)
LES	Large eddy simulation

LHS	Left-hand side
LPR	Linear polarisation resistance
M_w	Molecular weight (kg·mol^{-1})
m	Current density rate constant
n	Number of involved electrons
N_2	Nitrogen
N_j	Flux of arbitrary species j (mol·m^{-2}·s^{-1})
NaCl	Sodium chloride
N-S	Navier-Stokes
OCP	Open-circuit potential (V)
OH^-	Hydroxide ion
P	Total pressure (bar)
P_{CO_2}	Carbon dioxide partial pressure (bar)
P_s	Saturation pressure (bar)
ppm	Parts per million
PR	Precipitation rate (mm/year)
Pt	Platinum
PTFE	Polytetrafluoroethylene
q_H	Heat released by chemical reactions (W)
R	Universal gas constant (8.3145 J/mol·K)
r	Arbitrary reaction rate (mol/m^3·s)
r_i	Ionic radius (m)
R_j	Net rate of change of species j concentration (mol/m^3·s)
R_{ct}	Charge-transfer resistance (Ω)
R_p	Polarisation resistance (Ω)
R_s	Solution resistance (Ω)
RANS	Reynolds-averaged Navier Stokes
RCE	Rotating cylinder electrode

RDE	Rotating disk electrode
Re	Reynold's number
S	Supersaturation
Sc_T	Turbulent Schmidt number
SI	Saturation index
S_{ox}	Oxidising species concentration(M)
SR	Saturation ratio
S_{red}	Reducing species concentration(M)
SST	Shear-stress transport
ST	Scaling tendency
T_c / T_f / T_K	Temperature (°C / °f / K)
u	Fluid velocity (m/s)
u^+	Dimensionless fluid velocity
u_∞	Freestream velocity (m/s)
V	Volume (m^3)
v_f	Film growth velocity (m/s)
v_{ox}	Stoichiometric coefficient of oxidising species
v_{red}	Stoichiometric coefficient of reducing species
v_s	Surface regression velocity (m/s)
$v_{w,\varphi}$	Rotational velocity (m/s)
W	Mass loss of corroding metal (g)
W_f	Work of external volume forces (J)
x	Characteristic length (m)
y	Wall distance (m)
y^+	Dimensionless wall distance
Z	Impedance (Ω)
Z_{Im}	Imaginary component of impedance
Z_{Re}	Real component of impedance

z_j	Charge of arbitrary species j
α	Dimensionless parameter
γ_j	Activity coefficient of arbitrary species j
δ	Boundary layer height (m)
δ_{99}	Boundary layer height at 99% freestream velocity (m)
ε	Energy dissipation per unit mass (W/kg)
ε_s	Surface roughness
ε_V	Volumetric porosity
ϵ	Relative permittivity of solution
ϵ_0	Permittivity of free space (8.854×10^{-12} F/m)
η	Overpotential (V)
η_a	Anodic overpotential (V)
η_c	Cathodic overpotential (V)
η_K	Kolmogorov length scale
κ	von Kármán constant
κ_f	Permeability of surface film
μ	Dynamic viscosity (Pa·s)
μ_t	Eddy viscosity
ν	Kinematic viscosity (m^2/s)
ρ	Density ($kg/^3$)
σ_s	Electrical conductivity of surface (s^{-1})
$\bar{\bar{\sigma}}$	Internal stress tensor
τ	Tortuosity
τ_{ij}	Reynolds stress tensor
τ_η	Kolmogorov time scale
τ_ω	Wall shear stress (Pa)
θ	Surface porosity
Φ_l	Electrolyte potential (V)

Φ_s	Electrode potential (V)
Φ	Phase shift
φ	Fugacity (Pa)
ω	Turbulent kinetic energy ($m^2 \cdot s^{-2}$)
ω_s	Rotation speed (m/s)
ξ	Temperature dependent dielectric constant

Chapter 1 - Introduction, Theory and Literature Review

1.1 Introduction

1.1.1 Industrial Impact of Corrosion

When assessing the global impact of corrosion, the focus is often on the industrial context due to the significant economic losses it causes each year. A 2016 IMPACT study conducted by NACE International[1] estimated the global cost of corrosion to be around $2.5 trillion annually across major industries such as energy, transport, construction, manufacturing, and mining. The same study also goes on to estimate that between 15-35% of this could be saved each year by properly employing current corrosion control practices. Possible methods of corrosion control include the use of corrosion inhibitors, organic coatings, pH adjustment, cathodic protection, steam scrubbing, or even simply careful selection of materials[2, 3]. Each of these approaches have their own associated costs, challenges, benefits and drawbacks, however by correctly understanding and utilising these techniques, the cost of corrosion could be significantly reduced.

Whilst the financial aspect is undeniably the primary driver behind research into corrosion management, there are also other factors that must be considered when evaluating the overall impact of corrosion. In many of the industries for which corrosion is a significant issue, health and safety is common and important consideration due to the scale on which they operate. In the United States alone, incidents of collapsed bridges, floods due to burst water mains, failure of commercial aircrafts, and even serious issues with nuclear reactions have all been either partly or wholly attributed to the effects of corrosion[4]. In each of these cases, the failure was not necessarily related to the initial condition of the infrastructure but rather the corrosive degradation and wear over time. Without proper consideration and management, each of these systems has the potential to pose real and significant risk to human life.

The risks associated with the failure of industrial systems due to corrosion can be extended even further when environmental effects are taken into account. Corrosion within hydrocarbon or natural gas pipelines can result in leaks, potentially leading to the contamination of fresh water supplies[5]. It is also a problem in the nuclear industry, in regard to the disposal of nuclear waste.

Localised corrosion within stainless steel waste cannisters can result in their failure, releasing harmful radionuclides into the surrounding environment[6]. The total impact of such environmental effects is often difficult to quantify, however their importance cannot be ignored.

1.1.2 Project Aims and Objectives

The primary aim of this project is to advance the understanding of the environmental and hydrodynamic conditions which impact corrosion within industrial pipelines via numerical simulation. The objectives associated with this aim are as follows:

- Build two comprehensive mechanistic models of carbon dioxide (CO_2) corrosion based on existing literature.
- Design a methodology to perform a comprehensive numerical exploration of each model across a range of environmental and hydrodynamic conditions.
- Conduct a large-scale numerical exploration of both models and generate output plots to visualise to relative effects of the input conditions.
- Identify the unique behaviours associated with each model and perform specific analysis of each model under these conditions to assess the underlying cause and effect.

The secondary aim of this project is to assess the performance of existing mechanistic corrosion models via experimental methods. The objectives associated with this aim are as follows:

- Design a methodology to directly link the new corrosion models to a controlled hydrodynamic laboratory set-up.
- Conduct experiments across various environmental and hydrodynamic conditions to gather relevant electrochemical data.
- Recreate the experimental conditions within the simulated environment and perform a direct comparison between the simulated and real-world corrosion data.

The final aim of this project is to explore the capabilities of mechanistic corrosion models and identify methods by which they can further developed. The objectives associated with this aim are as follows:

- Conduct a thorough literature review to identify the current known limitations of corrosion models.

- Compile a detailed list of all limitations and inaccuracies identified during the creation of the corrosion models.
- Design methodologies that may be used to improve the models by addressing each of the identified limitations and sources of inaccuracy.
- Generate proof-of-concept simulations for each methodology to demonstrate how it may be applied to improve existing corrosion models.

1.2 Background Theory and Literature Review

1.2.1 Forms of Corrosion

Part of the difficulty in preventing corrosion arises from the number of mechanisms by which it can occur. In 2018, Nogara and Zarrouk[7] published a paper detailing the impact of fluid on corrosion in geothermal environments and listed 10 different mechanisms, namely: uniform attack, pitting, crevice corrosion, stress corrosion cracking, hydrogen embrittlement, erosion-corrosion, inter-granular corrosion, galvanic corrosion, de-alloying, and microbiologically influenced corrosion. Karlsdóttir[2] adds to this list detailing hydrogen-induced cracking, sulphide stress cracking, corrosion fatigue, and exfoliation when discussing material selection in geothermal power production and Kaya and Hoşhan[8] mention hydrogen bubbling and cavitation. The wide range of mechanisms listed by these authors demonstrates the highly complex nature of corrosion and as such these mechanisms will not all be discussed in detail here. However, some of these processes occur much more frequently than others and/or have a more significant impact. These more common and problematic corrosion mechanisms are discussed below:

- **Uniform attack** - The most common form of corrosion, uniform attack is caused by chemical or electrochemical reactions at the metal surface, resulting in uniform mass loss of the metal across the exposed area. In geothermal systems this is usually caused by the presence of CO_2, hydrogen sulphide (H_2S), hydrogen ions (H^+) and chloride ions (Cl^-).
- **Pitting corrosion** - Unpredictable, highly localised form of corrosion characterised by the formation of small holes, or pits, in the material surface. Pitting can be a serious issue, breaking through passive films and deepening, ultimately resulting in failure due to perforation despite low total mass loss.
- **Crevice corrosion** - Geometry dependent form of localised corrosion, accelerated by H^+ and Cl^- ions, which occurs in small crevices. The

crevice causes the flow to stagnate, causing oxygen depletion due to the lack of convection. This causes an excess of positive ions, causing an influx Cl^- ions and lowering the pH, increasing the dissolution rate of the metal.

- **Erosion-corrosion** - Erosion occurs when wearing particles within the fluid traveling at high velocity impact upon the metal surface, resulting in grooves and troughs. The abrasive wear strips away protective surface films, making the metal more vulnerable to corrosive wear. Erosion-corrosion can cause rapid failure, particularly in areas of high flow rates.
- **Galvanic corrosion** – Occurs when two dissimilar metals are immersed in a corrosive solution at different corrosion potentials. The potential difference induces an electron flow between the two materials, accelerating the corrosion rate of the more reactive material.

1.2.2 CO_2 Corrosion

For carbon steels the corrosion rate within a CO_2 saturated environment is primarily driven by the presence of hydrogen (H^+) ions in solution[8]. The presence of these H^+ ions result in the dissolution of iron within the steel at the surface via the following anodic process[9]:

$$\mathrm{Fe_{(s)} \rightarrow Fe^{2+}_{(aq)} + 2e^-} \tag{1.1}$$

The electrons produced by this reaction are consumed by the H^+ ions in an oxidisation reaction, creating hydrogen gas.

$$\mathrm{2H^+_{(aq)} + 2e^- \rightarrow H_{2(g)}} \tag{1.2}$$

Due to this, the production and supply of H^+ ions to the surface are important, and in geothermal environments, this is commonly driven by the high concentrations of dissolved CO_2[2]. The extent to which CO_2 dissolves in water is determined by its fugacity and can be calculated via Henry's Law:

$$a_{CO_2(aq)} = K_H \cdot \varphi \cdot P_{CO2} \tag{1.3}$$

Where $a_{CO_2(aq)}$ is the activity of aqueous carbon dioxide (M), K_H is the Henry's Law constant ($M \cdot atm^{-1}$), φ is the fugacity coefficient and P_{CO_2} is the partial pressure of CO_2 (atm).

The Henry's Law constant changes depending upon the exact composition of ions within the brine, as well as the temperature of the solution. Typical values are approximately $1x10^{-1.5}$ $M \cdot atm^{-1}$ at 25 °C and $1x10^{-1.7}$ $M \cdot atm^{-1}$ at 50 °C[10],

this reduction representing the decreased solubility of CO_2 at higher temperatures.

The dissolved CO_2 then gradually hydrates to form H_2CO_3. It should be noted that due to relatively slow rate of reaction compared to subsequent reactions and the low concentration of H_2CO_3 in relation to CO_2 (≈ 1/1000)[11], the concentrations of both the
dissolved and hydrated forms are commonly abbreviated to $a_{CO_{2(aq)}}$[10, 12].

$$\mathrm{CO_{2(aq)} + H_2O_{(l)} \leftrightarrow H_2CO_{3(aq)}} \tag{1.4}$$

A more precise, temperature dependent value of the hydration constant (K_{hyd}) can be calculated based on the Arrhenius law:

$$K_{hyd} = \frac{a_{H_2CO_{3(aq)}}}{a_{CO_{2(aq)}} \cdot a_{H_2O_{(l)}}} = A_0 e^{\left(-\frac{E_a}{RT_K}\right)} \tag{1.5}$$

Where $a_{H_2CO_{3(aq)}}$ is the activity of H_2CO_3 (M), $a_{H_2O_{(l)}}$ is the activity of water (M), A_0 is the pre-exponent parameter, E_a is the activation energy (J·mol^{-1}), R is the gas constant (J·K^{-1}·mol^{-1}) and T_K is the temperature in Kelvin (K)[12].

Following this, two dissociation reactions take place, resulting in the production of H^+ ions at each stage, as well as bicarbonate (HCO_3^-) and carbonate (CO_3^{2-}) ions:

$$\mathrm{H_2CO_{3(aq)} \leftrightarrow HCO^-_{3(aq)} + H^+_{(aq)}} \tag{1.6}$$

$$\mathrm{HCO^-_{3(aq)} \leftrightarrow CO^{2-}_{3(aq)} + H^+_{(aq)}} \tag{1.7}$$

Additionally, H^+ ions are produced through the dissociation of water, alongside hydroxide (OH^-) ions[12]:

$$\mathrm{H_2O_{(l)} \leftrightarrow OH^-_{(aq)} + H^+_{(aq)}} \tag{1.8}$$

1.2.3 $FeCO_3$ Corrosion Product Formation

It has previously been found that at higher temperatures the corrosion rate in CO_2 saturated environments can begin to decrease[13, 14], this is due to the formation of a protective iron carbonate ($FeCO_3$) layer on the corroding surface. $FeCO_3$ is a form of scaling which commonly accompanies the CO_2 corrosion found in geothermal environments. This is due to the combination of dissociation (Equations 1.6 and 1.7) and surface (Equation 1.1) reactions introducing both Fe^{2+} and CO_3^{2-} ions into solution. When the concentrations of Fe^{2+} and CO_3^{2-} ions in solution become large enough, they precipitate out in the form of $FeCO_3$[9, 15].

$$Fe^{2+}_{(aq)} + {CO_3^{2-}}_{(aq)} \rightarrow {FeCO_3}_{(s)} \quad (1.9)$$

In order for this to occur, the product of the concentrations must exceed the solubility limit (K_{sp}), which is defined as:

$$K_{sp} = [Fe^{2+}]_{eq}[CO_3^{2-}]_{eq} \quad (1.10)$$

Where $[Fe^{2+}]_{eq}$ and $[CO_3^{2-}]_{eq}$ are the aqueous equilibrium concentrations (M)[16].

The precipitated $FeCO_3$ then nucleates on the steel surface in the form of crystals, which grow and reduce the corrosion rate by blocking areas of the surface and acting as a diffusion barrier for the corrosive species[14, 15]. The rate of precipitation is driven by the degree of supersaturation[17] (also known as the saturation ratio) within the solution, which is defined as:

$$SR = \frac{[Fe^{2+}][CO_3^{2-}]}{K_{sp}} \quad (1.11)$$

Where SR is the saturation ratio and $[Fe^{2+}]$ and $[CO_3^{2-}]$ are the species concentrations (M).

When the saturation ratio is above 1, $FeCO_3$ nucleation occurs and forms a uniform protective layer across the surface. Nucleation is possible in undersaturated conditions $(SR < 1)$, however the film formed will be porous and only partially protect the surface beneath, potentially leading to more localised corrosion. As the degree of supersaturation increases, the rate of nucleation increases exponentially, whilst crystal growth increases linearly. Due to this, there are 3 categories into which $FeCO_3$ formation can fall[18]:

- **Metastable/Seeded Growth** - Long induction times for nucleation means that growth only occurs from seed crystals.
- **Heterogeneous Nucleation/Growth** - Nucleation is initiated by surface impurities and imperfections before growth occurs.
- **Homogenous Nucleation/Growth** - Nucleation dominates, limiting crystal growth and producing a nano-crystalline film.

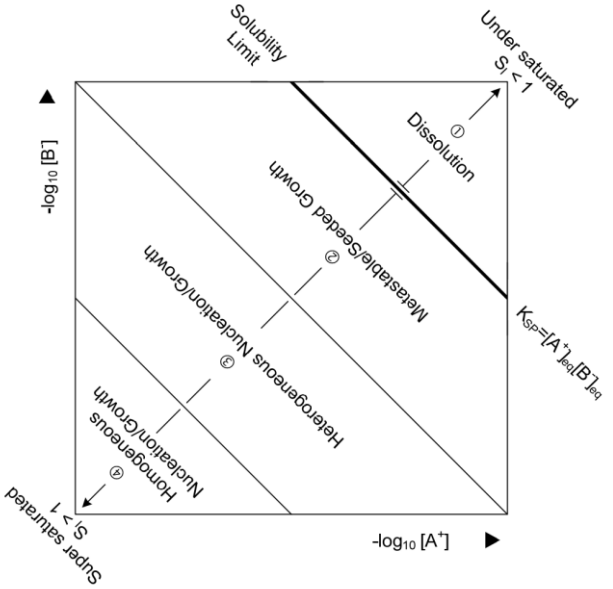

Figure 1-1 – Diagram by Burkle[18], **based on work by Lasaga**[19], **showing the regions of crystal growth depending upon species concentrations, where A^+ and B^- are component species of salt AB.**

In the literature there are four semi-empirical models which have been developed to predict the rate of $FeCO_3$ precipitation, produced by: Sun and Nesic[15], Greenberg and Tomson[20], Johnson and Tomson[21] and van Hunnik et al.[22] The models by Greenberg and Tomson, and Johnson and Tomson assessed seeded crystal growth, whilst the Sun and Nesic, and van Hunnik et al. models assessed precipitation on a steel surface. Therefore, some variation in results is to be expected due to the geometric differences between the two systems and the different growth mechanisms. Despite this, each of these models gives the precipitation rate in the same general form:

$$PR_{FeCO_3} = K_r \left(\frac{A}{V}\right) K_{sp} \sigma(SR) \tag{1.12}$$

Where PR_{FeCO3} is the precipitation rate for $FeCO_3$, and K_r is the rate constant which follows the Arrhenius function (see Equation 1.5), A is the surface area, V is the volume, K_{sp} is the solubility limit and $\sigma(SR)$ is the driving force given as a function of the saturation ratio.

It should be noted that in each of the models the driving force $\sigma(SR)$ is always given in terms of a value of $(SR - 1)$. This is to account for there being zero driving force for precipitation in undersaturated solutions, in which the saturation ratio is below 1.

The model by van Hunnik et al.[22] introduces the concept of the scaling tendency, relating the precipitation rate to the corrosion rate (Equation 1.13).

A high scaling tendency indicates a fast rate of precipitation and therefore a dense protective layer, where as a low scaling tendency indicates a much more porous, less protective film.[9] Van Hunnik et al.[22] also discuss the concept of a critical scaling tendency value, above which an $FeCO_3$ film will begin to grow and the corresponding corrosion rate will decrease.

$$ST = \frac{PR_{FeCO3}}{CR} \tag{1.13}$$

An important distinction made by Sun and Nesic[15] and later reiterated by Barker et al.[14] is the difference between the precipitation rate and the corrosion layer accumulation rate (CLAR). Whilst the precipitation rate describes the amount of $FeCO_3$ within the system, the CLAR relates only to the formation of $FeCO_3$ on the corroding surface. In a review of $FeCO_3$ formation[9] within the oil and gas industry, Sun and Nesic's model was found to be more reliable than other models which did not make this distinction. The three other models, which were based upon measuring the overall change in Fe^{2+} concentration, were found to over-estimate the precipitation rate by several orders of magnitude[9, 23].

However, there is still a significant issue with even the more accurate models in that they define $FeCO_3$ growth in terms of the bulk chemistry and do not account for the surface changes. As shown in Section 1.2.2, CO_2 corrosion causes Fe^{2+} to be released from the metal surface, meaning the local concentration and thus the degree of supersaturation is greater than that of the bulk. Hence, the rate of precipitation at the surface is likely to be greater than that predicted by the models[18]. Another implication of this is that it is possible for $FeCO_3$ to precipitate on the surface at bulk saturation ratios below 1[9].

1.2.4 History of Mechanistic Modelling

In 1992, Turgoose *et al.*[24] developed the first comprehensive mechanistic model for CO_2 corrosion. In this early model, existing understanding of the bulk chemistry and corrosive mechanisms were combined using a finite element model to predict corrosion rates and boundary layer speciation for a rotating disk electrode. Although the model formed a solid starting point for future work, it assumed complete consumption of H_2CO_3 and H^+ at the surface and was therefore only valid under mass-transfer limited conditions. Additionally, the model could not account for the migratory effects of charge separation, nor could it accurately account for the convective term in the near-wall region.

These issues were, however, addressed in a subsequent model produced by Nordsveen *et al.*[25, 26]

The Nordsveen *et al.*[26] model utilised a modified version of the species flux equation to predict the movement of species through the boundary layer. For continuum hydrodynamic models, the velocity of a fluid is taken as zero at the surface[27] (see section 1.2.5). However, turbulent eddies may still permeate through the boundary layer making it difficult to accurately model the instantaneous velocity in the near-wall region. To account for this, the effect of turbulent eddies and their dissipation closer to the surface were incorporated via a turbulent diffusivity term rather than a convection term, an approach originally proposed by Davies in 1972[28].

As well as unifying and simplifying the transport terms, the Nordsveen model implemented an expression for the charge-transfer rate by way of the Tafel equation (see section 1.2.6). The use of the Nernst-Planck equation to calculate the local change in species concentration, alongside the Tafel equation allows for the calculation of the exchange current density from the local surface concentrations of all electroactive species, expanding the applicability of the model past mass-transfer limiting conditions.

However the model by Nordsveen *et al.*[26] did not include calculations of activity coefficients in the equilibrium calculations, which may lead to inaccuracy at higher ionic strengths ($I > 0.01\ M$)[29]. Additionally, they included direct reduction of carbonic acid (H_2CO_3) at the surface, originally proposed by De Waard and Milliams[30], as a secondary cathodic reaction has since been disputed in the literature[31-34]. Despite this, the model provided a solid model framework that has been employed in subsequent comprehensive mechanistic models, such as the models by Song *et al.*[35], Remita *et al.*[32] and, more recently, Kahyarian and Nešić[12, 36].

The 2003 paper by Nordsveen *et al.*[26] formed the first in a series of three papers based around this corrosion model, with subsequent papers by Nešić *et al.*[37] and Nešić and Lee[38]. These additional works highlight the benefit of a comprehensive mechanistic CO_2 corrosion model by utilising the predicted surface speciation to model the formation of protective $FeCO_3$ films. It was shown that bulk pH, temperature, CO_2 partial pressure, dissolved iron concentration, and fluid velocity are all highly influential factors in the formation of $FeCO_3$ films, whilst also demonstrating the importance of understanding surface chemistry in these predictions due to the noticeable divergence from the bulk properties.

In 2019, Kahyarian *et al.*[36] produced a new comprehensive mechanistic model that introduced a number of updates to the earlier work by Nordsveen *et al*.[25, 26] The most significant change was the removal of the direct carbonic acid reduction reaction, utilising the proposed buffering mechanism to describe the surface behaviour with the only cathodic reaction being hydrogen reduction. However, there were further changes made to the equilibrium and rate constants, the hydrodynamic inputs, as well as the anodic mechanisms. A year later, an updated version of the model was published[12] providing additional insights into the model as well as including the effect of activity coefficients. Building on this work, in 2022 Alsalem *et al.*[39] followed a similar approach to predict corrosion across the surface of a rotating cylinder electrode (RCE). As with the earlier model by Nordsveen *et al.*[26], Alsalem *et al*.[39] advanced the corrosion model further by incorporating precipitation of $FeCO_3$ via the surface species concentrations. The model was validated against experimental data from an RCE and therefore included some analysis of the influence of hydrodynamics on the corrosion behaviour, examining how the changes in the tangential surface velocity affected the corrosion rate as well as the coverage and thickness of the $FeCO_3$ layer.

1.2.5 Boundary Layer Theory

When fluid flows parallel to a wall, the generalised flow profile resembles that shown in Figure 1-2. Characterisation of this flow profile is a very useful tool in the prediction of corrosion behaviour as the flow becomes much less turbulent in this region, making it more predictable. The reason for this is due to a phenomenon commonly known as the ‘no-slip condition’, which states that the velocity of a fluid directly adjacent to the wall is zero relative to the surface[27]. The resulting velocity gradient between the fluid at the wall and in the freestream produces the curved flow profile in a region known as the ‘boundary layer’, the height of which is denoted by δ.

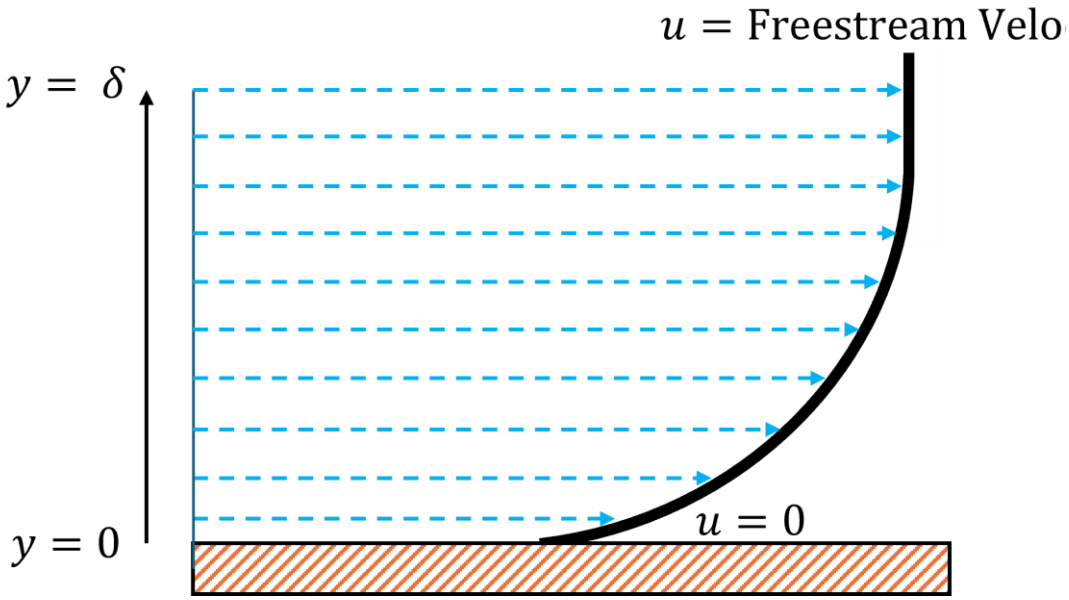

Figure 1-2 - Diagram of the flow profile showing the decreasing velocity of laminar flow approaching a wall due to the no-slip condition

Several different approaches have been developed over the years to characterise and calculate the properties of the flow within the boundary layer. The first challenge with doing so is defining the value of δ, as the transition from static flow to the freestream velocity is continuous, and as such there is no clearly defined point at which the boundary layer ends. One solution to this is simply designate an arbitrary point to represent the end of the boundary layer, which is commonly specified to be the point at which the fluid velocity reaches 99% of the freestream velocity (δ_{99})[28]. A formula for the estimation of this value was proposed by Blasius in 1908 for fluid flowing parallel to a flat plate[40]:

$$\delta_{99} = 5\sqrt{\frac{\nu x}{u_\infty}} \tag{1.14}$$

Where ν is the kinematic viscosity ($m^2 \cdot s^{-1}$), x is the length of the plate (m), and u_∞ is the freestream velocity ($m \cdot s^{-1}$).

Whilst a useful method for rapidly evaluating the change in the boundary layer as a function of the bulk flow, the calculation of δ_{99} does not provide much insight as to the behaviour of the flow within this near-wall region. A more detailed description of the boundary layer profile was put forth by Theodore von Kármán in 1931[41]. Von Kármán's proposal, later termed the 'law of the wall'[42, 43], used dimensionless values for the fluid velocity (u^+) and wall

distance (y^+) to split the boundary layer into three sublayers[44]. These sublayers, known as the viscous sublayer, transitional layer, and log-law region respectively were initially defined via a piecewise function:

$$\begin{cases} 0 \leq y^+ < 5 & u^+ = y^+ \\ 5 \leq y^+ < 30 & u^+ = 5\,(\ln y^+) - 3.05 \\ 30 \leq y^+ & u^+ = 2.5(\ln y^+) + 5.5 \end{cases} \tag{1.15}$$

The form of the equations for the transitional layer and log-law regions can be written more generally as:

$$u^+ = \frac{1}{\kappa}(\ln y^+) + c \tag{1.16}$$

Where κ and c are both constants, with κ being known as the von Kármán constant[45].

In 1961 an updated formula was proposed by Spalding[46], based on the work of Von Kármán and experimental data gathered by Laufer[47], which combined the three functions into a single equation:

$$y^+ = u^+ + 0.1108\left(e^{0.4u^+} - 1 - 0.4u^+ - \frac{(0.4u^+)^2}{2!} - \frac{(0.4u^+)^3}{3!} - \frac{(0.4u^+)^3}{3!}\right) \tag{1.17}$$

A plot of the Spalding equation is shown in Figure 1-3, alongside the original formulae for the viscous sublayer and log-law regions which highlights its effectiveness in capturing the behaviour in both regions.

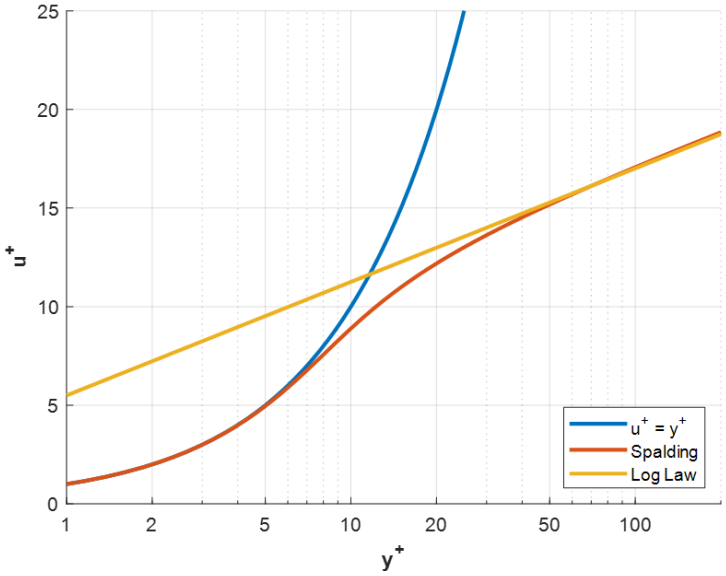

Figure 1-3 - Plot of Spalding function alongside the von Kármán equations for the viscous sublayer and log law region (κ = 0.4 and c = 5.5).

For simple wall-bound flow, the law of the wall is a useful tool for accurately predicting the velocity profile close to the surface. Particularly for common applications such as flow through a smooth pipe or over a flat plate[48]. However, the law of the wall does have its limitations when it comes to more complex flows. Steep pressure/temperature gradients, swirling, impinging, and separating flow can all nullify the applicability of the law. This limitation was demonstrated by Stanković et al.[49] who compared numerical simulations using the law of the wall for both channel flow and a backward-facing step to experimental data. Strong agreement was found between the simulated and experimental data in the case of channel flow, but the model failed to accurately predict near-wall flow in the recirculating region of the backward-facing step. Careful consideration of the complexities of a given flow is therefore required before employing the law of the wall.

1.2.6 Electrochemical Techniques

When corrosion occurs via an electrochemical reaction, it is possible to determine the rate of corrosion from the associated exchange current. This exchange current, also known as the corrosion current, is the current produced by the exchange of electrons in the electrochemical half-reactions (Equations 1.1 and 1.2 for CO_2 corrosion of Fe). It is therefore possible to directly relate the corrosion current to the mass loss of the corroding metal via a relationship known as Faraday's Law:

$$W = \frac{I_{corr} \cdot t \cdot M}{n \cdot F} \tag{1.18}$$

Where W is the mass loss of the corroding metal (g), I_{corr} is the corrosion current (A), t is the time (s), M_w is the molecular weight of the corroding metal (g·mol^{-1}), n is the number of electrons involved, and F is the Faraday constant (96,485 C·mol^{-1}).

The corrosion rate can then be calculated from the mass loss via Equation 1.19.

$$CR = \frac{W}{100 \cdot \rho \cdot A \cdot t} \tag{1.19}$$

Where CR is the corrosion rate (m·s^{-1}), ρ is the density of the metal (g·cm^3), and A is the area of the corroding surface (cm^2).

Hence, if I_{corr} can be determined experimentally, it becomes possible to calculate the corrosion rate of a sample in-situ, without the need for mass-loss measurements. However, this corrosion current cannot be directly measured at the rest potential as both half-cell reactions are occurring at the same rate. The consequence of this is that, despite there being electron transfer in both directions, the net current is zero[4]. Another approach must therefore be taken to determine the magnitude of the corrosion current. In order to understand how this can be achieved, it is first important to review the fundamental principles of electrochemistry.

1.2.6.1 Butler-Volmer Equation

For a single reversible reaction, such as is the case for a metal immersed in a solution of its own ions, the exchange current (i_0) under standard conditions occurs at a standard electrode potential (E^o). When operating under standard conditions, this standard potential represents the reversible potential for the reaction (E_{rev}). However, when the system is under non-standard conditions, the reversible potential changes, and the degree by which it changes is described by the Nernst equation:

$$E_{rev} = E^o - \frac{RT}{nF} \ln\left(\frac{\prod a_p}{\prod a_r}\right) \tag{1.20}$$

Where E^o is the standard electrode potential for the reacting metal (V), R is the gas constant (J·K^{-1}·mol^{-1}), T is the temperature (K), n is the number of involved electrons, F is the Faraday constant, a_p is the activity of the products, and a_r is the activity of the reactants.

When a potential is applied to an electrochemical cell, this is known as 'polarisation', and the degree of polarisation defined by the overpotential (η). The overpotential is calculated as the difference between the electrode potential (E) and the reversible potential.

$$\eta = E - E_{rev} \tag{1.21}$$

Polarising a sample away from the reversible potential shifts the exchange current to favour either the anodic or cathodic components of the reaction. Works by Butler[50-52] and Erdey-Grúz and Volmer[53] between the years of 1924-1932 are credited with combining both these processes into a single equation for the net exchange current density (i_{net})[54]. The resulting equation, commonly termed the Butler-Volmer equation, is comprised of two exponential terms describing the anodic and cathodic current density response:

$$i_{net}^{\leftarrow} = i_0 \left(e^{\frac{\alpha n F \eta}{RT}} - e^{\frac{-(1-\alpha) n F \eta}{RT}} \right) \tag{1.22}$$

Where $i_{net}^{\leftarrow}$ is the net anodic current density (A·m^{-2}), i_0 is the exchange current density (A·m^{-2}), α is a dimensionless parameter between 0-1, n is the number of involved electrons, F is the Faraday constant, η is the overpotential (V), R is the gas constant (J·K^{-1}·mol^{-1}), and T is the temperature in Kelvin (K).

It should be noted that the form of the Butler-Volmer equation given by Equation 1.22 relates to the net anodic current. A corresponding expression can also be formed to calculate the net cathodic current by switching the forwards and backwards components of the reaction[4]:

$$|i_{net}^{\rightarrow}| = i_0 \left(e^{\frac{-(1-\alpha) n F \eta}{RT}} - e^{\frac{\alpha n F \eta}{RT}} \right) \tag{1.23}$$

Where $|i_{net}^{\rightarrow}|$ is the net cathodic current density (A·m^{-2}).

At high anodic overpotentials, the rate of the cathodic reaction is reduced sufficiently as to become negligible. This is known as the 'Tafel region' and under this condition, the Butler-Volmer equation to be simplified:

$$i = i_0 e^{\frac{\alpha n F \eta}{RT}} \tag{1.24}$$

This simplified equation is known as the Tafel equation and, by taking logarithms of both sides, the Tafel equation can then be rearranged into the form:

$$\eta_a = b_a \log\left(\frac{i}{i_0}\right) \tag{1.25}$$

Where η_a is the anodic overvoltage ($E - E_{rev}$ when $E > E_{rev}$) and b_a is the anodic Tafel slope, which is equal to:

$$b_a = \frac{2.303RT}{\alpha nF} \tag{1.26}$$

Applying the same approach to the cathodic branch gives:

$$\eta_c = b_c \log\left(\frac{i}{i_0}\right) \tag{1.27}$$

$$b_c = -\frac{2.303RT}{(1-\alpha)nF} \tag{1.28}$$

Where η_c is the anodic overvoltage ($E - E_{rev}$ when $E < E_{rev}$) and b_c is the cathodic Tafel slope.

In either case, it can be seen that the overpotential is zero ($E = E_{rev}$) when $i = i_0$. This means that either reaction can be plotted on a graph of η against $\log|i|$ and extrapolated back in order to determine i_0.

1.2.6.2 Theory of Mixed Potentials and Tafel Extrapolation

The Butler-Volmer equation is very useful in calculating current density responses for single reversible reactions. However, in corrosive environments it is often the case that the electrochemical behaviour is comprised of multiple reactions which occur irreversibly. A pertinent example of this is the corrosion of Fe in a CO_2 saturated solution which is divided into the anodic dissolution of Fe and the cathodic evolution of H^+ (Equations 1.1 and 1.2). Each of these reactions has their own associated E_{rev} value and as such the Butler-Volmer equation cannot be applied in its standard form.

For cases such as these, the Wagner and Traud theory of mixed potentials is applied instead. The mixed potential theory states that any electrochemical process can be split into two or more partial oxidation and reduction reactions and that the total of all anodic and cathodic reactions must be equal[4]. It is easiest to visualise the information conveyed in the mixed potential theory via an Evans diagram showing the two reactions, such as is shown in Figure 1-4 below.

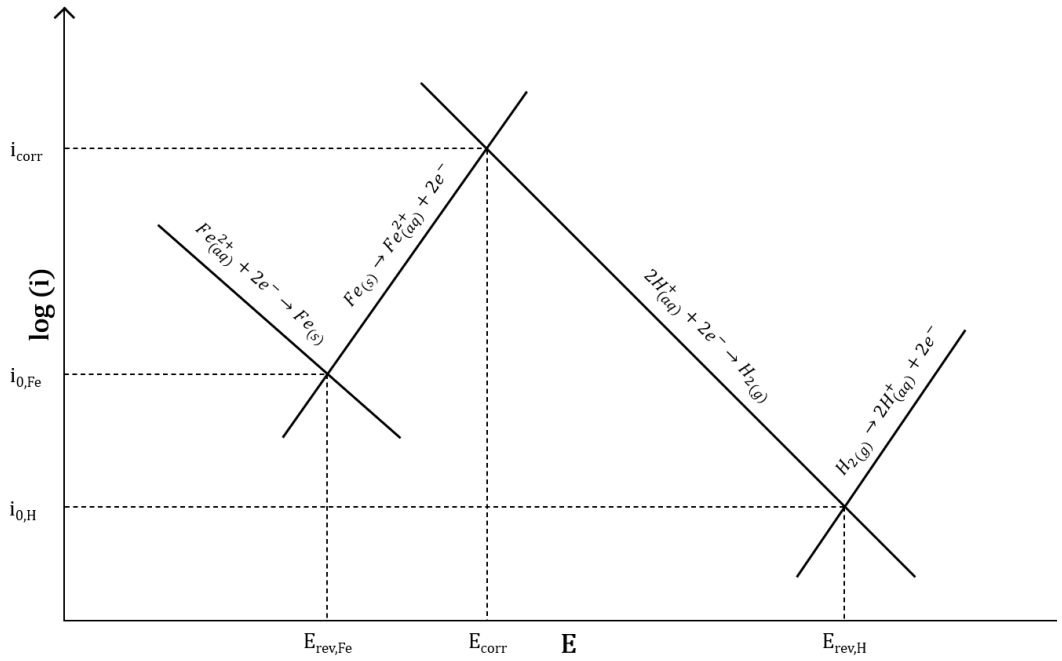

Figure 1-4 - Evans diagram plotting log of current density against potential showing the half-cell reactions for iron dissolution and hydrogen evolution.

The point at which the two half-cell reactions intersect represents the corrosion potential for the system when at equilibrium (E_{corr}). The corrosion potential is similar in concept to the reversible potential of the individual reactions however, it cannot be calculated from thermodynamic principles via the Nernst equation (Equation 1.20), as it is a mixed potential.

At E_{corr}, there is a corresponding corrosion current density (i_{corr}), which represents the exchange current for the corrosion reaction; the net anodic and cathodic reaction rates are equal at this point E_{corr}, also known as the open circuit potential (OCP), is the freely corroding condition for a non-polarised surface and can be directly measured. As discussed previously, the net current at the OCP is zero, meaning that i_{corr} cannot be directly measured. However, based on the understanding the mixed potential theory, polarisation techniques have been derived to predict the value of i_{corr}.

Perhaps the simplest method of determining i_{corr} through polarisation is known as Tafel extrapolation. When a significant anodic overpotential is applied to the surface, it is known that the current response falls in the Tafel region, described by Equation 1.25. Combining this with the theory of mixed potentials gives:

$$\eta_a = b_a \log\left(\frac{i_{Fe} + i_H}{i_{corr}}\right) = b_a \log\left(\frac{i_{net}}{i_{corr}}\right) = b_a \log\left(\frac{i}{i_{corr}}\right) \quad (1.29)$$

This is true for sufficiently high anodic overpotentials since the cathodic currents are small enough to be considered negligible.

For the cathodic branch:

$$\eta_c = b_c \log\left(\frac{i_{Fe} + i_H}{i_{corr}}\right) = b_c \log\left(\frac{i_{net}}{i_{corr}}\right) = b_c \log\left(\frac{i}{i_{corr}}\right) \quad (1.30)$$

Based on this, it is possible to ignore the two negligible reactions and combine the two Butler-Volmer equations (Equation 1.22) for a corroding metal in the following form[4]:

$$i_{net} = i_{corr}\left(e^{\frac{a_a nF(E-E_{corr})}{RT}} - e^{-\frac{(1-a_c)nF(E-E_{corr})}{RT}}\right) \quad (1.31)$$

Where α_a is associated with the anodic reaction and α_c is associated with the cathodic reaction.

Equations 1.29 and 1.30 confirm that when $\eta = 0$ the exchange current is equal to the corrosion current ($i = i_{corr}$) for both branches. Therefore, either branch can be extrapolated back to E_{corr} in order to determine i_{corr}. The process of polarising a sample into the Tafel region in order to determine the Tafel slopes is called Tafel extrapolation.

Using this method the corrosion rate can be determined from either branch of the polarisation curve. If only one is used, it is usually the cathodic curve due to the more well-defined Tafel region as well as the non-destructive nature of the cathodic reaction. However, it is generally more accurate to use both curves as the Tafel slopes should intersect at i_{corr} (see Figure 1-4), and so this method is often preferred. The primary issue with this is that by accelerating the anodic reaction through polarisation, the corrosion rate becomes very high, damaging the surface and preventing re-measurement. Additionally, the method is only valid if well-defined Tafel regions exist and in cases in which the change in potential does not induce any additional electrochemical reactions. For example, in aqueous solutions very negative potentials can induce the reduction of water which will affect the electrochemical measurement.

1.2.6.3 Linear Polarisation Resistance (LPR)

In order to avoid some of the issues with Tafel extrapolation, a new in-situ corrosion measurement technique known as linear polarisation resistance

(LPR) was developed by Stern and Geary[55] in 1957. LPR provides a significant advantage in that it allows for the determination of corrosion rate through the use of small overpotentials, removing the need to significantly polarise the surface.

The method is based upon the observation of small region close to E_{corr} in which the net current density is a linear function of the applied potential. For small overvoltages, the exponentials terms within Equation 1.31 can be expanded via a MacLaurin series; a Taylor series used to approximate the function around $x = 0$. The MacLaurin series takes the form:

$$\sum_{n=0}^{\infty} \frac{f^n(0)}{n!} x^n = f(0) + \frac{f'(0)}{1!}x + \frac{f''(0)}{2!}x^2 + \frac{f'''(0)}{3!}x^3 + \cdots \tag{1.32}$$

When applied to exponential functions $f(x) = e^x$ and $f(x) = e^{-x}$ the resulting expansions are:

$$e^x = 1 + x + \frac{x^2}{2!} + \frac{x^3}{3!} + \cdots \tag{1.33}$$

$$e^{-x} = 1 - x + \frac{x^2}{2!} - \frac{x^3}{3!} + \cdots \tag{1.34}$$

For small values of x, the 2nd order terms and above in this expansion become very small and as such can be considered negligible and removed from the expansion. Applying the Maclaurin series expansion to Equation 1.31 and dropping the 2nd order terms onwards, results in the following expression for the net current density:

$$i_{net} = i_{corr}\left(\left(1 + \frac{a_a nF(E - E_{corr})}{RT}\right) - \left(1 - \frac{(1 - a_c)nF(E - E_{corr})}{RT}\right)\right) \tag{1.35}$$

$$i_{net} = i_{corr}\left(\frac{a_a nF(E - E_{corr})}{RT} + \frac{(1 - a_c)nf(E - Ecorr)}{RT}\right) \tag{1.36}$$

Combining Equation 1.36 with Equations 1.26 and 1.28 allows the net current density to be written in terms of the Tafel constants:

$$i_{net} = i_{corr}\left(\frac{2.303(E - E_{corr})}{b_a} + \frac{-2.303(E - E_{corr})}{b_c}\right) \tag{1.37}$$

$$i_{net} = 2.303 \cdot \eta \cdot i_{corr}\left(\frac{1}{b_a} + \frac{1}{-b_c}\right) \tag{1.38}$$

Remembering that $(E - E_{corr})$ is the overpotential represented by η.

Given that the cathodic current is always negative with respect to the anodic current, the $-b_c$ term can be substituted with $|b_c|$.

Rearranging to give η in terms of the current densities gives:

$$\eta = \frac{i_{net}}{2.303 \cdot i_{corr}\left(\frac{1}{b_a} + \frac{1}{|b_c|}\right)} \tag{1.39}$$

Taking derivatives with respect to i_{net} as η approaches zero:

$$\left(\frac{d\eta}{di_{net}}\right)_{\eta \to 0} = \frac{1}{2.303 \cdot i_{corr}\left(\frac{1}{b_a} + \frac{1}{|b_c|}\right)} \tag{1.40}$$

The differential in Equation 1.40 represents the resistance of the system around i_{corr} and is therefore known as the polarisation resistance (R_p).

$$R_p \equiv \left(\frac{d\eta}{di_{net}}\right)_{\eta \to 0} \tag{1.41}$$

Substituting R_p back into Equation 1.39 and rearranging produces a final expression to calculate i_{corr}, known as the Stearn-Geary equation:

$$i_{corr} = \frac{1}{2.303 \cdot R_p \cdot \left(\frac{1}{b_a} + \frac{1}{|b_c|}\right)} \tag{1.42}$$

If the Tafel constants b_a and b_c are known for a given system, the Stearn-Geary equation allows for the determination of i_{corr} by applying a small potential either side of E_{corr} and measuring the current response. The gradient of the resulting linear slope is equal to R_p (Equation 1.41).

The corrosion current density (i_{corr}) can be converted into a corrosion current (I_{corr}) by multiplying by the surface area of the corroding metal.

$$I_{corr} = i_{corr} \cdot A \tag{1.43}$$

Equations 1.18 and 1.19 can then be used to convert I_{corr} into an associated mass loss and a corresponding corrosion rate.

1.2.6.4 Electrochemical Impedance Spectroscopy (EIS)

LPR is an efficient technique for rapidly evaluating the corrosion rate of a surface, however it cannot distinguish between the sources of the polarisation resistance. Resistances introduced by the formation of a protective layer or even within the solution itself can introduce inaccuracies into LPR

measurements[3]. In such cases, a different technique is often used known as electrochemical impedance spectroscopy (EIS).

EIS functions by applying a sinusoidal input signal to an electrochemical cell and then measuring the magnitude and phase shift of the corresponding sinusoidal output. Using a potentiostat, a low amplitude alternating voltage can applied to the system at a specific frequency[56]:

$$E(t) = E_0 \sin(\omega t) \tag{1.44}$$

Where $E(t)$ is the applied potential as a function of time, E_0 is the amplitude of the applied potential, and ω is the frequency of the applied potential.

Assuming the same output frequency, the measured current response can be written in the form:

$$i(t) = i_0 \sin(\omega t + \Phi) \tag{1.45}$$

Where $i(t)$ is the output current as a function of time, i_0 is the magnitude of the output current, and Φ is the phase shift.

The magnitude of the impedance ($|Z|$) at the specified frequency can then be determined by:

$$|Z| = \frac{E_0(t)}{i_0(t)} \tag{1.46}$$

By combining $|Z|$ and Φ, the impedance can be split into its real and imaginary components (Z_{Re} and Z_{Im} respectively):

$$Z_{Re} = |Z| \cos(\Phi) \tag{1.47}$$

$$Z_{Im} = |Z| \sin(\Phi) \tag{1.48}$$

This impedance response will vary at different frequencies based upon the timescales of the underlying electrochemical processes[57]. Therefore, by applying signals across a wide range of frequencies, it is possible to obtain a characteristic response which separates the individual contributions of different reactions. The real and imaginary impedance values for each frequency are plotted on a single graph, known as a Nyquist plot (see Figure 1-5 as an example).

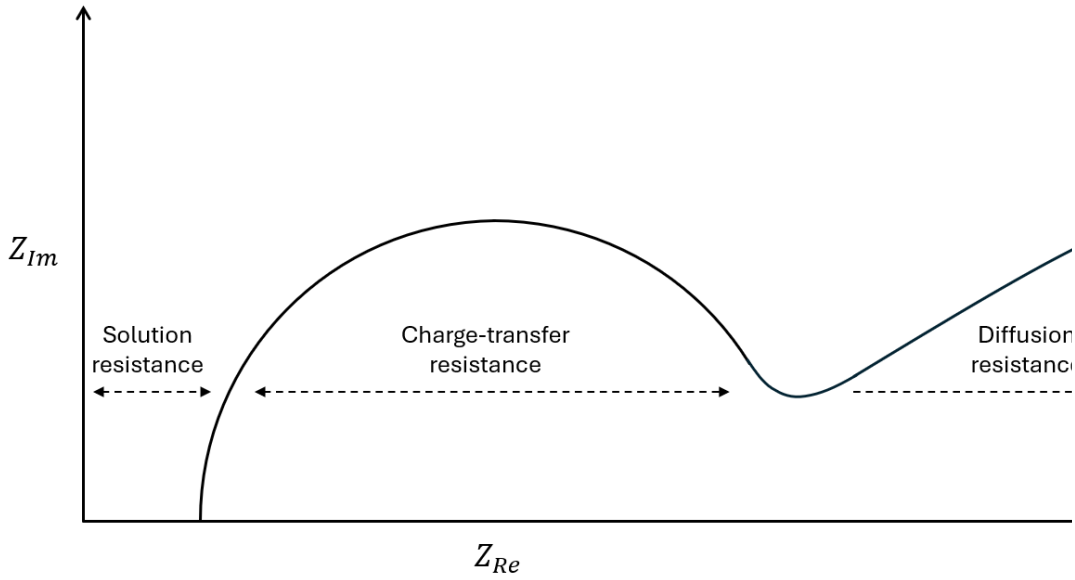

Figure 1-5 – Example schematic of a Nyquist plot showing various electrochemical contributions to impedance measurements.

Interpreting Nyquist plots can be difficult as the impedance of specific processes are not known. However, common circuit elements such as resistors, capacitors, and inductors have known impedance values, and so by equating electrochemical processes to these elements, an equivalent circuit can be designed[56]. Using the known impedance values, curve fitting software can then be used to mathematically describe the impedance response. This can provide valuable insight into the electrical properties of the individual reactions and therefore be used to evaluate specific characteristics of the electrochemical cell, such as the growth of surface films[58], or the resistance of the solution between the working and reference electrodes[33, 59].

1.3 Bulk Chemistry Model

In general, the starting point in the development cycle for computational corrosion models is the calculation of the bulk chemistry. As detailed in section 1.2.2, when water is saturated with gaseous CO_2, a proportion of the CO_2 will become dissolved in solution, depending on the pressure (Equation 1.3). A series of reversible reactions then occur (Equations 1.4 and 1.6-1.8) which introduce 5 additional species into solution, namely H_2CO_3, HCO_3^-, CO_3^{2-}, H^+, and OH^-. The proportional concentrations of each of these species will change dependent upon the environmental conditions, in particular the temperature and the pH of solution.

Mathematically, the steady-state concentration of species in each reversible reaction is described using an equilibrium constant. These constants describe the relative rates of the forwards and backwards reactions and can be integrated into a system of equations to describe the overall solution chemistry. The list of equilibrium constants within a simple CO_2-H_2O system and their associated definitions are summarised.

Table 1.1 – Summary of equilibrium constants and definitions for a CO_2-H_2O system.

Reaction	Equilibrium Constant	Definition
$CO_{2_{(g)}} \leftrightarrow CO_{2_{(aq)}}$	K_H	$\frac{a_{CO_{2(aq)}}}{P_{CO_2}}$
$CO_{2_{(aq)}} + H_2O_{(l)} \leftrightarrow H_2CO_{3(aq)}$	K_{hyd}	$\frac{a_{H_2CO_3}}{a_{CO_{2(aq)}} \cdot a_{H_2O}}$
$H_2CO_{3(aq)} \leftrightarrow HCO_3^-{}_{(aq)} + H^+_{(aq)}$	K_{ca}	$\frac{a_{HCO_3^-} \cdot a_{H^+}}{a_{H_2CO_3}}$
$HCO_3^-{}_{(aq)} \leftrightarrow CO_3^{2-}{}_{(aq)} + H^+_{(aq)}$	K_{bi}	$\frac{a_{CO_3^{2-}} \cdot a_{H^+}}{a_{HCO_3^-}}$
$H_2O \leftrightarrow OH^-_{(aq)} + H^+_{(aq)}$	K_w	$\frac{a_{OH^-} \cdot a_{H^+}}{a_{H_2O}}$

Where a_j represents the activity of species j.

$$a_j = \gamma_j \cdot c_j \tag{1.49}$$

Where γ_j is the activity coefficient and c_j is the concentration of species j.

It should be noted that the definitions of the equilibrium constants provided in Table 1.1 are in the form:

$$K_{eq} = \frac{a_p}{a_r} \tag{1.50}$$

Where a_p is the activity of the products and a_r is the activity of the reactants.

In most instances this aligns with the format provided within the literature[3, 12, 26, 36, 60-62]. However, there is some inconsistency regarding how K_H is presented, with some authors preferring to define it as the inverse of Equation 1.50[60, 61]. For consistency, all equilibrium constants within this work are defined in the form shown above.

1.3.1 MATLAB Model

From the definitions of the equilibrium constants provided in Table 1.1, it is possible to define a set of equations which may be solved to calculate the species concentrations for a given set of conditions. As a starting point for the corrosion modelling within this work, an initial bulk chemistry model was created within MATLAB. The purpose of this model is to form a reference point for the more complex models discussed in subsequent chapters, providing an initial point of verification for the bulk chemistry calculations included within those models.

For this simple model, the solution was assumed to be ideal, meaning species activity was not considered and as such y_i was set equal to unity for all species. The reason for this was so that all species activity values could be substituted with their concentrations, reducing the complexity of the calculations. For dilute solutions, it is known the species activity does not significantly affect the solution chemistry[29]. Therefore, given that the purpose of this model is only to provide an initial approximation for the species concentrations, this is simplification is justified.

1.3.1.1 Equilibrium Constants

The equilibrium constants K_H, K_{ca}, and K_{bi} were calculated according to the 2007 paper by Li and Duan[61], with the ion product of water (K_w) being based on prior work from Marshall and Franck[62]. Table 1.2 summarises the parameters used in the calculation of the equilibrium constants, assuming the density of water (ρ_w) to be 1,000 kg·m^{-3} at a pressure of 1 bar and temperatures < 373.15 K.

Table 1.2 – Parameters for the calculation of equilibrium constants in bulk chemistry model.

Input Parameters	K_H	K_{ca}	K_{bi}	K_w
a_1	14.00	233.52	-1.51×10^2	-4.10
a_2	-1.33×10^{-2}	0	-8.87×10^{-2}	-3.25×10^3
a_3	-5.59×10^2	-1.20×10^4	-1.36×10^3	2.24×10^5
a_4	-4.23×10^5	0	0	-3.98×10^7
a_5	0	-36.51	27.80	–

Using the parameters provided in Table 1.2, K_H is calculated via Equation 1.51, K_{ca} and K_{bi} are calculated via Equation 1.52, and K_w is calculated via Equation 1.53.

$$K_H = a_1 \cdot e\left(\frac{a_2}{R} \cdot T_K\right) \tag{1.51}$$

$$\ln(K) = a_1 + a_2 \cdot T_K + \frac{a_3}{T_K} + \frac{a_4}{T_K^2} + a_5 \cdot \ln(T_K) \tag{1.52}$$

$$\log_{10}(K_w) = a_1 + \frac{a_2}{T_K} + \frac{a_3}{T_K^2} + \frac{a_4}{T_K^3} + \tag{1.53}$$

The hydration constant (K_{hyd}) was set to a value 2.58×10^{-3} based on values provided by Palmer and van Eldik[63].

1.3.1.2 Speciation Equations

From the definitions of the calculated equilibrium constants provided in Table 1.1, it is possible to devise a set of simultaneous equations in which the number of equations and the number of unknowns is equal, making them solvable. These equations are shown below, in each case the unknown variables have been moved to the left-hand side of the equal.

Note that the gaseous CO_2 is assumed to be ideal in this case, meaning the fugacity coefficient (φ_{CO_2}) is set equal to one.

$$f_{CO_2} = P_{CO_2}\varphi_{CO_2} \tag{1.54}$$

$$[H^+] = 10^{-pH} \tag{1.55}$$

$$\left[CO_{2(aq)}\right] - K_H \cdot f_{CO_2} = 0 \tag{1.56}$$

$$[H_2CO_3] - K_{hyd} \cdot \left[CO_{2(aq)}\right] = 0 \tag{1.57}$$

$$[HCO_3^-] \cdot [H^+] - K_{ca} \cdot [H_2CO_3] = 0 \tag{1.58}$$

$$[CO_3^{2-}] \cdot [H^+] - K_{bi} \cdot [HCO_3^-] = 0 \tag{1.59}$$

$$[H^+] \cdot [OH^-] = K_w \tag{1.60}$$

1.3.1.3 Matrix Solver

Whilst solvable by hand for a given set of conditions, it is much more efficient to solve the set of simultaneous equations given in Equations 1.54-1.60 using a matrix method. By generating matrices of coefficients ($[A]$), unknown variables ($[C]$), and known values ($[S]$), it is possible to rewrite the equations in the form:

$$[A] \cdot [C] = [S] \tag{1.61}$$

The values of the unknown variables can therefore be calculated by multiplying the inverse of the matrix of coefficients by the matrix of known values.

$$[C] = [A]^{-1} \cdot [S] \tag{1.62}$$

The structure of theses matrices as they relate to the reactions being evaluated here are displayed in Table 1.3.

Table 1.3 - Summary of equilibrium reactions and associated matrix contributions for the calculation of bulk species concentrations.

Equations / Species	f_{CO_2}	C_{CO2}	C_{H^+}	$C_{H_2CO_3}$	$C_{HCO_3^-}$	$C_{CO_3^{2-}}$	C_{OH^-}		
$f_{CO_2} = P_{CO_2}\varphi_{CO_2}$	1	0	0	0	0	0	0	f_{CO_2}	$P_{CO_2}\varphi_{CO_2}$
$[H^+] = 10^{-pH}$	0	0	1	0	0	0	0	$[CO_{2(aq)}]$	10^{-pH}
$[CO_{2(aq)}] - K_H \cdot f_{CO_2} = 0$	$-K_H$	1	0	0	0	0	0	$[H^+]$	0
$[H_2CO_3] - K_{hyd} \cdot [CO_{2(aq)}] = 0$	0	$-K_{hyd}$	0	1	0	0	0	$[H_2CO_3]$	0
$[HCO_3^-] \cdot [H^+] - K_{ca} \cdot [H_2CO_3] = 0$	0	0	0	$-K_{ca}$	10^{-pH}	0	0	$[HCO_3^-]$	0
$[CO_3^{2-}] \cdot [H^+] - K_{bi} \cdot [HCO_3^-] = 0$	0	0	0	0	$-K_{bi}$	10^{-pH}	0	$[CO_3^{2-}]$	0
$[H^+] \cdot [OH^-] = K_w$	0	0	0	0	0	0	10^{-pH}	$[OH^-]$	K_w
	$[A]$							$[C]$	$[S]$

Combining Equation 1.62 with the information provided in Table 1.3 results in the matrix shown below, which when solved via MATLAB produces an output matrix of bulk concentration values.

$$[C] = \begin{bmatrix} 1 & 0 & 0 & 0 & 0 & 0 & 0 \\ 0 & 0 & 1 & 0 & 0 & 0 & 0 \\ -K_H & 1 & 0 & 0 & 0 & 0 & 0 \\ 0 & -K_{hyd} & 0 & 1 & 0 & 0 & 0 \\ 0 & 0 & 0 & -K_{ca} & 10^{-pH} & 0 & 0 \\ 0 & 0 & 0 & 0 & -K_{bi} & 10^{-pH} & 0 \\ 0 & 0 & 0 & 0 & 0 & 0 & 10^{-pH} \end{bmatrix}^{-1} \cdot \begin{bmatrix} f_{CO_2} \\ [CO_{2(aq)}] \\ [H^+] \\ [H_2CO_3] \\ [HCO_3^-] \\ [CO_3^{2-}] \\ [OH^-] \end{bmatrix}$$

Structuring the equilibrium equations allows for rapid calculation of the bulk species concentrations. By combining this with a for loop, it is possible to iterate through input conditions and evaluate how the concentrations change. For example, Figure 1-6 shows how the concentration of bulk species changes as a function of pH.

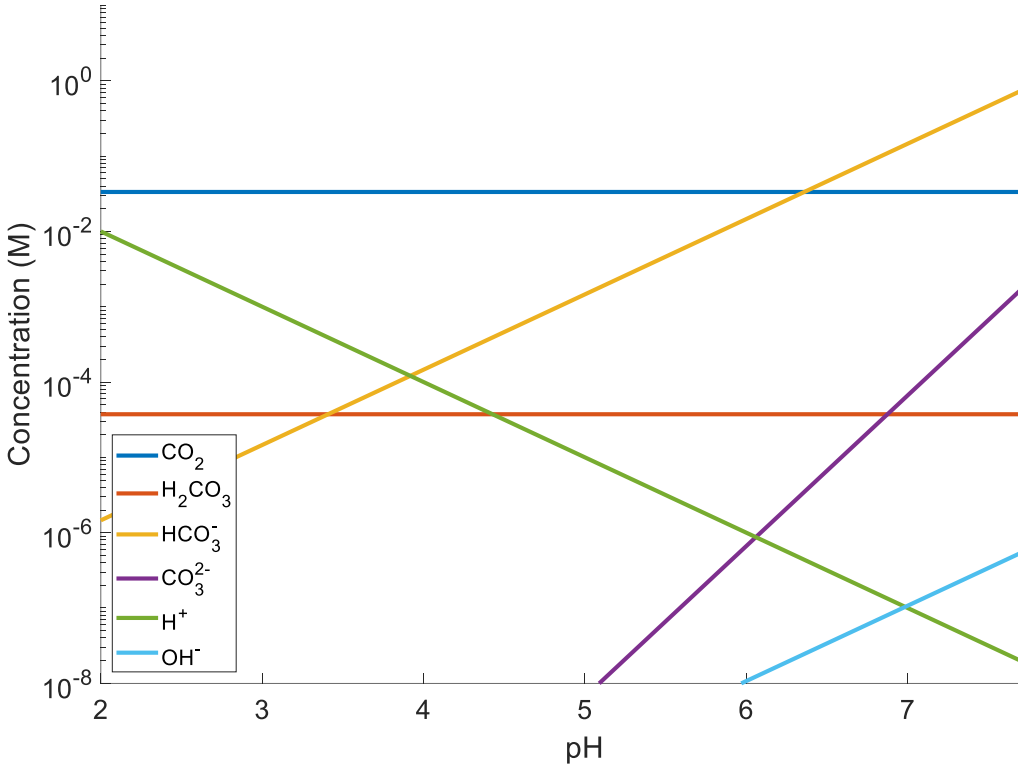

Figure 1-6 - Plot of bulk species concentrations as a function of solution pH at a temperature of 298.15 K and pressure of 1 bar.

1.3.2 Unbuffered pH

Alongside the equilibrium state of the dissolved species, it is also possible to use the MATLAB model described in section 1.3.1 to calculate the equilibrium state of the system as a whole. For a given set of environmental conditions, the CO_2-H_2O system will default to a natural pH based on the chemical equilibria of the contributing reactions. This is the pH the solution will reach and maintain without the introduction of additional species. The calculation of the natural pH is based upon the understanding that the total charge sum within a system at equilibrium is zero.

$$\sum_j z_j c_j = 0 \tag{1.63}$$

When c_i and z_i are the concentration and associated charge of species j respectively.

Based on the species included within the bulk chemistry model, the charge sum for any given set of conditions is calculated as:

$$\sum_j z_j c_j = [H^+] - [HCO_3^-] - 2[CO_3^{2-}] - [OH^-] \tag{1.64}$$

By calculating the total charge sum across the range of pH values it is therefore possible to identify the natural pH. For example, the charge balance at a temperature of 298.15 K and a CO_2 partial pressure of 1 bar are shown in Figure 1-7. The common logarithm of the absolute values is plotted to provide a clear indication of the natural pH, as occurs at the lowest point when the charge sum is approximately zero.

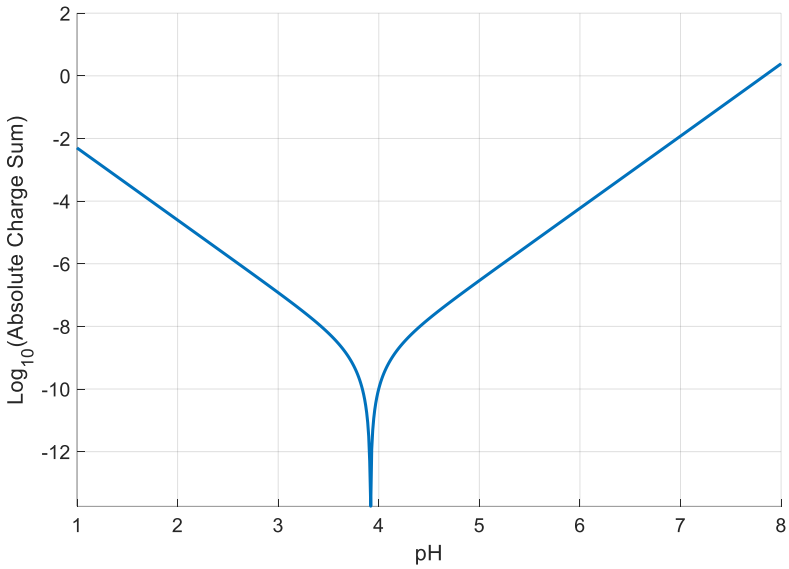

Figure 1-7 - Plot of the charge balance as a function of pH for a CO_2-H_2O system at 298.15 K and 1 bar P_{CO2}.

For the conditions shown in Figure 1-7, the natural pH of the system is calculated to be 3.92 to 2 decimal places. Using this approach, the natural pH the system can be readily calculated for any set of initial conditions. The pH of the system can be adjusted through the addition of either anions or cations which shift the charge balance. However, these will shift the ionic strength of the solution, and so knowing the natural pH of the system is important to accurately account for the concentration of these added species when calculating the ionic strength.

1.4 Fluid Flow Modelling

Accounting for the movement of fluids is a highly important consideration in a wide range of industries. In the aerospace industry for example, a strong understanding of aerodynamics, the field of study which focuses on the motion

of gases, is vital in the design and optimisation of aircraft. Similarly, in the geothermal industry, a strong understanding of hydrodynamics, which focuses on the motion of liquids, is necessary when identifying high risk areas of geothermal wells[2, 7]. Both aerodynamics and hydrodynamics fall under the field of fluid dynamics, which looks at the motion and forces associated with fluids in general. Part of the difficulty in predicting the movement of fluids is their often highly erratic nature and as such modelling this behaviour can become highly complex. The field of study which looks at numerically predicting fluid motion is known as computational fluid dynamics (CFD). The following section outlines the general approach used within CFD, as well as how this can then be applied to real-world problems.

1.4.1 Basics of Fluid Flow Modelling

In order to understand how the motion of a fluid can be modelled, it is first necessary to understand the fundamental principles of fluid dynamics which control the behaviour. There are three physical laws of particular importance when calculating the motion of a fluid:

1. Conservation of mass – For a closed system, the mass of the system must remain constant over time.

2. Conservation of momentum – For a closed system, the total momentum within the system must remain constant over time.

3. **Conservation of energy** – For a closed system, the total energy of the system must remain constant over time.

From these fundamental principles, a set of equations were developed in the 1800s by Claude-Louis Navier and George Gabriel Stokes which describe the motion of viscous fluids[64]. These equations, now known as the Navier-Stokes equations, are the basis for all modern fluid flow modelling:

$$\frac{\partial \rho}{\partial t} + \rho \vec{\nabla} \cdot \vec{u} = 0 \tag{1.65}$$

$$\rho \frac{\partial \vec{v}}{\partial t} + \rho\left(\vec{v} \cdot \vec{\nabla}\right)\vec{u} = -\vec{\nabla} p + \mu \Delta \vec{u} + \rho \vec{f_e} \tag{1.66}$$

$$\frac{\partial \rho E_T}{\partial t} + \vec{\nabla} \cdot (\rho \vec{u} E_T) = \vec{\nabla} \cdot \left(k \vec{\nabla} T\right) + \vec{\nabla} \cdot (\bar{\bar{\sigma}} \cdot \vec{u}) + W_f + q_H \tag{1.67}$$

Where ρ is the density of the fluid, u is the fluid velocity, f_e is the contribution of external volume forces, E_T is the total energy, k is the thermal diffusivity coefficient, T is the absolute temperature, $\bar{\bar{\sigma}}$ is the internal stress tensor, W_f is the work of external volume forces, and q_H is the heat released by chemical reactions[65].

The Navier-Stokes equations may also be accompanied by an equation of state, which relates 'state variables' such as pressure, volume, temperature, and internal energy[66]. A simple, yet common example of such an equation is the 'ideal gas law', which relates the density of an ideal gas to the pressure and temperature:

$$PV = nRT \tag{1.68}$$

Combined, these equations make it possible to predict the movement of a fluid continuum (fluid that is not considered as discrete particles) on both macroscopic and microscopic length scales.

1.4.1.1 Turbulence Models

Whilst the form of the Navier-Stokes equations is well-understood, actually solving the equations presents an entirely new challenge. In fact, the complexity of these equations is so great that proving an analytical solution to the Navier-Stokes equations constitutes one of the still unsolved Millenium Prize Problems posed by the Clay Institute back in 2000[67].

Numerical solutions to the Navier-Stokes problems are however possible to calculate via a method known as 'direct numerical simulation' (DNS), which resolves turbulence variables across all spatial and temporal length scales. The lower limits of the length scales necessary to be resolved within DNS are generally quoted to be the Kolmogorov microscales, calculated as functions of the kinematic viscosity (ν) and the average rate of energy dissipation per unit mass (ε)[68].

$$\eta_K = \left(\frac{\nu^3}{\varepsilon}\right)^{\frac{1}{4}} \tag{1.69}$$

$$\tau_\eta = \left(\frac{\nu}{\varepsilon}\right)^{\frac{1}{2}} \tag{1.70}$$

Where η_K and τ_η are the Kolmogorov length and time scales respectively.

The problem with the DNS method however is that the Kolmogorov microscales are incredibly small (typically 10^{-4} or smaller[68]) and as such vast amounts of computational power are required to solve the Navier-Stokes equations using this method. Due to this, DNS is not currently a viable method for the vast majority of complex flow problems. A much more common approach therefore is to instead approximate the solution, which can be achieved via the use of turbulence models.

Turbulence models are mathematical models which attempt to predict the effects of turbulence without directly solving the Navier-Stokes equations. The most prevalent category of turbulence models used today are known as Reynolds-Averaged Navier-Stokes (RANS) turbulence models. RANS models function by dividing the flow into time-averaged and fluctuating components in a process known as Reynolds decomposition[69].

$$u_i = \overline{u_i} + u_i' \tag{1.71}$$

$$P = \overline{P} + P' \tag{1.72}$$

Where $\overline{u_i}$ and $\overline{P}$ are the mean values, and u_i' and P' are the fluctuating values of the velocity and pressure, respectively.

By averaging these values over time, it is possible to achieve a reasonable approximation for the motion of a fluid without needing to fully solve the Navier-Stokes equations. However, this averaging process results in an additional term known as the Reynolds stress tensor (τ_{ij}), which leads to a closure problem for the equations[69].

$$\tau_{ij} = \overline{u_i' u_j'} \tag{1.73}$$

A common approach to deal with this problem is via the Boussinesq hypothesis, which expresses this tensor in terms of the gradient of the mean velocity field[70]. But the Boussinesq hypothesis also requires an additional term known as the 'eddy viscosity' (μ_t), which can be calculated using a turbulence model.

In general, RANS models can be categorised based upon the number of additional equations they employ to obtain the value of eddy viscosity. They can be grouped into algebraic, one-equation, or two equation models[71]. Algebraic, or zero-equation, models are the simplest class of RANS turbulence models which attempt to calculate eddy viscosity by relating it directly to the mean flow velocity[72]. Examples of algebraic turbulence models include the mixing length model[73], the Cebeci-Smith model[74], and the Baldwin-Lomax model[75]. These models are easy to implement and so have been useful in the modelling of simple aerodynamic problems. The issue however is that they massively simplify the effects of turbulence by assuming a single length and time scale, and as such are generally not valid in more complex turbulent scenarios[69].

One-equation models attempt to account for non-local turbulent effects via the inclusion of a transport equation to calculate average turbulent kinetic

energy[69]. In effect, this allows the models to account for history effects within the flow, such as the generation of turbulence upstream of a given point. Examples of one-equation models include the Spalart-Allmaras model[76] and the Baldwin-Barth model[77]. One-equation models have been found to be useful for certain specific applications, such as modelling external flows in aerospace applications. However, in general, these simple models have been found to be generally inaccurate due to their limited description of turbulence[69, 78].

By far the most widely used RANS turbulence models are the two-equation models. These build upon the one-equation models by introducing a second equation alongside the transport which calculates the characteristic turbulent length scale[78]. This allows for a more complete description of turbulent behaviour by also modelling the dissipation of turbulent eddies. In general, this is done using one of two categories of model: k-ε models which calculate the turbulent dissipation rate (ε), or k-ω models which calculate the specific rate of dissipation (ω)[79]. Due to their combination of accessibility and generally strong performance, both k-ε and k-ω models have seen widespread use in a range of industries, including the automative[80], medical[81], energy[82, 83], and agricultural[84] sectors. As a result of this, sub-categories of these models have been developed including the Realizable k-ε, Renormalization Group (RNG) k-ε, and k-ω SST variations[85]. Each of these variations has slightly different formulations for the turbulence calculations which improve their performance in different scenarios.

There does also exist another method for modelling fluid flow which is an intermediary between DNS and RANS models, known as ‘Large Eddy Simulation’ (LES). LES directly solves the Navier-Stokes equations for large scale eddies, whilst modelling the small-scale eddies[78]. In doing so the method is not as computationally expensive as DNS, but it is able to accurately model transient effects on the larger scale, which may not be captured in a RANS model. However, despite, the reduced computational cost, LES still requires significant computational power to fully resolve. There have therefore been advancements in recent years looking at developing hybrid models which combine the RANS and LES approaches[69, 86].

1.4.1.2 Meshing and Discretization

Instead of solving a single set of continuous equations across the entire domain, numerical models function by solving their associated equations at a number of discrete points. In order to do this, a domain must be divided into a

number of smaller sections in a process called discretization. The result of the discretization process, known as a mesh, is comprised of a number of elements and nodes which can then be used as reference points to solve turbulence models.

The are two main types of meshes that can be generated: structured and unstructured. Structured meshes are comprised of regular element shapes distributed throughout the domain which may be skewed to follow the boundaries of the domain. Unstructured meshes on the other hand allow cells to be freely assembled within the domain, resulting in a combination of different mesh shapes. Both methods have their advantages and disadvantages. Structured meshes tend to have much more consistent co-ordinate systems making it much easier to manage and process output data. Additionally, the uniformity of structured meshes allows more sophisticated numerical techniques to be utilised to calculate higher order approximations of derivative terms, thereby improving the accuracy of solutions[87, 88]. However, structured meshes can be difficult to fit to complex geometries and may lead to the generation of highly skewed, non-orthogonal elements which increase complexity and can affect both solver times and accuracy. Unstructured meshes on the other hand are much more suited to arbitrary geometries, particularly those with high curvature due to the flexibility in their arrangement. However, the data is much less organised than in a structured mesh, and their tendency to generate long, thin elements adjacent to wall boundaries can lead to inaccuracies when approximating diffusive fluxes[89].

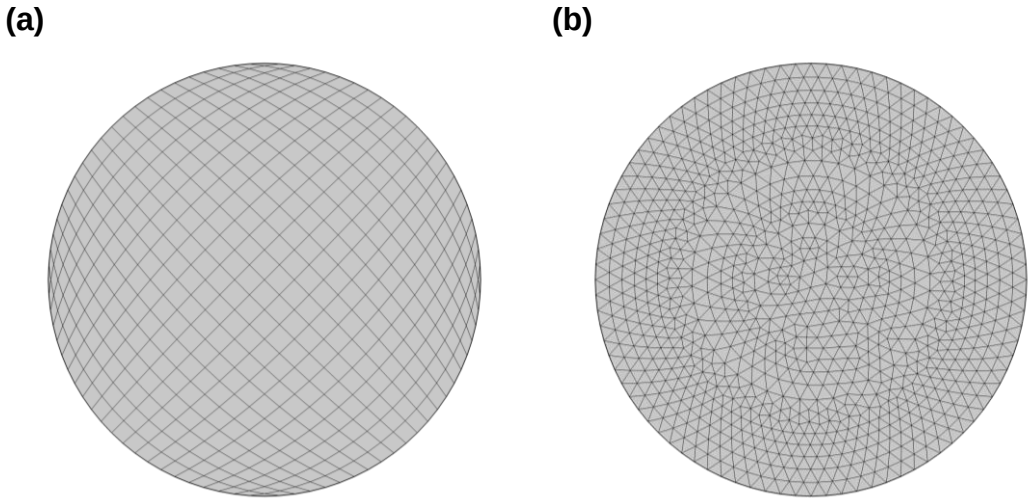

Figure 1-8 - Examples of (a) structured and (b) unstructured meshes within a circular domain.

1.4.1.3 Discretization Methods

When it comes to actually solving the equations within a CFD model, there are several numerical techniques that can be employed. There are three methods which are used for the vast majority of CFD problems, namely the finite difference method (FDM), the finite volume method (FVM), and the finite element method (FEM). These numerical methods differ based upon how they store dependant variables and discretize the differential equations across the domain. Put simply, once the domain has been meshed:

- FDM stores both dependant variables and solves the differential equations at each of the discrete node points.
- FEM stores dependant variables at the nodes points but solves the differential equations along the elements connecting the nodes.
- FVM stores dependant variables at the cell centres and solves the differential equations within a control volume[90].

The performance of each of these methods can vary significantly, making direct comparisons between them difficult. FDM is perhaps the simplest of the methods with a low computational cost, however unlike FEM and FVM it is limited in that it can only be applied to structured grids[91]. FVM also has advantages when dealing with discontinuities and sharp gradients, as the method involves calculating fluxes across control volume boundaries, guaranteeing conservation properties throughout the domain. FEM on the other hand is perhaps the most flexible technique, making it beneficial for use in highly complex geometries[92, 93]. Each of the numerical methods can generally be used to provide a reasonable approximation of a given system, however an understanding of each approach can help to optimize solutions for specific applications.

For steady-state problems, solutions can be calculated either directly or iteratively using a stationary solver. Stationary solvers assume no transient effects and as such only need to calculate one solution, allowing for much shorter solve times. However, for scenarios which vary with time, time-dependent solvers must be used instead. These introduce an additional consideration, as time-dependent solutions can be calculated either explicitly or implicitly. Explicit methods calculate the solution at the next time step based upon known values form the current state, whilst implicit methods extrapolate forward to use implicit values from the next time and therefore cannot be calculated directly. Due to the additional calculations required, implicit solvers

tend to be more computationally expensive per incremental step, however they are also much more stable and allow for calculations over much greater increments than explicit solvers. Implicit solvers therefore tend to be used for slower, more linear problems and explicit solvers tend to be used for rapid, highly non-linear problems[94].

COMSOL Multiphysics®, the modelling software that will be used throughout this thesis, is FEM-based and primarily utilizes implicit methods to solve simulations[95]. The software was chosen due to its in-built functionality to set-up and solve both electrochemical and CFD-based problems, either independently or as a coupled set of equations. However, as the software is designed to capture a wide range of physical phenomena, it generally solves for additional variables that may not be required. This can be problematic in running large-scale parametric studies due to the memory demand and so in some instances additional software, such as MATLAB, may be necessary for data management.

1.4.2 CFD in Corrosion Research

As technology has advanced, the use of CFD has become more and more prevalent within corrosion research. A large part of the appeal of using CFD in combination with electrochemistry stems from the flexibility in its application; the generalised numerical approach allows it to be utilised in a wide range of scenarios. Additionally, by simulating the behaviour of a system it is possible to significantly reduce the amount of experimental testing that needs to be done, which can often be expensive and time consuming. CFD modelling also removes many practical limitations, as conditions that would be difficult to achieve in the real world, such as high temperatures and pressures, can be readily adjusted.

In relation to CO_2 corrosion modelling, the incorporation of hydrodynamics via CFD is a growing area of research as accurately capturing flow effects would represent a major advancement of the existing models. Recent examples of this include the work by Owen *et al.*[96] in which a k-ω SST model was used alongside a species transport model to predict corrosion rates following a rapid pipe expansion by modelling the flux of H^+ ions at the surface. The flux was used to calculate a mass-transfer coefficient throughout the pipe and then combined with an empirical relationship obtained from an RCE experiment to calculate the rate of corrosion. Validation of the model against an experimental flow loop data showed a high level of accuracy in predicting local corrosion rates within the specified geometry. However, as only a single species was

modelled in this instance, the model could not be readily expanded to different environmental conditions and solution chemistries.

A 2021 paper by Dana and Javidi[97] also attempted to investigate corrosion within a complex flow by looking at CO_2 corrosion in outlet piping for a heat exchanger. A k-ε turbulence model was first utilised to determine the flow properties through a complex pipe arrangement. These value were then used as inputs for the NORSOK M-506 standard model[98] to determine local corrosion rates. The model did not however two-way couple these interactions, meaning it could not account for changes in the local chemistry or the transportation of species. As a result, the same approach cannot be used if factors such as protective scale formation, local depletion of ions, or galvanic effects need to be considered. Therefore, whilst a useful indicator for areas of high risk for corrosion, the simplicity of this approach raises concerns about its reliability in accurately predicting local corrosion.

A similar approach was taken in a 2023 publication by Thorat *et al*.[99], coupling hydrodynamic data from a k-ω SST turbulence model with the mechanistic corrosion model proposed by Nordsveen *et al*.[26] In this work, much greater emphasis was placed on the turbulent behaviour within the hydrodynamic boundary layer. FEM was used to numerically derive hydrodynamic properties in the boundary layer of a straight pipe, which were then input into the 1-D corrosion model and solved via FVM. When compared to the results in the original paper in which the hydrodynamics were derived from empirical relationships, this method was found to improve accuracy when comparing to experimental data gathered by Nešić *et al*.[100]

Lin and Ferng[82] also investigated the use of CFD in the prediction of boundary layer hydrodynamics, with their research being focused on the corrosion of piping within pressurised-water reactor power plants. As the emphasis within such systems is flow accelerated corrosion (FAC) only mass-transport effects were considered. An RNG k- ε to model a 3-D flow within a pipe elbow, due to its improved accuracy over the standard k-ε model in modelling constrained flows. FVM was used to solve the flow equations throughout the domain, but due to the size of the model, enhanced wall functions were used alongside a fine mesh to account for flow effects near the wall. As such, near-wall effects were not necessarily fully resolved, however reasonable approximations of mass-transport rates were obtained. These were then combined with a simple mass-transfer corrosion model which assumed diffusion control and complete consumption of oxygen at the surface.

Due to the simplifications and assumptions of this model, exact corrosion rates could not be accurately predicted, however the model provided useful indications as to the points along the elbow likely to see the highest corrosion rates. Liu *et al*.[101] conducted similar research looking at different elbow configurations containing oil-water two phase flow. However, in this work the corrosion processes were not actually modelled, instead the focus was on the use of an RNG k-ε model to predict the interaction between oil and water. The results were then used to calculate values for the wall shear-stress and mass-transfer coefficient throughout the pipe to identify regions most susceptible to corrosion.

CFD is also often used in the field of erosion-corrosion to account for the influence of particles such as sand within solution. Gnanavelu *et al*.[102] used an RNG k-ε model to predict erosion caused by a solid suspension of sand and water within a jet impingement system at various flow velocities. A reasonable correlation was found between the CFD model and experimental data, however assumptions related to properties of the particle and material properties limited the accuracy. However, in 2015 Ige and Umoru[103] did utilise the same CFD model, combined with mass-loss and profilometry techniques for the purposes of calculating shear-stress and particle tracking within a submerged jet impingement system. Similarly, Stack and Abdelrahman[104] used a standard k-ε model to investigate erosion-corrosion but in their case looking at the effects within a 90° pipe bend. The turbulence model was combined with simple models of erosion, corrosion, and passivation to evaluate the relative effects of a dilute slurry of water containing alumina particles. By modelling each process individually, it was possible to identify the conditions and locations within the pipe bend under which either erosion or corrosion were dominant.

1.5 Contribution to Literature

Based on the review of the current body of literature above, several areas have been identified in which the author believes this work can provide valuable contributions. The first of these is through comprehensive numerical evaluation of the existing models of CO_2 corrosion. The currently available published models[12, 24-26, 35, 36, 39, 105] generally conduct an in-depth analysis of a small number of conditions, often for the purposes of experimentally validating the results. Additionally, it may be the case that the models have not been designed in such a way as to facilitate the production of large data sets. It is in this regard that the current work can provide a

significant level of insight, by recreating established models in a way that allows them to be run for thousands of input conditions. In doing so, the wider implications of the approaches used to generate the models can be explored in much greater details. Such a method would also allow for analysis of behavioural trends, investigating how the model predictions change as a function of multiple key input variables. Conducting such a vast numerical exploration of these models would provide a significant amount of highly useful output data that would constitute a valuable contribution to the existing field of research.

The second area in which there exists gaps in the literature is in the connection between turbulent flow models and comprehensive mechanistic corrosion models. Currently, models of CO_2 rely heavily on empirical equations to account for the effects of turbulence on the corrosion behaviour. As a consequence of this, they are restricted to the conditions for which the empirical equations are known to be true, most commonly a straight pipe flow. However, as discussed in section 1.4.2, it has been previously shown that it is possible to effectively model the turbulent behaviour using CFD. Thus far, works attempting to link the two fields of study have been focused on modelling specific scenarios[97, 102, 103], or have utilised simplified corrosion models in their analysis[82, 96, 101, 104]. There does not currently exist in the literature, a general methodology by which a comprehensive mechanistic model of CO_2 corrosion can be integrated into a computational model of fluid flow. This is, however, possible to achieve this through the use of multiphysics software, and so creating such a methodology provide significant benefit to the development of future models.

Both of the areas discussed here present significant challenges in the addressing the current gaps in the literature, but also have the potential to provide significant benefit. It is for these reasons that they have been selected as the focus for this thesis. Regarding the numerical exploration of existing CO_2 corrosion models, it would not be feasible to analyse all of the models discussed here. Therefore two well-established comprehensive mechanistic models have been selected for this work, namely the 2003 model published by Nordsveen *et al*.[26] and the 2020 model published by Kahyarian *et al*.[12, 36].

Chapter 2 - Nordsveen Model Implementation within COMSOL

When creating a predictive model of carbon dioxide corrosion in steel pipelines, there are three main approaches identified by Kahyarian *et al.*[31] that are employed in current literature, namely: empirical/semi-empirical, elementary mechanistic, and comprehensive mechanistic. In this work, the focus is on the latter, the comprehensive mechanistic models, as these provide the most detailed and accurate representations of the physical corrosion processes. Furthermore, such models facilitate the inclusion of additional physical phenomena as well as extrapolation to a wider range of conditions than the other modelling approaches.

Previous one-dimensional mechanistic models evaluating the near-wall chemistry in a corrosive CO_2 saturated environment have been created using various software packages. However, these numerical models are limited in their exploration of potential data and interrogation of the process. Small data sets are used to highlight specific phenomena, however the overall effect of the various input conditions such as pressure, temperature, and bulk pH are not fully examined. In this chapter, a new methodology is outlined for the implementation of a CO_2 corrosion model within COMSOL Multiphysics® version 6.1. The advantage of building the standard model within this software is that it allows for the generation of large sets of results which can be used to produce comprehensive contour plots showing the direct impact of input conditions on relevant outputs such as the corrosion rate or surface supersaturation. Additionally, changes to the chemistry and conditions being modelled can be readily made, facilitating rapid advancement of the current 'state of the art' models. The incorporation of complex flow fields in both two and three dimensions also becomes a possibility, removing the need for empirical formulae to account for the effect of turbulence.

Here, an overview is provided, outlining the process by which a one-dimensional model can be produced within COMSOL, alongside a comparison of results with current literature and a numerical exploration of the model. All relevant chemistry, equations, and settings have been detailed.

2.1 Background - Current Models

In this work, an existing mechanistic model has initially been utilised in order to validate the use of COMSOL as a tool for assessing CO_2 corrosion. For this purpose, a model initially created by Nordsveen *et al.*[26] in 2003 was selected due to the wide range of available results against which to compare. The original paper by Nordsveen *et al.* formed the first in a series of 3 papers based around this corrosion model, with subsequent papers by Nesic *et al.*[37] and Nesic and Lee[38]. For the sake of brevity, these papers will referred to as 'part 1', 'part 2', and 'part 3' in the Nordsveen series in the following sections.

The model created by Nordsveen *et al.* is a numerical analysis of a straight corroding carbon steel pipeline due to CO_2 saturated flow along a one-dimensional line, protruding outwards form the surface into the surrounding fluid. The model describes the behaviour of the system within the boundary layer between the surface and the bulk, based upon known corrosive mechanisms. The chemistry of the model can be split into 3 distinct sections:

1. Bulk chemistry and initial conditions
2. Reaction kinetics within the boundary layer
3. Electrochemical reactions at the steel surface

It should be noted that the 'boundary layer' here refers to the viscous sublayer close to the surface, in which the dimensionless parameters u^+ and y^+ are equal. For pipe flow this generally follows the universal 'law of the wall' (see Figure 2-1) and therefore extends out to approximately $y^+ = 5$, where[44]:

$$u^+ = \frac{u}{u_\tau} \tag{2.1}$$

$$y^+ = \frac{y u_\tau}{\nu} \tag{2.2}$$

$$u_\tau = \sqrt{\frac{\tau_w}{\rho}} \tag{2.3}$$

Where u^+ is the dimensionless velocity, y^+ is the dimensionless wall distance, u_τ is the friction velocity (m/s), u is the fluid velocity (m/s), ν is the kinematic viscosity (m^2/s), τ_w is the wall shear stress (N/m^2), and ρ is the density of the fluid (kg/m^3).

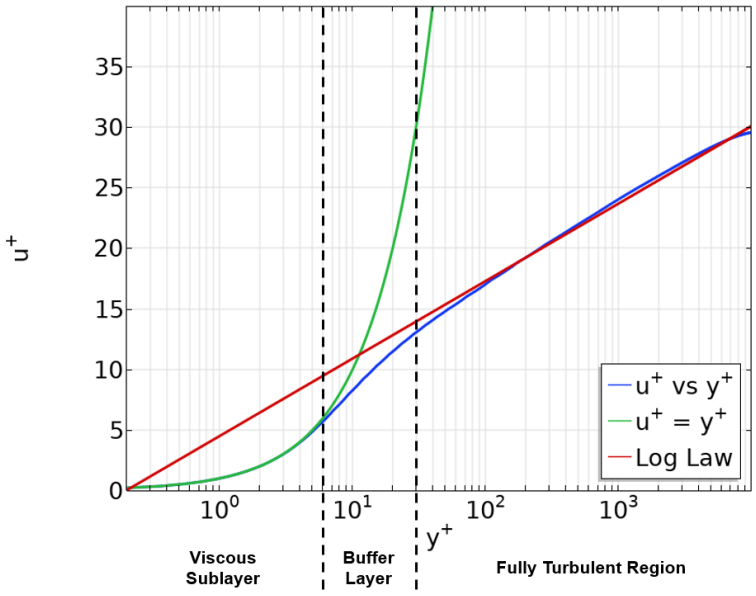

Figure 2-1 - Universal law of the wall for flow through a straight pipe indicating the location of the viscous sublayer at $y^+ < 5$.

The chemistry and mechanisms within the Nordsveen model are based upon the principles of general CO_2 corrosion, which is driven by the presence of hydrogen ions (H^+) at the metal surface. The approach implemented follows the theoretical direct reduction model originally devised by De Waard and Milliams[30] in their 1975 paper on carbonic acid corrosion of steel. Within the bulk solution, gaseous CO_2 is initially dissolved in water to produce aqueous CO_2. The extent to which this dissolution can occur is determined by its partial pressure and can be calculated via Henry's Law:

$$[CO_2] = K_H P_{CO2} \tag{2.4}$$

Where $[CO_2]$ is the concentration of CO_2 (M), K_H is the Henry's Law constant, and P_{CO2} is the partial pressure (atm).

As discussed in Chapter 1, the dissolved CO_2 then gradually hydrates to form H_2CO_3. It should be noted that due to relatively slow rate of reaction compared to subsequent reactions and the low concentration of H_2CO_3 in relation to dissolved CO_2 (≈ 1/1000)[11], the concentrations of both the dissolved and hydrated forms are commonly abbreviated to $[CO_2]$ [10, 12].

$$\mathrm{CO_{2(aq)}} + \mathrm{H_2O_{(l)}} \leftrightarrow \mathrm{H_2CO_{3(aq)}} \tag{2.5}$$

Following this dissolution, two dissociation reactions take place, resulting in the production of H^+ ions at each stage:

$$H_2CO_{3(aq)} \leftrightarrow HCO^-_{3(aq)} + H^+_{(aq)} \quad (2.6)$$

$$HCO^-_{3(aq)} \leftrightarrow CO^{2-}_{3(aq)} + H^+_{(aq)} \quad (2.7)$$

The reactions shown in Equations 2.4-2.7 are modelled as equilibrium reactions in the bulk fluid, producing a constant set of initial and boundary concentrations.

Through the boundary layer, these reactions are instead modelled using their separate forwards and backwards rates. Modelling in this way allows for the rate of reaction and local species concentrations to be accounted for when the concentrations deviate from that of the bulk. Transport of species in the model is described using a modified version of the flux equation, mathematically determining the movement of ions due to diffusion and electrochemical migration. As the instantaneous velocity is unknown without the use of direct numerical simulation, the convection term is instead incorporated into the diffusion via the use of turbulent diffusivity. The value of this turbulent diffusivity, as well as the boundary layer thickness, which determines the length of the domain, are described by existing empirical relationships provided by Davies[28]. More specific detail of this implemented is described in section 2.3.

Separate electrochemical reactions are modelled at the steel surface, with the corrosion rate being determined by the anodic dissolution of iron:

$$Fe_{(s)} \rightarrow Fe^{2+}_{(aq)} + 2e^- \quad (2.8)$$

The electrons produced by this reaction are consumed by one of two cathodic reactions. The first of which is the reduction of the H^+ ions produced in the dissolution reactions, creating hydrogen gas:

$$2H^+_{(aq)} + 2e^- \rightarrow H_{2(g)} \quad (2.9)$$

The second cathodic reaction, which is debated in literature[31-34], is the direct reduction of carbonic acid, which produces additional bicarbonate ions which act as an additional source of H^+ ions:

$$2H_2CO_{3(aq)} + 2e^- \rightarrow H_{2(g)} + 2HCO_3{}^-_{(aq)} \quad (2.10)$$

It should be noted that although the direct reduction of carbonic acid can be disabled in the Nordsveen model, it has been included when generating plots and therefore is included here for validation purposes. Another reaction noted by Nordsveen *et al.* is the direct reduction of water at the surface, however this

is not included in the model due to the low partial pressures and high pH values needed for it to become significant.

$$2H_2O_{(aq)} + 2e^- \rightarrow H_{2(g)} + 2OH^-_{(aq)} \quad (2.11)$$

Alongside the analysis of corrosion, the Nordsveen series also looks at the precipitation of $FeCO_3$ and its protective properties in reducing the corrosion rate, with particular emphasis in parts 2 and 3.

$$Fe^{2+}_{(aq)} + CO^{2-}_{3\ (aq)} \rightarrow FeCO_{3(s)} \quad (2.12)$$

In the implementation described in the following section, the precipitation reaction is not modelled, however the potential for stable formation is discussed in section 2.5.

2.2 Model Structure and Overview of Underlying Physics

Before progressing with the creation of a CO_2 corrosion model within COMSOL, it is important to understand the scenario that is being modelled. The Nordsveen model is a 1D representation of the interaction between aqueous CO_2 and the internal surface of a mild steel pipeline. The model evaluates corrosion and speciation outwards from a single point on the steel surface and is sectioned into three key domains: bulk steel, boundary layer, and bulk solution. These can be modelled as a straight line representing the boundary layer, with the two endpoints being representative of the corroding bulk steel surface and the bulk fluid, respectively. The behaviour of the active species in each of these domains is described by different sets of equations to model the production, consumption, and transport of the ions. An overview of the system is provided in Figure 2-2, alongside complete sets of equations for each of the three domains.

Uniform corrosion is assumed in the model when calculating corrosion rates, along with zero precipitation of solid corrosion product either within the boundary or at the metal surface. It should be noted that within the Nordsveen series, a precipitation model of $FeCO_3$ was included to assess the effect of corrosion product growth on the steel surface, however the underlying corrosion model remained unchanged. Empirical relationships are used to calculate the thickness of the boundary layer and effect of turbulence, based on data for a fully developed straight pipe flow. These relationships assume uniform flow throughout the straight pipe and axis-symmetric flow about the centre.

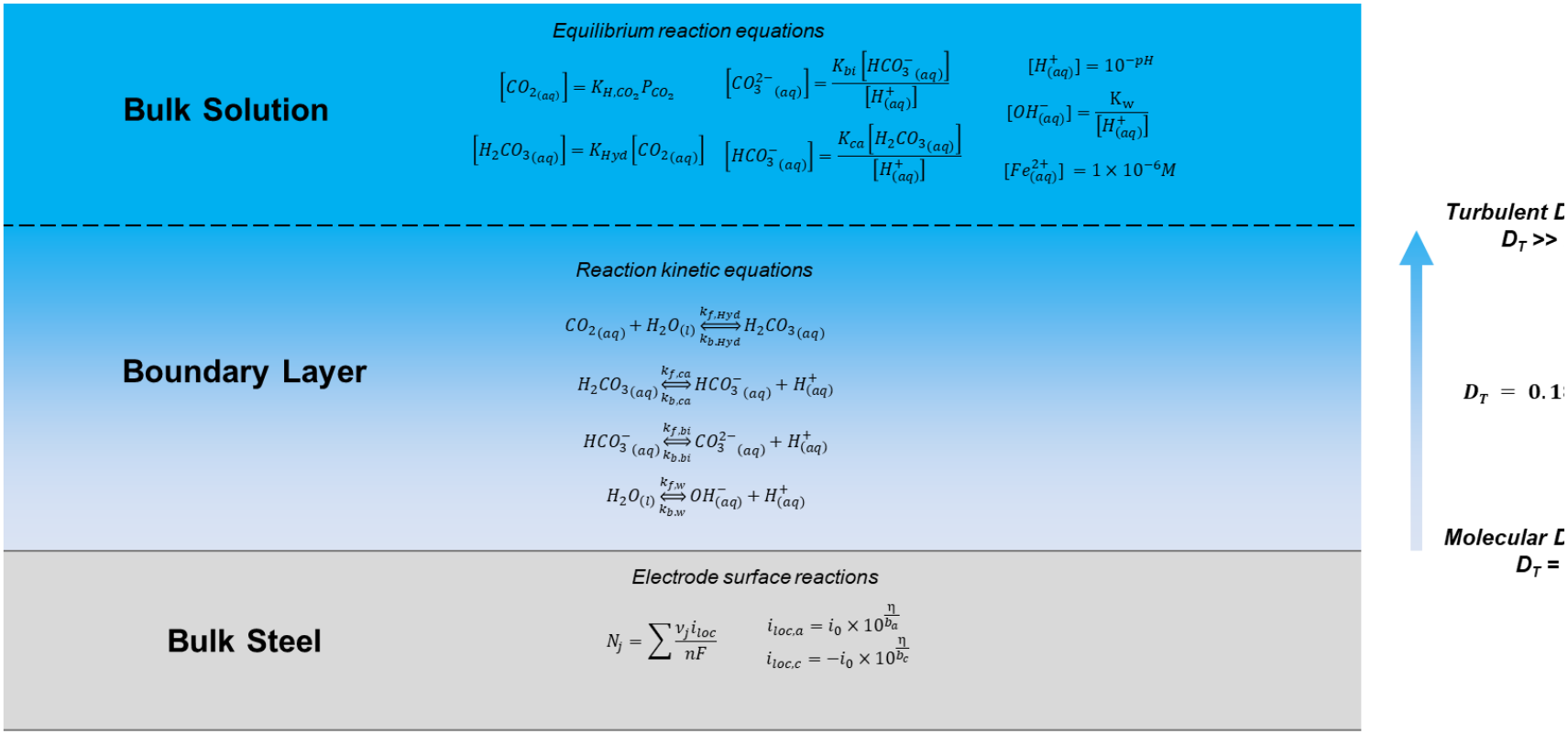

Figure 2-2 - Diagram showing the system being modelled within system, represented by a one-dimensional line between the steel surface and the bulk solution.

2.2.1 Fluid Properties

As the 1-D model is representative of straight pipe flow, the standard formula for Reynolds number within a straight pipe was used:

$$Re = \frac{\rho u d}{\mu} \tag{2.13}$$

Where ρ is the density of the fluid (kg/m^3), u is the mean velocity of the bulk flow (m/s), and μ is the dynamic viscosity of the fluid (Pa·s).

The material properties assigned were those of water, as quoted by Nordsveen[26] referencing the CRC Handbook of Chemistry and Physics[106]. A summary of the values used is provided in Table 2.1, a standard temperature of 293.15 K (20 °C) is used as an example throughout.

Table 2.1 - Summary of formulae used in the calculation of the boundary layer height and an example value for a temperature (T) of 293.15 K.

Parameter	Symbol	Formula	Value (SI Units)
Boundary layer height	δ	$25Re^{-\frac{7}{8}}d$	1.0578×10^{-4} m
Reynolds number	Re	$\frac{\rho u d}{\mu}$	99619
Density	ρ	$(753.596 + 1.87748T_K - 0.003564T_K^2)$	997.7 kg·m^{-3}
Mean bulk velocity	u	-	1 m·s^{-1}
Hydraulic diameter	d	-	0.01 m
Dynamic viscosity	μ	$0.001002 \times 10^{\frac{1.3277(293.15-T_K)-0.001053(298.15-T_K)^2}{T_K-168.15}}$	0.0010015 Pa·s

2.2.2 Bulk Fluid Chemistry

For a given set of conditions, each species within a CO_2/H_2O system will reach a stable equilibrium concentration, these values represent the conditions within the bulk fluid. As can be seen from the reactions outlined in Section 2.1 (Equations 2.5-2.7), each reaction in the solution occurs simultaneously forwards and backwards. For an isothermal system, these reactions reach a

steady state, and the concentrations of each species remain constant. The composition of the bulk fluid can be calculated via equilibrium constants, which are simply the relative ratios of the forwards to backwards reactions. Table 2.2 shows a complete summary of these equilibrium constants.

Table 2.2 - List of equilibrium constant definitions and formulae used to calculate the composition of the bulk fluid based on the temperature in Fahrenheit / Kelvin (T_f/T_K), pressure (p), and ionic strength (I).

Constant	Definition	Formula[26]
K_{H,CO_2}	$\frac{[CO_2]}{P_{CO2}}$	$\frac{14.5}{1.00258} \times 10^{-\left(2.27+5.65x10^{-3}T_f-8.06x10^{-6}T_f^2+0.075I\right)}$ M/bar
K_{Hyd}	$\frac{[H_2CO_3]}{[CO_2]}$	2.58×10^{-3}
K_{ca}	$\frac{[H^+][HCO_3^-]}{[H_2CO_3]}$	$387.6 \times 10^{-\left(6.41-1.594x10^{-3}T_f+3.52x10^{-6}T_f^2-3.07x10^{-5}p-0.4772I^{0.5}+0.1180I\right)}$ M
K_{bi}	$\frac{[H^+][CO_3^{2-}]}{[HCO_3^-]}$	$10^{-\left(10.61-4.97x10^{-3}T_f+1.331x10^{-5}T_f^2-2.624x10^{-5}p-1.166I^{0.5}+0.3466I\right)}$ M
K_w	$[H^+][OH^-]$	$10^{-\left(29.3868-0.0737549T_K+7.47881x10^{-5}T_K^2\right)}$ M^2

Note, the Table 2.2 features a correction in the value of K_{ca} based on the original work by Oddo and Tomson[107], in which the prefactor of T_f^2 is given as 3.52x10^{-6} as opposed to the 8.52x10^{-6} value stated by Nordsveen *et al.*

The equilibrium constants can be used to calculate the bulk concentrations of the reacting species, however they also require the concentration of H^+ ions to be known. The concentration of H^+ is determined by the system pH, and can be calculated from the standard definition of pH:

$$pH = -\log\left(a_{H^+}\right) \tag{2.14}$$

$$a_{H^+} = \gamma_H[H^+] \tag{2.15}$$

Where a_{H^+} is the hydrogen ion activity, γ_H is the activity coefficient, and $[H^+]$ is the H^+ ion concentration[108].

The resulting species concentrations for the bulk fluid over a range of pH values are shown in Figure 2-3 for a temperature of 293.15K, pressure of 1 bar and ionic strength of 0.1711 M (1 wt% NaCl).

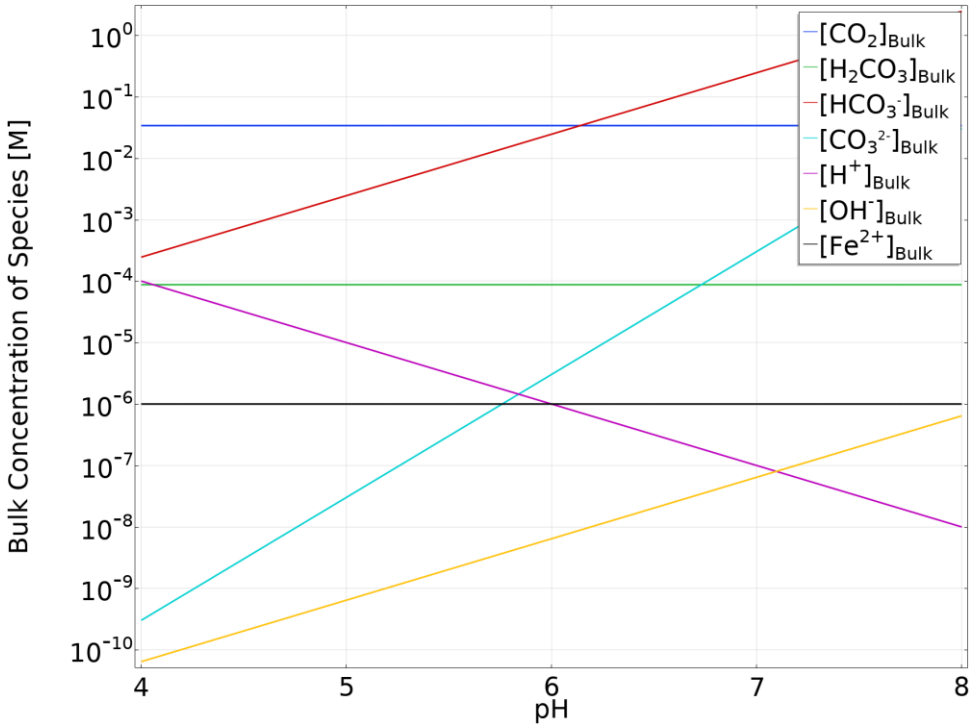

Figure 2-3 - Plot of bulk species concentration as a function of pH for input values of 20 °C, 1 bar P_{CO_2} and ionic strength of 0.1711 M.

It should be noted that a nominal concentration of 1 ppm_{Molar} is given for the concentration of Fe^{2+}, despite not being involved in any reactions in the bulk. This is to account for the accumulation of iron in the bulk resulting from the surface reactions in the system, which cannot be calculated for a stand-alone one-dimensional model. Although not clearly stated in the literature, this is in-line with assumptions made in the Nordsveen series[26, 37, 38], as well as in similar models by Kahyarian *et al.*[12, 36].

2.3 COMSOL Implementation

In this section, a detailed account of the process followed to implement a functional corrosion model within COMSOL is outlined; the implementation follows the approach suggested by the Nordsveen series of papers. Although primarily a recreation of the existing model using new software, several typographic and/or systematic errors have been identified and corrected. Justification for any changes to the model described within the literature is clearly stated, as are any assumptions made throughout.

2.3.1 Geometry and Discretization

To represent the geometry within COMSOL an interval between two points was used. These points represented the metal surface and the bulk-boundary

interface respectively, with x-coordinates of zero and δ respectively where δ denotes the boundary layer thickness. The calculation of this value is determined by the Reynolds number of the system and is adapted by Nordsveen from a formulation originally provided by Davies[26, 28]:

$$\delta = 25Re^{-\frac{7}{8}}d \tag{2.16}$$

Where δ is the boundary layer thickness (m), Re is the Reynolds number and d is the hydraulic diameter (m). Note the thickness of the surface film (δ_f) has been removed from this equation.

Nordsveen *et al.*[26] used a coarse mesh ranging from 25-100 nodes non-uniformly spaced across the boundary, using grid refinement to ensure a mesh independent solution. The reason given for this to was reduce solver times due to the time dependent nature of the film formation component of the model. As this is not required for a pure corrosion model, a much finer mesh could be used to ensure mesh independence across the entire range of expected boundary layers. As suggested in the 1st paper in the Nordsveen series[26], the boundary layers range between 10-300 μm, which if using shortest distance and the maximum 100 nodes, would result in an average element size of 10^{-7}m. Therefore, the COMSOL model was discretized using a mesh comprised of 794 linearly distributed edge elements, with a maximum element size of 10^{-7}m.

2.3.2 Initial Conditions

In this model, the initial conditions relate to the concentration of each species before surface reactions introduce a flux of ions at the surface. These act as a starting point for the iterative solver. For this, the bulk concentrations, as detailed in section 2.2.2, were applied throughout the model as these represent the equilibrium point of the system. Utilising the bulk concentrations as initial values reduces the time for a solver to reach a solution by providing the software with a reasonably close 'first guess' for the speciation through the boundary. The bulk concentrations also act as a boundary condition at the end of the boundary layer ($x = \delta$) as these values are fixed.

The formulae shown in Table 2.2 alongside Equation 2.14 were used to calculate the bulk concentrations for each species as parameters within COMSOL. In order to do this, the fluidic conditions needed to also be specified as parameters, these are shown in Table 2.1 and Table 2.3.

Table 2.3 - Operating conditions of the fluid used to determine initial and bulk species concentrations.

Parameter	Symbol	Formula	Value
pH	pH	-	6
Partial Pressure of CO_2	P_{CO_2}	-	1 bar
Operating Pressure	P	$14.5038P_{CO_2}$	14.5038 psi
Ionic Strength	I	$\frac{1}{2}\sum_{i=1}^{n} c_i z_i^2$	0.1711 M
Temperature (Kelvin)	T_K	-	293.15 K
Temperature (Celsius)	T_c	$T_K - 273.15$	20 °C
Temperature (Fahrenheit)	T_f	$1.8T_c + 32$	68 °F

2.3.3 Species Transportation

Electroanalysis physics was added to introduce the 7 key species into the COMSOL model, namely: CO_2, H_2CO_3, HCO_3^-, CO_3^{2-}, H^+, OH^- and Fe^{2+}. The electroanalysis interface allows for specification of the chemical reactions in each of the 3 domains (see Figure 2-2), as well as the initial concentrations. However, it also allows for the movement of the chemical species throughout the model to be defined following the same equations as the Nordsveen model. In general, the species transport is defined by the flux equation:

$$N_j = -D_{M,j}\frac{\partial c_j}{\partial x} - z_j u_j F c_j \frac{\partial \Phi}{\partial x} + c_j v \tag{2.17}$$

Where N_j is the flux of species, $D_{M,j}$ is the molecular diffusion coefficient, c_j is the concentration, x is the distance to the surface, z_j is the electrical charge, u_j is the mobility of species, F is the Faraday constant, Φ is the electrical potential and v is the solution velocity.

A simplification to the flux equation was made within the COMSOL to improve solver times. The electroanalysis charge-transfer model was used which assumes zero potential gradient in the electrolyte $\left(\frac{\partial \Phi}{\partial x} = 0\right)$, therefore

neglecting the effect of the electromigration term ($z_j u_j F c_j \frac{\partial \Phi}{\partial x}$). As discussed by both Stephens and Mauzeroll[109] and Britz and Strutwolf[110], this assumption is valid when the inert electrolyte concentration is significantly larger than the concentrations of the other charged species. Despite this, the potential gradient is solved for within the Nordsveen model from a linear equation for the electrical potential:

$$\frac{\partial}{\partial x}\left(\kappa_f \xi \frac{\partial \Phi}{\partial x}\right) = -\varepsilon_V F \sum_j z_j c_j \tag{2.18}$$

Where $\frac{\partial \Phi}{\partial x}$ is the electrical potential field, κ_f is the permeability of surface films, ξ is the temperature dependent dielectric constant, ε_V is the volumetric porosity, F is the Faraday constant and $\sum_j z_j c_j$ is the total charge imbalance.

Additionally, when modelling the boundary layer it is important to remember that there is a no-slip condition at the wall, meaning that the velocity (v) at $x = 0$ is zero[27]. As the boundary layer is very small ($\delta \approx 10^{-4} m$), this effect means that convection term ($c_j v$) becomes negligible in the absence of external stirring[109]. However, it is important to note that in turbulent flow, eddies may still permeate into the boundary layer. Therefore, in order to account for this, the convection term is instead approximated with a term known as the turbulent diffusivity (D_T), which is given as a function of the distance from the surface[28]:

$$D_T = 0.18\left(\frac{x}{\delta}\right)^3 \frac{\mu}{\rho} \tag{2.19}$$

The result of the changes to the transport model within the COMSOL model produced a modified version of the flux equation, which has a similar form to Fick's first law of diffusion:

$$N_j = -(D_{M,j} + D_T(x))\frac{\partial c_j}{\partial x} \tag{2.20}$$

A list of the molecular diffusion coefficients (D_M) for the 7 chemical species in the electrolyte is provided in Table 2.4.

Table 2.4 - Molecular diffusion coefficients for the chemical species being modelled [26].

Species	Molecular Diffusion Coefficient (D_M) (m^2/s)
CO_2	1.96×10^{-9}
H_2CO_3	2.00×10^{-9}
HCO_3^-	1.105×10^{-9}
CO_3^{2-}	0.92×10^{-9}
H^+	9.312×10^{-9}
OH^-	5.26×10^{-9}
Fe^{2+}	0.72×10^{-9}

2.3.4 Chemical Reaction Kinetics

Section 2.2.2 details the steady state conditions of the bulk fluid, however the species concentrations between the surface and the bulk are not in a state of equilibrium. The corrosion caused by the electrochemical reactions at the metal surface (see Section 2.3.5), introduces a flux of ions which shifts the system from the bulk equilibrium. In order to model the response of the system to this change it is important to factor in the relative rates of each reaction. The reason for this is due to the very slow rate at which the CO_2 hydration reaction (Equation 2.5) occurs relative to the diffusion of species. The movement of ions during this reaction stage means the system is no longer in equilibrium and so makes it necessary to model the reaction kinetics.

As discussed previously, the reactions given by Equations 2.4-2.7 occur simultaneously forwards and backwards. Modelling the transient response of the species to the surface flux requires that these individual reaction rates are isolated, as opposed to dealing solely with the equilibrium ratio. Therefore each of the reactions were rewritten, in terms of their forwards and backwards components (Equations 2.22-2.26), with the corresponding rate constants provided in Table 2.5. It should also be noted that the dissociation of water (Equation 2.21) has also been added into this model for a more complete set of reactions. Although the constants for this reaction are provided by

Nordsveen *et al.*[26], it is not included in the model, presumably due to the minimal effect.

$$H_2O \leftrightarrow H^+ + OH^- \tag{2.21}$$

$$r_1 = k_{f,H}\left[CO_{2_{(g)}}\right] - k_{b,H}[CO_{2_{(aq)}}] \tag{2.22}$$

$$r_2 = k_{f,Hyd}\left[CO_{2_{(aq)}}\right] - k_{b,Hyd}[H_2CO_3] \tag{2.23}$$

$$r_3 = k_{f,ca}[H_2CO_3] - k_{b,ca}[HCO_3^-][H^+] \tag{2.24}$$

$$r_4 = k_{f,bi}[HCO_3^-] - k_{b,bi}[CO_3^{2-}][H^+] \tag{2.25}$$

$$r_5 = k_{f,w}[H_2O] - k_{b,w}[OH^-][H^+] \tag{2.26}$$

Table 2.5 - Kinetic reaction rate constants for reversible reactions in solution.[26]

Constant	Definition	Formula	Units
$k_{f,H}$	$K_{H,CO_2} \cdot k_{b,H}$	1×10^{10}	$M \cdot s^{-1} \cdot bar^{-1}$
$k_{f,Hyd}$	$K_{Hyd} \cdot k_{b,Hyd}$	$10^{329.85-110.541\left(\log_{10} T_K - \left(\frac{17265.4}{T_K}\right)\right)}$	s^{-1}
$k_{f,ca}$	$K_{ca} \cdot k_{b,ca}$	$10^{5.71+0.0526T_c-2.94\times10^{-4}(T_c)^2+7.91\times10^{-7}(T_c)^3}$	s^{-1}
$k_{f,bi}$	$K_{bi} \cdot k_{b,bi}$	1×10^9	s^{-1}
$k_{b,w}$	$\frac{k_{f,w}}{K_w}$	7.85×10^{10}	$M^{-1}s^{-1}$

These equations can then be used to create a system of ordinary differential equations which describe the rate of change of each species concentration. The rate of change can be determined by taking the rate reactions in which each of the species are produced and subtracting the reactions in which they are consumed. Doing so for each of the aqueous species results in the following ordinary differential equations (ODEs):

$$\frac{d}{dt}\left[CO_{2(g)}\right] = 0 \tag{2.27}$$

$$\frac{d}{dt}\left[CO_{2(aq)}\right] = -r_2 \tag{2.28}$$

$$\frac{d}{dt}[H_2CO_3] = r_2 - r_3 \tag{2.29}$$

$$\frac{d}{dt}[HCO_3^-] = r_3 - r_4 \tag{2.30}$$

$$\frac{d}{dt}[CO_3^{2-}] = r_4 \tag{2.31}$$

$$\frac{d}{dt}[H^+] = r_3 + r_4 + r_5 \tag{2.32}$$

$$\frac{d}{dt}[OH^-] = r_5 \tag{2.33}$$

Note in that in Equation 2.27 the rate of change of gaseous CO_2 is equal to zero. This is due to the assumption that the partial pressure in the system remains constant, hence the concentration of gaseous CO_2 in solution does not change. Additionally, as the system is closed there is no production term for aqueous CO_2 (r_1) in the boundary due to the lack of available gaseous CO_2.

As these reactions are in the form of ODEs, they are dependent upon the current local concentration, which is non-constant. Each of the reactions ($r_1 - r_5$) were therefore defined within COMSOL as variables and used to define the rate of change of each species concentration throughout the domain. The rate of change of $[Fe^{2+}]$ was set to zero as it does not react further once dissolved in solution.

Although the reactions and rate of species concentration change are specified separately within the COMSOL model, these reactions can then still be grouped into a matrix form. It can be seen that the part of the matrix relating to the first and second dissociation steps match those shown in Nordsveen part 1[26].

$$\begin{bmatrix} R_{CO2} \\ R_{H_2CO_3} \\ R_{HCO_3^-} \\ R_{CO_3^{2-}} \\ R_{H^+} \\ R_{OH^-} \end{bmatrix} = \begin{bmatrix} -1 & 0 & 0 & 0 \\ 1 & -1 & 0 & 0 \\ 0 & 1 & -1 & 0 \\ 0 & 0 & 1 & 0 \\ 0 & 1 & 1 & 1 \\ 0 & 0 & 0 & 1 \end{bmatrix} \begin{bmatrix} \left(K_{f,Hyd}\left[CO_{2_{(aq)}}\right] - K_{b,Hyd}[H_2CO_3]\right) \\ \left(K_{f,ca}[H_2CO_3] - K_{b,ca}[HCO_3^-][H^+]\right) \\ \left(K_{f,bi}[HCO_3^-] - K_{b,bi}[CO_3^{2-}][H^+]\right) \\ \left(K_{f,w}[H_2O] - K_{b,w}[OH^-][H^+]\right) \end{bmatrix}$$

Figure 2-4 - Matrix form of the equations modelling the heterogeneous reactions within the boundary layer, where R represents the net rate of change of a species concentration.

2.3.5 Electrochemical Surface Reactions

The model set-up to this point has been in regard to the reaction of the species in solution. Now, the focus will be shifted to the interface between the fluid and the metal surface; the location of the corrosion reactions. Three electrode reactions were defined at the electrode surface within COMSOL ($x = 0$), describing the reactions shown in Equations 2.8-2.10. Equation 2.8 relates to the anodic dissolution of iron at the surface and as such requires the specification of a dissolving-depositing species. Material properties were added to represent that of mild steel, namely the density (ρ_{Steel}) and the molecular weight (M_{Steel}). These values are shown in Table 2.6.

Table 2.6 - Material properties of mild steel, representing the dissolving species at the electrode surface.

Material Property	Symbol	Value[111]
Density	ρ_{steel}	7,850 kg·m^{-3}
Molecular Weight	M_w	55.845×10^{-3} kg·mol^{-1}

These two material properties are necessary to determine corrosion rate of the electrode based upon the reaction rate of the dissolving material, which in this case is Fe within the steel. The formulae used to calculate the mass and thickness change at the surface are shown in Equations 2.34 and 2.35.

$$\Delta S = M_w \, N_{Fe} \tag{2.34}$$

$$CR = \frac{\Delta S}{\rho} \tag{2.35}$$

Where ΔS is mass reaction rate at the surface (kg/m^2·s), M_w is the molecular weight (kg·mol^{-1}), N_{Fe} is the molar flux of Fe from the surface (mol/m^2·s), and CR is the corrosion rate at the surface (m/s).

Determining the reaction rate of the dissolving iron is complex and requires the specification of both the cathodic dissolution reaction and the anodic surface reactions occurring. Each of the reactions can be expressed by the general electrochemical reaction formula in order to determine the stoichiometric coefficients:

$$\sum_{ox} \nu_{ox} S_{ox} + ne^- \leftrightarrow \sum_{red} \nu_{red} S_{red} \tag{2.36}$$

Where ν is the stoichiometric coefficient, S is the species, and n is the number of participating electrons. Subscript red and ox indicate products and reactants respectively in a reduction reaction[112].

Three electrode reactions were defined, namely iron oxidation (Equation 2.8), hydrogen evolution (Equation 2.9), and carbonic acid reduction (Equation 2.10). These reactions are shown in Table 2.7, alongside the number of participating electrons and the stoichiometric coefficients associated with each reaction.

Table 2.7 - Participating electrons and stoichiometric coefficient values for iron oxidation (anodic), hydrogen evolution (cathodic), and carbonic acid reduction (cathodic) surface reactions.

Coefficient	$Fe_{(s)} \rightarrow Fe^{2+}_{(aq)} + 2e^-$	$2H^+_{(aq)} + 2e^- \rightarrow H_{2(g)}$	$2H_2CO_{3(aq)} + 2e^- \rightarrow H_{2(g)} + 2HCO_{3(aq)}^-$
n	2	2	2
ν_{CO_2}	0	0	0
$\nu_{H_2CO_3}$	0	0	-2
ν_{HCO_3}	0	0	2
ν_{CO_3}	0	0	0
ν_H	0	-2	0
ν_{OH}	0	0	0
ν_{Fe}	-1	0	0

Note that ν_{Fe} above refers the stoichiometric coefficient of aqueous Fe^{2+} rather than solid Fe at the surface.

According to Faraday's laws, the molar species fluxes perpendicular to the surface can be calculated as the sum of all the flux contributions from the electrode reactions[112]:

$$N_j = \sum \frac{\nu_j i_{loc}}{nF} \tag{2.37}$$

Where N_j is the molar flux of species j, ν_j is the stoichiometric coefficient of species j, i_{loc} is the local current density, n is the number of participating electrons, and F is the Faraday constant.

The local current density (i_{loc}) for each reaction can be determined from the exchange current density (i_0), the overpotential (η), and either the anodic or cathodic Tafel slope values (b_a and b_c respectively). These calculations of i_{loc} for the anodic (Equation 2.38) and cathodic (Equation 2.39) reactions are as follows:

$$i_{loc} = i_0 \times 10^{\frac{\eta}{b_a}} \tag{2.38}$$

$$i_{loc} = -i_0 \times 10^{\frac{\eta}{b_c}} \tag{2.39}$$

Note that, by convention, the negative sign for the cathodic reaction, indicating electrons flowing in the opposite direction.

The overpotential (η) is given by:

$$\eta = E - E_{rev} \tag{2.40}$$

Where E is the electric potential and E_{rev} is the reversible potential. The electric potential is calculated within COMSOL as the difference between the electrode potential (Φ_s) and the electrolyte potential (Φ_l) at the interface:

$$E = \Phi_s - \Phi_l \tag{2.41}$$

Due to the zero potential gradients assumption, Φ_l becomes zero. The potential therefore becomes equal to Φ_s, which is solved iteratively using the total current and an initial guess for the electrode potential.

$$\Phi_s^{n+1} = i_{tot} \times A_c \times \Phi_s^n \tag{2.42}$$

Where i_{tot} is the total current density and A_c is the cross-sectional area.

$$i_{tot} = \sum i_{loc} \tag{2.43}$$

In order to calculate the species flux given by Equation 2.37 (and therefore mass loss at the electrode), values for i_0, b_a, b_c, and E_{rev} need to be defined. These values are shown in Table 2.8 and were adapted from the values provided by Nordsveen *et al.*[26]

Table 2.8 - Adjusted table of values for surface electrochemical reaction modelling.

$$i_0 = i_{0,ref}\left(\frac{c_H^+}{c_{H^+,ref}}\right)^{a_1}\left(\frac{c_{CO_2}}{c_{CO_2,ref}}\right)^{a_2}\left(\frac{c_{H_2CO_3}}{c_{H_2CO_3,ref}}\right)^{a_3} e^{-\frac{\Delta H}{R}\left(\frac{1}{T}-\frac{1}{T_{ref}}\right)} \quad (2.44)$$

Reaction	$i_{0,ref}$ $\frac{A}{m^2}$	a_1	$c_{H^+,ref}$ $molar$	a_2	$c_{CO_2,ref}$ $molar$	a_3	$c_{H_2CO_3,ref}$ $molar$	ΔH $\frac{kJ}{mol}$	T_{ref} $°C$	E_{rev} V	b V
$2H^+ + 2e^- \rightarrow H_2$	0.05	0.5	10^{-4}	0	N/A	0	N/A	30	25	$-2.303\frac{RT}{F}pH$	$2.303\frac{2RT}{F}$
$2H_2CO_3 + 2e^- \rightarrow H_2 + 2HCO_3^-$	0.06	−0.5	10^{-5}	0	N/A	1	10^{-4}	50	20	$-2.303\frac{RT}{F}pH$	$2.303\frac{2RT}{F}$
$Fe_{(s)} \rightarrow Fe^{2+}_{(aq)} + 2e^-$	1	2 for pH < 4 1 for 4 ≤ pH < 5 0 for pH ≤ 5	10^{-4}	1 for $P_{CO_2} < 1$ 0 for $P_{CO_2} \geq 1$	0.0366	0	N/A	37.5	25	−0.488	0.03 for pH < 4 0.08 for 4 ≤ pH < 5 0.12 for pH ≥ 4

As noted above, some of the values in Table 2.8 have been adjusted due to errors in the referenced paper. Firstly, the E_{rev} value for carbonic acid reduction has been multiplied by 2.303 rather than 2 to account for the conversion between log base 10 and the natural log in the derivation. This brings it in line with the other values in the table, which have also been adjusted to 2.303 from 2.3 for improved accuracy.

Secondly, the Tafel slope values for both cathodic reactions have been divided by 0.5 (multiplied by 2) as opposed to being divided by 2, as the transfer coefficient must be between zero and one. The value of $\alpha_c = 0.5$ is confirmed in the 1996 paper by Nesic *et al.*[113], referenced in the paper by Nordsveen *et al.*[26].

Additionally, all the conditional statements for the anodic dissolution reaction have been adjusted to ensure all values in the range are covered in order to provide greater clarity as to which value should be used at pH values of exactly 4 or 5, or a P_{CO_2} value of greater than 1 bar. Lastly, the conditional statements for a_1 and a_2 in this reaction have be switched. The reason for this is that, in the exchange current density (i_0) formula (Equation 2.44), a_1 relates to the H^+ ion concentration and a_2 relates to the CO_2 concentration. It should therefore be the case that a_1 is dependent upon the pH and a_2 is dependent upon the partial pressure of CO_2.

All temperature dependent constants, including the cathodic Tafel values provided in Table 2.8, were input as global parameters into COMSOL due to

the assumption of an isothermal fluid through the boundary. However, all pH dependent values were input as local variables in order to allow for the values to be defined in terms of the local surface concentration rather than the bulk pH. This is important as the pH, and therefore the dependent values, changes significantly close to the surface. The exchange current densities were also input as variables for the same reason, accounting for the changes in species concentration at the surface.

2.4 Results

Once the model had been generated following the procedure outlined in section 2.3, a parametric sweep was created in order to generate results for a range of temperature and pH values. These results were then compared to plots provided in the available literature in order to validate the COMSOL model.

2.4.1 Concentration Deviation Through the Boundary

Looking firstly at the speciation through the boundary layer, Figure 2-5 shows the deviation of the species concentration from the bulk, as well as the local pH values. The local concentrations of each species were extracted from COMSOL at each point within the boundary and their bulk concentration was subtracted (Figure 2-3). The pH value was calculated using the local H^+ concentration via Equation 2.14.

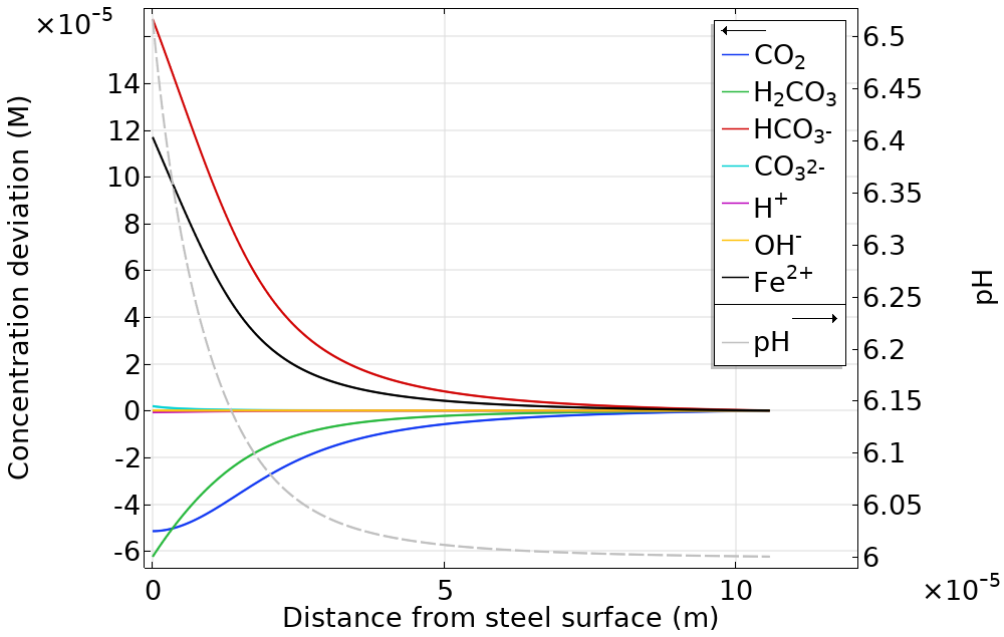

Figure 2-5 - Deviation of species concentration from the bulk through the boundary with input values: 20 °C, 0.1 m pipe diameter, 1 ms^{-1} flow velocity, pH 6 and 1 bar P_{CO_2}.

From Figure 2-5, the effect of the surface reactions can be clearly seen, with significant variation in the concentration of most species between $x = 0$ and the bulk. As expected, there is a large increase in the Fe^{2+} concentration as the Fe dissolves from the steel surface, as well as the generation of HCO_3^- due to the reduction of carbonic acid at the surface (shown by the decrease in H_2CO_3). Additionally, the concentration of H^+ shows the expected decrease as the ions are consumed to drive the anodic reaction. The consumption of these ions produces a noticeable change in the pH of the system, increasing from the bulk value of 6 up to around 6.51. This reinforces the importance of using the local pH value rather than the bulk value when evaluating the pH dependent values shown in Table 2.8.

Importantly, the concentration deviation plot also converges to a value of zero for all species, meaning that each of the species reaches its bulk value by the end of the boundary layer. This demonstrates both that the reactions defined throughout the boundary (Equations 2.27-2.33) are functioning to move the system towards equilibrium, and that the boundary conditions have been defined correctly.

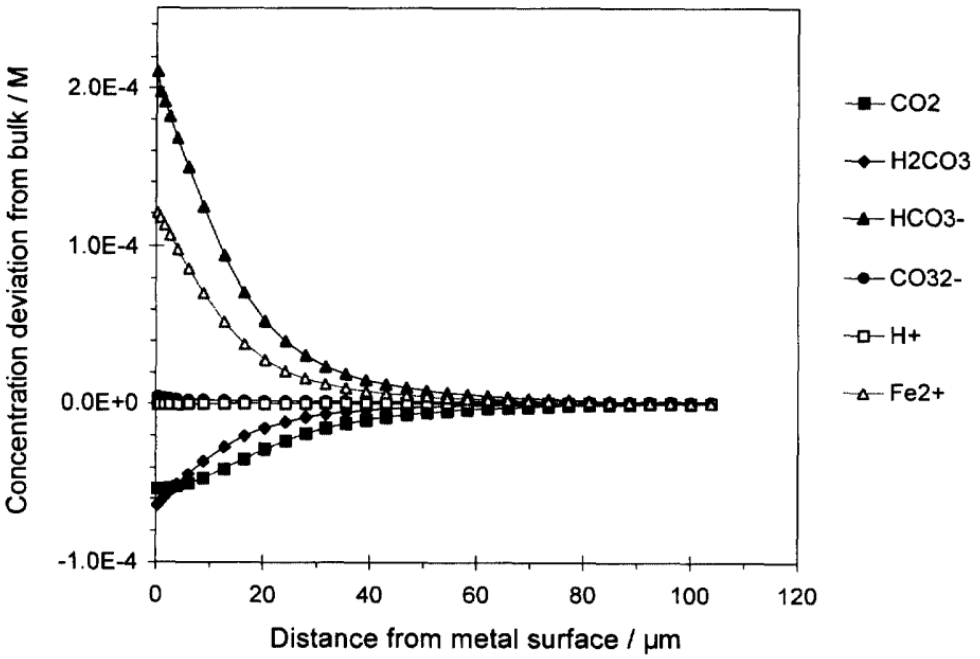

Figure 2-6 - Concentration deviation plot showing speciation through the boundary produced by Nordsveen *et al.*[25, 26] with input values: 20 °C, 0.1 m pipe diameter, 1 ms^{-1} flow velocity, pH 6 and 1 bar P_{CO_2}.

When compared to the equivalent plot provided by Nordsveen *et al.*[26] (Figure 2-6), a strong correlation between the results is found. The overall shapes of the curves are very similar, as well the length of the boundary layer and the magnitude of the deviations. A slight difference can be seen in the concentrations of Fe^{2+} and HCO_3^- close to the surface. However, a degree of disagreement at the electrode surface is to be expected due to the previously discussed changes to the modelling of the electrochemical reactions (see section 2.3.5).

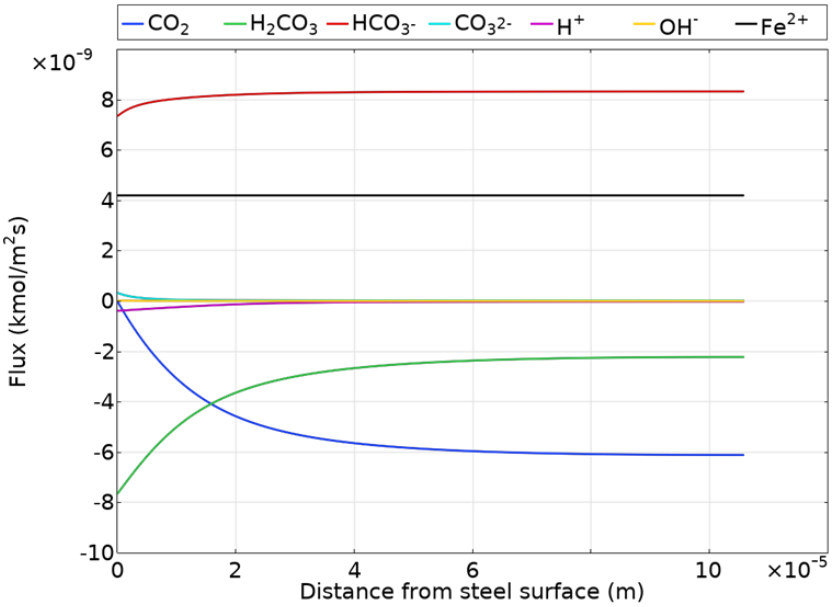

Figure 2-7 - Flux of species through the boundary with input values 0.1 m pipe diameter, 1 ms^{-1} flow velocity, pH 6 and 1 bar P_{CO_2}.

Examining the flux of species appears to confirm that the species transport defined by Equation 2.37 is functioning as expected. As previously discussed in section 2.2, the movement of the species is primarily determined by the concentration gradients throughout the boundary layer. This is shown by the x-component of the total flux, which in this case represents the flux normal to the metal surface. Species with increased concentrations at the surface when compared to the bulk, such as Fe^{2+} and HCO_3^-, have positive flux values, indicating movement away from the surface, whilst species with decreased concentrations, such as H_2CO_3, have a negative flux values indicating movement towards it. Together, Figure 2-5 and Figure 2-7 show how the flux varies as the concentrations change, with steeper concentration gradients resulting in greater diffusive transport. This is evident by the flux of Fe^{2+}, which maintains a constant value due to the lack of further reactions away from the surface. Interestingly, the flux of CO_2 tends towards zero close to the surface which is due the relatively small change in concentration relative to the bulk (10^{-5} M compared to 10^{-2} M, see Figure 2-3 and Figure 2-5). As the concentration gradient is small, the effect of diffusion is minimal and therefore the flux is primarily driven by turbulent diffusion which, as described by Equation 2.19, tends towards zero at the surface. The reason for the small change in concentration is once again down to the slow rate of the hydration reaction which, as seen in Equation 2.28, is the only reaction controlling the change in $[CO_2]$ through the boundary.

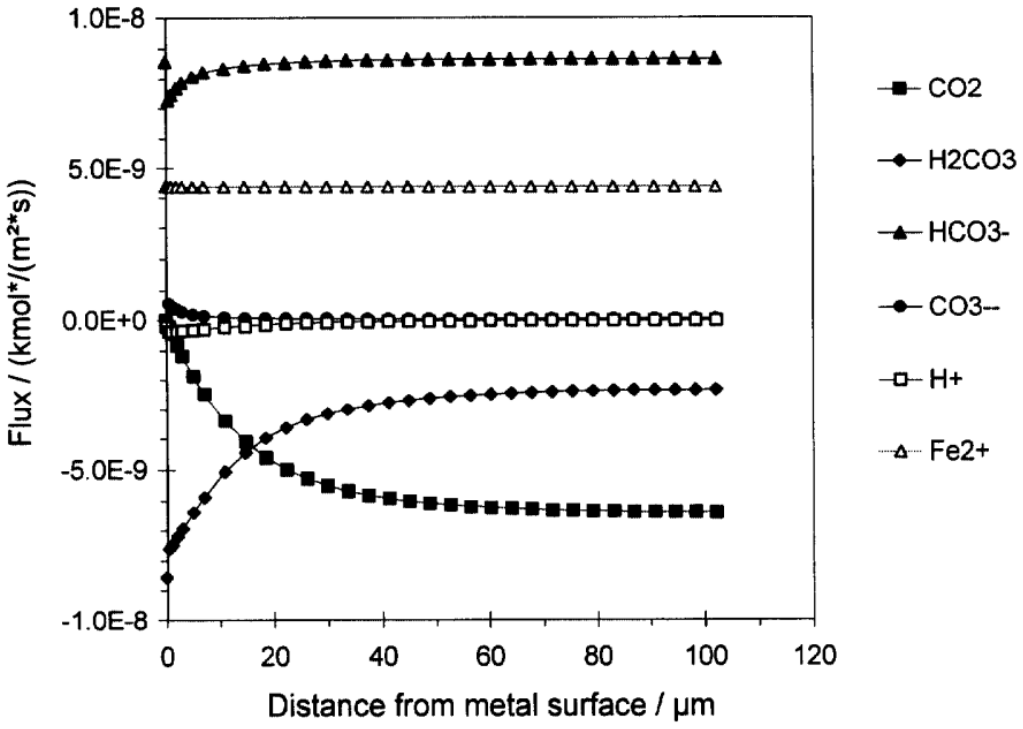

Figure 2-8 - Flux of species through the boundary produced by Nordsveen *et al.*[25, 26] with input values 0.1 m pipe diameter, 1 ms^{-1} flow velocity, pH 6 and 1 bar P_{CO_2}.

Comparing Figure 2-7 to the same plot by produced Nordsveen *et al.* (Figure 2-8), shows that the results produced by the two models are almost identical. Despite some small differences at $x = 0$ in the flux of H_2CO_3 and HCO_3^-, likely due to the changes to the modelling of the surface reactions, the magnitude and variation in the flux of each species show very good agreement. The similarity of these results is to be expected as both models use the same transport equation (Equation 2.17) to describe the movement of species through the boundary.

The next comparison plots the predicted corrosion rate at the electrode surface against the bulk pH of the system. Figure 2-9, shows that there is the expected increase in the corrosion rate as the bulk pH drops due to the increased concentration of H^+ in solution. As the bulk pH increases, there are fewer H^+ ions available to drive the anodic dissolution reaction, reducing the corrosion rate. But, as noted by Nesic *et al.*[37] for the conditions being modelled, above a pH of 6 the rate begins to rise due to the increased rate of the carbonic acid reduction reaction at higher pH values. The carbonic acid reaction becomes dominant due to the sum of the anodic and cathodic currents needing to be equal.

$$\sum i_{anodic} = \sum i_{cathodic} \tag{2.45}$$

$$i_{Fe} = i_H + i_{H_2CO_3} \tag{2.46}$$

As the supply of H^+ reduces with pH, the carbonic acid reduction becomes the dominant cathodic current, increasing the corrosion rate due to the inverse relationship between the reduction reaction and pH. This is explored further in section 2.5.1 (see Figure 2-20).

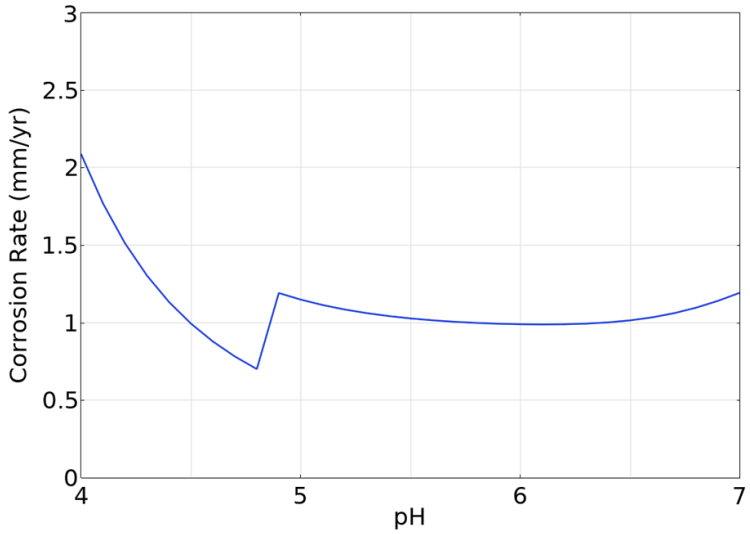

Figure 2-9 - Plot of predicted corrosion rate at the electrode surface vs the bulk pH, with input values 0.01 m pipe diameter, 1 ms^{-1} flow velocity, 293.15 K temperature, and 1 bar P_{CO_2}.

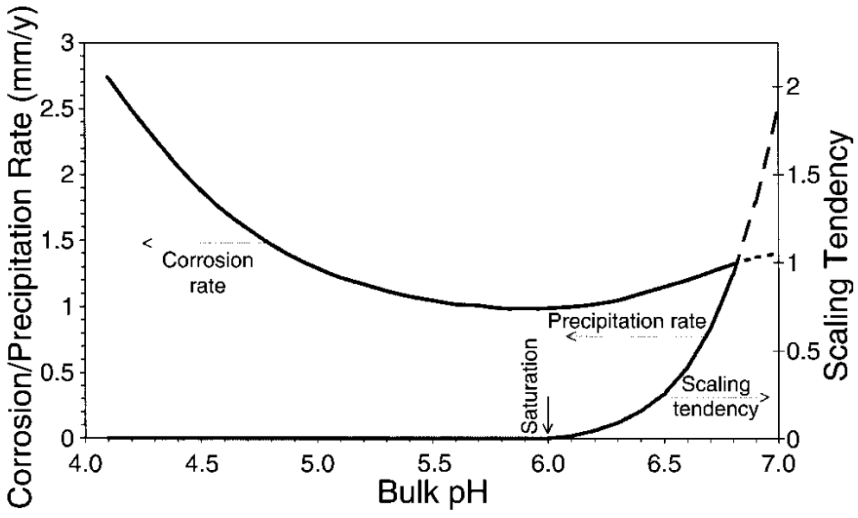

Figure 2-10 - Plot of prediction corrosion rate at the electrode surface as well as scaling tendency against the bulk pH produced by Nesic *et al.*[37] , with input values 0.01 m pipe diameter, 1 ms^{-1} flow velocity, 293.15 K temperature, and 1 bar P_{CO_2}.

The plot show in Figure 2-9 highlights a significant issue with the current model structure in that there is a clear step change in the corrosion rate that occurs at a pH of 4.85. The step change is not representative of a real life system but is predicted by the model due the conditional a_1 power constant for the anodic reaction shown in Table 2.8. For a pH of between 4 and 5 the value is given as a constant of 1, however in the original conference paper detailing the anodic reaction it was said to transition between 2 to 1 and then towards 0 in this region[114]. Hence, when the surface pH transitions to a value above 5 (which occurs at a bulk pH of 4.85 as shown in Figure 2-9), a sudden change in the predicted corrosion rate is observed. In order to improve the accuracy of the model in the transitional region, a more accurate description of the functional response exchange current would be required such as in the more recent CO_2 corrosion model proposed by Kahyarian and Nesic[12, 36]. When comparing the results to the corresponding plot in the literature (Figure 2-10), agreement between the two models is found for higher pH values. Within the transitional region there is some discrepancy which has already been discussed, however the changes made to adjust for the changing power constant are not detailed in the literature[26, 37, 38, 114]. It is possible that a more accurate pH-based function was produced to provide a smoother curve, but this is not shown.

The last key area of interest for the current model is the prediction of $FeCO_3$ supersaturation at the electrode surface, which is the driving factor in the precipitation of iron carbonate[17]. The degree of supersaturation is given by Equation 2.47:

$$SR = \frac{[Fe^{2+}][CO_3^{2-}]}{K_{sp}} \tag{2.47}$$

Where SR is the saturation ratio, $[Fe^{2+}]$ and $[CO_3^{2-}]$ are the species concentrations, and K_{Sp} is the solubility limit.

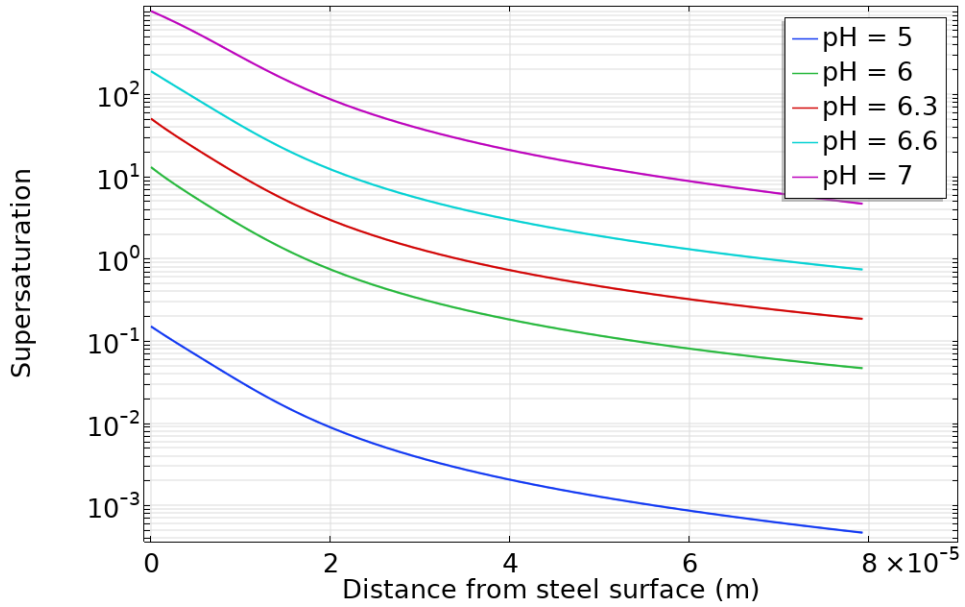

Figure 2-11 - Plot of supersaturation as a function of the distance from the steel surface using K_{sp} formula by Greenberg and Tomson[20] with input values: 20 °C, 0.01 m pipe diameter, 1 ms^{-1} flow velocity, pH 6 and 1 bar P_{CO_2}.

Figure 2-11 shows the supersaturation predicted by the COMSOL model, using a formula produced by Greenberg and Tomson[20] to calculate the K_{sp} value given by Equation 2.48.

$$\log K_{sp} = -59.2385 - 0.041377T_K - \frac{2.1963}{T_K} + 24.5724\log(T_K) \qquad (2.48)$$

Where T_K is the temperature in Kelvin.

Based on Figure 2-5, the supersaturation increases rapidly close to the surface due to the release of Fe^{2+} from the metal as well as the increased CO_3^{2-} concentration. This once again highlights the importance of using the surface rather than bulk values when evaluating the corrosion behaviour of the system. The determination of the surface supersaturation is important when incorporating $FeCO_3$ formation kinetics into the model, as $FeCO_3$ precipitation only occurs when the supersaturation is above 1[18]. Figure 2-11 clearly demonstrates how this occurs more readily at higher pH values, which may instead lead to an opposing issue of scale formation.

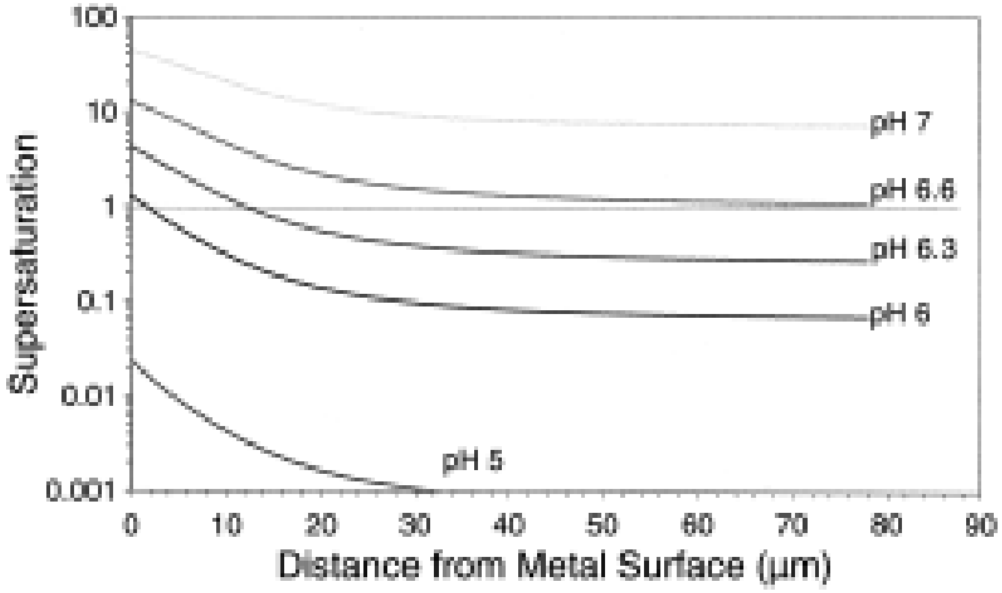

Figure 2-12 - Plot of supersaturation as a function of the distance from the steel surface produced by Nesic *et al.*[37] with input values: 20 °C, 0.01 m pipe diameter, 1 ms^{-1} flow velocity, pH 6 and 1 bar P_{CO_2}.

Comparing the values predicted by COMSOL against the plot produced by Nesic *et al.*[37] (Figure 2-12), there is an obvious disagreement in the shape of the two plots. The plot provided in the literature appears to reach a constant value much sooner than in the COMSOL model. It is not entirely clear as to why this is the case, however it seems as though in the literature the plot may have been produced using the surface CO_3^{2-} concentration but the bulk Fe^{2+} concentration. Adjusting Figure 2-11 to perform the calculations in this way produces a much closer agreement:

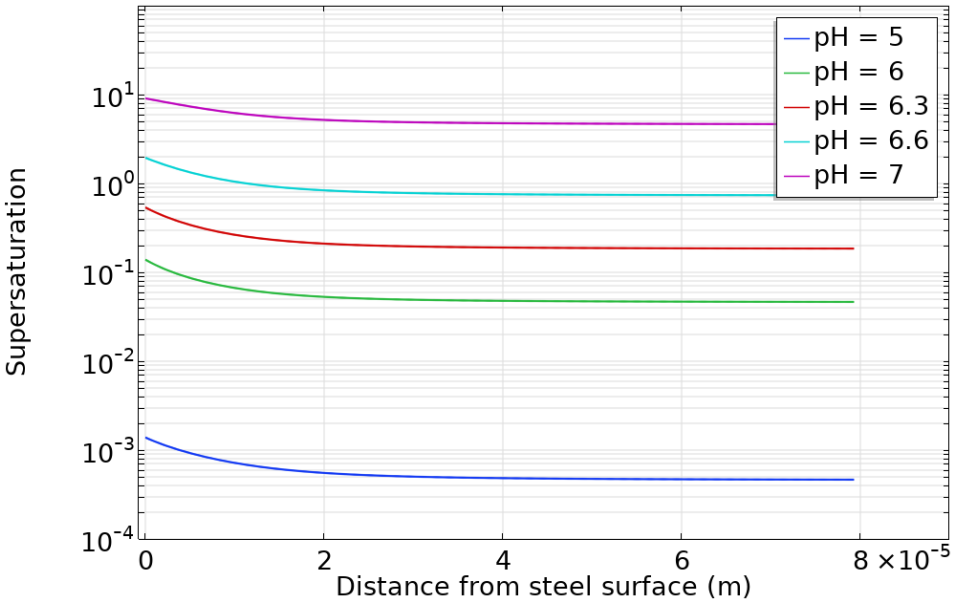

Figure 2-13 - Plot of supersaturation as a function of the distance from the steel surface using bulk Fe^{2+} to calculate supersaturation, with input values: 20 °C, 0.01 m pipe diameter, 1 ms^{-1} flow velocity, pH 6 and 1 bar P_{CO_2}.

There is however still some discrepancy between Figure 2-12 and Figure 2-13 in regard to the magnitude of the supersaturation. But, as previously stated, it is not entirely clear which formula was used by Nesic *et al.*[37] to calculate the value of K_{sp}. There are multiple formulae available in the literature and so it is possible that a different value was used, which would lead to linear scaling of the supersaturation values.

The plots discussed thus far demonstrate the functionality of the COMSOL model and its ability to model species behaviour both at the surface and throughout the boundary. However, in order to validate the model for a range of values and conditions a comparison plot has been produced to compare against a number data points from the available literature. Using the OriginPro® graph digitizer function, data was extracted from a total of 7 plots available in the literature, namely Figures 7 and 8 from Part 1[26] and Figures 1-5 from Part 2[37] of the Nordsveen series. The use of the graph digitizer was necessary due to the low resolution of many of the plots. Clear data points were selected from each plot and compared to the COMSOL model, which was run under the stated input conditions. The results are shown in Figure 2-14, alongside a dotted line ($y = x$) along which perfectly matched data would sit.

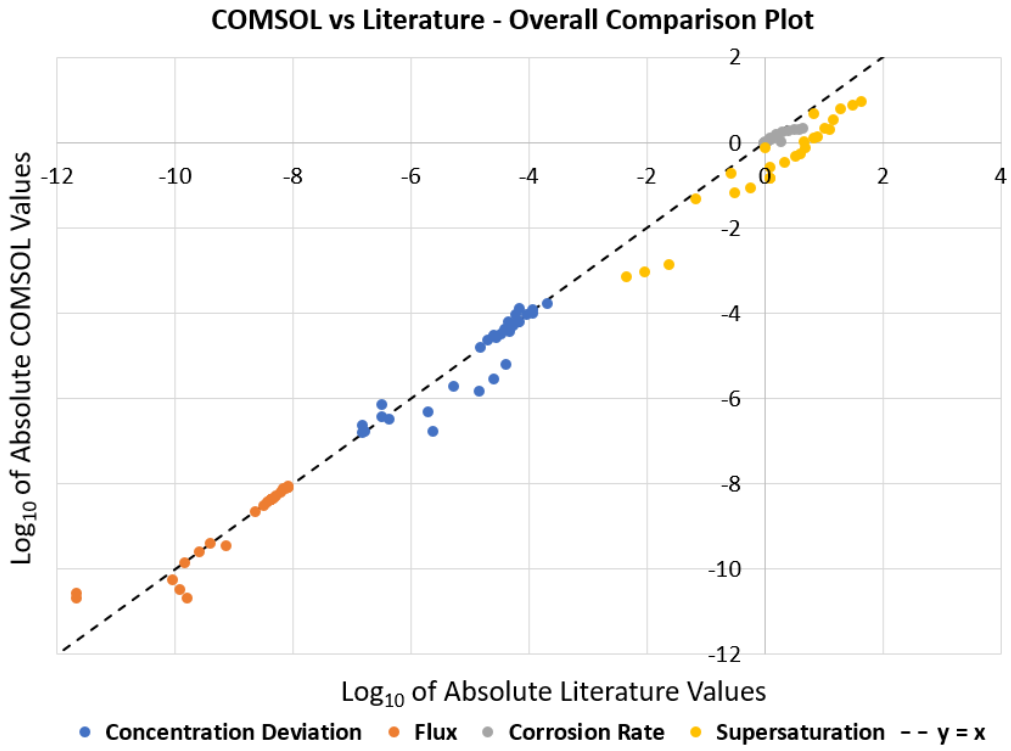

Figure 2-14 - Comparison of various values and a range of input conditions of results from the COMSOL model against the corresponding result from the literature.

As can be seen in Figure 2-14, the two models show a high degree of a correlation, particularly when looking at the concentration deviation and flux plots. A small amount of variation is expected due to the error introduced when extracting data from the literature. For the flux plots this explains the data points with the largest discrepancy as they occur at very low magnitudes and so are difficult to accurately define; for larger values a much greater level of agreement is seen. In regard to the concentration deviation plot, there are 6 data points which are clearly below their expected value based upon the literature. These values all relate to the carbonate concentration in the plot, indicating a potential difference in the models when modelling the reaction kinetics of this species in the boundary (see Equations 2.25 and 2.31). It has been assumed that the model in the literature has been kept consistent between the each of the papers by Nordsveen, Nesic, Nyborg and Strangeland[26, 37, 38].

Considering the supersaturation comparison in Figure 2-14, the values produced in the COMSOL are consistently below that of the literature. At first glance, this once again appears suggests that a different solubility limit value (K_{sp}) has been used in the calculations. However, there are 4 data points that are much closer to the COMSOL values and all of these values correspond to

the supersaturation values compared at $x = \delta$. As the same equilibrium constants have been used to calculate the bulk concentrations between the two models, this must mean that the K_{sp} value is not the main reason for the discrepancy. Additionally, as the flux of Fe^{2+} is constant and matching in both models (see Figure 2-7 and 10), this strongly suggests a difference in the calculation of the carbonate concentration throughout the boundary.

The final set of data points in Figure 2-14 relate to the predicted corrosion rates of the models. For the most part there is very good agreement between the two for a range of pH values at standard temperature and pressure, which can be seen in Figure 2-9 and 12. The only noticeable disparity between the models under these conditions occurs at a pH of 4.5, the reason for which has been previously discussed. However, when comparing the values over a range of temperatures, the values begin to diverge at higher temperatures with the COMSOL model predicting lower corrosion rates, as shown in Figure 2-15.

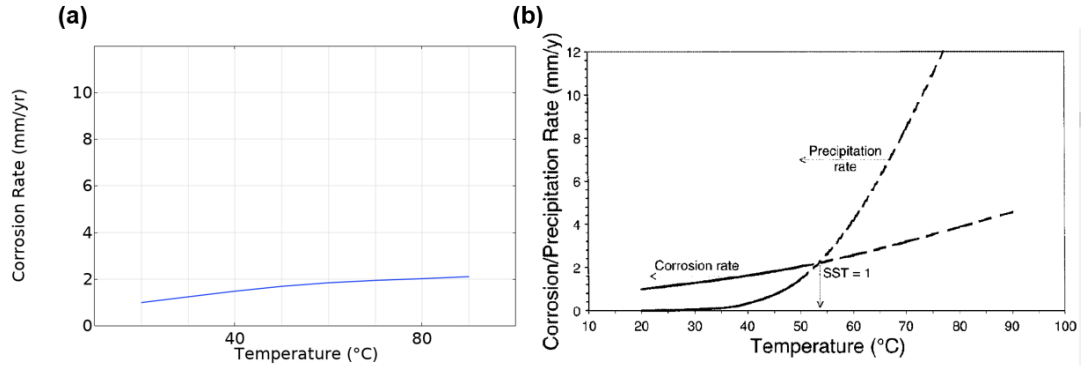

Figure 2-15 - Predicted surface corrosion rates from the COMSOL (a) and Nesic *et al.*[37] (b) models over a range of temperatures with input values: 0.01 m pipe diameter, 1 ms^{-1} flow velocity, pH 6 and 1 bar P_{CO_2}.

It is generally expected that the corrosion rate increases with temperature in the absence of surface films. However, as the comparison in Figure 2-15 is done at a relatively high pH value of 6, the low concentration of H^+ ions in the bulk becomes a factor. Within the COMSOL model, the low availability of ions transported to the surface at this pH becomes a limiting factor in the corrosion process leading to a plateau in the corrosion rate. This mass-transport limiting effect is seemingly not captured by the model created by Nesic *et al.*, however as discussed by the authors, this becomes less important at high temperatures due to the formation of protective $FeCO_3$ films above temperatures of around 50 °C[37]. Therefore, although not explicitly stated, it seems likely that these higher temperatures were not modelled and that the dashed line simply represents an extrapolation of the data.

2.5 Numerical Exploration

As previously stated, the advantage of building the model within COMSOL Multiphysics® is that it allows for the rapid generation of data over a wide range of conditions. Thus far, the COMSOL model has been validated against all comparable plots available in the literature and has shown a high level of agreement across in all aspects. In this section, a deep numerical exploration of the model is conducted which goes beyond the data provided by the previous CO_2 corrosion models. A large parametric study was run for thousands of input conditions, with temperatures ranging from 0-100 °C and partial pressures ranging from 0.1-10 bar at bulk pH values of 5, 5.5, 6, and 6.5. Fluid velocity and pipe diameter were kept constant at 1 ms^{-1} and 0.01 m, respectively.

Contour plots, generated using the coding software MATLAB, are utilised in order to visualise this data and evaluate the direct impact of changes in the bulk conditions upon the corrosion process occurring at the steel surface. Particular attention is given to the effect of these input conditions on the predicted corrosion rate, pH, and supersaturation at the surface. An even distribution of points was used to generate the plots at each of the bulk pH values, these are shown in Figure 2-16.

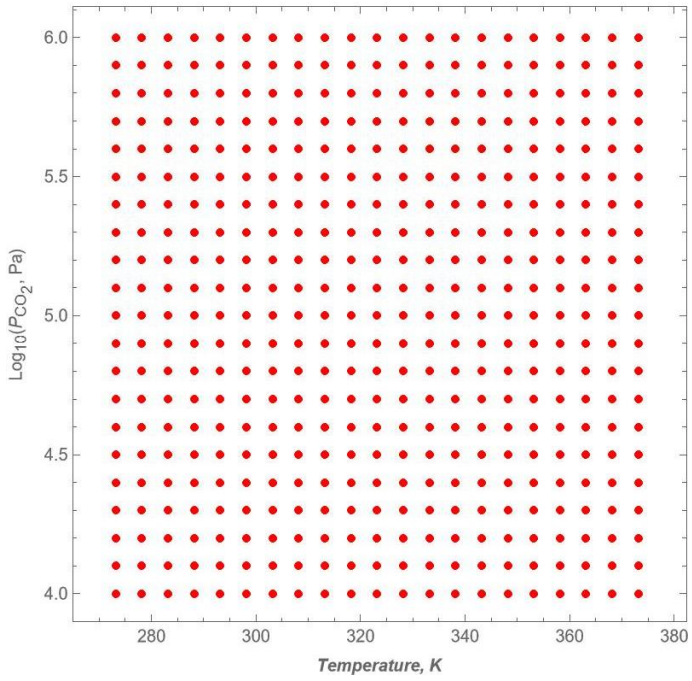

Figure 2-16 - Distribution of temperatures and partial pressures used to generate contour plots for each bulk pH values.

2.5.1 Effect on Corrosion Rate

The impact of bulk pH and temperature upon the surface corrosion rate have previously been discussed under a single set of specific conditions, see Figure 2-9 and Figure 2-15, respectively. Here however, the effect of these input parameters is evaluated across a wide range of conditions. Additionally, the effect of the partial pressure of CO_2 within the system is introduced into the analysis; an important factor which was not previously explored in the Nordsveen series of papers. A contour plot for each of the corrosion outputs at bulk pH values of between 5 and 6.5 has been produced using the data distribution shown in Figure 2-17.

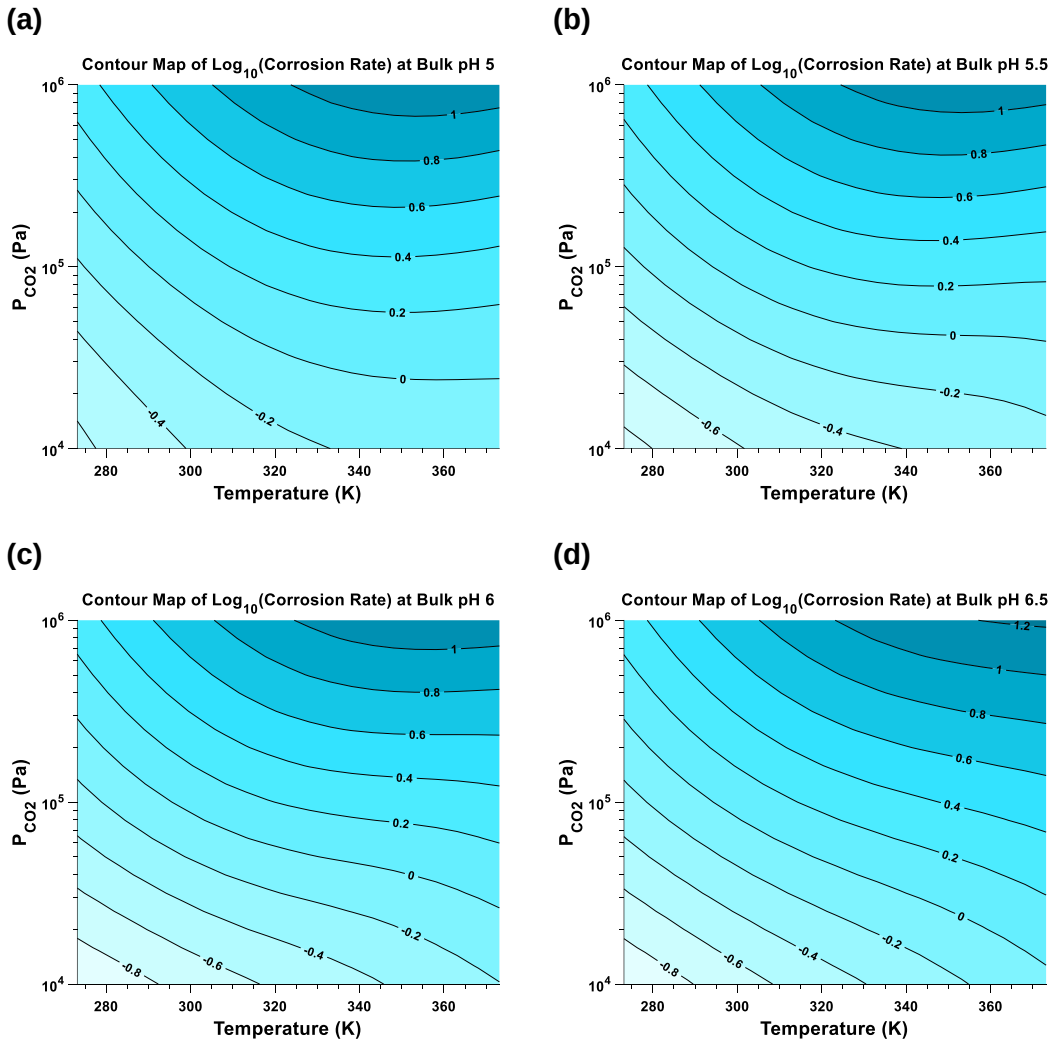

Figure 2-17 - Contour plots of predicted corrosion rates as a function of the log of partial pressure and temperature for bulk values of: (a) pH 5 (b) pH 5.5 (c) 6 and (d) 6.5.

Across the full range of bulk pH values, similar trends are found within the contour plots of corrosion rate, shown in Figure 2-17. In general, it is the case

that as the partial pressure of CO_2 is increased, there is a corresponding rise in the corrosion rate. The reason for this can be explained by the increase in the surface pH, seen in Figure 2-18.

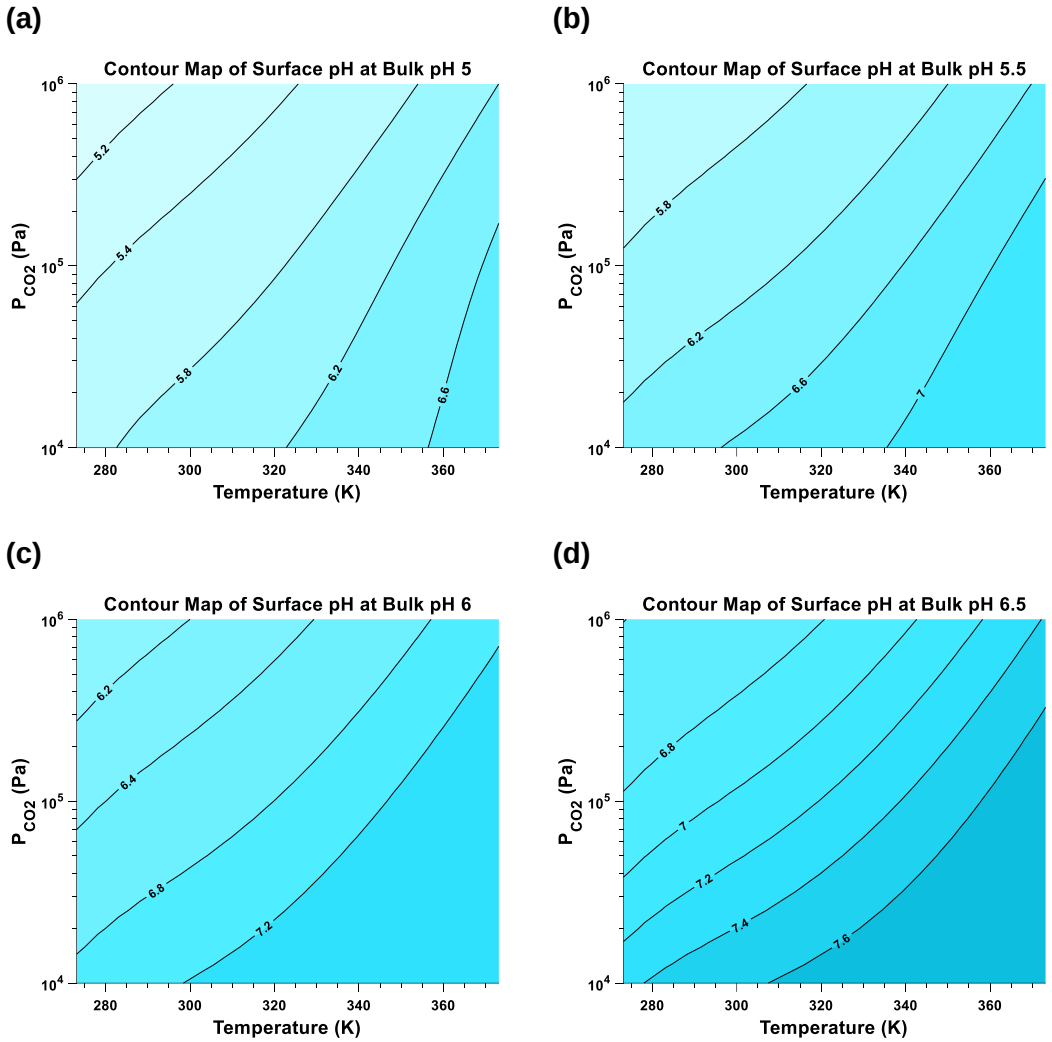

Figure 2-18 - Contour plots of surface pH as a function of the log of partial pressure and temperature for bulk values of: (a) pH 5 (b) pH 5.5 (c) 6 and (d) 6.5.

Although there is no change in the bulk pH, the increased pressure introduces more carbonic acid available into solution, which then dissociates to produce additional H^+ ions to drive the corrosion process. To a lesser extent, this is also the reason that lower bulk pH values raise the corrosion rate. The increased concentration of H^+ in the bulk produces a steeper concentration gradient within the boundary, resulting in a faster rate of transport between the bulk and surface.

The change in corrosion rate with temperature however, is noticeably more complex, as is shown by the inconsistent shapes of the contour lines across

the range of conditions shown. The reason for this due to the interactions between a large number of temperature dependent constants within the system. Looking firstly at the effect on the flow, at higher temperatures the viscosity of the fluid is reduced, resulting in a thinner boundary layer. Ions in solution therefore have a shorter distance to travel between the bulk fluid and the surface, resulting in steeper concentration gradients and a more rapid exchange between the two. However, it should be noted that as temperature increases, the reduction in kinematic viscosity is much greater than the reduction in fluid density (see Table 2.1), resulting in a reduction in D_T at higher temperatures (see Equation 2.19). This acts to slow diffusion through the boundary and therefore reduces the corrosion rate due to it being a mass-transport controlled process. These competing factors are indicative of the type of behaviour that is seen when examining the temperature dependence of this system.

The next key aspect to assess is the temperature dependence of the rate constants, both in the bulk and throughout the boundary. As has been shown previously by Li and Duan[61] and Marshall and Frank[62], each of the equilibrium constants K_{H,CO_2}, K_{bi}, K_{ca}, and K_w are strongly reliant upon the temperature. These graphs are shown in Figure 2-19.

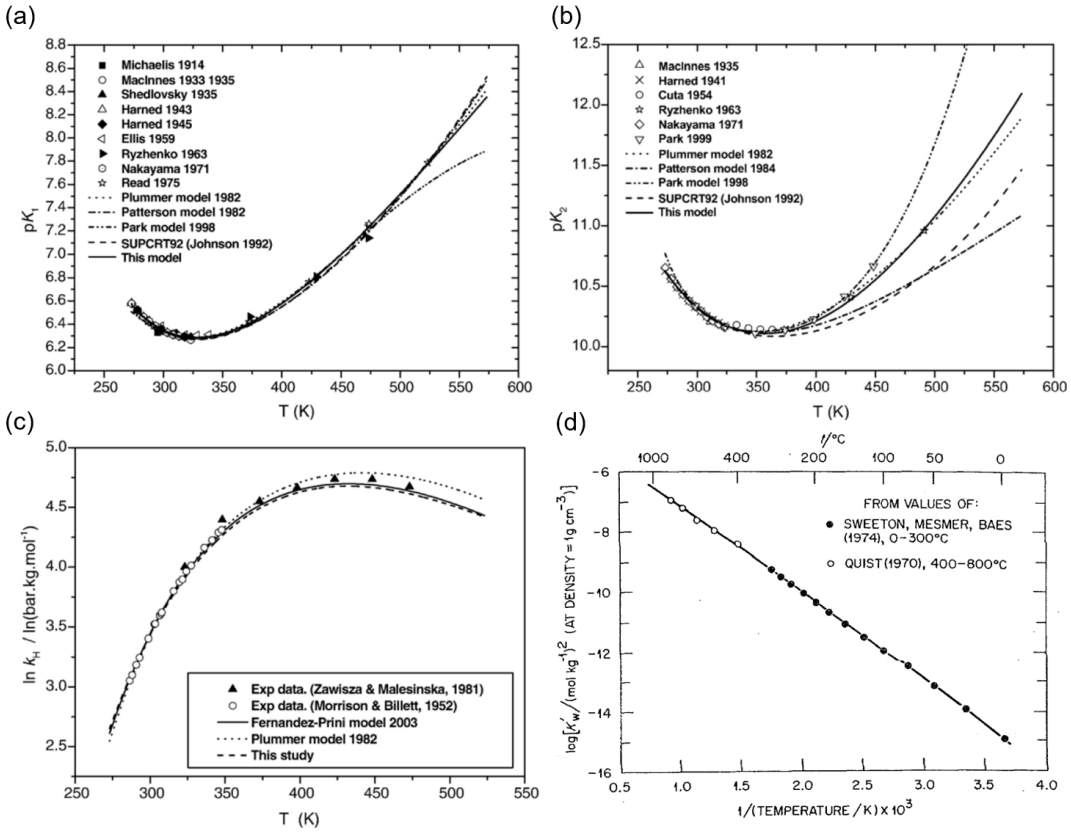

Figure 2-19 - Plots of the equilibrium constants: (a) K_{bi} (b) K_{ca} (c) K_{H,CO_2} and (d) K_w as a functions of temperature produced by Li and Duan[61] (K_{bi}, K_{ca}, K_{H,CO_2}) and Marshall and Franck[62] (K_w)

In section (c) of Figure 2-19, it should be noted that the definition of K_{H,CO_2} used by Li and Duan is defined as pressure divided by molar concentration; the reciprocal of the definition used throughout this report (see Table 2.2). The relationship between K_{H,CO_2} and temperature as defined here would therefore be the inverse of that shown in the data provided by Li and Duan.

Figure 2-19 displays a number of important parameters that explain complex system response to a change in temperature. The first and most obvious observation is that each of the equilibrium values change as a function of temperature. In general, the two dissociations constants increase at higher temperatures (graphs (a) and (b)), producing a greater number of H^+ ions at a faster rate as the forwards reaction becomes dominant. Despite this, the overall solubility of CO_2 is seen to decrease (graph (c)) which implies less carbonic acid available in solution; a similar effect to if the partial pressure is dropped. Looking at the water dissociation constant K_w (graph (d)), it is found to increase exponentially with increasing temperature. Therefore, at lower temperatures this reaction can be assumed to be negligible, but as the

temperature is increased it becomes more and more significant in the production of H^+ ions.

It is also important to observe the shape of the curves as, with the exception of K_w, the correlation between temperature and the constants changes. Each of the constants have clearly defined maxima and minima, which occur at different temperature values. For example, K_{bi} reaches its minimum value at around 325 K, whereas for K_{H,CO_2} the peak is closer to 425 K. The misalignment of these peaks is partially responsible for some of the wave patterns seen in Figure 2-17.

The last point that will be explored here is the impact of the temperature on the electrochemical reactions at the surface. As previously discussed, within the model, there are two cathodic reactions taking place simultaneously at the steel surface: hydrogen reduction and carbonic acid reduction (Equations 2.9 and 2.10). The rates of each of these reactions depend on the surface concentrations of H^+ and H_2CO_3, respectively. Figure 2-20 displays the ratio of the exchange currents of these two reactions over a range of temperature and pH values, effectively showing the relative contributions of each to the overall corrosion process. It can be seen that for low bulk pH and pressure values, the H^+ reduction is the dominant reaction ($\log\left(\frac{i_{H^+}}{i_{H_2CO_3}} > 0\right)$) for the given Reynold's number. As either of these input values are increased however, there is a noticeable shift towards the carbonic acid reduction being dominant. The shift with bulk pH being due to the decreased number of H^+ ions available in solution, whilst the shift with pressure is due to the increase in aqueous CO_2 being hydrated and forming H_2CO_3. As both of these cathodic reactions have different responses to temperature change, it causes the variation in the contour plots for different pH and P_{CO_2} values seen in Figure 2-17.

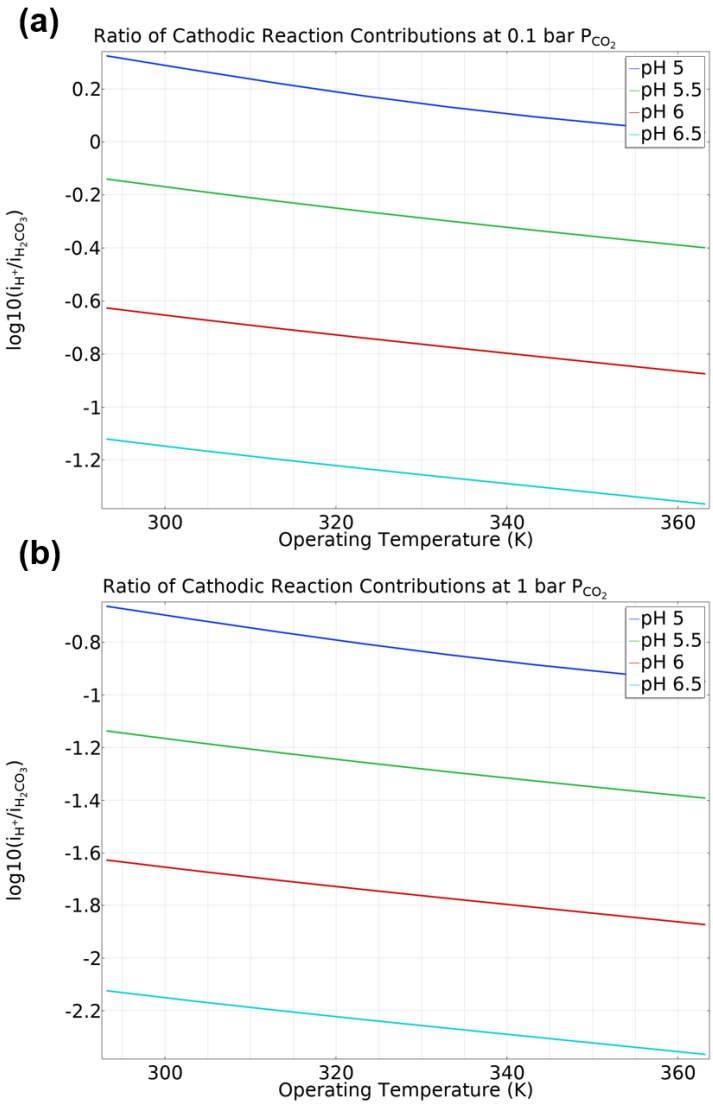

Figure 2-20 - Plots of the ratio of exchange current densities for H^+ and H_2CO_3 surface reductions over a range of temperatures at (a) 0.1 bar and (b) 1 bar for Re = 9961.9.

The high degree of complexity when evaluating temperature dependence of this system makes it very difficult to establish a clear cause and effect relationship. In general, it can be said that higher temperatures result in greater corrosion rates, however, as shown in graphs (a), (b), and (c) of Figure 2-17 there are regions in which the opposite is true. The overall conclusion from these plots is that there is a complex interrelation between many factors that must be considered when assessing the relative effect on corrosion rate. Whilst general expected trends can be identified, it is almost impossible to accurately quantify the direct impact of changing input conditions without the aid of computer simulation or experimental data.

2.5.2 Effect on Saturation Ratio

It is known that changes to the temperature, pressure, and bulk pH have a noticeable impact on the behaviour of the system. The concentrations of key species can vary by orders of magnitude, impacting not just the corrosion rate, but also the formation of protective corrosion products on the surface. However, by looking at the effect of the input conditions on the surface saturation ratio, it is possible identify areas of stability for the formation of iron carbonate. Figure 2-21 shows the surface saturation index of $FeCO_3$ over the range of input conditions shown in Figure 2-16. The surface saturation index represents the log of the saturation ratio (as defined by Equation 2.47), which is dependent upon the local concentrations of Fe^{2+} and CO_3^{2-}.

$$SI = \log_{10}(SR) = \log_{10}\left(\frac{[Fe^{2+}][CO_3^{2-}]}{K_{sp}}\right) \tag{2.49}$$

Where SI is the saturation index and SR is the saturation ratio.

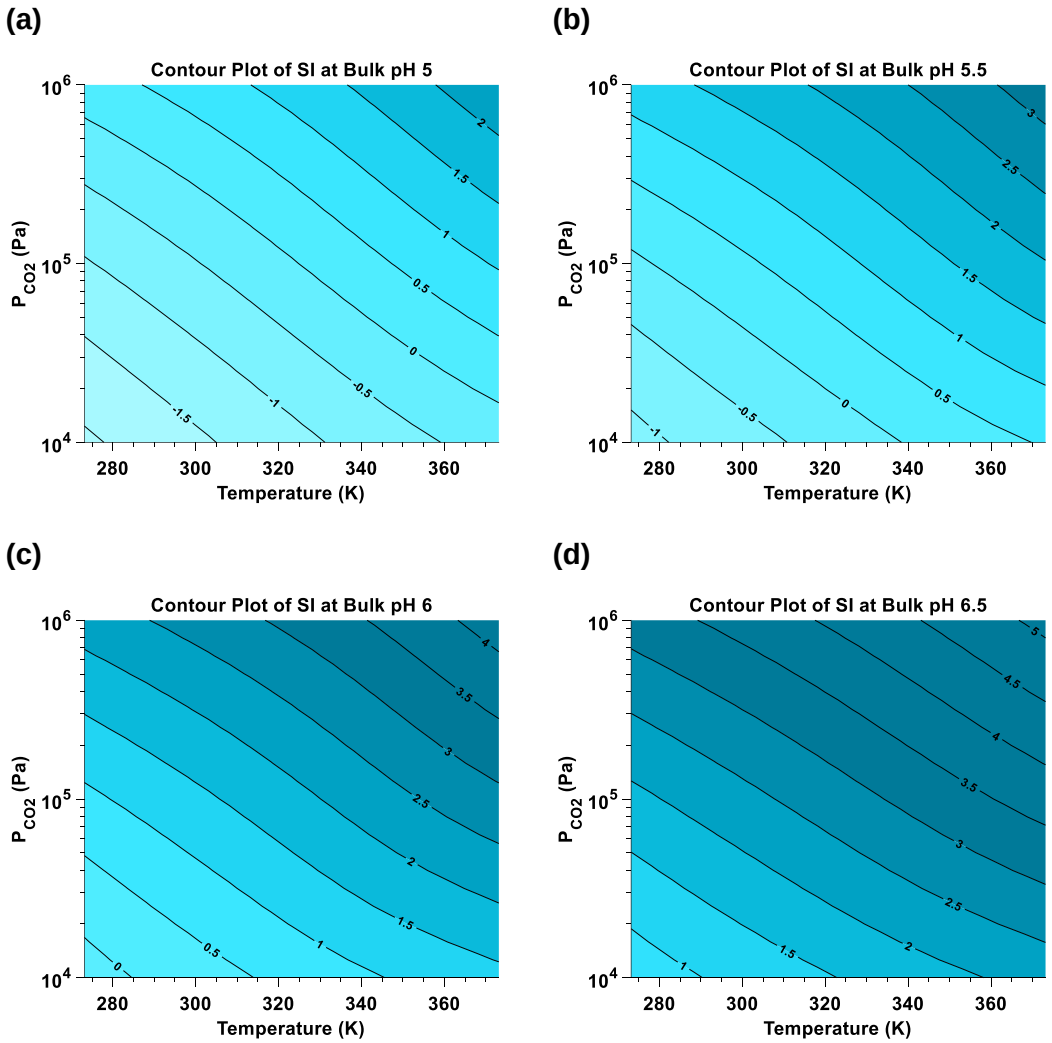

Figure 2-21 - Contour plots of surface saturation index of $FeCO_3$ as a function of the log of partial pressure and temperature for bulk values of: (a) pH 5 (b) pH 5.5 (c) 6 and (d) 6.5.

From Figure 2-21, it appears that that is almost a log-linear relationship between pressure and temperature in order to produce a stable $FeCO_3$ saturation ratio across the range of bulk pH values. Whilst not a perfect relationship, the data suggests that a constant saturation ratio can be maintained following a drop in either temperature or pressure, provided there is a corresponding increase in the other variable. As the corrosion rate is intrinsically linked to the release of iron from the surface, the surface concentration of Fe^{2+} follows a very similar trend to the corrosion rates shown in Figure 2-17. However, the contour plots of the saturation index show a much more consistent increase with temperature, pressure, and bulk pH. The reason must therefore be due to the surface concentration of carbonate ions, which is shown in Figure 2-22.

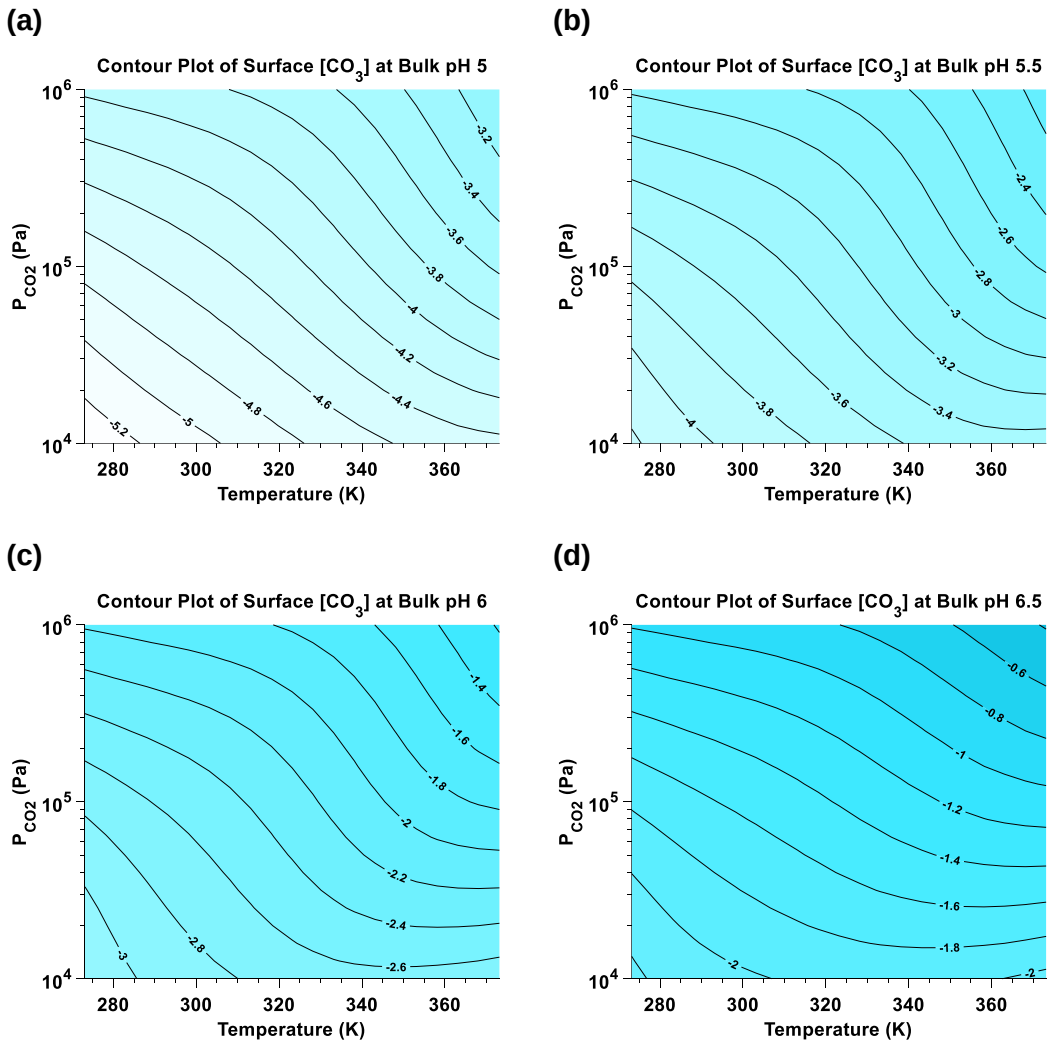

Figure 2-22 - Contour plots of surface CO_3^{2-} concentration (M) as a function of the log of partial pressure and temperature for bulk values of: (a) pH 5 (b) pH 5.5 (c) 6 and (d) 6.5.

Figure 2-22 presents a much more complicated picture of what is happening at the corroding surface. The reasons for this are similar to those discussed in section 2.5.1 regarding the contour plots of corrosion rates. At higher partial pressures, the solubility of CO_2 is increased, leading to increased concentrations of both iron and carbonate ions throughout the domain. The increase due to the changing pressure is fairly consistent across all temperature and bulk pH values. However, when looking at temperature in isolation, the effect on the carbonate concentration varies. The complex interactions between the changing boundary layer thickness, equilibrium values, rate constants, CO_2 solubility, and the dominance of the cathodic reaction all come into play once again. It would not be possible to analytically determine the surface concentration of CO_3^{2-} for a given set of conditions.

Interestingly, despite the complex contour patterns shown in Figure 2-22, the contour plots of the saturation index are much more predictable. This demonstrates the interconnected nature of the system, as fluctuations in one species are balanced by an equal change in the other. A faster corrosion rate results in increased Fe^{2+} production, but the mechanisms by which this occurs result in lower CO_3^{2-} concentrations, either due to reduced CO_2 solubility or the dominance of the carbonic acid reduction reaction.

It should be noted raising the bulk pH of the system causes an increase in both the carbonate concentration and the overall saturation index. This is a well-known phenomenon that is explained in detail by Stumm and Morgan[115] and relates to the relationship between the equilibrium constants and the H^+ concentration. By evaluating the equilibrium concentrations of the relevant aqueous species in a closed system over a range of pH values, this effect can be shown.

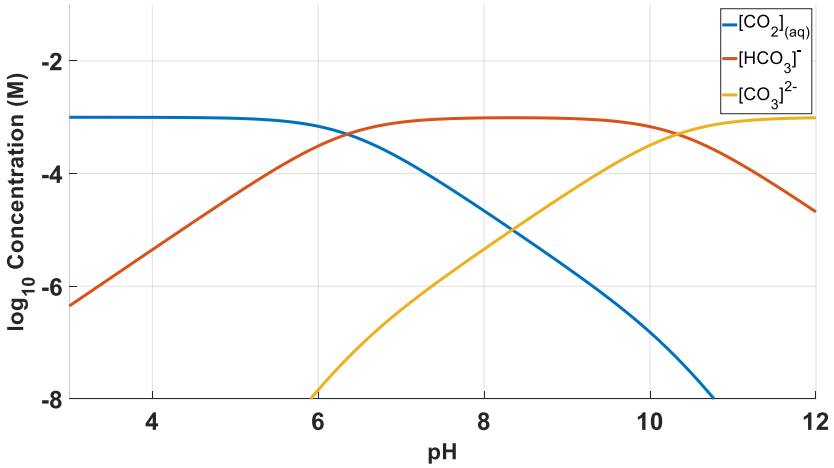

Figure 2-23 – Bjerrum plot showing the concentrations of aqueous and dissociated CO_2 over a range of pHs in a closed fresh water system, as detailed by Stumm and Morgan[115].

Note, in Figure 2-23 $[CO_2]_{(aq)}$ refers to the total dissolved CO_2, including the hydrated form of carbonic acid.

Figure 2-23 shows that, as the pH in a closed system changes, there is a shift from aqueous CO_2 towards the dissociated forms, raising the concentration of carbonate ions. This is analogous to what is occurring in the boundary layer as there is no additional gaseous CO_2 introduced at this point and helps explain the high HCO_3^- concentrations seen in the previous comparison to the Nordsveen model (see Figure 2-5). The increased carbonate concentration results in higher degree of supersaturation and means that $FeCO_3$ is more

likely to precipitate out and form a protective layer on the surface. The result is in even lower corrosion rates than those shown in Figure 2-17 for the higher bulk pH values, and therefore the effect of changing the bulk pH is amplified.

Chapter 3 - Kahyarian Model Implementation within COMSOL

In 2019, Aria Kahyarian and Srdjan Nesic of Ohio University published a new model for carbon dioxide corrosion of mild steel[36], which notably does not include the direct reduction of carbonic acid. Instead, a 'buffering effect' mechanism is utilised in which H_2CO_3 dissociates at the surface to compensate for the lower pH, producing H^+ ions to drive the cathodic half-reaction. A second version of this model was published by the same authors a year later[12] with updated constants and minor corrections to the text. Although modelling the same scenario, this model introduced several significant changes when compared to the model by Nordsveen *et al.*[26], discussed in the previous chapter. Alongside the treatment of H_2CO_3, further changes were made to the anodic kinetics, bulk chemistry calculations, species transport formulae, and species activity.

In this chapter, the 2020 version of the Kahyarian *et al.*[12, 36] model is implemented within COMSOL Multiphysics® version 6.1 to provide insight as to how the mechanistic modelling decisions made during its development affect the predicted output. A thorough numerical exploration of the model is conducted to identify the behaviour of the model over a range of temperatures, CO_2 partial pressures, bulk pH values, and hydrodynamic conditions.

3.1 Background

Comprehensive mechanistic models of CO_2 corrosion are inherently the most complex form of corrosion model as they attempt to capture, and fully couple all relevant chemical, electrochemical, and physical influences[31]. As such, there are two primary factors that are considered during their development:

1. Understanding of the underlying physicochemical mechanisms that drive the corrosion process.
2. Empirical data to determine the rate of associated processes across a range of conditions.

Over time, both of these factors are susceptible to change, as additional experiments are conducted and both technological advancements and improved methodologies allow for the gathering of higher quality data. As such, it is common that in the years between production of different

comprehensive mechanistic models, significant scientific advancements have been made as to fundamentally influence their design.

3.1.1 Role of Carbonic Acid

Possibly the most fundamental mechanistic development since the early model developed by Turgoose *et al*.[24] in the 1990s, is the change in understanding of the cathodic surface reactions, in particular the role of H_2CO_3. Early models follow a mechanism proposed by De Waard and Milliams[30] in which two cathodic half reactions take place; H^+ reduction and H_2CO_3 reduction. Under this mechanism, H_2CO_3 reacts directly with the corroding surface to form H^+ and HCO_3^- (Equation 3.1).

$$2H_2CO_{3(aq)} + 2e^- \rightarrow H^+_{(g)} + 2HCO_{3(aq)}^- \quad (3.1)$$

Due to the direct interaction between H_2CO_3 and the surface, this became known as the 'direct reduction' model and is the mechanism utilised by Nordsveen *et al.*[26].

For years, the direct reduction model was the standard in CO_2 corrosion modelling. However, in 2008 Remita *et al*.[32] revisited a different mechanism originally proposed back in 1998 by Linter and Burstein[34] following observations made by Hurlen *et al*.[116, 117] regarding the importance of buffering capacity on the rate of the cathodic reaction. It was suggested that, instead of reacting directly with the surface, H_2CO_3 instead rapidly dissociates near the surface, with the dissociation reaction producing additional ions to drive the H^+ reduction reaction. In the work by Remita *et al*.[32], cathodic polarisation of a rotating disk electrode (RDE) was used to compare the limiting currents of a CO_2 saturated solution and a nitrogen (N_2) purged solution for a pH of approximately 4. It was first shown that, for a given rotation speed and pH, the limiting cathodic current was greater for the CO_2 saturated solution when compared to the N_2 solution. This confirmed that, at a fixed pH, a system containing CO_2 undergoes a higher rate of corrosion than a system without CO_2, independent of the mass-transport behaviour. The experimental data was then combined with a simple mechanistic model to investigate whether the buffering effect alone could be the cause of the difference. It was concluded that, provided the dissociation reactions were properly accounted for, the buffering effect was sufficient to account for the higher current, without the need for a secondary cathodic reaction.

As noted in the review paper by Kahyarian *et al*.[31], the limited range of experimental conditions investigated by Remita *et al*.[32] (solely pH 4 and 1

bar P_{CO2}) prevented their conclusions from being extended to conditions with much greater H_2CO_3 concentrations. However, in 2015 a more extensive experimental study was conducted by Tran *et al*.[33]. Stainless steel electrodes in both a glass cell rotating cylinder electrode (RCE) set-up, and an autoclave were used to measure the cathodic polarisation response at pHs 4, 5, and 6 for temperatures of 25 °C and 80 °C at 1 bar and 10 bar P_{CO2}. In each case, the results clearly showed that for a given pH, increasing the partial pressure extended the mass-transport region without affecting the charge-transfer current. If a secondary direct reduction reaction were present, it would be expected that the charge-transfer current would increase alongside the partial pressure. As this was not the case, it was concluded that the direct reduction of H_2CO_3 was not significant under the conditions tested and that the increased corrosion rates were instead due to the increased supply of H^+ ions via the buffering mechanism.

As a result of this research, the model by Kahyarian *et al*.[12, 36] replaces the direct reduction reaction used previously by Nordsveen *et al*.[26] with the updated buffering mechanism. From a modelling perspective, this change is important in relation to the calculation of the surface chemistry due to the direct impact of the cathodic mechanism on the surface pH.

3.1.2 Anodic Reaction Kinetics

When considering the corrosion of steel in CO_2 saturated environments, it is known that the rate of the iron dissolution is influenced significantly by the pH of the solution[3]. As such it is important to consider the concentration H^+ ions at the surface when calculating the electrochemical response.

In the model by Nordsveen *et al*.[26], this effect is accounted for using discrete step changes as the pH increases. As discussed in the previous chapter, there is an issue with this approach in that it results in a corresponding step-change to the corrosion rate at the transition points between the different values. The original source paper for the anodic kinetics[114] indicates that these step changes are a simplification of the true mechanism. The clearest example of this is for pH values between 4 and 5 in which Nordsveen *et al*.[26] use a fixed reaction order of 1, when in fact the data shows a gradual transition in the reaction order from 2 to 0 under these conditions[114].

The model by Kahyarian *et al*.[12, 36] attempts to capture the mechanistic transition more completely by utilising a continuous function to describe the anodic kinetics. Rather than using a stepped function of pH, the reaction rate

is calculated as a function of the local H^+ and CO_2 activity. The result is a smooth transition in the anodic kinetics as the pH at the surface changes.

An additional layer of complexity is also added to the anodic kinetics within the Kahyarian model as it attempts to capture the effects of pre-passivation. Passivation is a phenomenon which occurs at high anodic potentials in which a passive layer beings to form on the surface resulting in a reduction to the corrosion rate[4]. The exact nature of the passive layer that forms varies based on the pH of the system and the magnitude of the applied potential. A Pourbaix diagram[118] can be used to predict the passivation kinetics based on the thermodynamic stability (Figure 3-1).

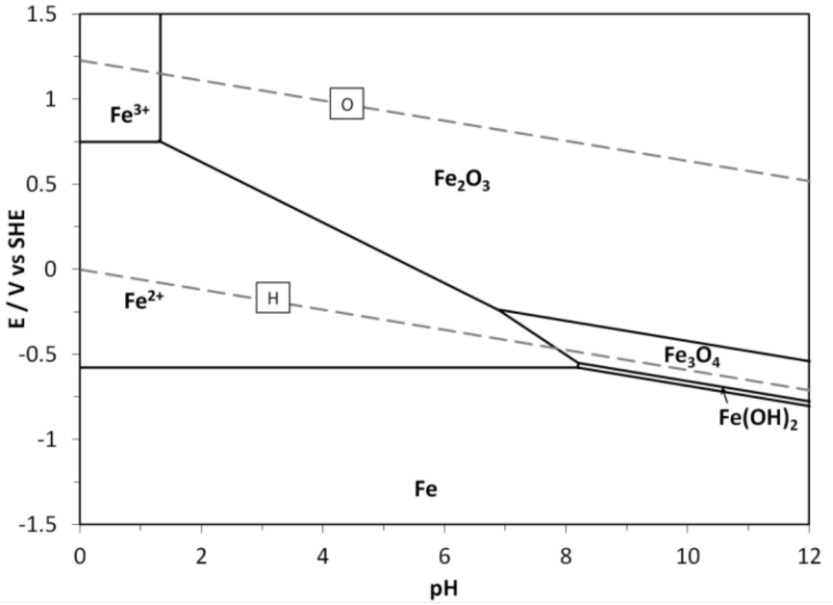

Figure 3-1 - Pourbaix diagram published by Tanupabrungsun *et al*.[119] indicating the conditions under which different passive oxide and hydroxide layers form in an Fe-CO_2-H_2O environment at 25 °C.

The pre-passive region refers to the part of the polarisation curve before passivation occurs, in which the increase in corrosion rate with applied potential begins to slow. Therefore, as the model only accounts for the anodic kinetics during the active dissolution, transitional, and pre-passive regions, the chemical composition of the passive layer does not need to be specifically defined. The change in the current density is therefore accounted for via a non-specific ‘intermediate species’, which is used to define the transition between the different anodic mechanisms.

3.1.3 Species Activity

One aspect of the solution chemistry often ignored in mechanistic CO_2 corrosion models is the influence of species activity, as the solution is commonly assumed to be ideal[25, 26, 32, 35, 105]. In practice, this means the activity coefficients associated with dissolved species are assumed to be 1 and the species concentration can therefore be used in place of activity. However, in reality this is not the case and, as the ionic strength of a solution increases, the ideal solution assumption becomes progressively more inaccurate. The distribution of ionic species and their interaction with the dipolar water molecules have an increasingly greater impact on the solution chemistry[29].

In order to account for this effect, Kahyarian *et al*.[12, 36] implement a series of equations known as the Pitzer equations, originally proposed by Kenneth Pitzer in 1973[120]. The Pitzer equations are complex as they take into account the specific ion interactions in solution, considering long-range electrostatic effects as well as the short-range interactions that arise in more concentrated solutions[121]. As such, depending on the solution chemistry, the number of equations can be extensive and rely on a number of experimentally derived parameters. The Pitzer model is often considered to be the most accurate method of accounting for species activity in solutions with high ionic strengths. However, as noted by both Misra[29] and Langmuir[121], in dilute solutions it is slightly less accurate than the more simplistic Debye-Hückel equation as it does not account for ion size when considering the long-range effects.

3.2 Overview of Underlying Physics

Before discussing the process of generating a version of a CO_2 corrosion model by Kahyarian *et al*.[12, 36] within COMSOL, it is once again important to properly define the scenario that is being modelled. As with the Nordsveen model discussed in the previous chapter, this model is a one-dimensional representation of the interaction between aqueous CO_2 and the internal surface of a mild steel pipeline. The model evaluates corrosion and speciation outwards from a single point on the steel surface and is split into three key domains: bulk steel surface, boundary layer, and bulk solution. These can be simplified into one-dimension by using a straight line to represent the boundary layer, with the two endpoints being representative of the corroding bulk steel surface and the bulk fluid, respectively. The behaviour of the active species in

each of these domains is described by different sets of equations to model the production, consumption, and transport of the species. For clarity, a two-dimensional visualisation of the system has been provided in Figure 3-2, including complete sets of equations describing each of the three domains.

Uniform corrosion is assumed in the model when calculating corrosion rates, along with zero precipitation of solid corrosion product either within the boundary or at the metal surface. Empirical relationships are used to calculate the thickness of the boundary layer and effect of turbulence, based on data for a fully developed straight pipe flow. These relationships assume flow is uniform throughout the pipe and axis-symmetric about the centre.

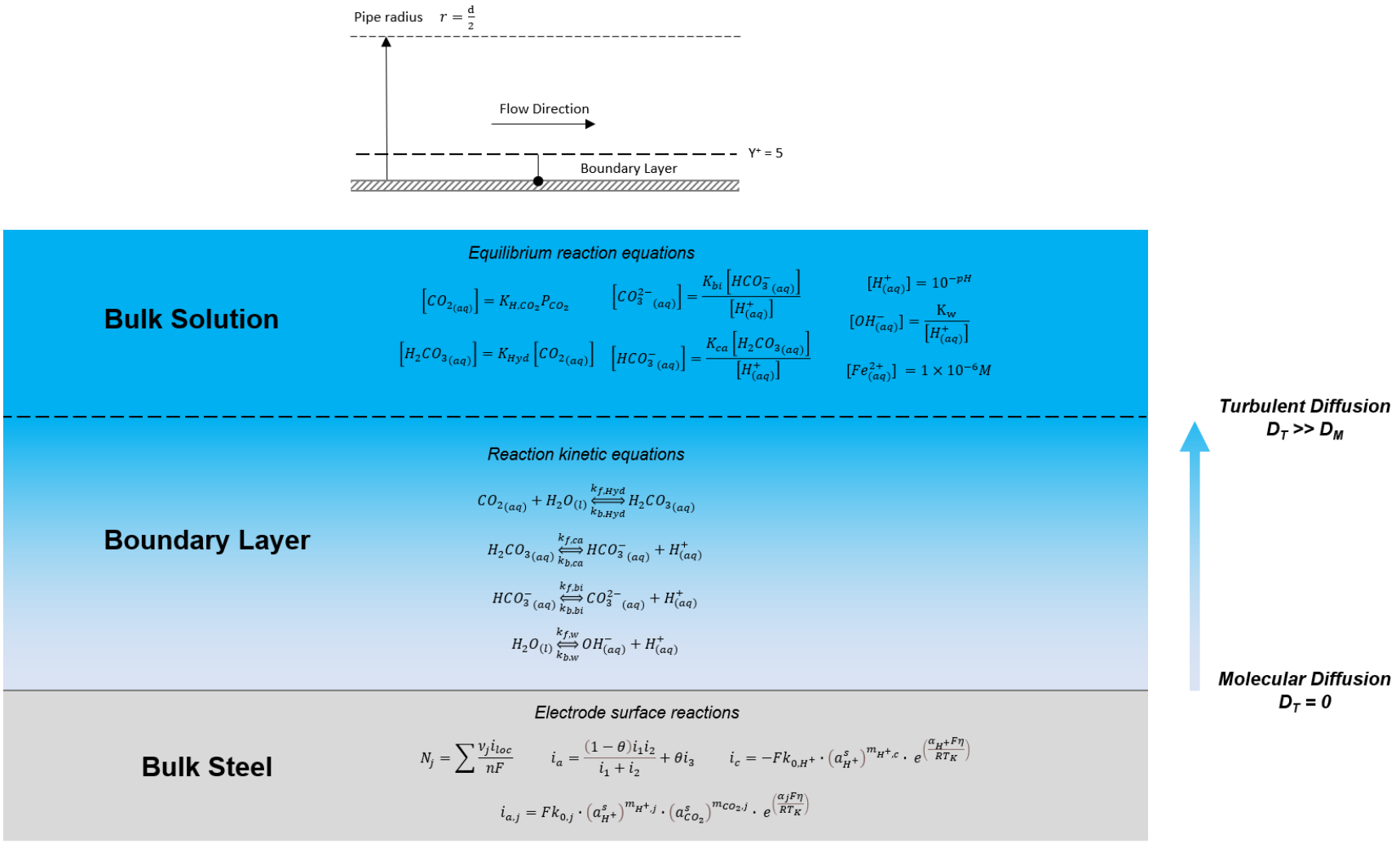

Figure 3-2 - Diagram showing the system being modelled within system, represented mathematically by a one-dimensional line between the steel surface and the bulk solution.

3.2.1 Fluid Properties

The fluid properties utilised within the model are representative of CO_2 saturated water flowing through a straight a pipe under turbulent hydrodynamic conditions. The hydrodynamic properties of the fluid are calculated as functions of the variable input parameters used to describe the environmental conditions; these are summarised in Table 3.1 below.

Table 3.1 - Summary of formulae used in the calculation of the hydrodynamic properties

Parameter	Symbol	Formula[12]	Equation
Density of Fluid	ρ_f	$(753.596 + 1.87748T_K - 0.003564T_K^2)$	(3.2)
Hydraulic Diameter	d	-	-
Dynamic Viscosity	μ	$0.001002 \times 10^{\frac{1.1709(293.15-T_K)-0.001827(293.15-T_K)^2}{(T_K-273.15)+89.93}}$	(3.3)
Reynolds Number	Re	$\frac{\rho_f v d}{\mu}$	(3.4)

The input parameters that can be varied within the model are the temperature, bulk pH, partial pressure of CO_2, and the free stream velocity of the bulk fluid. The range input conditions used within this work are summarised in and are in alignment with the limitations of the model discussed by Kahyarian *et al*.[12, 36] Notably, the temperature range explored here is limited to a maximum of 40 °C, this is due the hydration constant in this model being calculated in part based on the 1954 work of Wissbrun *et al*.[122], which was only been validated up to 45 °C.

Table 3.2 - Summary of input variables and the associated range of values used.

Variable	Symbol	Range of Values
Temperature (Kelvin)	T_K	$273.15 - 313.15$ K
pH	pH	$5 - 6.5$
Partial Pressure of CO_2	P_{CO_2}	$0.1 - 10$ bar
Bulk Fluid Velocity	u	$1 - 10$ m·s^{-1}

3.2.2 Active Species

A total of nine species are included within the speciation calculations (see Table 3.3), seven of which are chemically active species. Additional species Na^+ and Cl^- are included as ions to balance the charge when the bulk pH is specified and shifted from the equilibrium pH.

As discussed in section 3.1.3, a notable inclusion within the Kahyarian model is the inclusion of the species activity to represent the nonideality of the solution. Within the original publication, these species activities are calculated using full Pitzer coefficients, which describe the individual interactions between each of the aqueous species[121]. However, for dilute solutions as being assessed here, it has been shown that the extended Debye-Hückel approximation provides a strong approximation for the Pitzer equations[29].

The Debye-Hückel approximation, which is used here, was originally proposed by Peter Debye and Erich Hückel in 1923 and allows for the mean activity coefficient to be calculated for each ion in solution based on the ionic strength. The extended version of the Debye-Hückel equation is given by Equation 3.5.

$$\ln(\gamma_i) = -\frac{Az_i^2\sqrt{I}}{1 + Ba_i\sqrt{I}} \tag{3.5}$$

Where A and B are characteristic constants of the fluid and I is the ionic strength of the solution (M).

$$A = \frac{F^2\epsilon_0\sqrt{2}}{8\pi(\epsilon RT_K)^{\left(\frac{3}{2}\right)}} \tag{3.6}$$

$$B = \frac{F}{\sqrt{\frac{\epsilon RT_K}{2}}} \tag{3.7}$$

Where F is the Faraday constant (96,458 c/mol), ϵ_0 is the permittivity of free space, ϵ is the relative permittivity of the solution (80 for water at , 1 bar, 293.15 K[123]) and R is the universal gas constant (8.3145 $J{\cdot}mol^{-1}{\cdot}K^{-1}$).

The ionic strength (I) of the solution is given by Equation 3.8. For the purposes of this work, a 1 wt% sodium chloride (NaCl) solution is used, giving an ionic strength of 0.1711 M.

$$I = \frac{1}{2}\sum_{j=1}^{n} c_j z_j^2 \tag{3.8}$$

Where c_j and z_j are the concentration (M) and charge of species j respectively.

Each of the active species included within the model, as well as associated coefficients relating to its chemical activity, and diffusion coefficient are provided in Table 3.3.

Table 3.3 - Summary of active species with associated charge, ion size and reference diffusion coefficient.

Species	Diffusion Coefficient ($D_{j,ref}$)[12]	Charge (z_j)	Ionic Radius ($r_{i,j}$ nm)[29]
$CO_{2(aq)}$	1.92×10^{-9}	0	N/A
$H_2CO_{3(aq)}$	1.75×10^{-9}	0	N/A
$HCO_{3\,(aq)}^{-}$	1.185×10^{-9}	-1	0.45
$CO_{3\,(aq)}^{2-}$	0.923×10^{-9}	-2	0.45
$H_{(aq)}^{+}$	9.315×10^{-9}	$+1$	0.9
$OH_{(aq)}^{-}$	5.273×10^{-9}	-1	0.35
$Fe_{(aq)}^{2+}$	0.72×10^{-9}	$+2$	0.6
$Na_{(aq)}^{+}$	1.334×10^{-9}	$+1$	0.45
$Cl_{(aq)}^{-}$	2.032×10^{-9}	-1	0.3

3.2.3 Summary of Reactions

The reactions within a CO_2 saturated steel pipeline can be separated into two groups: the chemical reactions occurring in the fluid and electrochemical reactions occurring at the corroding surface. A summary of reactions relevant to the corrosion model is provided below, a more detailed review of the solution chemistry can be found in Chapter 1 of this thesis.

3.2.3.1 Solution Chemistry

When CO_2 is dissolved in water, a slow hydration reaction occurs to produce H_2CO_3:

$$CO_{2(aq)} + H_2O_{(l)} \rightleftharpoons H_2CO_{3(aq)} \tag{3.9}$$

Following the hydration reaction, two dissociation reactions take place, resulting in the production of hydrogen (H^+) ions at each stage:

$$H_2CO_{3(aq)} \rightleftharpoons HCO^-_{3(aq)} + H^+_{(aq)} \tag{3.10}$$

$$HCO^-_{3(aq)} \rightleftharpoons CO^{2-}_{3(aq)} + H^+_{(aq)} \tag{3.11}$$

Additionally, the dissociation of the water itself contributes to the production of ions in solution:

$$H_2O_{(l)} \rightleftharpoons H^+_{(aq)} + OH^-_{(aq)} \tag{3.12}$$

When the pH is high, hydroxylation reactions (Equations 3.13 and 3.14) act to reduce the hydroxide ion concentration. These reactions have been included in the model by Kahyarian *et al.*, however it is known that under acidic/low pH conditions the contribution of these reactions is negligible[12].

$$CO_{2(aq)} + OH^-_{(aq)} \rightleftharpoons HCO^-_{3(aq)} \tag{3.13}$$

$$HCO^-_{3(aq)} + OH^-_{(aq)} \rightleftharpoons CO^{2-}_{3(aq)} + H_2O_{(l)} \tag{3.14}$$

It should be noted that all of the reactions listed here (Equations 3.9-3.14) are reversible and occur forwards and backwards simultaneously. When under steady-state conditions, these rates of these two reactions are equal, resulting in an equilibrium condition. When shifted from the equilibrium state, as is generally the case within the boundary layer close to the surface, the reactions become imbalanced and either the forward or backward reaction becomes dominant.

3.2.3.2 Surface Reactions

As discussed in section 3.1.1, the Kahyarian model operates assuming the buffering mechanism to account for the contribution of H_2CO_3. There are therefore only two electrochemical half-reactions to consider at the interface between the fluid and the internal pipe surface. The first is the anodic dissolution of iron into the solution, given by Equation 3.15. It is this reaction

that produces a corrosion rate at the surface as material is transferred from the metal into solution.

$$\mathrm{Fe_{(s)}} \rightarrow \mathrm{Fe^{2+}_{(aq)}} + 2\mathrm{e^-} \tag{3.15}$$

The second half-reaction is the cathodic reduction of H+ ions to form hydrogen gas (Equation 3.16).

$$2\mathrm{H^+_{(aq)}} + 2\mathrm{e^-} \rightarrow \mathrm{H_{2_{(g)}}} \tag{3.16}$$

As hydrogen reduction is the sole cathodic reaction, the supply of H^+ ions to the surface acts as the limiting factor for the corrosion rate when the system is under mass-transport control.

3.3 COMSOL Implementation

3.3.1 Bulk Fluid Chemistry

Two important assumptions are made when defining the chemistry of the bulk flow. The first is that, due to the turbulent nature of the flow, there is perfect mixing of the chemical species producing a homogenous solution chemistry. The second is that the bulk volume is sufficiently large as to allow the solution chemistry to be considered independently of the surface reactions. By employing these two assumptions, the bulk chemistry can be considered to be in a state of equilibrium and therefore acts as a boundary condition within the COMSOL model.

Equilibrium constants are used to calculate the relative concentrations of species when in an equilibrium state. Each of the reactions discussed in section 3.2.3.1 has a corresponding equilibrium constant, which describes the ratios of the products to reactants, as seen in Equations 3.18-3.23. The initial concentration of aqueous CO_2 is a function of the partial pressure, following Henry's Law (Equation 3.17).

$$K_H = \frac{P_{CO_2}}{a_{CO_2(aq)}} \tag{3.17}$$

$$K_{Hyd} = \frac{a_{H_2CO_3(aq)}}{a_{CO_2(aq)} \cdot a_{H_2O_{(l)}}} \tag{3.18}$$

$$K_{ca} = \frac{a_{HCO_3^-(aq)} \cdot a_{H^+(aq)}}{a_{H_2CO_3(aq)}} \tag{3.19}$$

$$K_{bi} = \frac{a_{CO_3^{2-}(aq)} \cdot a^+_{H(aq)}}{a_{HCO_3^-(aq)}} \tag{3.20}$$

$$K_W = \frac{a_{OH^-(aq)} \cdot a_{H^+(aq)}}{a_{H_2O_{(l)}}} \tag{3.21}$$

$$K_{ca} \cdot \frac{K_{Hyd}}{K_W} = \frac{a_{HCO_3^-(aq)}}{a_{CO_{2(aq)}} \cdot a_{OH^-(aq)}} \tag{3.22}$$

$$\frac{K_{bi}}{K_W} = \frac{a_{CO_3^{2-}} \cdot a_{H_2O_{(l)}}}{a_{HCO_3^-(aq)} \cdot a_{OH^-(aq)}} \tag{3.23}$$

The values used to calculate the equilibrium constants are shown in Table 3.4, with the associated formulae shown in Equations 3.24-3.27. Note that some of these values differ from the values reported by Kahyarian and Nesic[12] due to minor differences relative to the original works. All values reported here reflect those in the source literature.

Table 3.4 - Parameters for the calculation of equilibrium constants.

	K^*_H[61]	K_{Hyd}[12]	K^*_{ca}[60]	K_{bi}[60]	K_w[62]
a_1	1.4000×10^1	6.6330×10^{-2}	2.3352×10^2	-1.5118×10^2	-4.0980
a_2	-1.3341×10^{-2}	9.5260×10^3	0.0000	-8.8696×10^{-2}	-3.2452×10^3
a_3	-5.5898×10^2		-1.1974×10^4	-1.3623×10^3	2.2362×10^5
a_4	-4.2258×10^5		0.0000	0.0000	-3.9840×10^7
a_5			-3.6506×10^1	2.7798×10^1	1.3957×10^1
a_6			-4.5080×10^1	-2.9514×10^1	-1.2623×10^3
a_7			2.1313×10^3	1.3890×10^3	8.5641×10^5
a_8			6.7143	4.4196	
a_9			8.3939×10^{-3}	3.2200×10^{-3}	
a_{10}			-4.0154×10^{-1}	-1.6445×10^{-1}	
a_{11}			-1.2402×10^{-3}	-4.7367×10^{-4}	

$$ln(K_H^*) = a_1 + a_2 T_K + \frac{a_3}{T_K} + \frac{a_4}{T_K^2} \tag{3.24}$$

$$\log(K_w) = a_1 + \frac{a_2}{T_K} + \frac{a_3}{T_K^2} + \frac{a_4}{T_K^3} + \left(a_5 + \frac{a_6}{T_K} + \frac{a_7}{T_K^2}\right)\log\left(\frac{\rho_w}{1000}\right) \tag{3.25}$$

$$K_{Hyd} = a_1 e\left(\frac{a_2}{RT_K}\right) \tag{3.26}$$

For K_{ca}^* and K_{bi}:

$$\begin{aligned}\ln(par.) = a_1 + a_2 T_K + \frac{a_3}{T_K} + \frac{a_4}{T_K^2} + a_5\ln(T_K) + \left(\frac{a_6}{T_K} + \frac{a_7}{T_K^2} + \frac{a_8}{T_K}\ln(T_K)\right)(P - P_s) \\ + \left(\frac{a_9}{T_K} + \frac{a_{10}}{T_K^2} + \frac{a_{11}}{T_K}\ln(T_K)\right)(P - P_s)^2\end{aligned} \tag{3.27}$$

It is important to clarify that the calculated values K_H^* and K_{ca}^*, are defined in relation to the total dissolved carbon dioxide (CO_2^*) which includes both dissolved CO_2 and hydrated dissolved CO_2 in the form of H_2CO_3. Adjusting these values to give the true dissociation constants, requires some mathematical manipulation. From Equation 3.18, assuming the activity of water to be equal to 1, it can be seen that:

$$a_{H_2CO_3} = a_{CO_2} \cdot K_{Hyd} \tag{3.28}$$

Hence:

$$\begin{aligned}K_H^* = \frac{P_{CO_2}}{a_{CO_2}^*} = \frac{P_{CO_2}}{\left(a_{CO_2} + a_{H_2CO_3}\right)} = \frac{P_{CO_2}}{a_{CO_2}\left(1 + K_{Hyd}\right)} \\ = \frac{P_{CO_2}}{a_{CO_2}} \cdot \frac{1}{\left(1 + K_{Hyd}\right)} = \frac{H_{CO_2}}{\left(1 + K_{Hyd}\right)}\end{aligned}$$

$$K_H = K_H^* \cdot (1 + K_{Hyd}) \tag{3.29}$$

For the calculation of K_{ca}:

$$K_{ca}^* = \frac{a_{HCO_3^-} \cdot a_{H^+}}{a_{CO_2}^*} = \frac{a_{HCO_3^-} \cdot a_{H^+}}{\left(a_{CO_2} + a_{H_2CO_3}\right)} \tag{3.30}$$

Combining Equations 3.28 and 3.30:

$$K_{ca}^* = \frac{a_{HCO_3^-} \cdot a_{H^+}}{\left(\frac{a_{H_2CO_3}}{K_{Hyd}} + a_{H_2CO_3}\right)} = \frac{a_{HCO_3^-} \cdot a_{H^+}}{a_{H_2CO_3}\left(1 + \frac{1}{K_{Hyd}}\right)} = \frac{a_{HCO_3^-} \cdot a_{H^+}}{a_{H_2CO_3}} \cdot \frac{1}{\left(1 + \frac{1}{K_{Hyd}}\right)} = \frac{K_{ca}}{\left(1 + \frac{1}{K_{Hyd}}\right)}$$

$$K_{ca} = K_{ca}^* \cdot \left(1 + \frac{1}{K_{Hyd}}\right) \tag{3.31}$$

The resulting species concentrations for the bulk fluid over a range of pH values are shown in Figure 3-3 for a temperature of 293.15 K, CO_2 partial pressure of 1 bar and ionic strength of 0.1711 M (1 wt% NaCl). The total charge sum, indicated by the dashed black line in Figure 3-3, is also calculated as an absolute value (Equation 3.32). The point at which the total charge is zero indicates the neutral pH of the system, equal to 3.81 for the conditions given here.

$$Charge\ Sum = \left| \sum_{j=1}^{n} (z_j c_j) \cdot N_A \cdot e \right| \tag{3.32}$$

Where N_A is Avogadro's constant ($\approx 6.022 \times 10^{23}$), and e is the elementary charge ($\approx 1.602 \times 10^{-19}$ C).

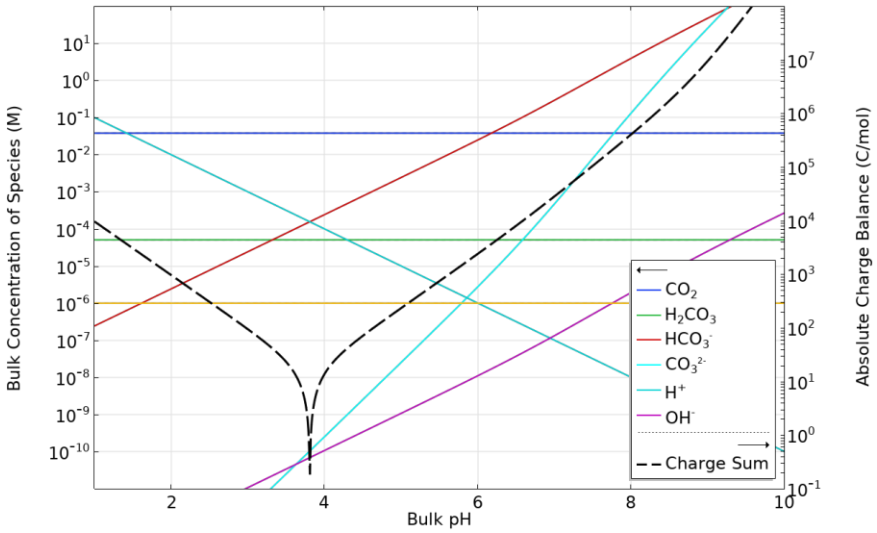

Figure 3-3 - Bulk species concentration and total charge as a function of pH for input values of 20 °C, 1 bar P_{CO_2} and ionic strength of 0.1711 M.

It should be noted that a nominal concentration of 1 ppm_{Molar} is given for the concentration of Fe^{2+}, despite not being involved in any reactions in the bulk. This is to account for the accumulation of Fe^{2+} in the bulk resulting from the surface reactions in the system, which cannot be calculated for a stand-alone one-dimensional model. As Fe^{2+} is being released from the surface, the bulk concentration cannot be zero as this would imply zero flux across the boundary.

As the pH of the solution increases, there are relative increases in both dissociated forms of dissolved CO_2, namely HCO_3^- and CO_3^{2-} (Figure 3-3). Figure 3-4 shows how the ratios of these species change as a function of bulk

pH, with undissociated aqueous CO_2 being the dominant form at low pH. At a pH of around 6, this shifts towards a HCO_3^- dominated solution, before transitioning again to a CO_3^{2-} dominated solution at around pH 9.

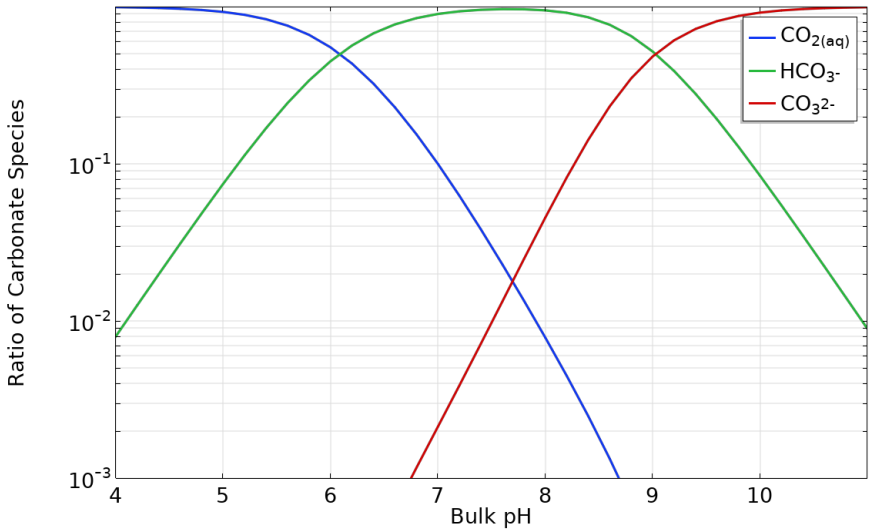

Figure 3-4 - Ratio of bulk carbonate species as a function of bulk pH.

3.3.2 Boundary Layer Kinetics

The constants provided in Equations 3.17-3.23 detail the equilibrium state of the bulk fluid, however the species concentrations between the surface and the bulk cannot be considered in the same way. The corrosion caused by the electrochemical reactions at the metal surface introduces a flux of ions which shifts the system from the bulk equilibrium. The slow rate of the CO_2 hydration reaction (Equation 3.9) relative to the diffusion rate of the active species prevents the system from readily adapting to the surface flux. Due to the non-equilibrium condition in the boundary layer it necessary to model the individual reaction kinetics in order to account for the boundary layer speciation.

As shown in Equations 3.9-3.14, the reactions occurring in the fluid are reversible, meaning that it is possible to model the transient response of the species to the surface flux by isolating their forward and backward reaction rates. The kinetic equations for each of the reversible reactions occurring in solution are shown in Table 3.5,with the corresponding rate constants in Table 3.6.

Table 3.5 – Kinetics equations for reversible reactions in solution.

Reaction	Kinetics Equation	
$CO_{2_{(aq)}} + H_2O_{(l)} \rightleftharpoons H_2CO_{3_{(aq)}}$	$r_1 = k_{f,Hyd} \cdot a_{CO_2} - k_{b,Hyd} \cdot a_{H_2CO_3}$	(3.33)
$H_2CO_{3(aq)} \rightleftharpoons HCO^-_{3(aq)} + H^+_{(aq)}$	$r_2 = k_{f,ca} \cdot a_{H_2CO_3} - k_{b,ca} \cdot a_{HCO_3^-} \cdot a_{H^+}$	(3.34)
$HCO^-_{3_{(aq)}} \rightleftharpoons CO^{2-}_{3(aq)} + H^+_{(aq)}$	$r_3 = k_{f,bi} \cdot - k_{b,bi} \cdot a_{CO_3^{2-}} \cdot a_{H^+}$	(3.35)
$H_2O \rightleftharpoons H^+ + OH^-$	$r_4 = k_{f,w} \cdot a_{H_2O} - k_{b,w} \cdot a_{OH^-} \cdot a_{H^+}$	(3.36)
$CO_{2(aq)} + OH^-_{(aq)} \rightleftharpoons HCO_3^-{}_{(aq)}$	$r_5 = k_{f,hyd,OH} \cdot a_{CO_2} \cdot a_{OH^-} - k_{b,hy-H} \cdot a_{HCO_3^-}$	(3.37)
$HCO_3^-{}_{(aq)} + OH^-_{(aq)} \rightleftharpoons CO_3{}^{2-}_{(aq)} + H_2O_{(l)}$	$r_6 = k_{f,bi,OH} \cdot a_{HCO_3^-} \cdot a_{OH^-} - k_{b,bi-H} \cdot a_{CO_3^{2-}} \cdot a_{H_2O}$	(3.38)

Table 3.6 – Kinetic reaction rate constants for reversible reactions in solution[12].

Constant	Definition	Formula	Units
$k_{b,hyd}$	$\frac{k_{f,hyd}}{K_{Hyd}}$	$4.86 \times 10^{12} e^{-\left(\frac{64485}{RT_K}\right)}$	s^{-1}
$k_{b,ca}$	$\frac{k_{f,ca}}{K_{ca}}$	4.7×10^{10}	$M^{-1}s^{-1}$
$k_{f,bi}$	$K_{bi} \cdot k_{b,bi}$	$2.03 \times 10^{7} e^{-\left(\frac{35269}{RT_K}\right)}$	s^{-1}
$k_{b,w}$	$\frac{k_{f,w}}{K_w}$	1.12×10^{11}	$M^{-1}s^{-1}$
$k_{f,hyd,OH}$	$k_{b,hyd,OH} \cdot \left(\frac{K_{ca} \cdot K_{Hyd}}{K_w}\right)$	$4.2 \times 10^{13} e^{-\left(\frac{55438}{RT_K}\right)}$	$M^{-1}s^{-1}$
$k_{f,bi,OH}$	$k_{b,bi,OH} \cdot \left(\frac{K_{bi}}{K_w}\right)$	6×10^{9}	$M^{-1}s^{-1}$

From the kinetic equations, it is possible to derive a set of ordinary differential equations describing the rate of change of each aqueous species. If a species is the product of a reaction, the contribution of the associated reaction can be considered positive as it results in an increase in concentration. On the other hand, if the species is a reactant, the reaction would be considered a negative contribution as it reduces the concentration. The summation of all relevant reactions can be used to calculate the rate of changes of each species and

therefore speciation through the boundary layer based on local species concentrations and individual rates of reaction (Equations 3.39-3.44).

$$\frac{d}{dt}\left[\mathrm{CO_{2(aq)}}\right] = -r_1 - r_5 \tag{3.39}$$

$$\frac{d}{dt}[\mathrm{H_2CO_3}] = r_1 - r_2 \tag{3.40}$$

$$\frac{d}{dt}[\mathrm{HCO_3^-}] = r_2 - r_3 + r_5 - r_6 \tag{3.41}$$

$$\frac{d}{dt}[\mathrm{CO_3^{2-}}] = r_3 + r_6 \tag{3.42}$$

$$\frac{d}{dt}[\mathrm{H^+}] = r_2 + r_3 + r_4 \tag{3.43}$$

$$\frac{d}{dt}[\mathrm{OH^-}] = r_4 - r_5 - r_6 \tag{3.44}$$

3.3.3 Surface Electrochemistry

At the interface between the fluid and the metal surface, electrochemical reactions occur resulting in corrosion of the surface due to the dissolution of iron (Fe). Two electrode half-reactions are specified within this model: the anodic dissolution of Fe (Equation 3.15) and the cathodic reduction of H^+ (Equation 3.16). Based on these reactions, a corrosion rate can be calculated within COMSOL by defining a dissolving-depositing species to represent the surface material. Material properties representative of mild steel assigned to the surface, specifically the density (ρ_s) and the molecular weight (M_w), these values are shown in Table 3.7.

Table 3.7 - Material properties of mild steel, representing the dissolving species at the electrode surface.

Material Property	Symbol	Value[111]
Density	ρ_s	7,850 kg·m^{-3}
Molecular weight	M_w	55.845 g·mol^{-1}

From these two material properties the corrosion rate of the electrode can be calculated from the reaction rate of the dissolving material, which in this case is Fe within the steel. This is done by first determining the rate of mass loss over a given surface area and then converting this to a surface velocity. The formulae used to calculate these values are given by Equations 3.34 and 3.35.

$$\Delta S = M_w \, N_{Fe} \tag{3.45}$$

$$CR = \frac{\Delta S}{\rho_s} \tag{3.46}$$

Where ΔS is mass reaction rate at the surface (kg·m^{-2}·s^{-1}), M_w is the molecular weight (kg·mol^{-1}), N_{Fe} is the molar flux of Fe from the surface (mol·m^{-2}·s^{-1}), and CR is the corrosion rate at the surface (m·s^{-1}).

Finding the molar flux of the dissolving Fe requires the specification of both the cathodic dissolution reaction and the anodic surface reactions occurring. Each of the reactions can be expressed by the general electrochemical reaction formula (Equation 3.47) to determine the stoichiometric coefficients:

$$\sum_{ox} \nu_{ox} S_{ox} + ne^- \leftrightarrow \sum_{red} \nu_{red} S_{red} \tag{3.47}$$

Where ν is the stoichiometric coefficient, S is the species, and n is the number of participating electrons. Subscript red and ox indicate products and reactants respectively in a reduction reaction[112].

The stoichiometric coefficients of the anodic dissolution reaction and cathodic reduction reaction are provided in Table 3.8. Note that ν_{Fe} in the table refers the stoichiometric coefficient of aqueous Fe^{2+} and not solid Fe at the surface.

Table 3.8 - Participating electrons and stoichiometric coefficient values for iron oxidation (anodic) and hydrogen evolution (cathodic) surface reactions.

Coefficient	$\mathbf{Fe_{(s)} \rightarrow Fe^{2+}_{(aq)} + 2e^-}$	$\mathbf{2H^+_{(aq)} + 2e^- \rightarrow H_{2(g)}}$
n	2	2
ν_H	0	-2
ν_{Fe}	-1	0

As the model is representative of uniform corrosion within a pipeline, an electroneutrality boundary condition was also defined at the surface (Equation 3.48). When combined with Equation 3.47, this ensures that the anodic and cathodic reactions are equal and opposite, preventing a build-up of charge at the surface.

$$\sum_j z_j c_j = 0 \tag{3.48}$$

According to Faraday's laws, the molar species fluxes perpendicular to the surface can be calculated as the sum of all the flux contributions from the electrode reactions (Equation 3.49)[112].

$$N_j = \sum \frac{\nu_j i_{loc}}{nF} \tag{3.49}$$

Where N_j is the molar flux of species j (mol·m^{-2}·s^{-1}), ν_j is the stoichiometric coefficient of species j, i_{loc} is the local current density (A·m^{-2}), n is the number of participating electrons, and F is the Faraday constant.

The local current density for the cathodic reaction is calculated from the surface activity of H^+ via Equation 3.50.

$$i_c = -Fk_{H^+} \cdot \left(a^s_{H^+}\right)^{m_{H^+,c}} \cdot e^{\left(\frac{\alpha_{H^+} F\eta}{RT_K}\right)} \tag{3.50}$$

Where $k_{,H^+}$ is provided by Equation 3.57, $m_{H^+,c}$ and a_{H^+} are constants provided in Table 3.9, $a^s_{H^+}$ is the surface concentration of H^+ (mol·m^{-3}), T_K is the temperature in Kelvin and η is the overpotential (V).

The local current density for the anodic reaction is calculated as a function of three current steps ($i_{a,n}$), any of which can be rate determining depending on surface conditions, as discussed by Kahyarian *et al.*[36] Each step is a function of the surface concentrations of the surface concentrations of both H^+ and aqueous CO_2. An intermediate function, θ is used to describe the transition between three currents as shown by Equations 3.51-3.53.

As discussed in section 3.1.2, these current steps represent the active dissolution of Fe, the transition towards pre-passivation, and the pre-passivation region respectively. The θ function is representative of the surface coverage of an intermediate species which initiates the passivation behaviour.

$$i_{a,j} = Fk_j \cdot \left(a_{H^+}^s\right)^{m_{H^+,j}} \cdot \left(a_{CO_2}^s\right)^{m_{CO_2,j}} \cdot e^{\left(\frac{\alpha_j F\eta}{RT_K}\right)} \quad (3.51)$$

$$\theta = \frac{K_\theta \cdot \left(a_{H^+}^s\right)^{m_{H^+,\theta}} \cdot \left(a_{CO_2}^s\right)^{m_{CO_2,\theta}} \cdot e^{\left(\frac{\alpha_\theta F\eta}{RT_K}\right)}}{1 + K_\theta \cdot \left(a_{H^+}^s\right)^{m_{H^+,\theta}} \cdot \left(a_{CO_2}^s\right)^{m_{CO_2,\theta}} \cdot e^{\left(\frac{\alpha_\theta F\eta}{RT_K}\right)}} \quad (3.52)$$

$$i_a = \frac{(1-\theta) i_{a,1} i_{a,2}}{i_{a,1} + i_{a,2}} + \theta i_{a,3} \quad (3.53)$$

Where the values of k_j are calculated via Equation 3.57, $a_{H^+}^s$ is the surface activity of H^+ in mol·m^{-3}, $a_{CO_2}^s$ is the surface activity of CO_2 (M), T_K is the temperature (K), η is the overpotential (V) and all other values are constants. The values of these constants are summarised in Table 3.9.

Table 3.9 - Summary of constants used in the calculation of both the cathodic and anodic current density calculations[12].

k_{0,H^+}	2×10^{-8} mol·m^{-2}·s^{-1}	$m_{H^+,c}$	0.5	α_{H^+}	0.43
$k_{0,1}$	4×10^{9} mol·m^{-2}·s^{-1}	$m_{H^+,1}$	-2.5	α_1	2.5
$k_{0,2}$	1×10^{13} mol·m^{-2}·s^{-1}	$m_{H^+,2}$	1	α_2	2
$k_{0,3}$	0.8×10^{-3} mol·m^{-2}·s^{-1}	$m_{H^+,3}$	-0.5	α_3	0.5
K_θ	5×10^{13}	$m_{CO_2,1}$	0	α_θ	2.5
$m_{H^+,\theta}$	-2.5	$m_{CO_2,2}$	0.5		
$m_{CO_2,\theta}$	-0.5	$m_{CO_2,3}$	0.5		

In each case, the overpotential (η) is given by:

$$\eta = E - E_{rev} \quad (3.54)$$

Where E is the electric potential (V) and E_{rev} is the reversible potential (V). The electric potential is defined within COMSOL as the difference between the electrode potential (Φ_s) and the electrolyte potential (Φ_l) at the interface:

$$E = \Phi_s - \Phi_l \quad (3.55)$$

The reversible potential is for the anodic reaction is constant at -0.440 V and for the cathodic reaction is calculated via Equation 3.56[26].

$$E_{rev,H^+} = -\frac{2.303RT_K}{F} \cdot pH_{bulk} \tag{3.56}$$

The Van't Hoff equation (Equation 3.57) is used to evaluate the temperature dependency of the surface kinetics by adjusting the kinetic constants k_{0,H^+}, $k_{0,1}$, and $k_{0,3}$ provided in Table 3.9. The activation energies used here are the updated values estimated by Kahyarian and Nesic in their 2020 paper[12].

$$k_j = k_{0,j} e^{\frac{-E_a}{R(T_K - T_{ref})}} \tag{3.57}$$

Where k_j is the temperature dependent kinetic parameter of reaction j, E_a is the activation energy (J), and T_{ref} is the reference temperature (283.15 K).

Table 3.10 – Activation energy of kinetic parameters used to calculate temperature dependency.

Kinetic Parameter	Activation Energy (J)
k_{H^+}	83,200
k_1	126,800
k_3	63,000

3.3.4 Transportation of Species

Alongside the chemical and electrochemical reactions occurring in the fluid and at the surface, it is important to consider the movement of species through the boundary layer. In general, there are three mechanisms by which charged species can be transported within a fluid: diffusion, electromigration, and convection. These three terms can be combined in a single equation to calculate the of species (Equation 3.58).

$$N_j = -D_{M,j}\frac{\partial c_j}{\partial x} - z_j u_j F c_j \frac{\partial \Phi}{\partial x} + c_j v \tag{3.58}$$

Where N_j is the flux of species j (mol·m^{-2}·s^{-1}), $D_{M,j}$ is the molecular diffusion coefficient (m^2·s^{-1}), c_j is the concentration (mol·m^{-3}), x is the distance perpendicular to the surface (m), z_j is the valence, u_j is the mobility of species (mol·s·kg^{-1}), F is the Faraday constant (C·mol^{-1}), Φ is the electrolyte potential (V), and v is the solution velocity (m·s^{-1}).

Within the boundary layer, the flow velocities are very low meaning mass-transport due to convection becomes very small within this region ($c_j v \approx 0$). However, turbulent eddies still permeate through the boundary and influence

the rate of species transport near the surface[28]. In order to account for this effect, the flux equation (Equation 3.58) is modified to remove the convection term and instead incorporate a turbulent diffusivity (D_T) value (Equation 3.59).

$$N_j = -(D_{M,j} + D_T)\frac{\partial c_j}{\partial x} - z_j u_j F c_j \frac{\partial \Phi}{\partial x} \tag{3.59}$$

The turbulent diffusivity is calculated as a function of the dimensionless wall distance (y^+, see section 3.3.5) as proposed by Notter and Sleicher[43]. In this work, the expression provided by Aravinth[124] is used, utilising the form of the Notter and Sleicher[43] equation with more recent values from Churchill[125].

$$D_T = \frac{0.0007{y^+}^3}{\sqrt{(1 + 0.00405{y^+}^2)}} \tag{3.60}$$

The conservation of mass principle is then applied to calculate the transport of species via the Nernst-Planck equation, given by Equation 3.61 for a one-dimensional model. The Nernst-Planck equation accounts the species flux as well as the production/consumption of species via the electrochemical surface reactions and boundary layer kinetic reactions discussed later.

$$\frac{\partial c_j}{\partial t} = -\frac{\partial N_j}{\partial x} + R_j \tag{3.61}$$

Where R_j is a source/sink term describing the local change in species j (mol·m^{-3}·s^{-1}).

3.3.5 Geometry and Discretization

3.3.5.1 Domain

As a one-dimensional representation of the geometry shown in Figure 3-2, an interval was defined within COMSOL. The interval is a straight-line representation of the boundary layer, bounded by two points. These points represented the metal surface and the bulk-boundary interface respectively, with x-coordinate limits of zero and δ respectively, where δ denotes the boundary layer thickness.

The value of δ, and therefore the size of the domain, is derived from a concept known as the universal law of the wall in which the near wall region can be separated into three flow regimes: the viscous (or laminar) sublayer, the buffer

(or transitional) layer, and the fully turbulent region[46]. These regions are generally defined using a dimensionless value for the perpendicular distance to the wall represented as y^+. The law of the wall concept is explored more comprehensively in Chapter 4, however for the purposes of the corrosion model being discussed here, δ refers to the size of the viscous sublayer. The transition from the viscous sublayer to the buffer layer can be assumed to occur when $y^+ = 5$[44], meaning the height of the boundary layer (δ) can be defined as the perpendicular distance from the surface (x) at this point. The value of y^+ is defined as:

$$y^+ = \frac{x\left(\frac{\tau_\omega}{\rho}\right)^{\frac{1}{2}}}{\nu} \tag{3.62}$$

Therefore, given that $x = \delta$ when $y^+ = 5$, these values can be substituted into Equation 3.62 to give:

$$\delta = \frac{5\nu}{\left(\frac{\tau_\omega}{\rho}\right)^{\frac{1}{2}}} \tag{3.63}$$

Where τ_ω is the wall shear stress (Pa), which can be found as a function of the Fanning friction factor (C_f) at the wall, calculated using the correlation provided by Swamee and Jain[126].

$$\tau_\omega = \frac{\rho C_f u^2}{2} \tag{3.64}$$

$$C_f = \frac{C_d}{4} = \frac{1}{16\left(\log\left(\frac{\varepsilon_s}{3.7D} + \frac{5.74}{Re^{0.9}}\right)\right)^2} \tag{3.65}$$

Where C_d is the Darcy friction factor, ε_s is the surface roughness (m) (assumed negligible here, $\varepsilon_s \approx 0$), and D is the pipe diameter (m).

3.3.5.2 Meshing

A mesh sensitivity study was conducted in order to determine an appropriate mesh size. In general, for numerical models a higher mesh density improves the accuracy of the results, however it also increases the time to solve. For one-dimensional models this increased computational cost is not significant due to the limited number of degrees of freedom. Even with a very high-density mesh, the solver time is unlikely to exceed the order of minutes. However, due to the large number of simulations being run in this work (see section 3.4.2.2),

a relatively small increase in the solve time per simulation becomes much more significant. Therefore, it is important that the balance between solution accuracy and mesh density is considered.

For this model, linearly distributed edge elements were used to generate a uniformly dense mesh. This is to ensure that both changes to the solution chemistry via the kinetic equations (detailed in section 3.3.2) and the flux of species (Equation 3.59) are accurately calculated throughout the entire domain.

A mesh sensitivity study was conducted in order to determine an appropriate element size for the model. A maximum element size was explicitly defined via a user-defined variable, which was then swept between values of 10^{-5} m to 10^{-9} m in increments of 20 points/decade.

Outputs of corrosion rate and surface pH were used to determine solution accuracy at temperatures of 273.15 K and 313.15 K and CO_2 partial pressures of 0.1 bar and 10 bar. These extreme conditions were selected in order to maximise corrosion and surface pH values, as well as to assess the accuracy for the smallest and largest domain sizes. The pH was kept constant at 5 as this is the highest H^+ concentration being examined (Table 3.2). Other input variables of velocity, pipe diameter, and ionic strength were kept constant at representative values of 5 $m \cdot s^{-1}$, 0.1 m and 0.1711 M respectively.

Figure 3-5 displays the results of the mesh sensitivity study as a comparison between percentage error and the maximum element size. The percentage error was calculated based on the assumption of the densest mesh (maximum element size of 10^{-9} m) being entirely accurate.

(a)

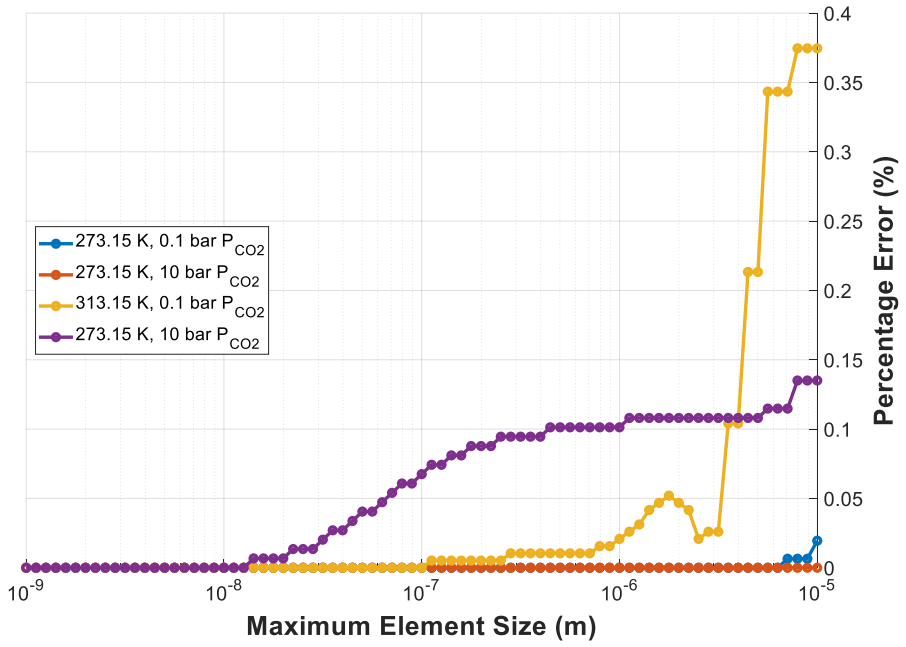

(b)

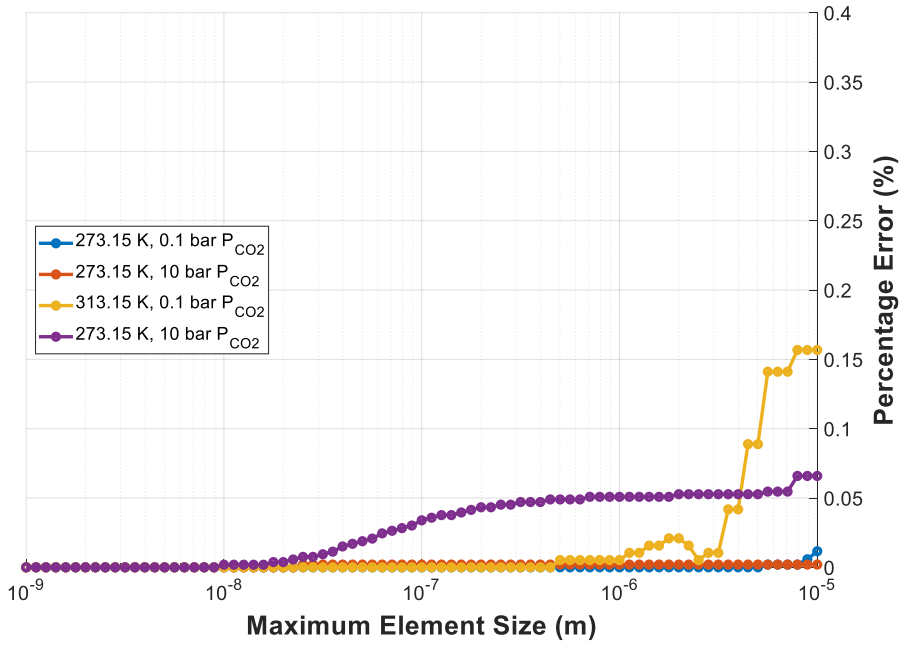

Figure 3-5 – Sensitivity study comparing maximum element size against percentage error for outputs of (a) corrosion rate and (b) surface pH.

For both the corrosion rate and surface pH outputs, the density of the mesh was found to be less influential than initially expected. Even under the coarsest conditions, consisting of fewer than 10 mesh elements, the maximum error was < 0.4%. However, meshes containing fewer elements were found to be

much more likely to result in divergence of the solver, causing errors which may be problematic within large data sweeps.

A maximum element size of 10^{-7} m was selected, producing a mesh of between 169 to 420 elements depending on the size of the boundary layer for this sensitivity study. The maximum error at this size was < 0.1% with no divergent results and solver times in the order of seconds. Reducing elements were found to have minimal influence on solution accuracy or reliability, but exponentially increased solver times due to the significant increase in the number of elements (Figure 3-6).

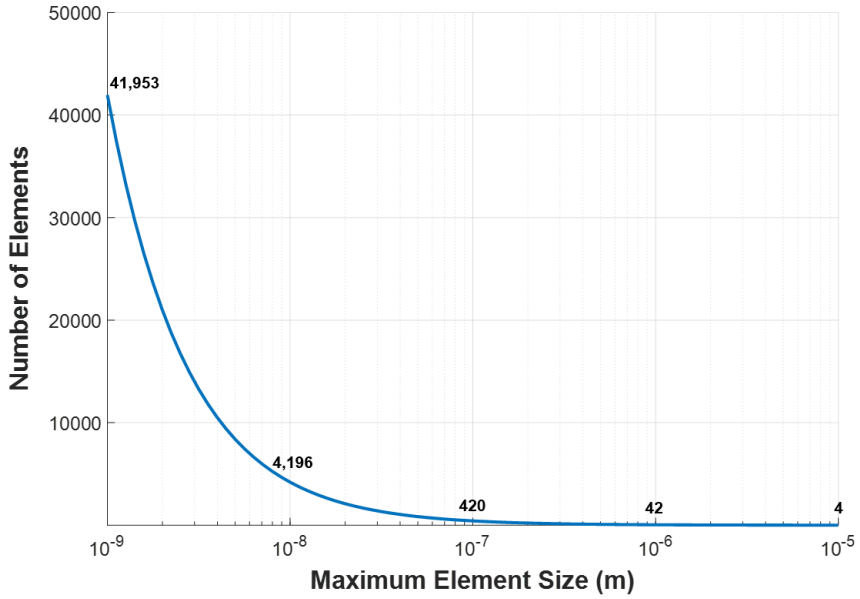

Figure 3-6 – Comparison between maximum element size and number of elements for a temperature of 273.15 K.

3.4 Results and Discussion

3.4.1 Validation Against Literature

Before conducting a numerical exploration of the COMSOL model, it first must be validated against the published values in order to ensure the results generated are representative of those in the original work. In order to verify that the model functions as intended, plots have been extracted from the 2020 paper by Kahyarian *et al*.[12] for comparison. The conditions stated in the paper were then introduced as inputs into the COMSOL model and the plots were recreated. Numerical analysis of the results is conducted to ensure a reasonable level of agreement between the two.

3.4.1.1 Corrosion Rate Validation

The plots provided by Kahyarian *et al.*[12] were used as points of comparison for the predicted corrosion rate. Figure 3-7 shows the comparison between the corrosion rate predicted by the COMSOL model (Figure 3-7(a)) and the published values (Figure 3-7 (b)). In Figure 3-7(b) the dashed lines represent the simulated data being used for comparison; the solid bars represent experimental data.

(a)

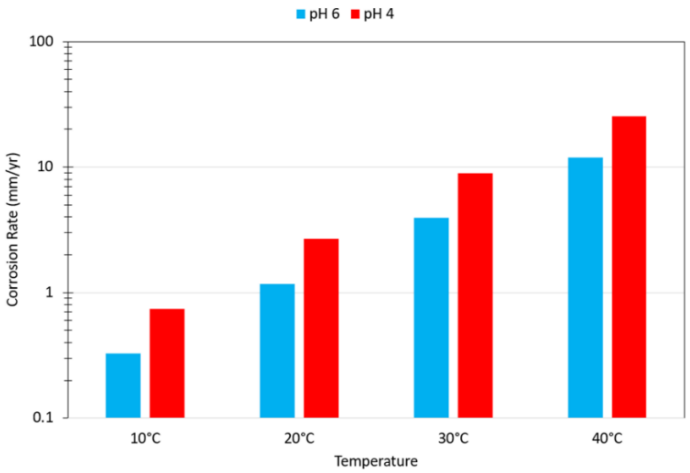

(b)

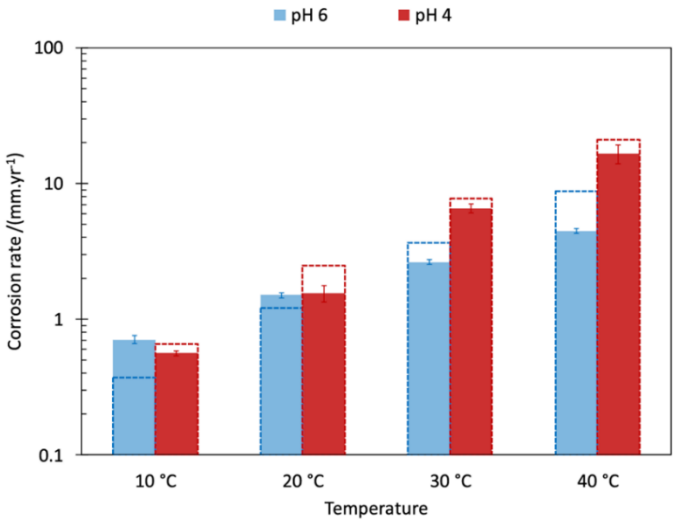

Figure 3-7 - Comparison of predicted corrosion rate between (a) COMSOL model and (b) literature[12] at various temperatures for pH 4 and pH 6 at 5 bar P_{CO2}, 4.4 ms^{-1} fluid velocity, and 0.1 M NaCl concentration. The simulated data being compared is shown by the dashed bars.

An initial visual comparison of the two plots indicates very strong agreement between the two models, with both producing a steady increase in corrosion as a function of temperature at both pH values. In both instances, the corrosion rate is also higher across all temperatures at pH 4 for the given conditions.

No specific data values are provided within the literature for quantitative comparison and so the graph was instead analysed using the digitizer within OriginPro 2020 software. Axes were superimposed over the top of the plot and the data points were selected manually. Doing so for each of the eight data points in Figure 3-7 produced an average 15% difference in the corrosion rate between the two models. The largest difference of 36% was seen at 40 °C, pH 6 and the smallest difference of 2% was seen at 20 °C, pH 6. Given the complexity of the model, the large number of temperature dependent variables, and the logarithmic scale of the plot, it is not unexpected to see some variation between the two. However, due to the strong agreement in the trends and the data spanning orders of magnitude, this is an acceptable level of percentage error.

3.4.1.2 Potentiodynamic Sweep Validation

The work by Kahyarian *et al.*[12] also provides several polarisation curves which can be used as a second point of validation. By replacing the electroneutrality boundary condition (Equation 3.48) at the surface with an applied potential within the COMSOL model, it is possible to generate simulated polarisation curves.

An auxiliary sweep was used to vary the applied potential (E_{app}) between -0.2 V and -1.2 V stepping in 0.01 V increments. The total current density (I_{tot}) was then calculated as the absolute difference between the anodic and cathodic currents for each potential.

$$i_{tot} = \left||i_c| - |i_a|\right| \tag{3.66}$$

The resulting values were then plotted on a semi-log graph for partial pressures of 1 bar, 5 bar, and 15 bar in order to directly compare to the plots provided in the reference paper[12] (Figure 3-8).

(a)

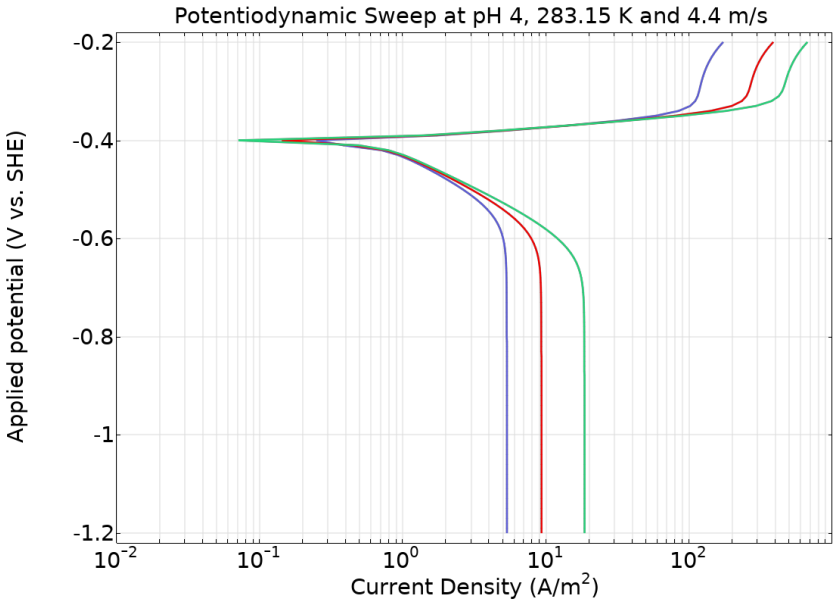

(b)

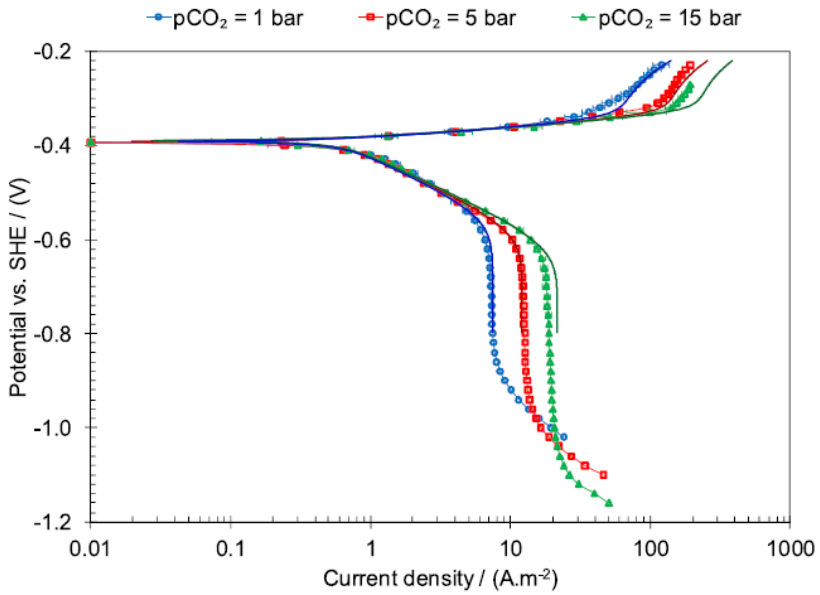

Figure 3-8 - Comparison of potentiodynamic sweeps between (a) COMSOL model and (b) literature[12] (shown by the black lines) for a bulk pH of 4 and fluid velocity of 4.4 ms^{-1} at 283.15 K.

Once again, very strong agreement can be seen between the two models across the entire range of applied potentials and for each of the partial pressures. In each case, the corrosion potential (E_{corr}) was found to be approximately -0.4 V with both the anodic and cathodic branches following the expected behaviour. The limiting current density for the cathodic reaction is

seen to increase with CO_2 partial pressure as increased species availability extends the charge-transfer controlled region.

At the higher potentials above E_{corr}, the influence of the individual current steps in the anodic kinetics (Equations 3.51-3.53) can be seen. The COMSOL model accurately reflects the reference model showing an initial linear slope, followed by a steep increase and a secondary linear slope. These represent current densities during the stages of active Fe dissolution ($i_{a,1}$), the transition region ($i_{a,2}$), and the pre-passivation range ($i_{a,3}$) respectively.

As with the corrosion rate data, there are some minor differences between two polarisation plots of the models which is to be expected with such a complex model being calculated using a different numerical solver method. However, the transitional behaviour between the charge-transfer limited region and the mass-transport limited region, as well as the 3 stages of the anodic kinetics are all captured and occur at very similar points. It is therefore reasonable to conclude that the COMSOL model can be considered valid is representative of the model originally developed by Kahyarian *et al.*[12, 36].

3.4.2 Numerical Exploration

One of the primary advantages to building the corrosion model within COMSOL Multiphysics® is the capacity to run parametric and auxiliary sweeps to rapidly analyse large numbers of input conditions. When combined with MATLAB LiveLink™, to both run the model and store only the outputs of interest, this facilitates a large-scale numerical exploration of the validated model. The purpose of the numerical exploration is to examine the overall effect of the many competing reactions occurring simultaneously. The high degree of complexity makes it very difficult to accurately predict how the model will react to any given change in the input conditions. However, by running a large number of input conditions and plotting the output response, it is possible to represent this visually. Here, thousands of unique combinations of input temperatures, CO_2 partial pressures, bulk pHs, and flow velocities and run through the COMSOL model. The outputs of corrosion rate, surface pH, and $FeCO_3$ saturation index have then been extracted and represented via contour maps.

3.4.2.1 Solver Approach

Within COMSOL Multiphysics®, a parametric sweep is used to vary one or more parameters to generate multiple data sets from a single run of the model. If the difference between each value in the sweep is sufficiently small, solver

times can be reduced by re-using the previous solution as an initial estimate. However, if the initial estimate is poor, which may be the case if there is a significant change in the input conditions, the solution may fail to converge.

In order to maximise the efficiency of the solver, MATLAB LiveLink^{TM} was used in conjunction with COMSOL. Within MATLAB it is possible to generate, solve, and store the solutions to a specified model set-up within COMSOL without the need for the graphical user interface. In order to utilise this, a parametric model was created within COMSOL to sweep a single parameter within the numerical solver. The code to generate this model was then transferred into a MATLAB script from which the other input variables could be specified. Nested loops could then be used to iterate through the input conditions and store the outputs in n-dimensional arrays, where n is the number of parameters being assessed. By only changing a single parameter with small incremental changes, this ensured that the re-used solution within the parametric sweep would always be a reasonable initial estimate. Once the outputs had been stored, the script would generate a new COMSOL model, resetting the initial guess for the new input conditions.

Early in the development of the methodology, an issue was identified within the parametric solver in which the COMSOL software would not always properly recalculate the domain size. Although small, this would have an effect on the results as the concentration gradient through the boundary layer would no longer be correct, changing the rates of diffusion. In order to prevent this issue, only inputs that did not affect the calculation of δ, such as pH or P_{CO_2}, were used within the sweep. The other values were adjusted within the MATLAB script to ensure accurate calculation of the domain.

3.4.2.2 Data Set

For each contour map presented in the subsequent sections (3.4.2.3 to 3.4.2.5), a consistent data set was used. A total of 26,708 unique input conditions were assessed for various combinations of temperature, bulk pH, P_{CO_2}, and bulk flow velocity. The range of values used as well as the distribution of these inputs is summarised in Table 3.11.

Table 3.11 - Summary of input values used to generate the data set within the numerical exploration.

Variable	Range of Values	Interval	Distribution
Temperature	273.15 – 315.15 K	1 K	Linear
Bulk pH	5 – 6.5	0.5	Linear
Partial Pressure of CO_2	0.1 – 10 bar	80 points/decade	Logarithmic
Bulk Flow Velocity	1 - 10 $m \cdot s^{-1}$	1 $m \cdot s^{-1}$	Linear

3.4.2.3 Corrosion Rate

For every combination of temperature, bulk pH, P_{CO_2}, and velocity values, the corrosion rate of the steel surface was evaluated based on the local anodic current density (Equations 3.51-3.53). These values were initially calculated with units of $m \cdot s^{-1}$ and so were then converted to the more usual form of $mm \cdot yr^{-1}$ via Equation 3.67. The resulting outputs across the data set have been plotted on contour maps (Figure 3-9) to show the change in the corrosion rate in response to the varying input conditions. As the results span multiple orders of magnitude, the common logarithm of the corrosion rate ($\log_{10}(CR)$) has been plotted.

$$CR\left(\frac{mm}{year}\right) = CR\left(\frac{m}{s}\right) \times 1000 \times 365.25 \times 24 \times 60 \times 60 \tag{3.67}$$

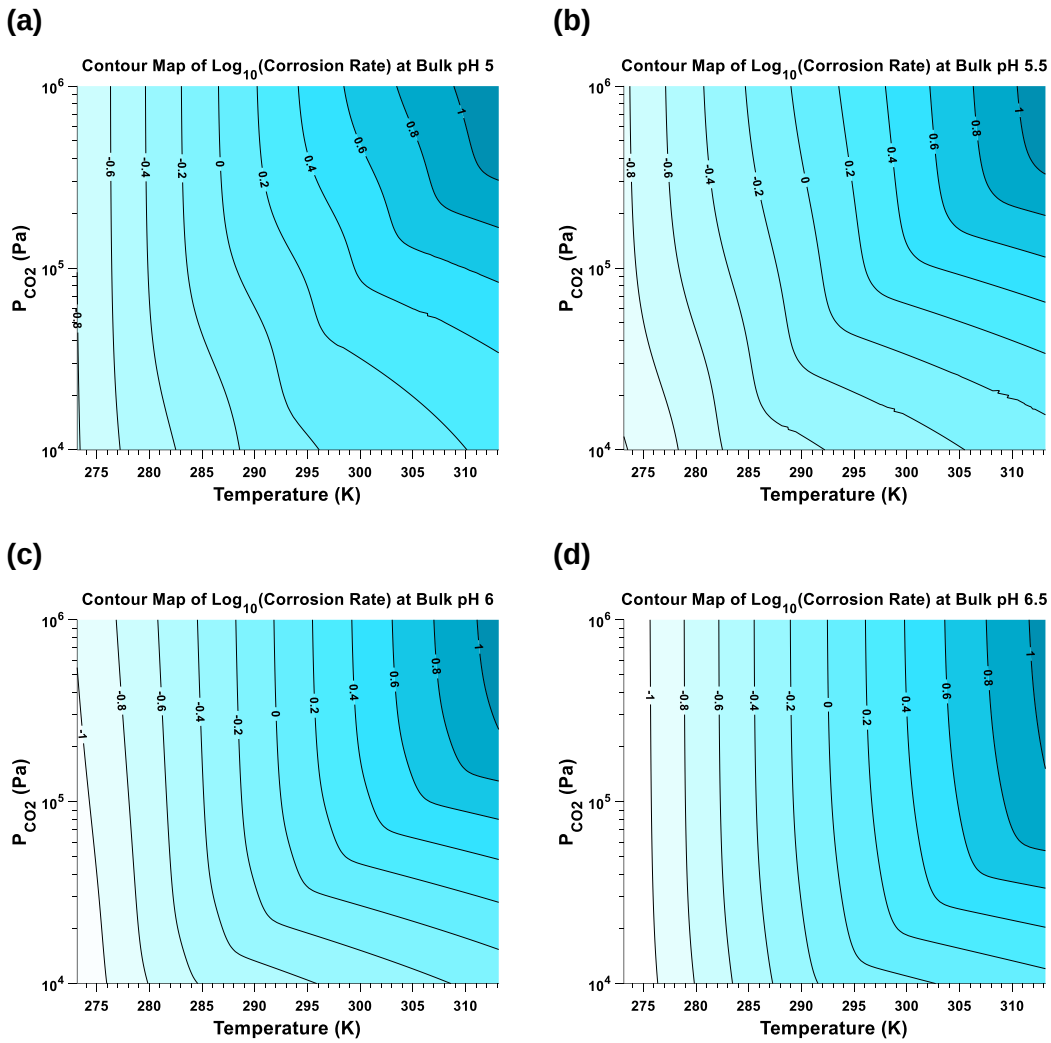

Figure 3-9 - Contour maps of the common logarithm of the corrosion rate (mm·year^{-1}) as a function of temperature and pressure at (a) bulk pH 5 (b) bulk pH 5.5 (c) bulk pH 6 and (d) bulk pH 6.5.

At each of the bulk pH values evaluated between 5 and 6.5, a similar corrosion rate output is produced with varying temperature and partial pressure. The highest rates of corrosion, reaching around 10 mm·year^{-1} in each instance, are consistently seen in the top right corner of the contour maps (Figure 3-9) where temperature and pressure are greatest. The higher rates of species transport, species dissociation and charge-transfer rates at the higher temperatures, combined with the increased availability of dissolved aqueous CO_2 species at higher pressures (Equation 3.17) all act to accelerate the anodic dissolution of Fe.

At lower temperatures however, there is a clear transition to a region in which the corrosion rate starts to become independent of P_{CO2}, indicated by the near-vertical contour lines. This represents the transition from the mass-transport

limited region to the charge-transfer limited region in which the cathodic current is insensitive to partial pressure, as observed by Kahyarian and Nesic[12]. Under these conditions the increased availability of electroactive H^+ ions at the surface, due to the greater solubility of CO_2, becomes less significant as the speed of the electrochemical reactions becomes the rate controlling factor. The corrosion response does however become more sensitive to temperature in this region as higher temperatures directly increase the anodic reaction rate. The change from the mass-transport limited control to charge-transfer control can be shown by plotting polarisation curves for each region, as shown in Figure 3-10.

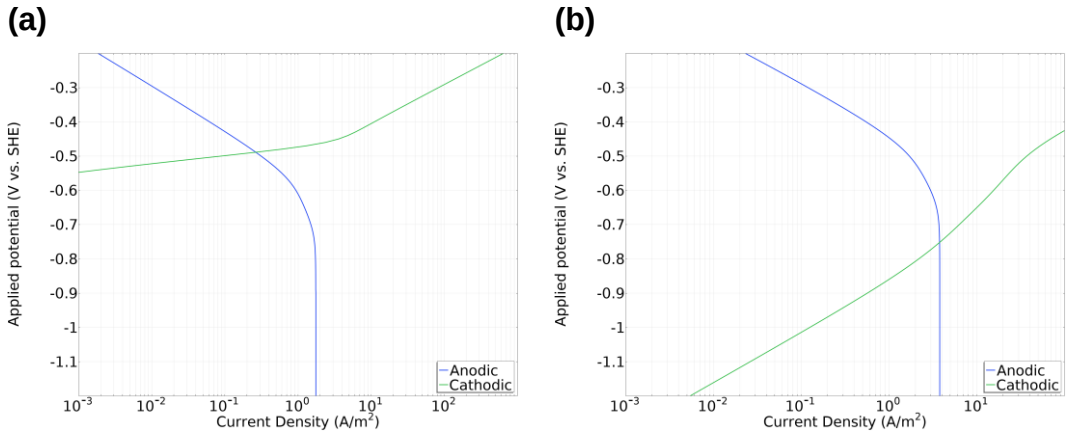

Figure 3-10 – Polarisation curves showing anodic and cathodic branches at (a) 283.15 K and (b) 308.15 K, at bulk pH 6, 1 bar P_{CO2}, 5 m/s flow velocity in a 0.1 m diameter pipe.

From Figure 3-10(a) it can be seen that, for a pH of 6 and CO_2 partial pressure of 1 bar, at 283.15 K the anodic curve crosses the cathodic curve in the charge-transfer controlled region. However, when the temperature is increased to 308.15 K (Figure 3-10(b)), and the corrosion response changes (Figure 3-9 (c)), the anodic curve instead crosses the cathodic curve in the mass-transport controlled region. This shows how the limiting mechanism changes between these two sets of conditions.

The influence of temperature on the mass-transport controlled region can be observed by evaluating the corrosion rate as a function of bulk fluid velocity. Due to the potential occurrence of the aforementioned solver issue when sweeping parameters that change the domain size, temperature and pressure were both adjusted individually within the MATLAB script. As a result, solver times were increased significantly and so to minimise the impact, the interval for temperature was increased from 1 K to 10 K. The resulting corrosion rates were calculated in the same way and are shown in Figure 3-11.

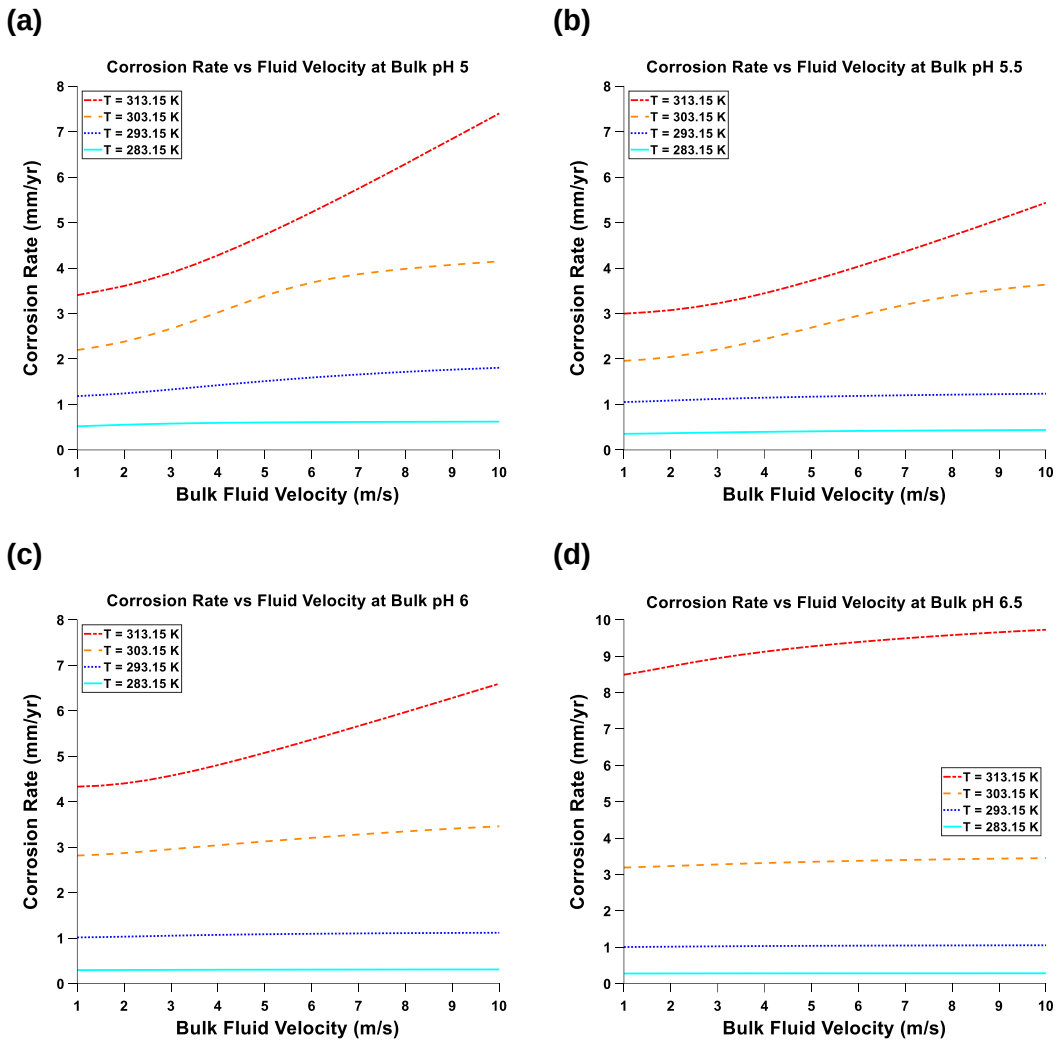

Figure 3-11 - Contour maps of corrosion rate as a function of velocity for a 0.1 m diameter pipe at 1 bar P_{CO_2} at (a) bulk pH 5 (b) bulk pH 5.5 (c) bulk pH 6 and (d) bulk pH 6.5.

While the velocity of the flow does not directly impact the fluid chemistry, higher flow rates accelerate mass-transport rates due to the increased turbulence. Additionally, the boundary layer thins, reducing the distance between the surface and the bulk solution. As a result, the corrosion rate will increase with fluid velocity while the system is mass-transport limited, reaching a plateau once the system becomes charge-transfer limited.

At the highest temperature of 313.15 K (40 °C), the plateau in the corrosion rate is only seen when the bulk pH is as high as 6.5 (Figure 3-11(d)), with the corrosion rate continuing to increase across the entire range of velocities for the lower pHs. This suggests that higher temperatures the surface reactions are sufficiently fast to maintain a rate of H^+ consumption above the rate of

supply. As temperature decreases, the system reaches the charge-transfer limit at progressively lower velocities as the rate of the surface reactions slow.

The relative increase in corrosion rate as a function of velocity can also be seen to reduce as the bulk pH is increased. This effect can be seen across all temperatures, indicating that this is likely due to the reduced bulk concentration of H^+ at the higher pH. A lower bulk H^+ concentration diminishes the impact of increased mass-transport rates as there are fewer ions available to be transported from the bulk to the surface.

An increase in the corrosion rate can be observed at bulk pH 6.5, particularly at the higher temperatures when compared to the lower pH values. Generally, it would be expected that corrosion rate decreases with pH due to the reduced availability of H^+ ions in the bulk solution[33, 127]. However, as can be seen in Figure 3-4, it is around this pH that the relative concentration of HCO_3^- starts to increase significantly. The additional HCO_3^- ions can dissociate (Equation 3.11) and increase the production of H^+ near the surface.

A consequence of supplying H^+ via the dissociation reaction is that the local CO_3^{2-} concentration is also increased. As a result, this means that under high pH, high temperature conditions it is more likely $FeCO_3$ would begin to form a protective layer on the surface, reducing the corrosion rate[9, 17, 128]. However, it is important to remember that the formation of surface films and their protective properties is not considered within this model. Therefore, the increase in HCO_3^- under the higher pH conditions correlates to a higher predicted corrosion rate.

3.4.2.4 Surface pH

For each run of the model used to evaluate the corrosion rate, the pH at the surface was also evaluated as a function of the surface activity of H^+ (Equation 3.68). The activity is a function of the concentration of H^+ ions at the surface, however this was evaluated on the node adjacent to the surface, not the surface node itself. The kinetic equations used to counterbalance the loss of H^+ ions in the surface reactions do not apply to the boundary, leading to artificially inflated values for the surface pH.

$$pH_{surface} = -\log_{10}\left(a_{H^+surface}\right) \tag{3.68}$$

Where $a_{H^+surface}$ is the hydrogen ion activity (M) at the surface.

Figure 3-12 shows the change in surface pH as a function of temperature and P_{CO_2} at each bulk pH value.

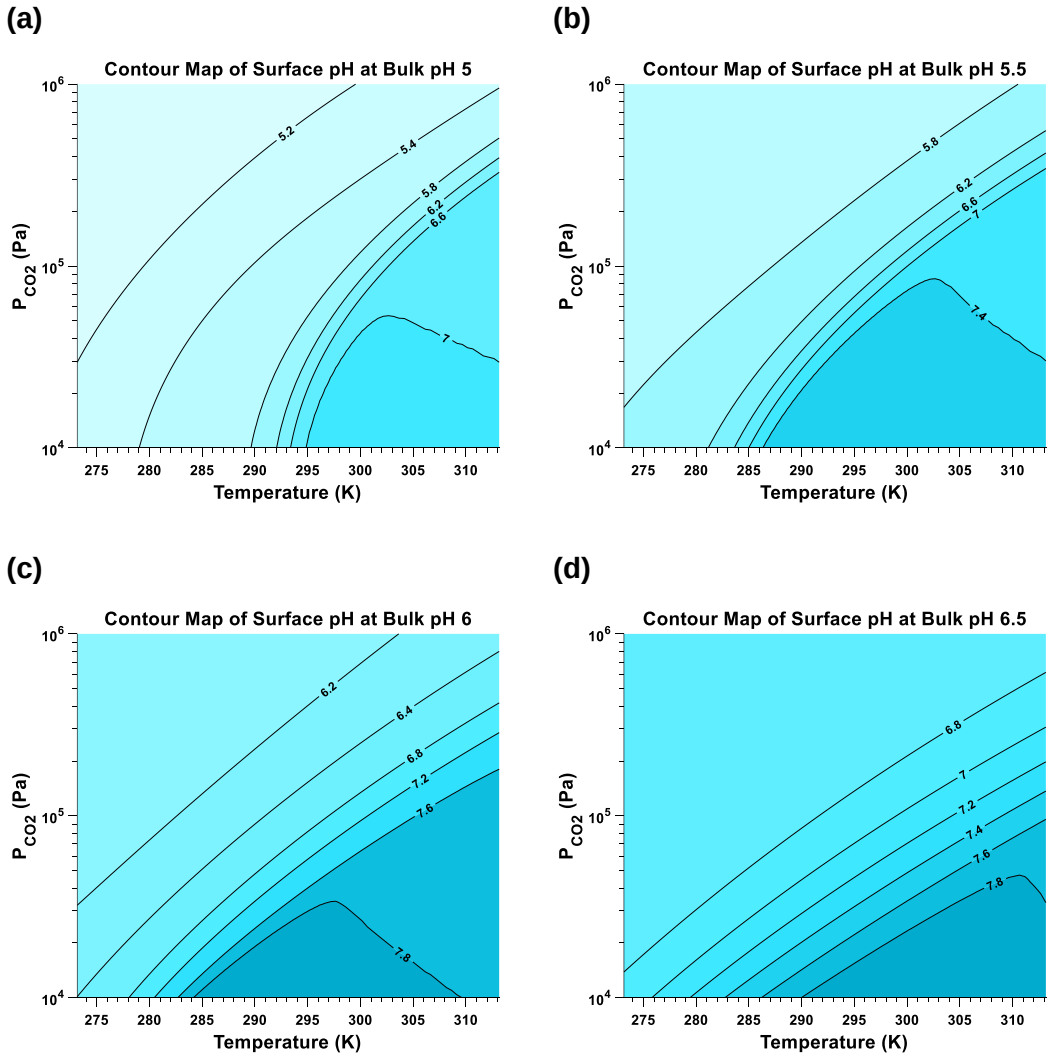

Figure 3-12 - Contour maps of the surface pH as a function of temperature and pressure at (a) bulk pH 5 (b) bulk pH 5.5 (c) bulk pH 6 and (d) bulk pH 6.5.

Across all the bulk pH conditions evaluated, a similar response was seen in the surface pH, with the surface pH being universally higher due to the consumption of H^+ ions as part of the cathodic reaction. Under high pressure, low temperature conditions the surface pH converged towards the bulk pH value as the high concentration of H_2CO_3 and low surface reaction rates allow for rapid replenishment of consumed ions through dissociation. The result of this is a charge-transfer limited system which does not result in significant depletion of H^+ ions close to the surface.

As the temperature is increased and the pressure is lowered, the system shifts towards mass-transport control, with ions being consumed almost immediately after reaching the surface, resulting in very high surface pH values relative to the bulk. Within this mass-transport controlled region, there is a clear transition point within each contour map at which surface pH begins to decrease with temperature.

From Figure 3-9, it is known that the corrosion rate, and therefore the rate of the cathodic reaction (Equation 3.16), become less sensitive to temperature once the system is no longer charge-transfer controlled. Consequently, the relative rate of consumption of H^+ ions with increasing temperature is reduced in the mass-transport controlled region.

On the other hand, the rate of supply of H^+ continues to increase with temperature due to increasing rates of dissociation and greater species transport from the bulk to the surface. This is supported by the higher surface pH causing a shift in the equilibrium state towards CO_3^{2-} production (Figure 3-4), resulting in rapid dissociation of the highly concentrated HCO_3^- ions (Equation 3.11) and the production of additional H^+ ions.

With the relative rate of H^+ consumption being reduced and the increasing production rate, an inverse relationship between temperature and surface pH can be observed in the high temperature, low pressure region.

The response of the surface pH to change in bulk velocity is shown in Figure 3-13 and once again two trends can be identified depending on the current limiting mechanism. Under mass-transport controlled conditions the surface pH tends towards the bulk pH values as fluid velocity is increased.

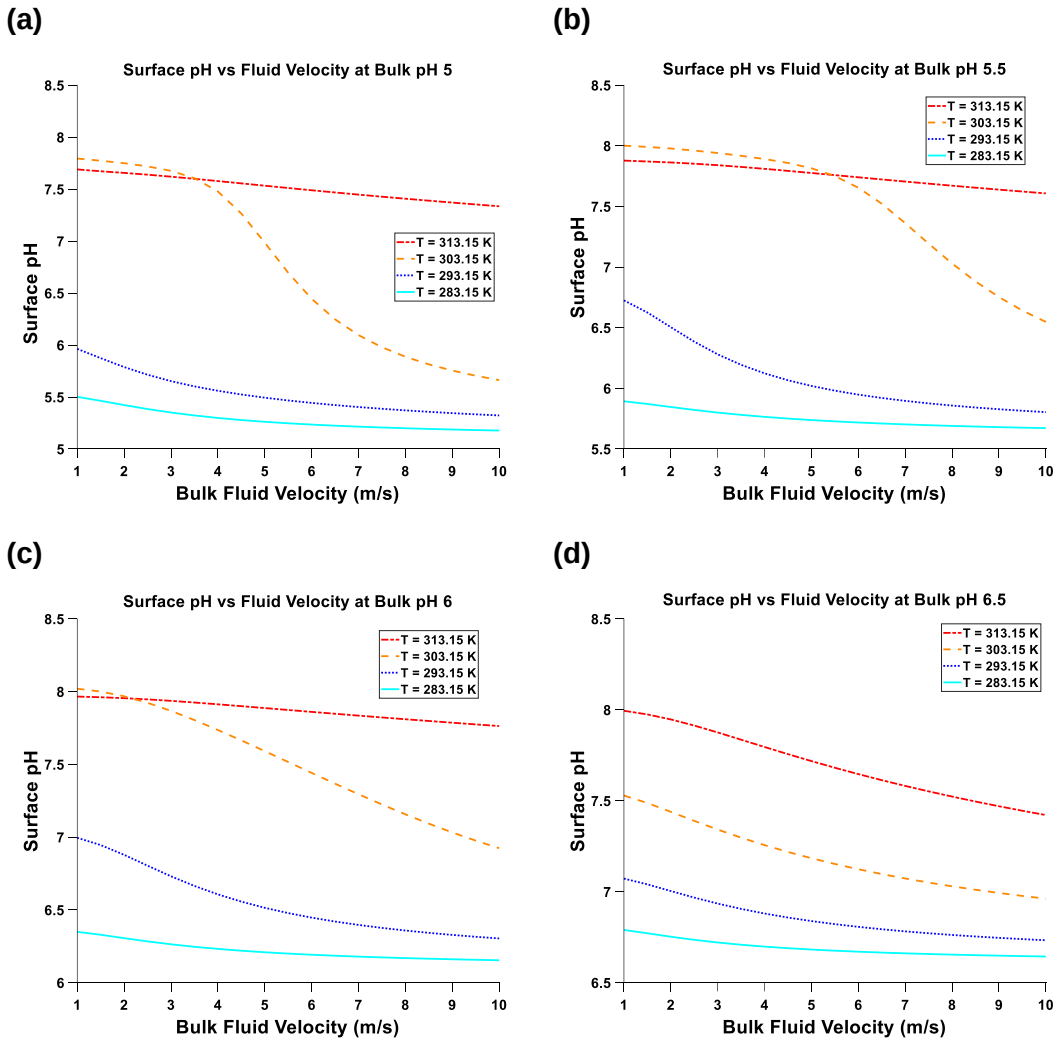

Figure 3-13 - Contour maps of surface pH as a function of velocity for a 0.1 m diameter pipe at 1 bar P_{CO_2} at (a) bulk pH 5 (b) bulk pH 5.5 (c) bulk pH 6 and (d) bulk pH 6.5.

The higher flow velocities reduce the height of the boundary layer resulting in steeper concentrations gradients while simultaneously inducing greater turbulence within the flow. Together this raises both the molecular and turbulent diffusion, increasing species transport between the surface and the bulk. As a result, when the surface reactions reach their limiting current, the increase in the supply of ions to the surface acts to reduce the deviation from the bulk pH. This effect is not seen in the mass-transport controlled region, however. This is shown by the 313.15 K lines at pHs 5, 5.5 and 6 where the surface pH remains high due to the rate of the surface reactions also being accelerated by the increased rate of supply. A small reduction in surface pH is observed due to the substantial increase in mass-transport rates, however the

response is linear, as opposed to the exponential decay produced in the charge-transfer regions. In some cases, the transition between the two regimes can be identified by a sudden change in the surface pH, as is the case at 303.15 K in Figure 3-13(a), seen at around 4 $m \cdot s^{-1}$.

3.4.2.5 Saturation Index

Although film formation is not considered here, it is possible to use the model to predict the point at which precipitation of $FeCO_3$ is likely to occur via a measure known as the saturation index (SI). A saturation index of zero represents the point at which a solution becomes supersaturated, and precipitation becomes thermodynamically favoured. As the $FeCO_3$ saturation increases beyond this point, precipitation becomes more thermodynamically favourable and the rate of nucleation and growth accelerates[9, 17]. The saturation index is a function of the saturation ratio, which is a calculated from the local activities of Fe^{2+} and CO_3^{2-}.

$$SI = \log_{10}(SR) \tag{3.69}$$

$$SR = \frac{a_{Fe^{2+}} \cdot a_{CO_3}^{2-}}{K_{sp}} \tag{3.70}$$

Where SI is the saturation index, SR is the saturation ratio, $a_{Fe^{2+}}$ and $a_{CO_3^{2-}}$ are the respective species activities (M), and K_{Sp} is the solubility limit (M^2). For the purposes of this work, the solubility limit formula proposed by Greenberg and Tomson[20] (Equation 3.71) has been used.

$$\log K_{sp} = -59.2385 - 0.041377T_K - \frac{2.1963}{T_K} + 24.5724\log(T_K) \tag{3.71}$$

The SI has been evaluated at the surface for each set of input conditions and the output as a function of temperature and P_{CO_2} at each bulk pH value is given in Figure 3-14. The contour maps clearly demonstrate two different response patterns depending on whether the surface reactions are charger-transfer limited or mass-transport limited.

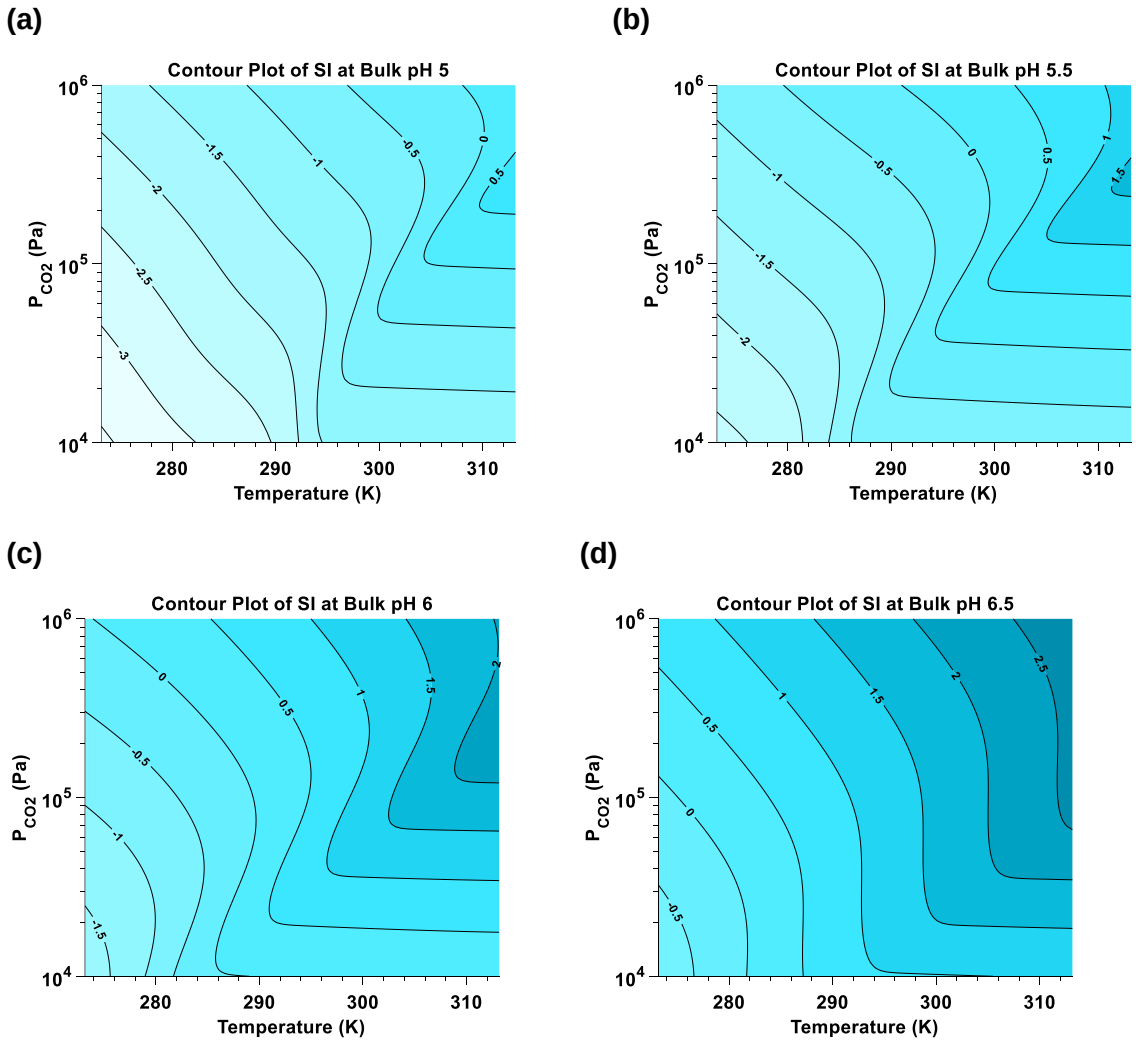

Figure 3-14 - Contour maps of surface saturation index of $FeCO_3$ as a function of velocity for a 0.1 m diameter pipe at 1 bar P_{CO_2} at (a) bulk pH 5 (b) bulk pH 5.5 (c) bulk pH 6 and (d) bulk pH 6.5.

Under both regimes there is a consistent increase in SI with pressure, as the increased concentration of H_2CO_3 consequently raises the CO_3^{2-} concentration in both the bulk and at the surface. As the dissolution of CO_2 occurs independently of the electrochemical surface reactions, the higher partial pressure acts to raise the SI regardless of the limiting mechanism. Therefore, in regions where the behaviour is stable, a consistent increase in SI is seen in response to increasing pressures primarily due to change in the CO_3^{2-} concentration.

Conversely, the local Fe^{2+} concentration closely follows the corrosion rate response (Figure 3-9) due to the anodic reaction resulting in the dissolution of Fe from the surface into solution. As the corrosion rate becomes less sensitive

to temperature when under mass-transport control, the saturation index also begins to plateau in this region. The production of CO_3^{2-} at the surface does increase with temperature due to the higher pH, however the corresponding increase in the species transport rates acts to move these ions away from the surface more rapidly. The overall effect is relatively stable surface SI for any given pressure, an effect which is not seen in the charge-transfer controlled region due to the strong dependence of iron dissolution on temperature.

In the transition between the two regions, a much more complex response is produced due to the competing interactions affecting both Fe^{2+} and CO_3^{2-}. The difficulty in accurately predicting the $FeCO_3$ saturation response is highlighted in this region, with the shapes of the contours varying significantly depending on the conditions.

The influence of the bulk pH on the SI, however, is much more consistent. As bulk pH is increased from 5 (Figure 3-14(a)) to 6.5 (Figure 3-14(d)) a steady increase in $FeCO_3$ saturation can be observed, with the surface being supersaturated ($SI > 0$) across almost all conditions at the highest pH. Once again, this can be explained via the shift in the equilibrium state from H_2CO_3 dominated towards CO_3^{2-} dominated (Figure 3-4). The significant rise in the concentration of CO_3^{2-} ions in the bulk solution is sufficient to determine the behaviour of the SI in response to pH, irrespective of the changes to the surface electrochemistry.

3.4.2.6 Corrosion Potential and Anodic Kinetics

As part of the analysis conducted during the numerical exploration, a limitation of the Kahyarian model in its current form has been identified relating to the corrosion potential. It has been previously noted that under mass-transport limited conditions, the predicted concentration of H^+ on the surface node can become unrealistically low, leading to artificially inflated pH values on this node. Thus far, this issue has been acknowledged and circumvented by performing the analysis based on the H^+ concentration of the 2nd node. However, the same approach cannot be readily applied in the generation of polarisation curves and as such the prediction of E_{corr} is not always accurate.

The reversible potential for the anodic reaction within the model is -0.440 V. Therefore, the anodic reaction should converge on this value as the current density tends to zero[129]. However, under mass-transport limited conditions, particularly when the surface reaction rates are very high and the bulk H^+ is

concentration low, it has been found that the anodic curve becomes significantly more negative at low current densities (Figure 3-15).

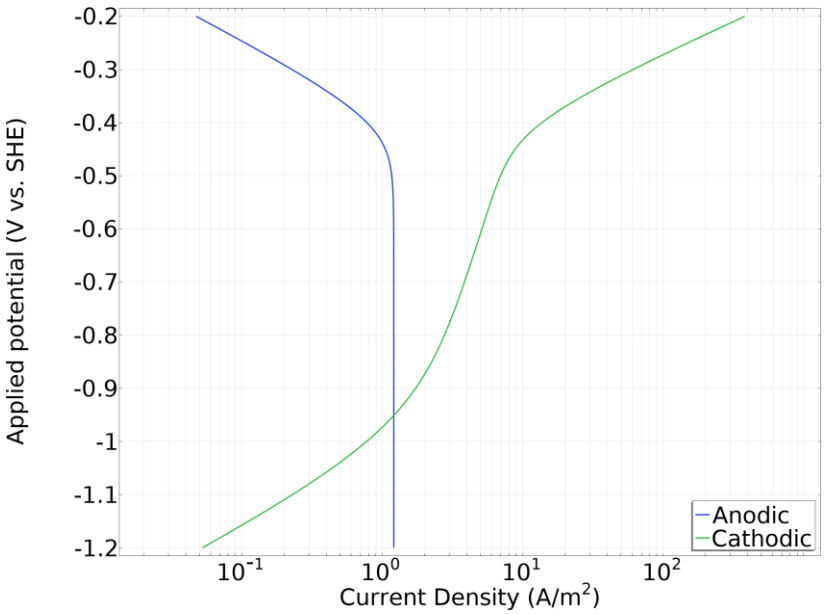

Figure 3-15 - Polarisation curves at 303.15 K, bulk pH 6, 1 bar P_{CO2}, and 5 m/s flow velocity in a 0.1 m diameter pipe showing the drop in the anodic potential under mass-transport limited conditions.

As a result of the shift in the anodic curve, the intersection with cathodic curve occurs at a lower potential, which in turn produces a more negative E_{corr} value. As it was found that E_{corr} dropped significantly with higher temperatures and lower pH and P_{CO2} values when under mass-transport control, it was suspected that the low H^+ concentrations were causing this effect.

From Equations 3.51-3.53, it can be seen that, for a given temperature, the anodic current density calculation is determined by the respective activities of CO_2 and H^+. In order to verify the underlying cause, these reactions were implemented within Microsoft Excel. The surface species concentrations for a given set of conditions were then exported from COMSOL and used as inputs within the Excel model to validate that the new model correctly replicated the existing model. H^+ concentrations were then extracted from the 2nd and 3rd nodes of the COMSOL model and used within the Excel model; the results are shown in Figure 3-16.

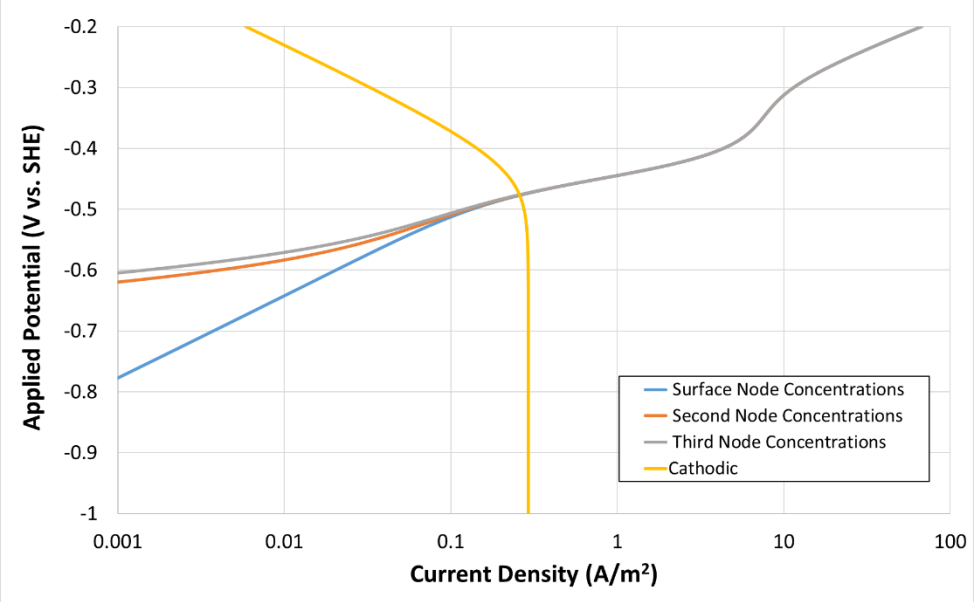

Figure 3-16 – Polarisation curves from Excel model using H^+ concentrations from COMSOL extracted from the surface, 2nd and 3rd nodes at 283.15 K, pH 5, 0.1 bar P_{CO2}, and 2 m/s in a 0.1 m diameter pipe.

The concentration profile out from the surface for the same conditions and a fixed applied potential of -0.8 V are shown in Figure 3-17. The locations of the 2nd and 3rd nodes are indicated to show the how the local pH, and therefore local H^+ concentration changes across the small distances.

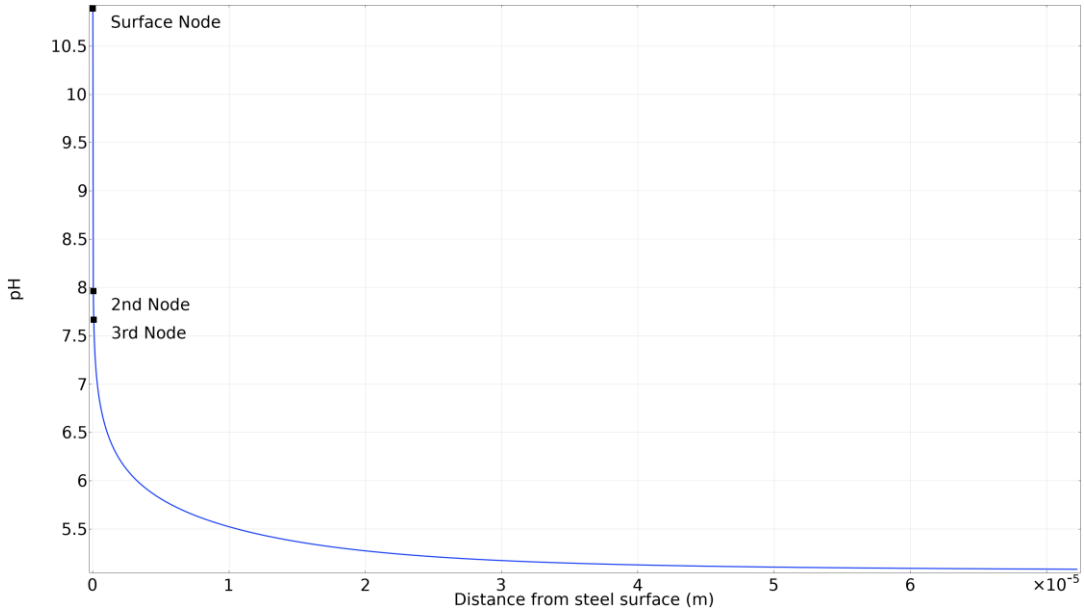

Figure 3-17 – COMSOL model predicted local pH as a function of the distance from the surface at 283.15 K, pH 5, 0.1 bar P_{CO2}, and 2 m/s in a 0.1 m diameter pipe for a fixed applied potential of -0.8 V.

From Figure 3-16 and Figure 3-17, it is clear that the sudden increase in the local pH directly influences the anodic polarisation curve. Despite still utilising the surface concentration of CO_3^{2-}, performing the same evaluation on the 2nd node noticeably shifts the anodic curve back towards the expected shape. Performing the evaluation on the 3rd node produces another, small shift in the same direction, indicating that, as the H^+ concentration returns to more reasonable levels, the effect on the anodic curve is removed.

As the system is under mass-transport control, this effect will have minimal effect on the corrosion rate predicted by the model. However, this will be an important consideration in future model developments, particularly if effects such as galvanic interactions are to be introduced[4].

3.5 Conclusion

The output response of a comprehensive mechanistic model of CO_2 corrosion has been evaluated across thousands of combinations of input conditions for temperature, partial pressure of CO_2, velocity, and bulk pH. Two distinct response patterns have been identified dependent upon the limiting behaviour of the system.

Under low temperature, high pressure conditions, the model predicts an output that is charge-transfer limited. As the bulk pH is increased from 5 to 6.5, the size of this charge-transfer limited region was extended to higher temperatures. Under these conditions, changes to the partial pressure of CO_2 had minimal impact on the corrosion rate and the surface pH did not deviate far from the bulk value. However, the corrosion rate and the surface $FeCO_3$ saturation index were highly sensitive to changes in temperature due to the associated increase in the anodic iron dissolution reaction.

At higher temperatures and lower pressures, the limiting behaviour transitioned to mass-transport control, with H^+ ions being consumed rapidly upon reaching the surface. Under the mass-transport limited regime, the predicted corrosion rates became much more sensitive to changes in pressure with the surface pH rising significantly above that of the bulk pH. Both corrosion rate and $FeCO_3$ saturation were less impacted by temperature changes in this region due to supply of H^+ ions to the surface limiting the rates of the surface reactions. Instead, the behaviour was found to be primarily determined by changes to the rates of species transport through the boundary layer, therefore becoming more sensitive to hydrodynamic changes.

Chapter 4 – Hydrodynamic Integration via CFD Turbulence Modelling

When considering corrosion behaviour, particularly under mass-transport limited conditions, it is crucial to consider the influence of turbulence within the bulk flow. Highly turbulent flows generate eddies which permeate the boundary layer, accelerating species transport via turbulent diffusion, as well as reducing the distance between the surface and bulk fluid (boundary layer thinning), increasing the rates of molecular diffusion. Currently, these effects are modelled using empirical equations based on experiments within straight pipe flows. However, by utilising turbulence models it is possible to simulate the behaviour via CFD. In this chapter, an approach is proposed to couple CFD models with the corrosion models discussed in previous chapters to generate the necessary hydrodynamic variables without employing empirical equations. In doing so, the applicability of existing corrosion models can be expanded beyond the conditions and geometries under which the experimental hydrodynamic data was generated. The examples of a converging channel and a rotating cylinder electrode are used here to demonstrate the application of this new method. Additionally, the limitations of the methodology in its current form are identified and potential future developments that can be made to expand the application even further are discussed.

Following the development of the hydrodynamic method, it is combined with the existing corrosion models to predict corrosion within an RCE test cell. This is combined with experimental testing to evaluate the performance of the corrosion models and identify their associated strengths and weaknesses.

4.1 Background

4.1.1 Hydrodynamic Influence on CO_2 Corrosion

It has long been established that the hydrodynamics of fluid flow within a corrosive environment directly influences the rates of reaction at the corroding surface when under mass-transport-limited conditions[130]. A system is under mass-transport control when the electrochemical reactions at the surface are being limited by the supply of reactants. In this instance, the surface reactions are sufficiently fast as to consume the electroactive species more readily than they are being supplied, leading to a local depletion of ions at the surface. It should be noted however that this is not always the case. In some instances,

the supply is greater than the consumption, meaning corrosion rates instead become dependent upon the speed of the surface reactions, this is known as charge-transfer control, or activation-control. Changes to the hydrodynamics are less impactful on the corrosion rate when the system is charge-transfer controlled, however the changes to the local solution chemistry may still be important when considering surface films[3].

As the degree of turbulence within the bulk flow increases, the transport rate of electroactive species both towards, and away from, the corroding surface is accelerated. As a result, there is a direct increase in the surface reaction rates when under mass-transport control, and the increased rate of transport away from the surface can influence the precipitation kinetics of surface films such as iron carbonate[131]. It is therefore important that the turbulence within the bulk fluid is accounted for when attempting to model corrosion behaviour accurately.

In many cases[12, 25, 26, 36, 39] this is achieved via two specific variables, namely the height of the boundary layer (δ) and the rate of turbulent diffusion (D_T). Together these terms account for the size of the laminar region near the wall, which represents the domain being modelled, as well as the acceleration of species transport due to turbulent eddies.

When discussing the boundary layer, it can be easy to confuse and conflate different terms due to the complexity in defining flow behaviour in the near-wall region. There are several ways in which a boundary layer can be defined, however for straight pipe flow possibly the most common is via a profile originally proposed by Theodore Von Kármán in 1931[41]. Termed the 'universal law of the wall' by Coles[42] in 1956, this profile uses dimensionless values for the fluid velocity (u^+) and wall distance (y^+) to define three distinct regions (Figure 4-1)[132]:

- Viscous (or laminar) sublayer – Region closest to the wall in which fluid velocity is lowest and viscous forces dominate.
- Buffer (or transition) layer - Transitional region beyond the viscous sublayer in which viscous forces and inertial forces are similar.
- Log-law (or inertial) layer – Fully turbulent region leading out into the bulk flow in which inertial forces dominate.

Within mass-transport models, the term 'boundary layer' is often used to refer solely to the viscous sublayer[12, 25, 26, 35, 36], however in some cases it is used to describe the sum of the three layers[39, 124]. The end of this near-wall region is commonly defined in-relation to the hydrodynamics of the bulk

flow, with the end of the inertial layer being the point at which the velocity is equal to 99% of free-stream velocity[44]. Throughout this work, the use of the term ‘boundary layer’ will reflect the most common meaning in referring specifically to the viscous sublayer.

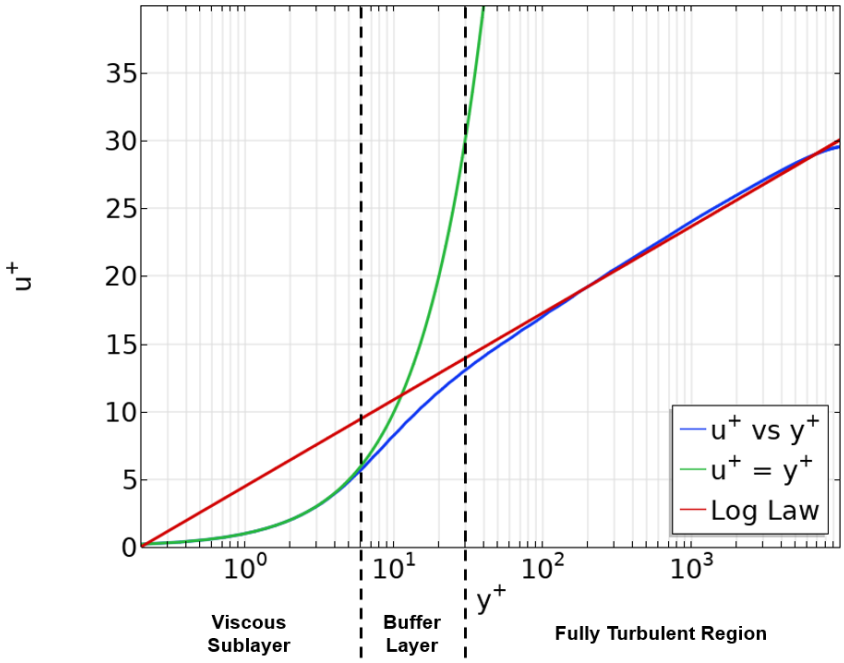

Figure 4-1 - Universal law of the wall plot showing the transition points between the viscous sublayer, buffer layer, and fully turbulent region.

By combining CFD modeling with comprehensive mechanistic corrosion models, the corrosive effects of various hydrodynamic profiles can be explored. In this work, a converging channel flow is initially used to demonstrate this process, detailing how these hydrodynamic parameters can be extracted and integrated into an established corrosion model.

4.1.2 Turbulence Modelling

Accurate modelling of turbulent flow can be difficult to achieve due to its highly erratic nature and its strong dependence on the surrounding boundary conditions. However, the movement of an incompressible viscous fluid can be described by a set of equations which describe the conservation of mass, momentum and energy, known as the Navier-Stokes equations.

In order to produce an accurate simulation of real-world flow, a solution to the Navier-Stokes equations needs to be calculated throughout the domain being modelled. Additionally, in the case of non-isothermal flows, the energy

equation must be solved to account for heat fluxes into, or out of the system, due to energy not being conserved within the domain.

As discussed in Chapter 1, complete solutions to these equations can be obtained via direct numerical simulation (DNS). DNS is however highly computationally expensive and can often take a long time to reach a solution, which is often unnecessarily precise. It is therefore common to instead use a turbulence model to provide an approximate solution[133]. Turbulence models aim to calculate a functionally accurate prediction for the movement of turbulent flow, whilst limiting the computational power needed to resolve the underlying equations. There are many types of turbulence models available and the type of model that should be used is highly dependent on the conditions being simulated. The accuracy of various models can vary drastically for a specific scenario and so it is important that an informed selection is made.

The most widely used category of turbulence models are the Reynolds Averaged Navier-Stokes (RANS) models. These models function by calculating the time-averaged values for turbulent quantities by separating the dependent variables into their mean and fluctuating components[69]. The equations are then averaged over a length of time that is large relative to the time-scale of the turbulence, but small relative to the time-scale for all other unsteady phenomena[65]. However, this averaging process results in an additional term known as the Reynolds stress tensor (τ_{ij}), which leads to a closure problem for the equations[69].

The closure problem can be addressed by expressing the stress tensor in terms of the gradient of the mean velocity field; this is known as the Boussinesq hypothesis[70]. Application of the Boussinesq hypothesis however generates an additional term known as the 'eddy viscosity' (μ_t), which needs to be calculated. Turbulence models are used to obtain a value for μ_t and the types of models are differentiated by the additional equations they employ in order to do so.

There are many RANS turbulence models that exist, which are generally classified by the number of additional transport equations required to solve for the eddy viscosity. There are zero equation models, such as the Prandtl mixing-length model, which use simple algebraic equations, as well one equation models, such as Spalart-Allamaras. However, generally accepted to be the most widely applicable and therefore widely used RANS models are the two equation models: k-ε and k-ω. Both of these models include the transport

equation for the turbulent kinetic energy (k), as well as an additional transport equation either the turbulent dissipation rate (ε) or the turbulent kinetic energy (ω)[95].

4.2 Methodology and Validation

One of the primary advantages of building the corrosion model discussed in Chapter 3 within COMSOL Multiphysics® is the ability to easily integrate additional physicochemical properties. Specifically, by utilising the turbulence models within the software it is possible simulate the hydrodynamic behaviour within the corrosive environment to remove the associated empiricism and expand the applicability of the models. The methodology discussed within this chapter is therefore divided into two stages:

1. Turbulence modelling to generate hydrodynamic data
2. Integration of hydrodynamic data into the corrosion model

The validity of the method can then be confirmed by comparing against the empirical data that has been previously generated for a straight pipe[28, 124]. The intention is to devise a generalised approach to numerically derive the hydrodynamic parameters used within the corrosion model for a range of geometries.

4.2.1 Turbulence Modelling within Pipeline Geometries

For the purposes of demonstrating the methodology, a straight pipe will be used as an example within this section as the associated hydrodynamics are already well-understood[28]. The approach can however be adapted and applied to any scenario in which the law of the wall is valid, as will be demonstrated later in this chapter.

4.2.1.1 Geometry and Meshing

The first stage in generating a hydrodynamic model is defining the geometry to which the physics is to be applied. The geometry being modelled here is a section of straight pipe with an internal pipeline diameter of 0.1 m and a length of 0.5 m. If it assumed that the flow within the straight pipe is uniform and that the pipeline material is homogeneous, the 3-dimensional (3-D) geometry can be simplified to be 2-dimensional (2-D) and axis-symmetric. Simplifying the model in this way significantly reduces the number of degrees of freedom (DoF) being solved for, allowing a much denser mesh to be utilised without excessively increasing the computational cost.

The rectangular shape of the 2-D geometry allows a uniform, high quality quadrilateral mesh (minimum element quality = 0.987) to be readily generated across the domain. For this work, it is most important the hydrodynamic behaviour within the boundary layer is accurately captured, as such boundary layers are applied at the surface to increase the mesh density in the near-wall region.

A visualisation of the geometry and associated mesh is shown in Figure 4-2.

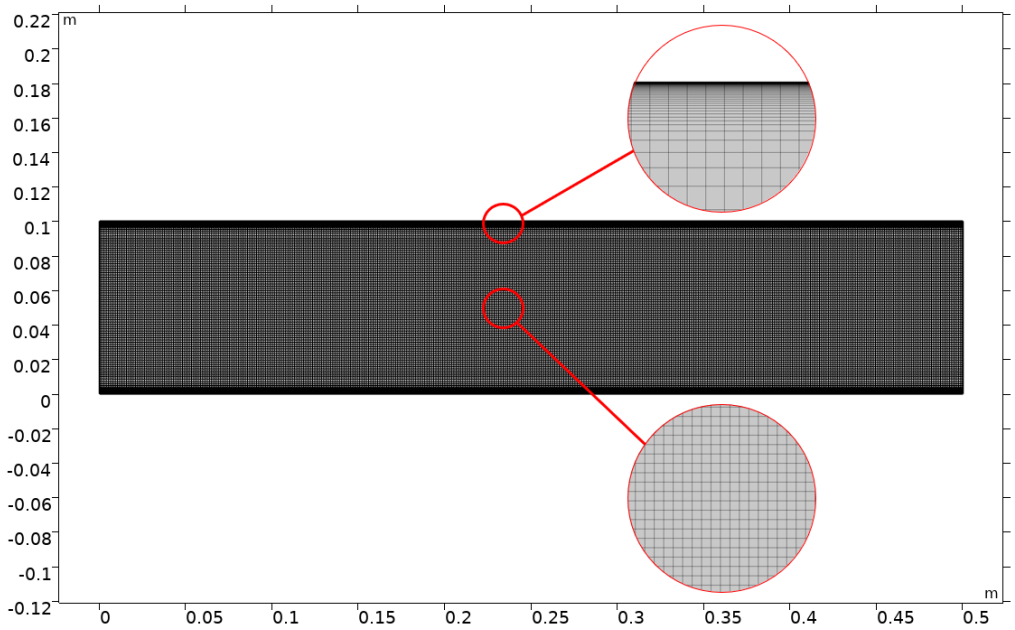

Figure 4-2 – Geometry and mesh for a 2-D axisymmetric straight pipe geometry with a pipe diameter of 0.1 m and length of 0.5 m.

4.2.1.2 Fluid Properties

For all flow models within this chapter, the fluid properties were assigned to those of water, including the temperature dependency. The fluid is assumed to be incompressible and as such only the density of the fluid (ρ_f) and the dynamic viscosity (μ) need to be calculated. The formulae for these fluid properties are shown in Table 4.1:

Table 4.1 – Formulae used to calculate the fluid properties of water

Property	Formula[26, 134]	Units	
μ	$0.001002 \times 10^{\frac{1.1709(293.15-T_K)-0.001827(293.15-T_K)^2}{(T_K-273.15)+89.93}}$	cP	(4.1)
ρ_f	$753.596 + 1.87748T_K - 0.003564T_K^2$	kg·m^{-3}	(4.2)

4.2.1.3 RANS k-ω SST Turbulence Model

As discussed in section 4.1.2, generally considered to be the most versatile of class of turbulence models are RANS turbulence models, specifically variations of the k-ε and k-ω models. There are numerous examples throughout literature of the applicability of these models to both pipe flows[96, 97, 99, 101, 135] and rotating cylinder experiments[136-138]. For the purposes of this work, the k-ω SST model has been selected as the most appropriate of the turbulence models. It has been previously found that the k-ε model performs strongly when modelling bulk flows and the k-ω model performs strongly in predicting near-wall behaviour[71]. The SST variant of the k-ω turbulence model takes advantage of this by using the k-ε approximation in the bulk and the k-ω approximation close the wall.

Originally devised by F. R. Menter in 1994[139], the k-ω SST models solves for μ_t by combining two equations, one for the turbulent kinetic energy (k) and one for the specific turbulent dissipation rate (ω):

$$\frac{\partial(\rho k)}{\partial t} + \frac{\partial(\rho U_i k)}{\partial x_i} = \tau_{ij}\frac{\partial u_i}{\partial x_j} - \beta^*\rho\omega k + \frac{\partial}{\partial x_j}\left[(\mu + \sigma_k\mu_t)\frac{\partial k}{\partial x_j}\right] \tag{4.3}$$

$$\frac{\partial(\rho\omega)}{\partial t} + \frac{\partial(\rho U_i \omega)}{\partial x_i} = \frac{\gamma}{\nu_t}\tau_{ij}\frac{\partial u_i}{\partial x_j} - \beta\rho\omega^2 + \frac{\partial}{\partial x_j}\left[(\mu + \sigma_\omega\mu_t)\frac{\partial \omega}{\partial x_j}\right] + 2\rho(1-F_1)\sigma_{\omega 2}\frac{1}{\omega}\frac{\partial k}{\partial x_j}\frac{\partial \omega}{\partial x_j} \tag{4.4}$$

Additionally, a modification is made to the definition of the eddy viscosity in order to account for the transport of the principal turbulent shear stress:

$$\nu_t = \frac{a_1 k}{\max(a_1\omega, \Omega F_2)} \tag{4.5}$$

Within Equation 4.4, there is a blending function (F_1) which varies as a function of the wall distance, transitioning between a value of one close to the wall and zero in the free-stream. The result of this is the gradual reduction of the final term in the calculation of ω which smoothly adjusts the equation from the k-ω formulation to the k-ε formulation.

The k-ω SST model is a low Reynolds number formulation, it is able to resolve the turbulence equations all the way down to the wall. This is in contrast to the wall function approximations used within the k-ε model[69, 140]. As the corrosion models used within this work operate within the hydrodynamic boundary layer near the surface, it is important that flow effects within this region are accurately captured, providing additional justification of the k-ω SST model.

The downside to utilising a low-Re model, however, is that it requires a dense mesh within the near-wall region to resolve the equations. Models which utilise wall functions can operate with a coarse mesh in this region as they utilise the law of the wall to approximate the behaviour. This is not the case for the k-ω SST model however, meaning that the mesh must be refined close to the boundary[140]. This can be achieved within COMSOL via the use of boundary layers, which define the position of mesh nodes in relation to a given boundary. These boundary layers are often very small due to the hydrodynamic boundary layer being comparatively very thin, which does increase the computational cost due to the increased number of degrees of freedom.

4.2.1.4 Extraction of Hydrodynamic Data

There are two outputs of interest that are needed when integrating the turbulence model into a corrosion model: the boundary layer height (δ) and the turbulent diffusivity (D_T). δ is a scalar value which corresponds to perpendicular distance from the corroding surface, while D_T is calculated as a function of the perpendicular distance from the surface. Therefore, before evaluating the corrosion on the internal pipe surface, the values for these two variables must be extracted from the turbulence model.

Firstly, in order to determine δ, the universal law of the wall profile (as seen in Figure 4-1) is utilised, requiring values of the dimensionless fluid velocity and dimensionless wall distance (u^+ and y^+ respectively) to be calculated. These are calculated via Equations 4.6 and 4.7, which combined the properties of the fluid with the outputs of the turbulence model.

$$u^+ = \frac{u}{\sqrt{\frac{\tau_\omega}{\rho}}} \tag{4.6}$$

$$y^+ = y \cdot \frac{u_\tau}{\nu} \tag{4.7}$$

Where u is the tangential fluid velocity (m·s^{-1}), τ_ω is the wall shear stress (Pa), ρ is the density of the fluid (kg·m^{-3}), y is the perpendicular wall distance (m), u_τ is the friction velocity (m·s^{-1}), and ν is the kinematic viscosity of the fluid (m^2·s).

Both dimensionless values are evaluated at each mesh node point along a perpendicular line protruding outwards from the surface of the pipe. The difference between $u^+$and y^+ is then calculated and the value of δ is equal to the value of y when this difference exceeds 0.01. This value is set as a

tolerance to determine the co-ordinate at which $u^+ \neq y^+$, indicating a deviation from the linear relationship described by the law of the wall and shown previously in Figure 4-1.

The values of D_T are then also evaluated along the same perpendicular line out from the surface. D_T is calculated as function of the turbulent flow properties (μ_t and Sc_t) and the fluid density:

$$D_T = \frac{\mu_T}{\rho Sc_t} \tag{4.8}$$

Where μ_T is the turbulent viscosity ($m^2 \cdot s^{-1}$) and Sc_T is the turbulent Schmidt number; the ratio of turbulent viscosity to turbulent diffusivity which generally varies between 0.7-0.9[141]. Due to the inherent uncertainty in accurately determining S_{C_T}, the standard value within COMSOL of 0.71[142] was used here.

As with u^+ and y^+, D_T is calculated at each mesh node point along the line, however this results in a number of discrete data points rather than a continuous function, which is needed by the corrosion model. Therefore, an interpolation function is fit to the data to convert the output to the correct form. A cubic function is used as this aligns with the form of the empirical functions used in mechanistic CO_2 corrosion models[12, 25, 26, 36].

4.2.2 Integration of Hydrodynamic Data into Corrosion Model

A detailed description of the CO_2 corrosion model being implemented has already been provided in Chapter 3 and so will not be reiterated here. However, a summary of the species included in the model as well as the chemical and electrochemical reactions are provided in Table 4.2.

Table 4.2 – Summary of species, boundary layer reaction kinetics, and electrochemical surface reactions included in the corrosion model.

Bulk Species	Reaction Kinetics	Electrochemical Surface Reactions
$CO_{2(g)}$ $CO_{2(aq)}$ $H_2CO_{3(aq)}$ $HCO_{3\,(aq)}^{-}$ $CO_{3\,(aq)}^{2-}$ $H_{(aq)}^{+}$ $OH_{(aq)}^{-}$ $Fe_{(aq)}^{2+}$ $Na_{(aq)}^{+}$ $Cl_{(aq)}^{-}$	$CO_{2_{(aq)}} + H_2O_{(l)} \rightleftharpoons H_2CO_{3_{(aq)}}$ $H_2CO_{3(aq)} \rightleftharpoons HCO_{3(aq)}^{-} + H_{(aq)}^{+}$ $HCO_{3_{(aq)}}^{-} \rightleftharpoons CO_{3_{(aq)}}^{2-} + H_{(aq)}^{+}$ $H_2O_{(l)} \rightleftharpoons H_{(aq)}^{+} + OH_{(aq)}^{-}$	$Fe_{(s)} \rightarrow Fe_{(aq)}^{2+} + 2e^{-}$ $2H_{(aq)}^{+} + 2e^{-} \rightarrow H_{2_{(g)}}$

Importantly for the methodology being discussed here, the influence of the hydrodynamics in the model is included via the species transport equation with utilises a modified form of the flux equation (Equation 4.9). The turbulent diffusivity is included as an additional diffusion term alongside the molecular diffusion. Species transport due to diffusion and electromigration are determined by the concentration gradient and electrolyte potential gradient, respectively, which will change based upon the thickness of the boundary layer.

$$N_j = -(D_{M,j} + D_{T,j})\frac{\partial c_j}{\partial x} - z_j u_j F c_j \frac{\partial \Phi_l}{\partial x} \tag{4.9}$$

Where N_j is the flux of species j, D_M is the molecular diffusion coefficient, D_T is the turbulent diffusivity, c_j is the species concentration, x is the distance perpendicular to the surface, z_j is the electrical charge, u_j is the mobility of species, F is the Faraday constant, and Φ_l is the electrolyte potential.

4.2.3 Validation Against Empirical Values

An initial validation of the methodology has been conducted for straight pipe flow to compare the outputs against empirical data and existing formulae. For a fully developed flow within a straight pipe, the boundary layer properties are consistent across the entire length, meaning the effect on corrosion rate is the same at any point on the surface. It is therefore possible to directly compare CFD data to the empirical equations used in the corrosion model to ensure agreement under the same conditions.

For the purposes of this comparison, the empirical relationships for δ and D_T proposed by Aravinth[124] (based on works by Notter and Sleicher[43] and Churchill[125]) have been used. These relationships, given by Equations 4.10 and 4.11, are employed in the work by Kahyarian *et al*.[12, 36] and in various other models throughout literature[143, 144].

$$\delta = \frac{5\nu}{\left(\frac{\tau_\omega}{\rho_{fluid}}\right)^{\frac{1}{2}}} \tag{4.10}$$

$$D_T = \frac{0.0007{y^+}^3}{\sqrt{(1 + 0.00405{y^+}^2)}} \tag{4.11}$$

It should be noted that δ is calculated in this instance under the assumption that the viscous sublayer ends at $y^+ = 5$, in accordance with the universal law of the wall theory[132].

The height of the boundary layer was determined from the computational model by plotting u^+ against y^+ (as shown in Figure 4-1) and comparing to the plot of $u^+ = y^+$. The point at which the two plots deviate above a set tolerance of 0.01 was used to define the boundary layer height. A comparison of these values for various flow velocities against the empirical values calculated via Equation 4.10 is shown in Figure 4-3.

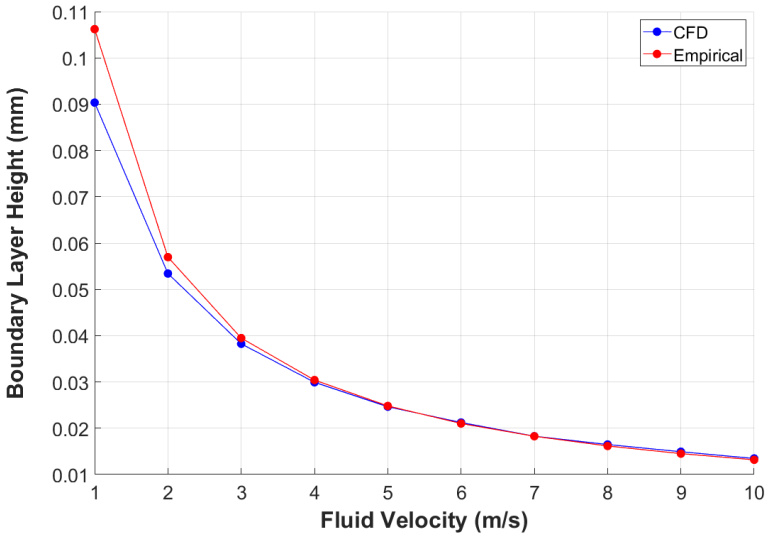

Figure 4-3 – Comparison of boundary layer height as function of fluid velocity in a 0.1 m diameter straight pipe between CFD data and empirical values at 293.15 K.

Strong agreement can be seen between the two approaches, particularly at higher fluid velocities where bulk turbulence is greater. For the purposes of this work, an inlet fluid velocity of 5 m/s is used, with an error of just 0.71% between the empirical and computational solutions for a straight pipe.

Figure 4-4 shows the calculated output of D_T at this velocity from the CFD model compared against the continuous empirical function given by Equation 4.11 for $0.01 < y^+ < 100$.

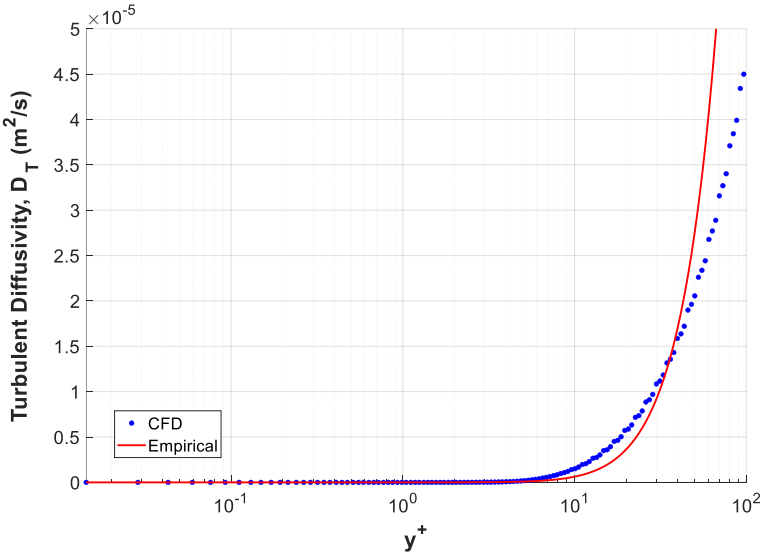

Figure 4-4 – Comparison of empirical and simulated turbulent diffusivity values as a function of wall distance in a 0.1 m diameter straight pipe values at 5 m/s and 293.15 K.

When plotted over a wide range of y^+ values, it can be seen that both the simulated and empirical values follow the same pattern, with the D_T increasingly cubically as a function of y^+. Looking more closely at the boundary layer region on a linear scale, it can be seen that there is very strong agreement between both calculations of D_T within the viscous sublayer:

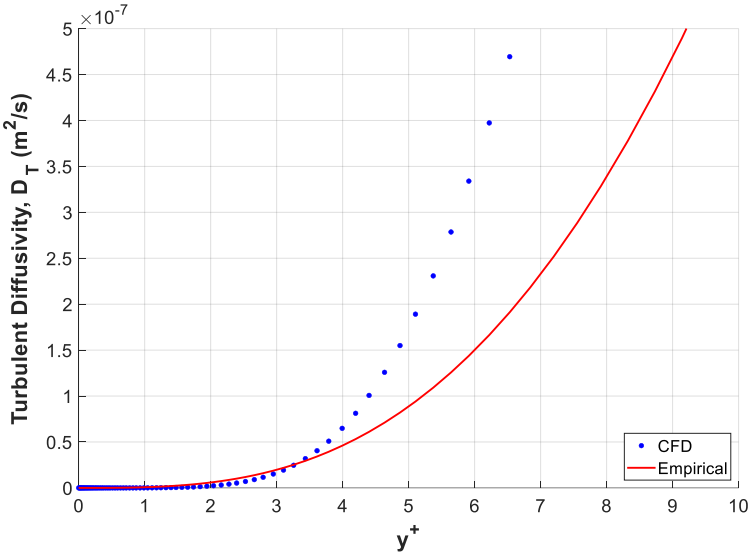

Figure 4-5 – Linearly scaled comparison of empirical and simulated turbulent diffusivity values as a function of wall distance within the viscous sublayer of a 0.1 m diameter straight pipe values at 5 m/s and 293.15 K.

A noticeable increase in the difference between the two values can be observed for $y^+ > 5$, which may be due to the transitional nature of the flow at this point. It may be possible to achieve greater agreement between the two by increasing the mesh resolution further from the wall. However, as the corrosion models employed utilise calculated δ values below $y^+ = 5$ in every case, this is not necessary as the deviation away from the wall does not significantly impact the results. The methodology proposed here can therefore be considered valid for the conditions explored in this work.

4.3 Converging Channel

With the successful validation of the methodology for a well-understood geometry, the approach can now utilise to explore alternative geometries, such as that of a converging channel.

From the conservation of mass principle, it is known that, for an incompressible fluid flowing through a control volume, the mass flow rate is constant (Equation 4.12). Therefore, in the case of a converging channel, as the cross-sectional area decreases the fluid velocity must increase to maintain the mass flow rate (Equation 4.13).

$$\dot{m}_1 = \dot{m}_2 \tag{4.12}$$

$$\rho u_1 A_1 = \rho u_2 A_2 \tag{4.13}$$

Where $\dot{m}$ is the mass flow rate (kg·s^{-1}), ρ is the density of the fluid (kg·m^{-3}), u is the fluid velocity (m·s^{-1}), and A is the cross-sectional area (m^2).

The acceleration of the bulk fluid flow, combined with the variation in the channel geometry, represents a change in the local hydrodynamics, which directly impact the corrosion behaviour. By evaluating the hydrodynamics at various points on a surface, it is possible to model the changes to the chemical and electrochemical responses.

4.3.1 Turbulent Flow Model

As with the straight pipe model, in order to minimise the computational cost, a 2-dimensional representation of the flow geometry has been created here. A 1 m long channel converging from a diameter of 0.1 m to 0.05 m, representing a 50% reduction in the cross-sectional area across the length.

A mapped quadrilateral mesh comprising 35,391 elements was applied with total of 60 boundary layers applied to the surface. A stretching factor of 1.15 was used to ensure a smooth transition between the bulk and a minimum element size of the order 10^{-8} m closest to the surface. By utilising a coarser mesh towards the centre of the channel and much finer mesh near the wall, hydrodynamics behaviour within the boundary layer can be captured without unnecessarily increasing solver times to increase the bulk flow resolution.

A series of vertical cut-lines, distributed evenly at 0.1 m intervals, were added across the length of the channel, as shown in Figure 4-6. These lines represent the locations at which the hydrodynamic profile is to be evaluated and integrated into the corrosion model.

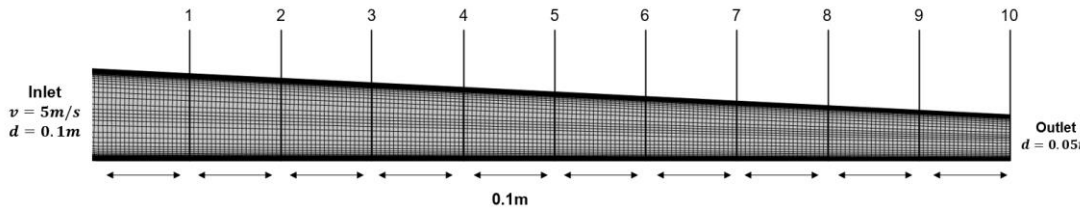

Figure 4-6 – Converging channel geometry diagram showing mesh distribution and position of cut lines.

The same RANS k-ω turbulence model discussed in section 4.2.1.3 was applied to the model, with a no-slip condition being defined at each of the walls.

A straight 0.2 m section was added prior to the converging section in order to allow a fully developed hydrodynamic profile to form prior to form at the inlet (see Figure 4-7). A uniform velocity of 5 ms^{-1} was defined at the start of this straight section.

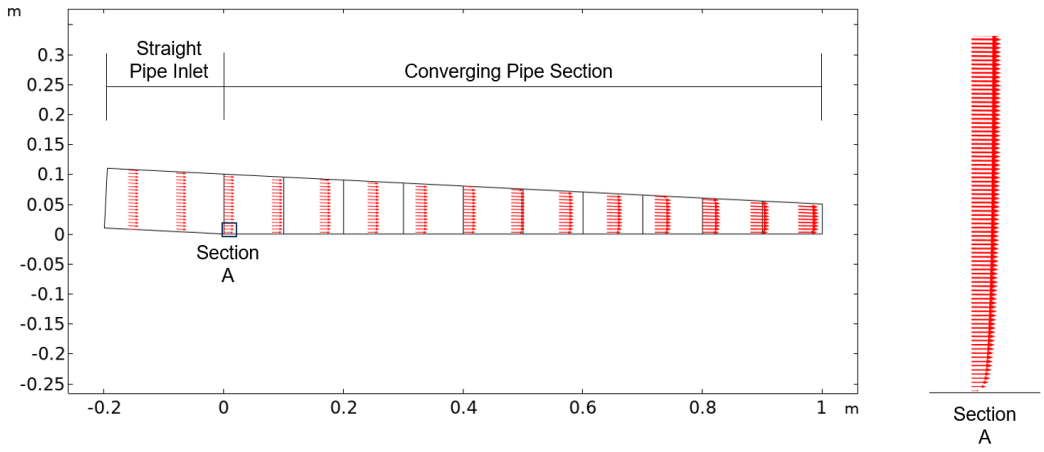

Figure 4-7 – Velocity profile showing additional straight section to ensure fully developed flow profile.

Figure 4-8 shows the resulting velocity profile of the converging section, with the reducing area resulting in an increase from the inlet velocity of 5 $m{\cdot}s^{-1}$ to an outlet velocity of around 10 $m{\cdot}s^{-1}$. The effect of the no-slip condition can also be seen here, with the fluid velocity decreasing in the near-wall region as the inertial forces are reduced.

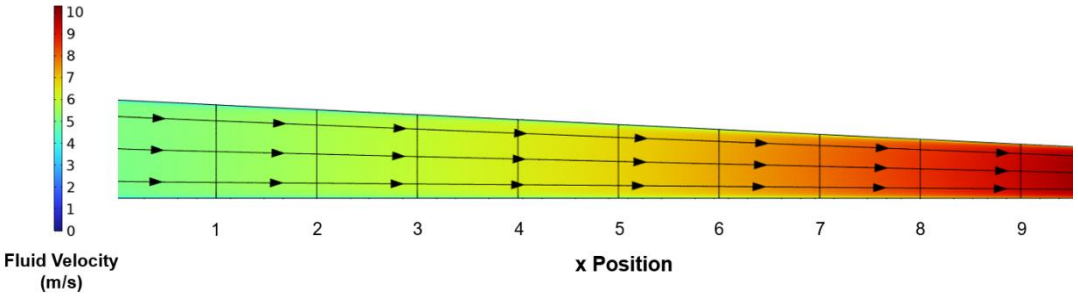

Figure 4-8 – Plot of the fluid velocity against the x-position in the converging channel flow model.

4.3.2 Corrosion Response

At each of the positions indicated by Figure 4-6, the value of δ was once again determined by calculating the point of separation between the values of u^+ and y^+ to a tolerance of 0.01. The corresponding values of D_T were then evaluated at each node point along the respective cut-line from the surface

($y = 0$) up to the end of the boundary layer ($y = \delta$), and a linear interpolation function was fit to the discrete values to generate a continuous function for D_T at each of the 10 positions. The outputs were then one-way coupled to the Kahyarian corrosion model to map the physicochemical response through the channel.

4.3.2.1 Corrosion Rate

Figure 4-9 shows the predicted corrosion rate in mm·yr^{-1} along the surface at each of the 10 positions indicated in Figure 4-6 for a temperature of 293.15 K, 1 bar P_{CO_2}, and pH 5.

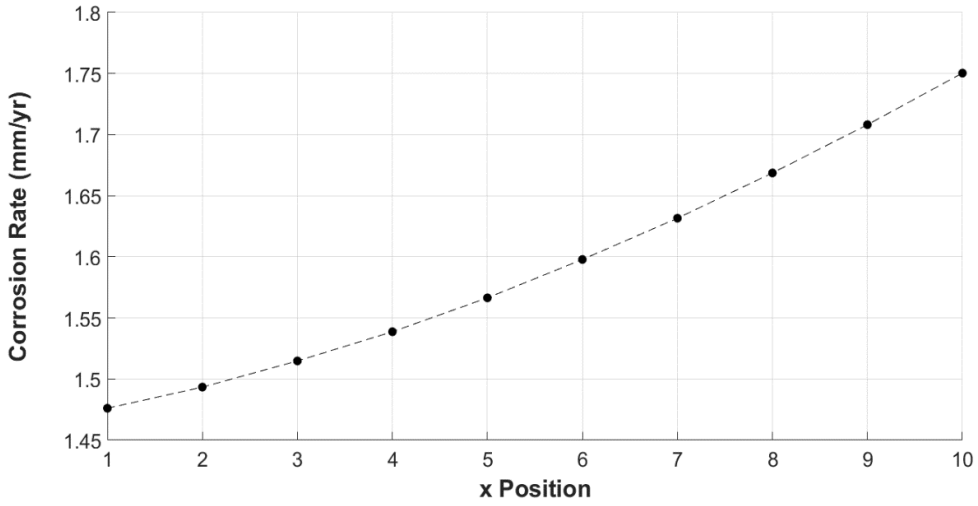

Figure 4-9 - Plot of the corrosion rate as a function of the x-position within the converging channel at 293.15 K, 1 bar P_{CO_2} and pH 5.

Along the length of the converging channel, a strong correlation between the corrosion rate and the area of the channel can be identified. The convergence of the channel produces a corresponding increase in the local corrosion rate as the species transport rates are increased. The relationship between these two values can be quantified by fitting a cubic equation to the output allowing the corrosion rate to be defined as function of the distance along the channel:

$$CR = -0.0251x^3 + 0.197x^2 + 0.116x + 1.462 \quad (4.14)$$

Where CR is the corrosion rate (mm·yr^{-1}) and x is the horizontal distance from the inlet (m).

As the channel converges, the fluid velocity increases to double the inlet velocity resulting in a thinning of the boundary layer and increase in the turbulent diffusivity (Figure 4-10). Within the corrosion model this means steeper concentration gradients between the surface and bulk, accelerating

the rate of molecular diffusion (D_M) alongside the increased turbulent diffusion. Under the conditions being assessed here the system is mass-transport controlled, hence an increase in the rate of species transport through the boundary layer produces a corresponding increase in the electrochemical surface reactions. The effect of this is seen in Figure 4-9, as the convergence of the channel causes an 18.6% increase in the corrosion rate between positions 1 and 10 (Figure 4-6).

(a)

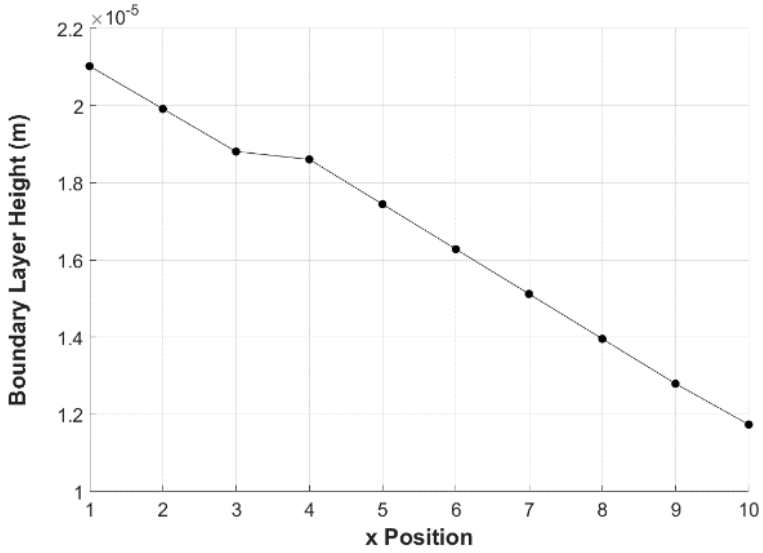

(b)

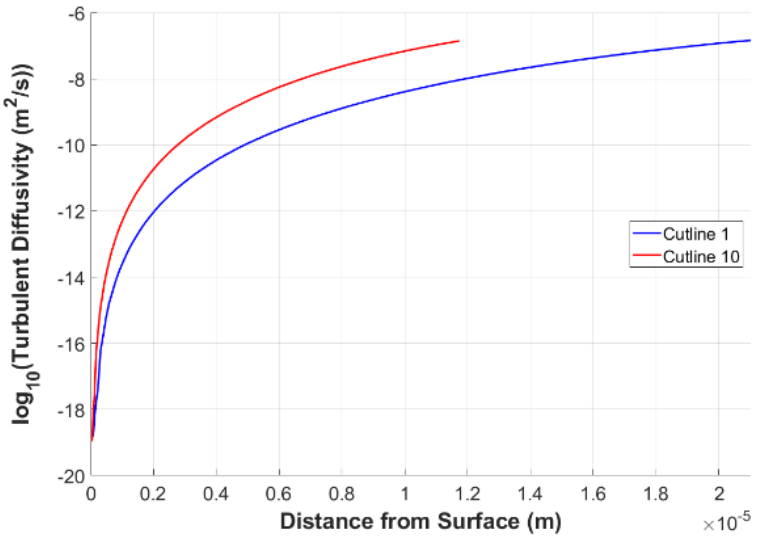

Figure 4-10 - Plots of (a) Boundary layer height at each x-position and (b) Turbulent diffusivity as a function of distance at x-positions 1 and 10.

4.3.2.2 Local Chemistry

The increase in the corrosion rate along the channel observed in Figure 4-9 implies a shift in the production and consumption rates of electroactive species, resulting in changes to the local chemistry. It is possible to investigate how the chemistry is affected by plotting how species deviate from their bulk concentrations along each of the cut-lines. As a continual increase in the corrosion rate is observed across the length of the channel, the two extreme points (positions 1 and 10) have been isolated for evaluation here, shown in Figure 4-11.

(a)

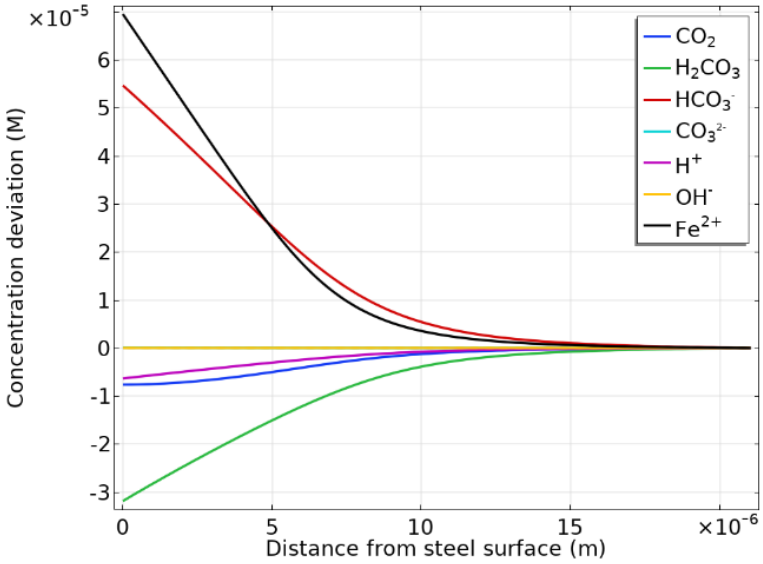

(b)

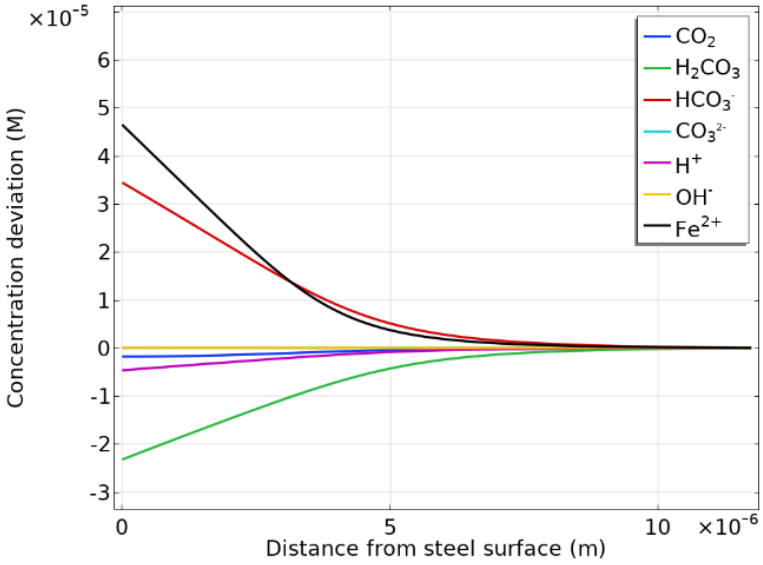

Figure 4-11 – Plot of concentration deviation through the boundary layers for (a) cut line 1 and (b) cut line 10.

Interestingly, despite the higher corrosion rate (and therefore anodic reaction rate) at position 10, the change in concentration through the boundary is actually smaller at the higher velocity. The effect can be most clearly seen in the aqueous iron (Fe^{2+}) concentration, as the release of Fe^{2+} from the surface is directly correlated with the rate of corrosion. Despite the greater rate of production at the surface, the increased rate of mass-transport away due to hydrodynamic effects means a lower build-up of ions on the surface itself. This effect is not solely limited to Fe^{2+} however, as all electroactive species see a proportional decrease in their concentration deviation. Species with reduced concentrations, such as H_2CO_3 and H^+ are more readily replenished, and species with increased concentrations, such as HCO_3^- are more rapidly transported into the bulk. This can be an important factor to consider in other areas of modelling research, such as the growth of $FeCO_3$ films, which are dependent on the surface concentration of species. A higher corrosion rate may imply a greater change in the local concentration, however if this is as a result hydrodynamic effects, Figure 4-11 indicates that the opposite may be true.

A slight difference can also be noted in the behaviour of the aqueous CO_2 concentration across the two positions. When the rate of mass-transport is higher, there is a greater proportional reduction in the concentration than the other species. It is likely that this is due to the rate of the CO_2 hydration reaction being significantly slower than the subsequent dissociation reactions. As such, the rate of supply becomes very close to the rate at which it is being converted to H_2CO_3, reducing the deviation between the bulk and the surface as the channel converges.

4.4 Rotating Cylinder Electrode

The rotating cylinder electrode (RCE) is an experimental set-up that is commonly used in corrosion research to study the effect of turbulence[145]. A cylindrical electrode is connected to an electrochemical set-up in order to measure the corrosion rate. Mass-transfer correlations, such as the one proposed by Eisenberg *et al*.[130] are then often used to map the hydrodynamic characteristics to an equivalent straight pipe. However, in doing so, the complexities of the flow are greatly simplified to be represented by a single mass-transport term.

In order to further demonstrate the applicability of the methodology proposed within this chapter, a series of corrosion tests have been conducted utilising

an RCE set-up. A model of an RCE has then been created within COMSOL and, as with the straight pipe and converging channel examples, the hydrodynamic properties of the boundary layer have been extracted and imported into a corrosion model. By combining experimental and simulated data for an identical hydrodynamic scenario, the accuracy of each corrosion model can be assessed. Modelling the complete RCE cell, as opposed to deriving an equivalent straight pipe scenario, ensures that all flow effects are accurately accounted for.

4.4.1 Experimental Testing

The RCE is a well-established experimental technique that has been studied extensively over the years[130, 145-148] and is a useful tool in corrosion research. By rapidly rotating a cylindrical electrode within a beaker, turbulent flow conditions can be simulated on a small scale under laboratory conditions. This allows for the conditions within the set-up to be carefully controlled and for electrochemical measurements of the corrosion rate to be taken.

For this work, a simple 3-electrode cell was set-up using an RCE to take corrosion rate measurements using the linear polarisation resistance (LPR) technique. Tests were conducted at temperatures of 298.15 K (25 °C) and 313.15 K (40 °C), bulk solution pHs of 4, 5, and 6, and at rotation rates ranging from 500 rpm to 2500 rpm. The experimental data is then compared to simulated data generated by combining a CFD model of an RCE with the previously developed corrosion models.

4.4.1.1 Equipment Set-Up

4.4.1.1.1 Equipment List

Table 4.3 below provides a complete list of all equipment used in the following experimental section. All quantities listed relate to the amount required to conduct a singular experiment with one RCE set-up.

Table 4.3 - List of all equipment used in the collection of experimental RCE corrosion rate and polarisation data.

Equipment	Quantity	Equipment	Quantity	Consumable	Quantity
RCE Motor	1	Hot Plate	1	Isopropyl-alcohol	~ 25 ml
1 L Glass Beaker	1	Weighing Scale	1	De-ionised Water (Testing)	1 L
X65 Carbon Steel Sample	1	AC Potentiostat	1	De-ionised Water (Cleaning)	100 ml
CO_2 Supply Line	1	PTFE Beaker Lid	1	NaCl	10 g
pH Probe	1	50 mm Magnetic Stirrer	1	$NaHCO_3$	0.01 – 2.1 g
Ag/AgCl Counter Electrode	1	Multimeter	1	P240 Grit Paper	1 sheet
Pt Reference Electrode	1	Spring Clamp	2	P600 Grit Paper	1 sheet
25 mm M6 Threaded Rod	1	M6 Hex Nuts	2	P800 Grit Paper	1 sheet

4.4.1.1.2 Rotating Cylinder Electrode Set-Up

X65 carbon steel was selected as the test material for the RCE experiments. A common material used in a range of corrosion tests throughout literature, X65 steel is representative of the carbon steel used in many pipeline systems. Small, cylindrical samples measuring 12 mm in diameter and 10 mm in height were fitted onto a vertically mounted stainless-steel shaft connected to a motor. A 12 mm diameter casing made from polytetrafluoroethylene (PTFE) was fixed to the shaft either side of the sample to ensure only the outer sample surface made contact with the test solution. The contact between the internal surface of the X65 sample and the stainless-steel shaft enabled electrical contact with the sample. This was verified using a multimeter to check for a

stable resistance of < 0.1Ω between the external surface of the sample and the RCE shaft.

The X65 sample functioned as the working electrode and a combined Mettler Toledo ORP Ag/AgCl reference electrode and platinum counter electrode were used to complete the 3-electrode cell. Each of the electrodes were then connected to an ACM Instruments Gill AC 4-channel potentiostat, which was used to apply a potential difference between the carbon steel sample and the reference electrode.

4.4.1.1.3 Brine Solution

For each static RCE test, a 1 wt.% NaCl brine solution was prepared and saturated with CO_2. A 1 L glass beaker was scrubbed clean with dish soap and water and then rinsed 3 times with deionised (DI) water with a resistivity of > 18.2 MΩ. The beaker was then thoroughly dried with compressed air. A measuring cylinder was used to measure 1 L of DI water which was added to the clean beaker.

Taking the density of water to be approximately 1,000 $kg \cdot m^{-3}$ due to the variation with temperature, 10 g of NaCl is needed to produce a 1 wt.% brine. A mass balance was therefore used to measure 10 g of NaCl which was then added to the beaker containing DI water. A 50 mm magnetic stirrer was cleaned with isopropyl alcohol and placed into the brine.

The beaker containing the brine solution was then placed on a hot plate and covered with a PTFE lid, secured in place with two spring clamps. A CO_2 supply tube was then fed through a small hole in the lid and the gas taps were opened to allow a steady stream of CO_2 to bubble through solution. The stirrer within the hot plate was turned on and set to a rotation rate of 250 rpm and the solution was left for a minimum of 12 hours to ensure it was fully saturated with CO_2.

Once saturated, the solution was adjusted to the required pH via the addition of sodium bicarbonate ($NaHCO_3$). Solution pH values of 4, 5, and 6 were achieved by adding 0.01 g, 0.2 g, and 2.1 g of $NaHCO_3$, respectively. A calibrated Orion™ Triode™ pH probe was used to confirm the pH was correct to a tolerance of ± 0.05.

4.4.1.1.4 Sample Preparation

Before beginning a test, each of the samples were wet-ground to remove any surface imperfections. An M6 threaded rod was fixed vertically into the RCE

motor and the samples were fixed in place between two M6 hex nuts. The motor was set to a rotation rate of 800 rpm and grit paper was then applied to the surface with light pressure. P240, P600, and P800 grit papers were used in sequence to remove progressively smaller surface imperfections, with the sample being clean with isopropyl-alcohol between each stage. The samples were then visually inspected to check for any surface irregularities before being rinsed with DI water. Compressed air was used to fully dry the samples before being place on the weighing scale. The mass of each sample was recorded and then samples were then fixed into the RCE set-up as described in section 4.4.1.1.2.

4.4.1.2 Experimental Methodology and Test Plan

4.4.1.2.1 Testing Matrix

For the purposes of experimentally validating the corrosion models discussed in previous chapters, a testing matrix was designed to capture a range of conditions. The parameters varied through testing were the temperature, the solution pH, and the RCE rotation rate. Due to the difficulties associated with high pressure testing, all tests were conducted at atmospheric pressure.

The input conditions used throughout testing are summarised in Table 4.4 below, all combinations of conditions listed in the testing matrix were investigated. For a given temperature and solution pH combination, the rotation rate was initially set to the lowest speed of 500 rpm and then incrementally increased throughout testing. Experiments were run 3 times for each set of conditions to ensure repeatable results and the average of the 3 results was then calculated.

Table 4.4 – Testing matrix for static RCE experiments, conducted at atmospheric pressure in 1 wt.% NaCl brine.

Parameter	Test Values					Units
Temperature	25			40		°C
Solution pH	4		5		6	
Rotation Rate	500	1,000	1,500	2,000	2,500	rpm

At each set of temperature and pH conditions, a secondary RCE test was conducted at a fixed 500 rpm rotation rate. The purpose of this secondary test was to provide mass-loss data to validate the Tafel constants derived from the polarisation of the primary sample (see Section 4.4.1.2.4).

4.4.1.2.2 Methodology

Throughout testing, two RCE set-ups were used simultaneously, a primary sample was used to gather electrochemical measurements, and a secondary sample was used to ensure the corrosion reactions did not significantly change the solution chemistry throughout the test duration. The rotation rate of the primary sample was altered throughout the testing window, whilst the secondary sample remained at a constant 500 rpm. LPR measurements were conducted on both samples.

Prior to each test, the RCE set-up, brine solution, and X65 carbon steel sample were prepared as detailed in section 4.4.1.1. After mounting the sample, the RCE shaft was set to a rotation rate of 250 rpm and cleaned with isopropyl alcohol. The rotation rate was then set to the initial test speed of 500 rpm and lowered into solution before being left for 10 minutes to allow the open circuit potential (OCP) to stabilise.

Once the OCP reached a stable potential, LPR sweeps were set to run at 5-minute intervals scanning at a rate of 0.25 $mV \cdot s^{-1}$ at ± 5 mV from the OCP. The rotation rate remained constant for 1 hour at each speed, resulting in a total of 12 LPR measurements before the rotation rate was increased by 500 rpm. The rate was increased every hour until the maximum rotation rate of 2,500 rpm had been reached. After 1 hour at the maximum speed, the RCE was slowed back down to 500 rpm for 30 minutes to ensure the corrosion rate hadn't changed significantly over the duration of the test.

At this point, the secondary sample was removed from the solution, rinsed with DI water and thoroughly dried with compressed air. The final pH of the solution was re-measured using a calibrated pH probe and recorded to assess changes to the solution chemistry.

The primary sample was left in solution at a rotation rate of 500 rpm in order to perform polarisation scans. The sample was first cathodically polarised to ensure the destructive nature of the anodic polarisation did not interfere with the results. A cathodic sweep was performed between +5 mv and – 400 mV from the OCP at a scan rate of 0.5 $mV \cdot s^{-1}$. The scan data was saved as .txt file and an anodic scan was then conducted between -5 mV and +400 mV from the OCP with the same scan rate. The scan data was saved as a .txt file and the sample was removed from solution, rinsed with DI water, and dried with compressed air.

4.4.1.2.3 Solution Resistance

A potential source of inaccuracy in the calculation of corrosion rates using the method described above is the influence of solution resistance. The LPR measurements calculate the corrosion rate by measuring the electrical resistance between the sample and the counter electrode when a potential difference is applied. However, for charge to be transferred between the two electrodes it must pass through the brine solution, which introduces a secondary source of resistance. For accurate measurement of the charge-transfer resistance (R_{ct}), the solution resistance (R_s) must be deducted from the polarisation resistance (R_p).

$$R_{ct} = R_p - R_s \tag{4.15}$$

In order to calculate R_s, a second electrochemical technique known as electrochemical impedance spectroscopy (EIS) is used. EIS is a highly complex technique which functions by applying an AC current to the system and measuring the output sinusoidal response over a range of frequencies[56]. The technique is often used to measure the formation and properties of protective films[57, 58, 149], however the purposes of this work, it was simply used to determine the value for R_S at for each set of conditions.

Two CO_2 saturated pH 4 brine solutions were prepared in accordance with the experimental procedure (see Section 4.4.1.1.3) and a wet-ground X65 sample was fixed in place within both. The combined counter/reference electrodes were placed in solution and the temperature was set to 25 °C in one and 40 °C in the other, with both RCE motors set to a rotation rate of 500 rpm. The sample was the polarised to ±5 mV relative to the OCP over a frequency range of 20 kHz to 0.1 Hz, taking a reading at every 10 points/decade. A Nyquist plot, which compares the imaginary vs real components of the impedance (Z_{Im} and Z_{Re} respectively), was then plotted to determine the solution resistance, equal to real axis value at the high frequency intercept (see Figure 4-12).

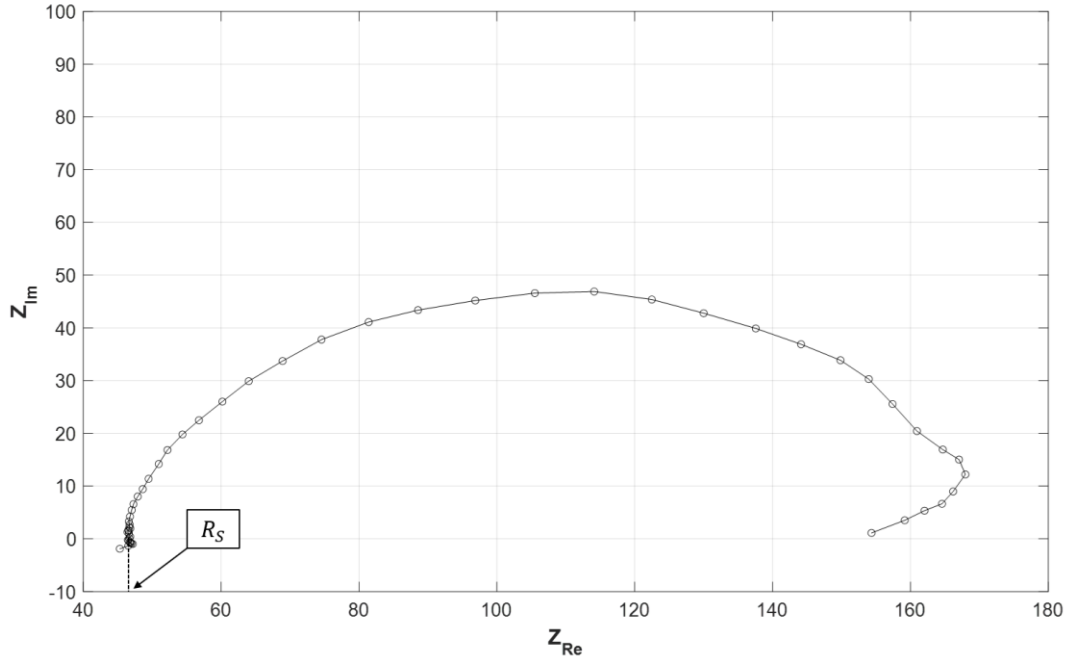

Figure 4-12 – Nyquist plot impedance measurements conducted at pH 4, 25 °C and 500 rpm showing the value of R_S .

Once R_S values had been obtained at pH, 0.19 g of $NaHCO_3$ was added to raise the pH to 5; the pH was confirmed using the pH probe. The process was repeated to collected R_S values for pH 5, before an additional 1.9 g of $NaHCO_3$ was added to raise the pH to 6, which was once again confirmed using the pH probe. A final set of R_S measurements were then collected at pH 6. Table 4.5 summarises all values for R_S measured using this method. These values were then used to determine the value of R_{CT} for all LPR measurements using Equation 4.15.

Table 4.5 – Measured solution resistances for brine solutions at pH 4, 5, and 6 at temperatures of 25 °C and 40 °C.

Temperature (°C)	pH	R_S (Ω·cm^{-2})
25	4	46.7
	5	46.2
	6	44.5
40	4	37.9
	5	37.8
	6	35.2

4.4.1.2.4 Tafel Constants

At the end of each experiment, polarisation scans were performed, the outputs of which can be used to determine the Tafel constants associated with the specific conditions. For each applied voltage in the scan, a current density value was measured. These values were then exported into Microsoft Excel and common logarithm of the absolute value of the current density ($\log_{10}|i|$) was calculated. The values were then exported into OriginPro in order to use its 'Tafel Extrapolation' function. This feature within OriginPro allows for the linear sections of the polarisation plot to be manually selected and linearly extrapolated automatically to ensure the anodic and cathodic slopes intersect at the corrosion potential (E_{corr}). Figure 4-13 provides an example of the identification of these slopes at 25 °C, pH 4, showing b_a and b_c values of 59.3 mV/decade and -117.6 mV/decade respectively.

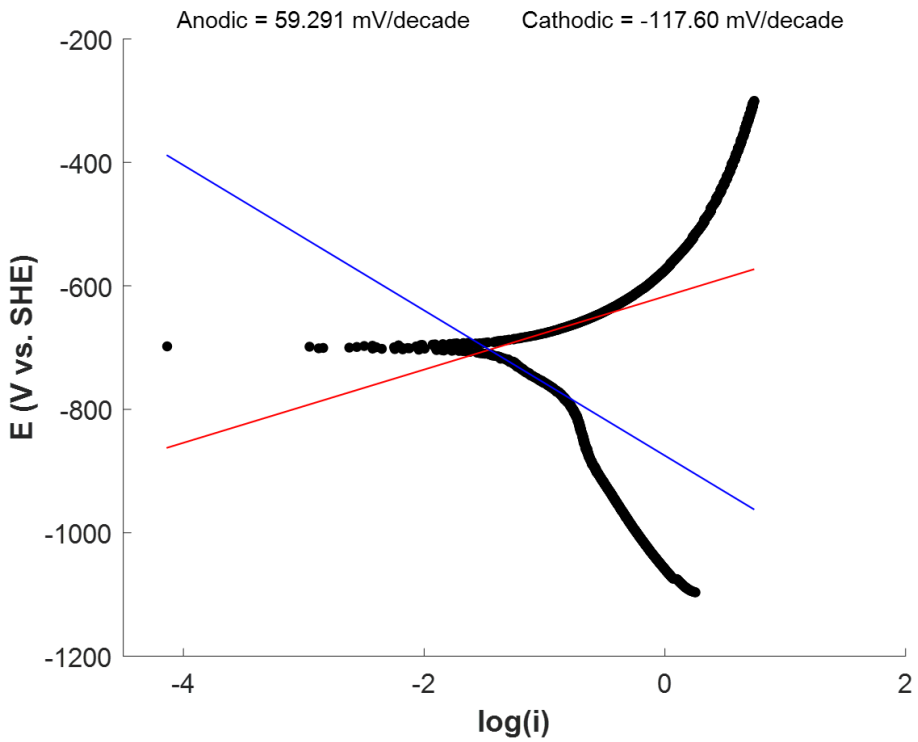

Figure 4-13 – Experimental polarisation scan at 25 °C, pH 6 showing the anodic and cathodic Tafel extrapolation.

Polarisations scans were conducted at the end of each experiment, producing 3 Tafel constants for each set of conditions, these values are summarised in Table 4.6. One set of values at 40 °C, pH 5 have not been included due to data loss during the experiment.

Table 4.6 – Summary of experimentally determined anodic and cathodic Tafel values

Temperature	pH	b_a (mV/decade)	b_c (mV/decade)
25	4	61.5	-118.7
		67.3	-108.0
		51.3	-86.0
25	5	58.8	-162.2
		54.9	-173.8
		52.7	-153.9
25	6	60.4	-167.2
		61.7	-149.5
		59.3	-117.6
40	4	66.3	-82.5
		60.6	-98.2
		58.6	-77.2
40	5	61.9	-164.3
		56.3	-142.7
		-	-
40	6	62.8	-136.3
		60.6	-125.8
		58.8	-118.0
Average		59.6	-128.3
Standard Deviation (σ)		4.1	30.2

For the anodic Tafel slope, the data provided in Table 4.6 shows strong agreement across all tests indicating a b_a value of 60 mV/decade, with some small deviation which can be reasonably attributed to degree of subjectivity included in identifying the location of the Tafel slopes.

The cathodic Tafel slopes however have much greater deviation in their measurement, with a σ value over seven times that of the anodic slopes. Even when test conditions are unchanged, large variations can be seen. For example, at 25 °C, pH 6, the measured b_c changes by as much as 50 mV/decade. This indicates that the variation is not due to changing conditions, but in the determination of the value. As the anodic and cathodic slopes were calculated during the same experiments, it is unlikely that the differences are due to inaccuracies in the measurement. It can however be attributed to the

very short linear section of the cathodic polarisation scans making it difficult to accurately locate the Tafel slope (see Figure 4-13). Averaging the data across all test conditions however produces a b_c of -128 mV/decade, which aligns with the value of -120 mV/decade commonly quoted in literature[3, 4, 30, 32].

Tafel values of 60 mV/decade and -120 mV/decade for b_a and b_c respectively have therefore been used in the following section when calculating corrosion rates.

4.4.1.2.5 Data Processing

The experimental testing to this point has produced data relating to the charge-transfer resistance and the associated anodic and cathodic Tafel constants (b_a and b_c respectively). Converting these values into an experimental corrosion rate for the RCE samples requires several data processing steps.

Firstly, the R_{CT} values must be converted into corrosion current densities (i_{corr}) via the Stern-Geary equation:

$$i_{corr} = \frac{1}{2.303 \cdot R_{ct} \cdot \left(\frac{1}{b_a} + \frac{1}{|b_c|}\right)} \tag{4.16}$$

The full derivation of the Stern-Geary equation as well as subsequent equations in this section can be found in section 1.4 of Chapter 1 of this thesis.

As the Tafel constants are given in mV/decade, the i_{corr} values calculated via Equation 4.16 have units of mA/cm^2. These values are therefore converted into A/cm^2 by divided by 1,000.

Faraday's Law can then be used to convert i_{corr} into a total mass loss:

$$W = \frac{I_{corr} \cdot t \cdot M_w}{n \cdot F} = \frac{i_{corr} \cdot A \cdot t \cdot M_w}{n \cdot F} \tag{4.17}$$

Where W is the mass loss of the corroding metal (g), I_{corr} is the corrosion current (A), A is the area of the corroding surface (cm^2), t is the time (s), M_w is the molecular weight of the corroding metal (g·mol^{-1}), n is the number of electrons involved, and F is the Faraday constant (96,485 C·mol^{-1}).

The mass loss of the sample can then be converted into a corrosion rate in m·s^{-1} via the following equation:

$$CR = \frac{W}{100 \cdot \rho_s \cdot A \cdot t} \tag{4.18}$$

Where ρ_s is the density of steel (g/cm^3).

Finally, the corrosion rate can be converted from $m \cdot s^{-1}$ to the more standard units of $mm \cdot yr^{-1}$:

$$CR\ (\mathrm{mm} \cdot \mathrm{yr}^{-1}) = CR(\mathrm{m} \cdot \mathrm{s}^{-1}) \times 1000 \times 365.25 \times 24 \times 60 \times 60 \qquad (4.19)$$

The material properties used in Equations 4.17 and 4.18 are representative of the X65 carbon steel used for the RCE samples. These properties are summarised in Table 4.7 below.

Table 4.7 – Summary of material properties of X65 carbon steel samples used in the calculation of the corrosion rate.

Material Property	Symbol	Value
Molar Mass	M	55.845 $g \cdot mol^{-1}$
Density	ρ_s	7.85 $g \cdot cm^3$
Surface Area	A	3.77 cm^2

4.4.1.3 Experimental Results

Across the duration of each experiment, a total of 12 LPR corrosion measurements were taken at each RCE rotation rate. Each experiment was then repeated twice more to give a total of 36 R_P measurements for every parameter combination. These R_P values were then converted into corrosion rates via the Equations 4.15-4.19. The mean value of these corrosion rates was then calculated, and these final average values are provided in Table 4.8.

Table 4.8 – Average corrosion rates derived experimentally from LPR measurements for all combinations of temperature, pH, and RCE rotation rate included in the text matrix.

		Corrosion Rate (mm/yr)		
Temperature (°C)	**Rotation Rate (rpm)**	**pH 4**	**pH 5**	**pH 6**
25	500	1.55	0.88	0.79
	1,000	1.68	0.91	0.76
	1,500	1.83	0.95	0.85
	2,000	1.95	0.96	1.06
	2,500	2.09	1.13	1.23
40	500	2.49	1.60	1.24
	1,000	2.78	1.64	1.32
	1,500	3.01	1.83	1.39
	2,000	3.20	1.94	1.47
	2,500	3.28	2.02	1.60

4.4.2 RCE Simulation

Following the collection of the experimental data, the next stage is to build a simulated version of the RCE set-up. By recreating the RCE geometry within COMSOL and introducing a turbulence model to predict the flow field at various rotation rates, it is possible to numerically derive the hydrodynamic parameters associated with experimental cell. The hydrodynamics can then be integrated into the previously built corrosion models in order to evaluate the predicted corrosion rates specific to the RCE geometry. This allows for a direct and fair comparison between the mechanistic CO_2 corrosion models and real-world empirical data.

4.4.2.1 Geometry and Discretization

4.4.2.1.1 RCE Geometry

The first stage in building a simulated representation of the experimental set-up is the construction of the geometry. As the RCE experiment is a cylindrical shaft rotating within a cylindrical beaker, it is possible to represent the

geometry as a 2-dimensional axis-symmetric model. The geometry used here is shown in Figure 4-14, representative of a 12 mm diameter RCE shaft rotating in a 1 L glass beaker containing a 30 mm stirrer. All measurements have been taken directly from the experimental set-up used to measure the corrosion rates provided in Table 4.8.

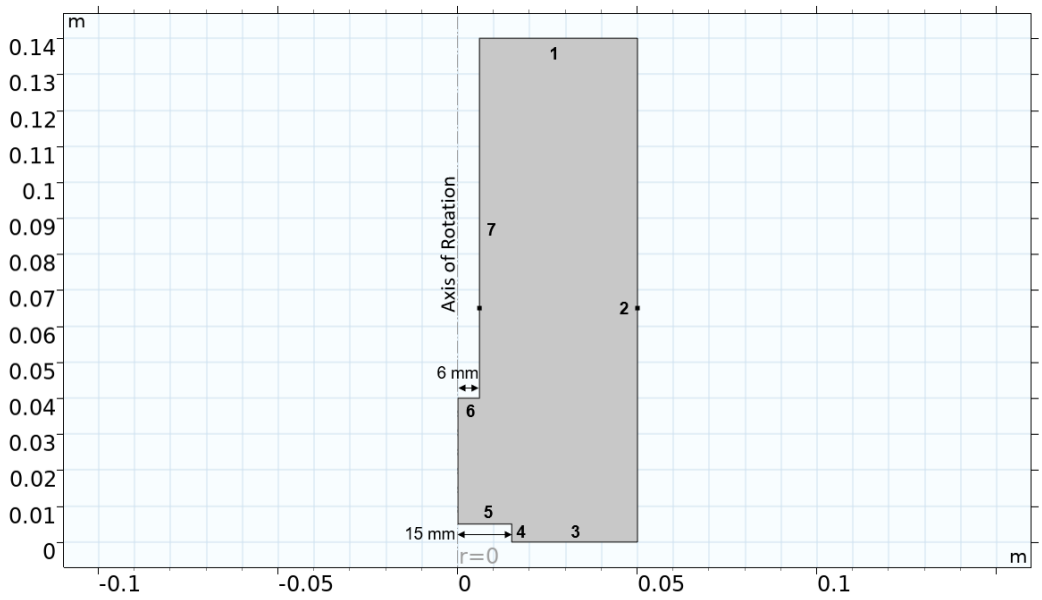

Figure 4-14 - 2D axis-symmetric geometry representing a RCE shaft and stirrer within a 1 L beaker.

4.4.2.1.2 Boundary Conditions

As indicated in Figure 4-14, a vertical axis of rotation was specified within the model at a radius of 0 m. Static walls were assigned with a no-slip condition to boundaries 1, 2, and 3 to represent the base, internal wall, and lid of the beaker respectively. Boundaries 4-7 were defined as moving walls, with zero translational velocity, but with a φ component defining rotational velocity ($v_{w,\varphi}$), calculated via Equation 4.20.

$$v_{w,\varphi} = r\omega_s \tag{4.20}$$

Where r is the radial position (m) and ω_s is the rotational speed (s^{-1}).

The boundaries representing (4 and 5) the stirrer were set to a fixed rotational speed of 250 rpm (4.17 s^{-1}) and the boundaries representing the RCE shaft (6 and 7) were set to speeds varying between 500 rpm (8.33 s^{-1}) and 2500 rpm (33.33 s^{-1}).

A pressure of 0 Pa was specified in the top-right corner of the model (at the intersection between boundaries 1 and 2) to constrain the pressure within the

model. This is representative of the experimental scenario with the surface of the brine solution being exposed to atmospheric pressure.

4.4.2.1.3 Meshing Parameters

When defining a mesh for the RCE model, it is important to consider the length scales of the hydrodynamic boundary layer used in the corrosion models. The element size used within the corrosion models is of the order 10^{-7} m, with the total domain spanning an order of 10^{-5} m. With this in mind, a series of boundary layers were defined along the surface of the rotating shaft with a first layer height specified at 1×10^{-7} m. However, with the total area of the model being 6.33×10^{-3} m^2, utilising such small elements across the entire domain would result in very long solver times and may even result in convergence issues for the less turbulent regions of the model.

As the flow effects within the bulk do not significantly influence the corrosion behaviour within the boundary layer, it is sufficient to apply a coarse mesh to this region. By using a refined mesh close to the surface and a coarse mesh in the bulk, it is possible to accurately resolve the steep near-wall velocity gradients without a large increase in computational cost.

However, a drastic change between two mesh resolutions can lead to poor quality elements and therefore convergence issues with the solver. To prevent this, a stretching factor of 1.1 was then applied with a total of 75 boundary layers to ensure a smooth transition between the surface and the bulk mesh. The number of boundary layers used results a total boundary layer size of 1.27×10^{-4} m, significantly above the 10^{-5} m domain size expected for the corrosion models.

COMSOL's pre-defined coarse, free triangular mesh was then applied to the remaining geometry, with elements ranging in size from 1.5×10^{-4} m to a maximum of 3.35×10^{-3} m. When combined with the defined boundary layers, this generated a mesh comprised of a total of 3,926 elements, shown in Figure 4-15.

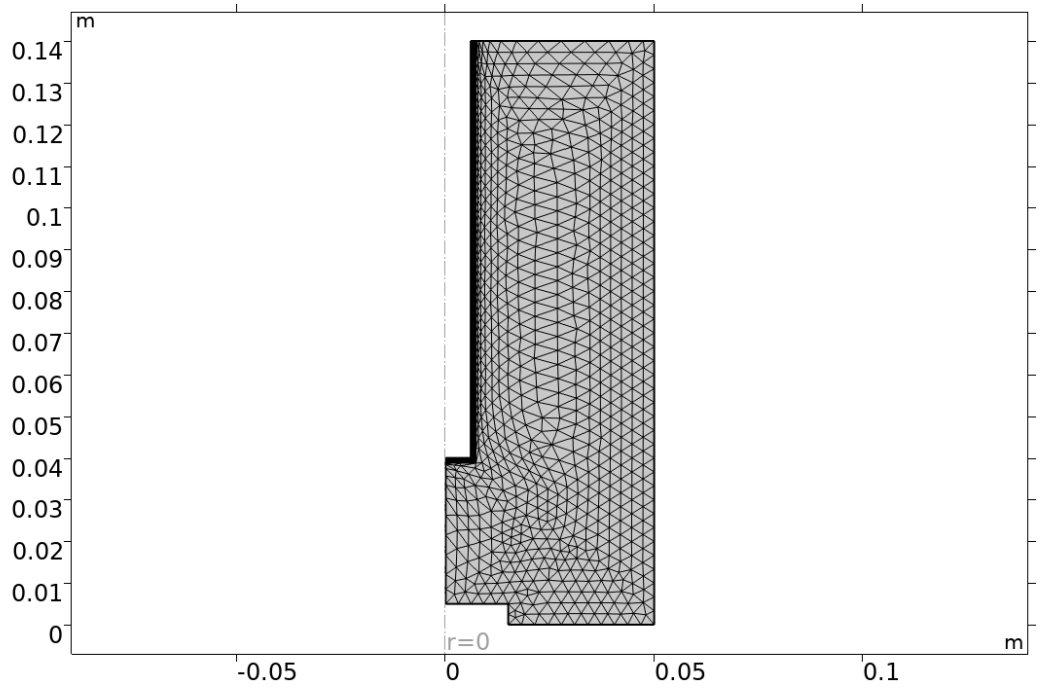

Figure 4-15 – RCE geometry showing free triangular mesh with boundary layer refinement close to the surface of the rotating shaft.

4.4.2.2 Flow Parameters

4.4.2.2.1 Cut-Line Evaluation

As was the case for both the straight pipe and converging channel flows examined thus far, the hydrodynamic parameters needed to model the corrosion behaviour must be evaluated along a straight line perpendicular to the corroding surface. For the case of an RCE, in which the flow behaviour is axisymmetric, the orientation of this line in the x-y plane does not affect the output. It is possible however, that slight differences may be observed based on the vertical position (z-coordinate) of the line due to the flow features at the base of the rotating shaft. These flow features are not expected to have a significant impact on the results, however, to minimise the potential for error, the hydrodynamics in each instance were evaluated at coordinates representing the centre of an RCE sample in an experimental set-up.

A cut-line was defined between the surface of the rotating shaft and the boundary of the cell, defined by end-point coordinates in m of (0.006,0, 0.065) to (1, 0, 0.065).

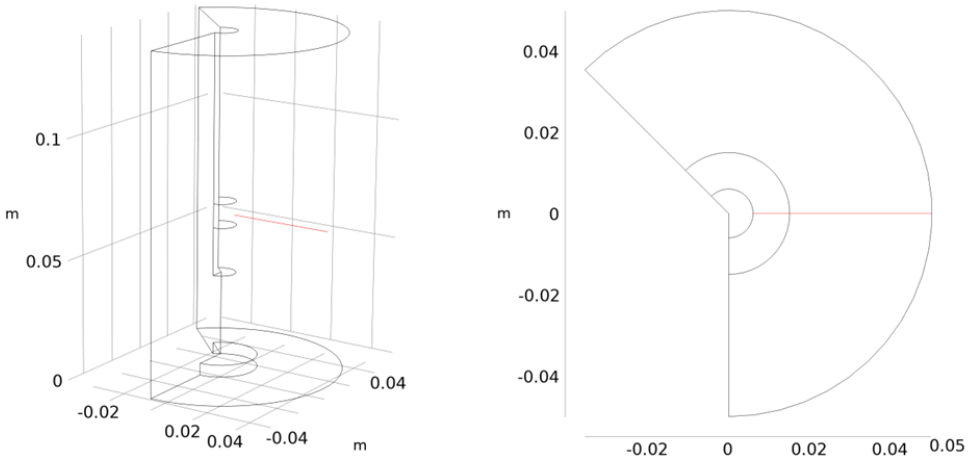

Figure 4-16 – 3-dimensional representation of the RCE geometry showing a cut-line out from the surface to be used for evaluation of hydrodynamic parameters.

4.4.2.2.2 Changes to δ Derivation

The RCE example presents a new challenge not present in the pipe flow examples in the calculation of the hydrodynamic boundary layer height in that the wall is not static. The no-slip boundary condition is still applied, meaning that the relative velocity of the fluid adjacent to the wall is still zero, however the movement of the wall means that the absolute value of the fluid is a non-zero value. As such, the dimensionless velocity u^+ does not converge to zero, meaning the standard law of the wall method of deriving δ cannot be used. However, the due to the nature of laminar flow, u^+ and y^+ still increase proportionally within the viscous sublayer. Therefore, by plotting these values on a log-log plot, it is possible to use the gradients of the lines to identify the end of the boundary layer. As seen in Figure 4-17, δ can be identified as the point which the gradient of the line deviates from that of the line $u^+ = y^+$, using a tolerance of 10%.

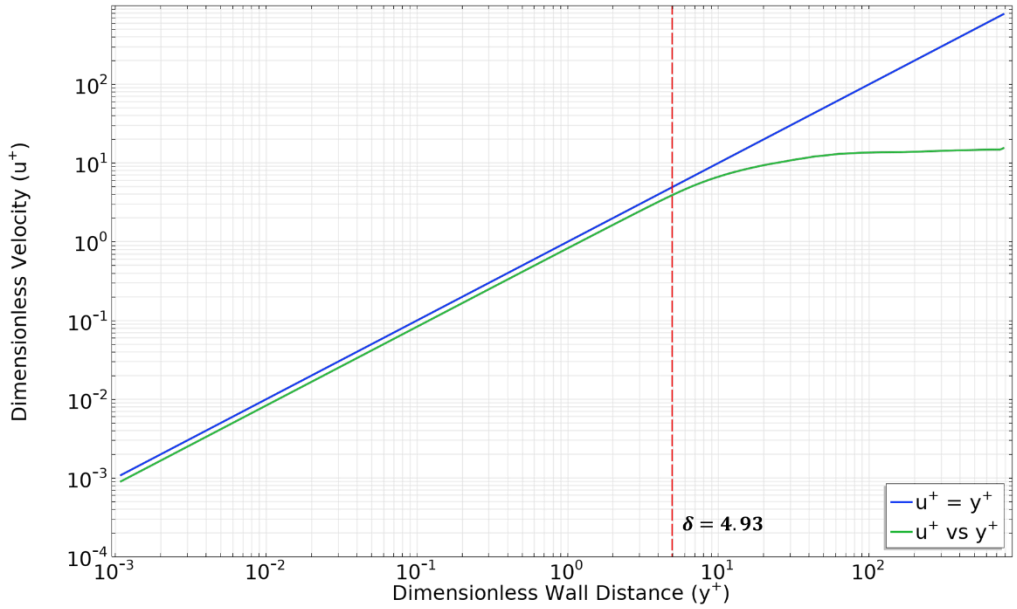

Figure 4-17 - Logarithmic plot of u^+ against y^+ showing the derivation of δ via the change in gradient for a temperature of 25 °C and a rotation rate of 2,500 rpm.

The value of δ obtained from the u^+ vs y^+ plot represents the distance between the surface and the end of the boundary layer in dimensionless units. In order to convert this into m, Equation 4.7 must be rearranged to calculate the value of y at this point:

$$y = y^+ \cdot \frac{\nu}{u_\tau} \tag{4.21}$$

4.4.2.2.3 Turbulent Diffusivity

The magnitude of turbulent diffusion is evaluated by calculating D_T each node point along cut-line via Equation 4.8. As the corrosion models only consider species transport within the boundary layer, this data can be truncated to remove any data points after this point ($y > \delta$). The result of this is a series of discrete data points which describe the change in D_T as a function of the distance from the surface. In order to convert this into continuous data, an interpolation function was used within COMSOL. Due to the high number of boundary layers used in this instance, a linear interpolation function was found to be the most appropriate in each case. Figure 4-18 shows the output function for a temperature of 25 °C and a rotation rate of 2,500 rpm where the height of the boundary layer is 2.75×10^{-4} m.

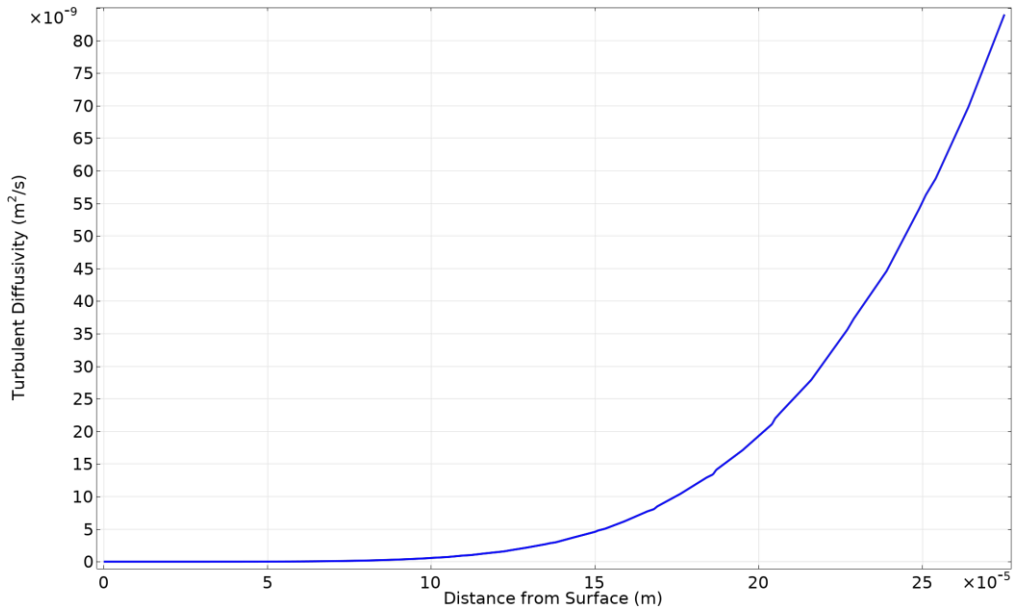

Figure 4-18 – Plot of interpolated D_T function against the distance from the surface for a temperature of 25 °C and rotation rate of 2,500 rpm.

4.4.2.3 Simulation Results

As the geometry is fixed, and the boundary layer is unaffected by the solution pH, the hydrodynamic properties need only to be calculated for each combination of temperature and shaft rotation rates. Table 4.9 shows the δ values calculated via the approach detailed in section 4.4.2.2.2 for rotation rates varying between 500-2500 rpm at a temperatures of 25 °C and 40 °C, in accordance with the testing matrix detailed in section 4.4.1.2.1. For each set of conditions, a corresponding D_T function was calculated as detailed in section 4.4.2.2.3.

Table 4.9 – Summary of calculated δ values for different rotation rates at temperatures of 25 °C and 40 °C.

Temperature (°C)	Rotation Rate (rpm)	Boundary Layer Height (y^+)	Boundary Layer Height (m)
25	500	3.05	6.04×10^{-4}
	1,000	3.93	5.01×10^{-4}
	1,500	4.80	4.16×10^{-4}
	2,000	5.03	3.38×10^{-4}
	2,500	4.93	2.75×10^{-4}
40	500	3.85	6.39×10^{-4}
	1,000	3.85	3.70×10^{-4}
	1,500	4.52	3.07×10^{-4}
	2,000	4.84	2.54×10^{-4}
	2,500	5.02	2.16×10^{-4}

The hydrodynamic parameters, alongside other input parameters (pH, CO_2 partial pressure, and NaCl concentration) were incorporated into the Nordsveen *et al*.[26] and Kahyarian *et al*.[12, 36] corrosion models discussed in Chapters 2 and 3, respectively. Table 4.10 summarises the predicted corrosion rates from each of the models at every condition specified in the testing matrix.

Table 4.10 – Simulated corrosions rates from the Nordsveen and Kahyarian models based on hydrodynamic inputs derived from CFD simulation.

		Corrosion Rate – Nordsveen ($mm \cdot yr^{-1}$)			Corrosion Rate – Kahyarian ($mm \cdot yr^{-1}$)		
Temperature (°C)	**Rotation Rate (rpm)**	**pH 4**	**pH 5**	**pH 6**	**pH 4**	**pH 5**	**pH 6**
25	500	1.07	1.02	1.00	1.43	1.45	1.73
	1,000	1.15	1.06	1.02	1.53	1.45	1.74
	1,500	0.88	1.10	1.03	1.71	1.50	1.74
	2,000	1.01	1.13	1.04	1.88	1.55	1.74
	2,500	1.14	1.14	1.04	2.03	1.58	1.74
40	500	1.61	1.54	1.54	2.64	2.82	5.22
	1,000	1.86	1.68	1.59	2.93	2.78	4.68
	1,500	2.02	1.73	1.61	3.20	2.88	4.55
	2,000	2.17	1.76	1.62	3.44	2.96	4.48
	2,500	2.34	1.79	1.62	3.70	3.02	4.44

Chapter 5 - Discussion

Through the combination of turbulence modelling, corrosion modelling, hydrodynamic theory, and experimental testing, three sets of corrosion data have now been assembled analysing corrosion within an RCE. The summary of the experimental results and the summary of both sets of simulated results are provided at the end of the previous chapter (Table 4.8 and Table 4.10 respectively). In the following chapter, direct comparisons are made between each of these data sets in order to gain insight as to the strengths and weakness of each of the corrosion models.

5.1 Experimental vs Simulated Corrosion Rates

With the large amount of corrosion rate data collected throughout this chapter, it is useful to first collate all of the information into a single comparison plot. Due to the variation of multiple parameters within the data sets, it is difficult to directly compare the outputs as functions of the inputs. However, it is possible to compare the simulated outputs against the actual values derived from the experimental set-up. Figure 5-1 plots each of the Nordsveen and Kahyarian model outputs against the experimental data. For each set of conditions within each model, 5 data points are shown which represent each of the 5 rotation rates specified in Table 4.4. Perfect prediction of the corrosion rates would therefore fall along the line $y = x$, and so this line has also been plotted.

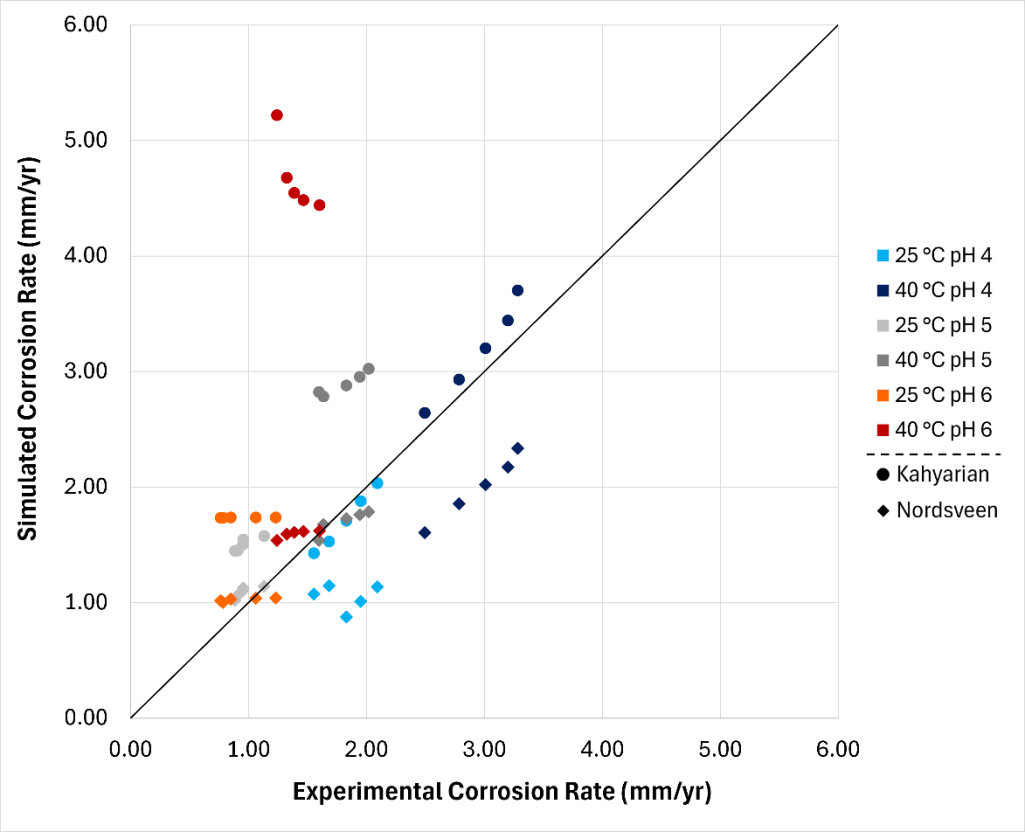

Figure 5-1 – Comparison of simulated and experimental corrosion rates for an RCE in a CO_2-H_2O environment at temperatures 25 °C and 40 °C and pHs of 4, 5, and 6 for rotation rates of 500-2500 rpm. Results from the Nordsveen *et al*.[26] model are indicated by ◆ and results from the Kahyarian *et al*.[12, 36] model are indicated by ●.

From Figure 5-1 some immediate observations can be made about the accuracy of the two corrosion models. In both cases a positive correlation can be seen between the simulated and experimental values, with higher experimental corrosion rates generally being reflected in the corrosion models. The values predicted by the Kahyarian model are higher and have a tendency to overpredict the corrosion rate, as opposed to the lower values of Nordsveen which tend to underpredict.

At lower corrosion rates (<1.5 mm/yr) a strong correlation can be seen between the Nordsveen model's predictions and the measured corrosion rates, with the difference between the two being < 0.2mm/yr in most cases. However, as the conditions become harsher and the corrosion rates increase, the accuracy begins to drop with the model underpredicting the corrosion rate by up to 52%.

The Kahyarian model on the other hand provides reasonably accurate predictions for both low and high corrosion rates, seemingly performing better

in the harsher environments. However, two clusters of data points can be clearly identified in which the model significantly overpredicts the corrosion behaviour (Figure 5-2). The most extreme of these points predicts a corrosion rate more than triple the experimental value.

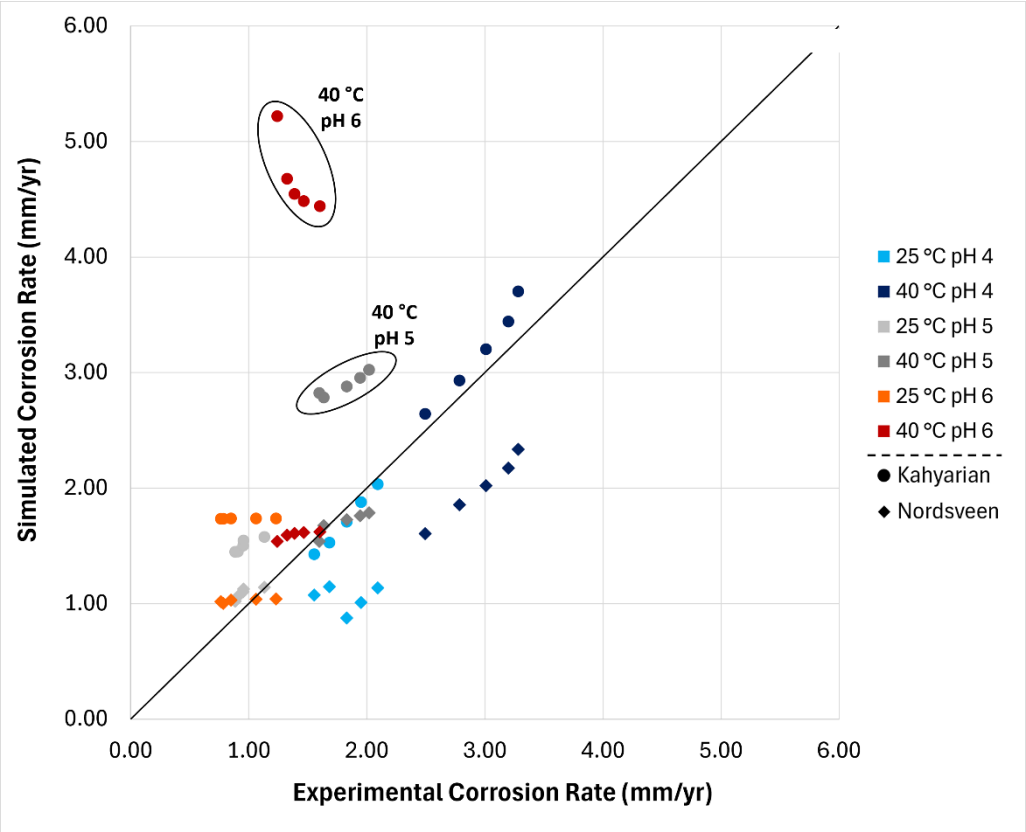

Figure 5-2 – Clusters of overpredicted data points within the Kahyarian model and the associated environmental conditions.

Further investigation reveals that both of these clusters represent individual sets of environmental conditions, with each of the 5 data points within them representing the RCE rotation rates. From this it seems that at 40 °C, the Kahyarian model begins to overpredict at the higher pH values, with the discrepancy becoming larger as the pH increases. The reason for this can be investigated by more closely examining the corrosion model under these conditions.

By replacing the electroneutral surface boundary condition with an applied potential, simulated polarisation curves can be generated for a given set of conditions by performing a parametric sweep of the applied potential. A more complete description of how this is achieved is detailed in Chapter 3 of the thesis. Figure 5-3 shows the polarisation curve generated for the Kahyarian

model at pH 6, 40 °C for a rotation rate of 500 rpm, the conditions for which the model produces the largest overprediction.

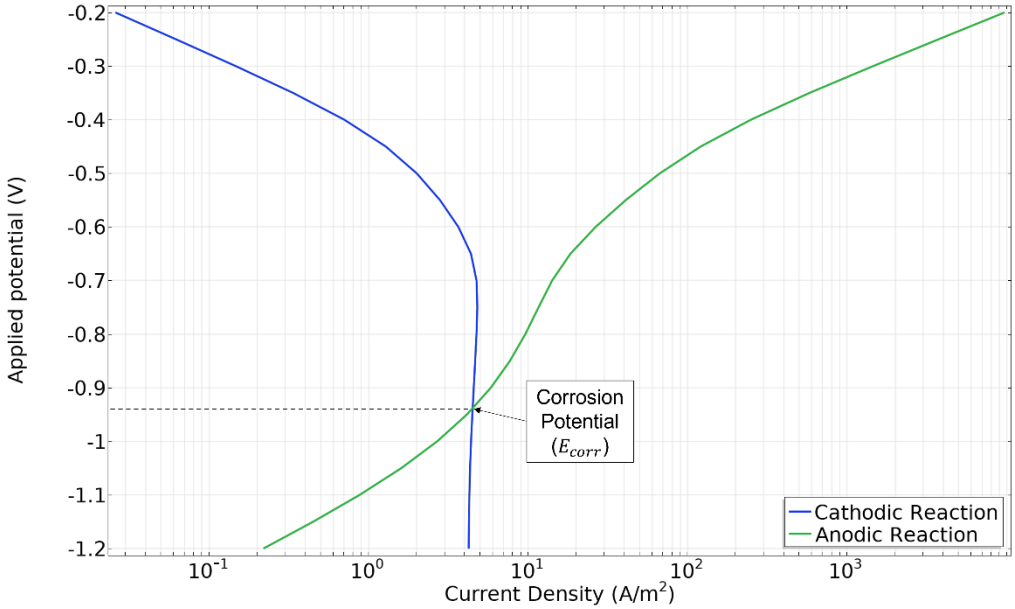

Figure 5-3 - Anodic and cathodic reaction simulated polarisation curves within the Kahyarian corrosion model at 500 rpm, 40 °C, and pH 6.

From the polarisation scan, it becomes evident that the over-prediction of the Kahyarian model is likely to be related to the known issue of the surface potential becoming highly negative in the mass-transport region. It is suspected that the reason for this is related to the method by which H^+ ions are supplied to the surface. At the surface there are two sources of H^+: H_2CO_3 dissociation, and transport from the bulk solution. When the pH is low, there is a large bulk concentration and as such the diffusive contribution is high due to the steep concentration gradient. However, when the pH is high, there is limited supply through diffusion and H_2CO_3 dissociation becomes the primary source of H^+ ions. This can be seen by plotting the rate of the dissociation reaction at the surface as a function of bulk pH, which clearly shows the increase in the rate of dissociation:

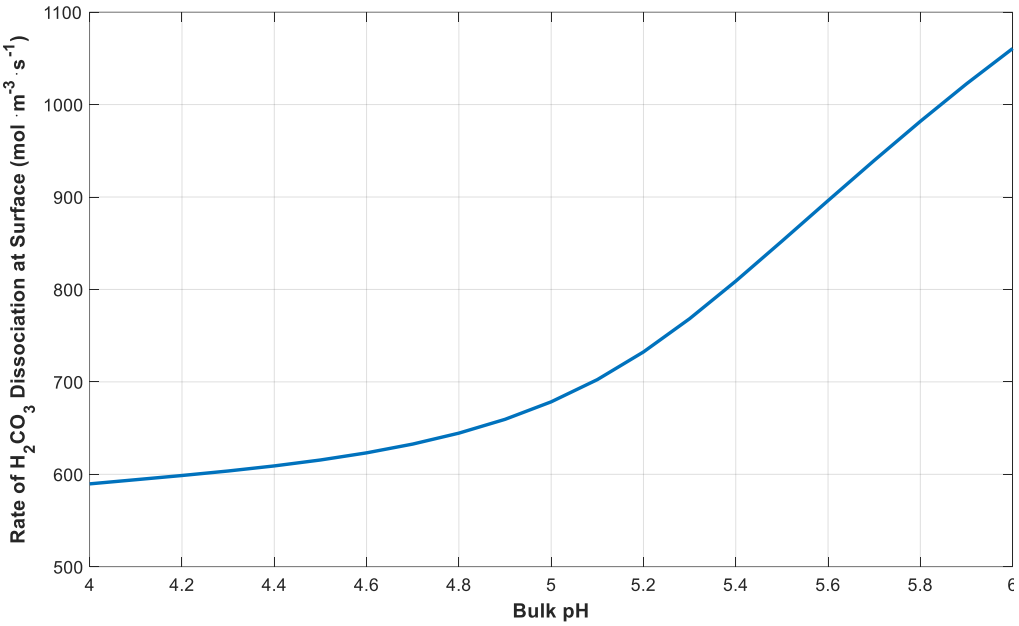

Figure 5-4 - Plot of the rate of H_2CO_3 dissociation at the surface within the Kahyarian model as a function of bulk pH at 500 rpm and 40 °C.

The local drop in the local H_2CO_3 concentration increases the rate of H_2CO_3 diffusion, supplying additional ions to the bulk. It is important to remember that the bulk H_2CO_3 concentration is independent of the pH and so remains constant for a given temperature and partial pressure. This compounded effect of increased H_2CO_3 diffusion and dissociation extends the mass-transport region of the polarisation curve, increasing the corrosion rate.

A by-product of the dissociation reaction being the primary source of H^+ ions under these conditions is a significant influx of HCO_3^- and CO_3^{2-} ions. The large number of cations present produces the very negative corrosion potential seen in Figure 5-3.

The same effect is not observed in the Nordsveen model due to the inclusion of a secondary reduction reaction. When the bulk pH is low, the relatively high concentration of H_2CO_3 results in the direct reduction of H_2CO_3 becoming the dominant reaction. When H_2CO_3 reduces directly, rather than dissociating at the surface, it acts as both a source of electrons for the electrochemical exchange and a source of H^+ ions at the surface. This prevents the surface H^+ concentration from becoming too small, limiting the corrosion rate. This effect can be seen by plotting the ratio of the cathodic currents within the Nordsveen model as a function of bulk pH:

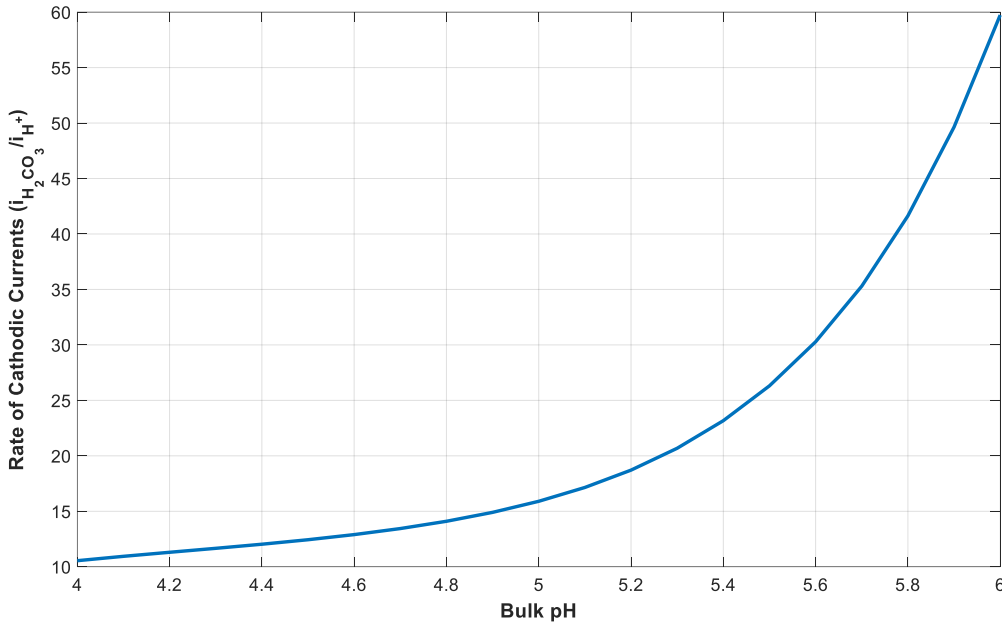

Figure 5-5 - Ratio of cathodic currents within the Nordsveen model as a function of bulk pH at 500 rpm and 40 °C.

5.2 Prediction of Specific Trends

Perhaps the most fundamental benefit of corrosion models is their ability to predict the response to changing conditions. Even if the predicted corrosion rate is not completely accurate, knowing whether or not a change in a certain parameter will increase or decrease the corrosion rate is incredibly useful.

In Figure 5-6 the corrosion rate data from both models, as well as the experimentally determined values are compared for each specific combination of temperature, pH, and RCE rotation rate.

(a)

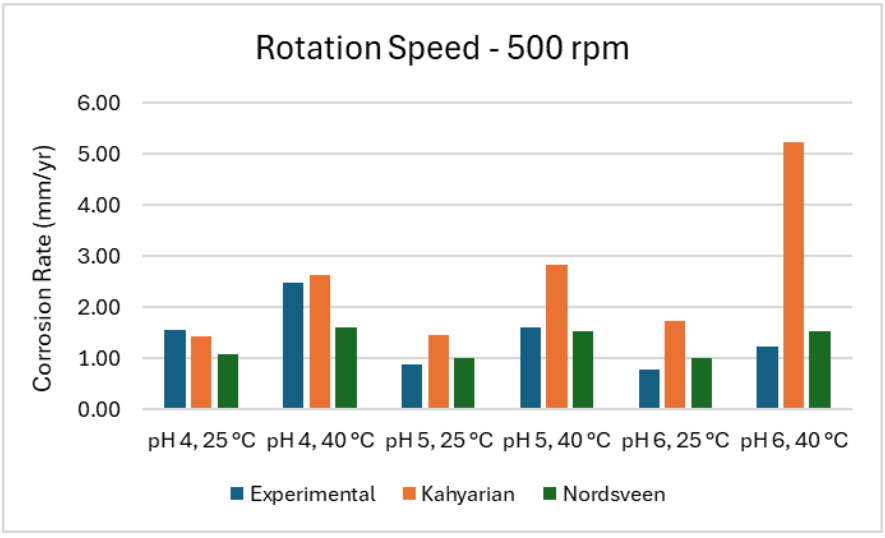
Rotation Speed - 500 rpm
Corrosion Rate (mm/yr)
6.00
5.00
4.00
3.00
2.00
1.00
0.00
pH 4, 25 °C
pH 4, 40 °C
pH 5, 25 °C
pH 5, 40 °C
pH 6, 25 °C
pH 6, 40 °C
Experimental
Kahyarian
Nordsveen

(b)

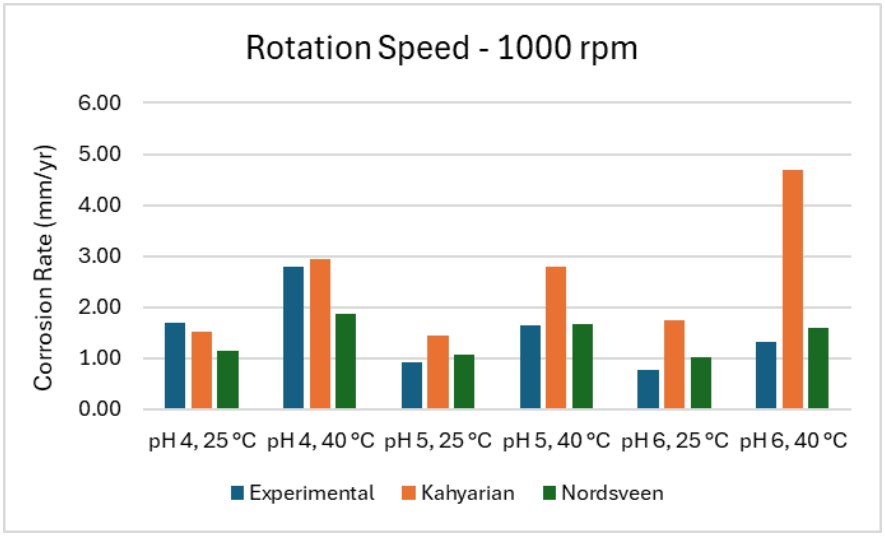
Rotation Speed - 1000 rpm
Corrosion Rate (mm/yr)
6.00
5.00
4.00
3.00
2.00
1.00
0.00
pH 4, 25 °C
pH 4, 40 °C
pH 5, 25 °C
pH 5, 40 °C
pH 6, 25 °C
pH 6, 40 °C
Experimental
Kahyarian
Nordsveen

(c)

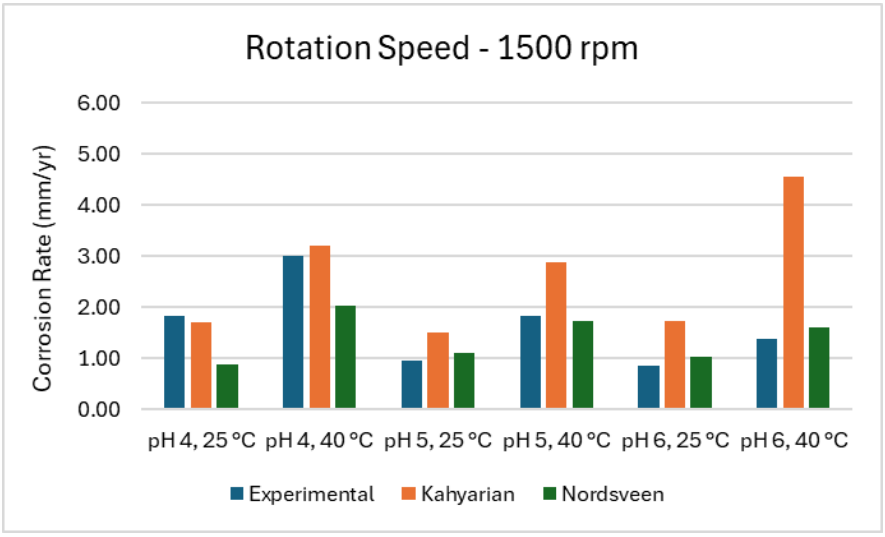
Rotation Speed - 1500 rpm
Corrosion Rate (mm/yr)
6.00
5.00
4.00
3.00
2.00
1.00
0.00
pH 4, 25 °C
pH 4, 40 °C
pH 5, 25 °C
pH 5, 40 °C
pH 6, 25 °C
pH 6, 40 °C
Experimental
Kahyarian
Nordsveen

(d)

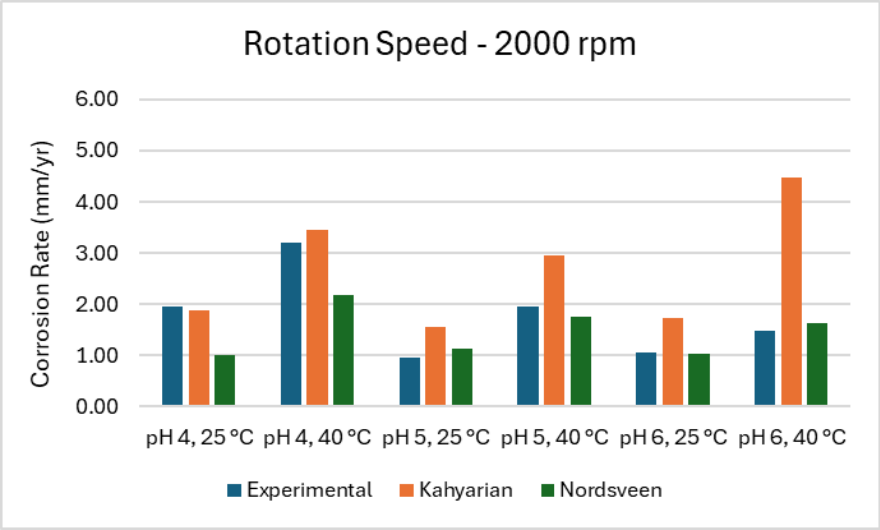

(e)

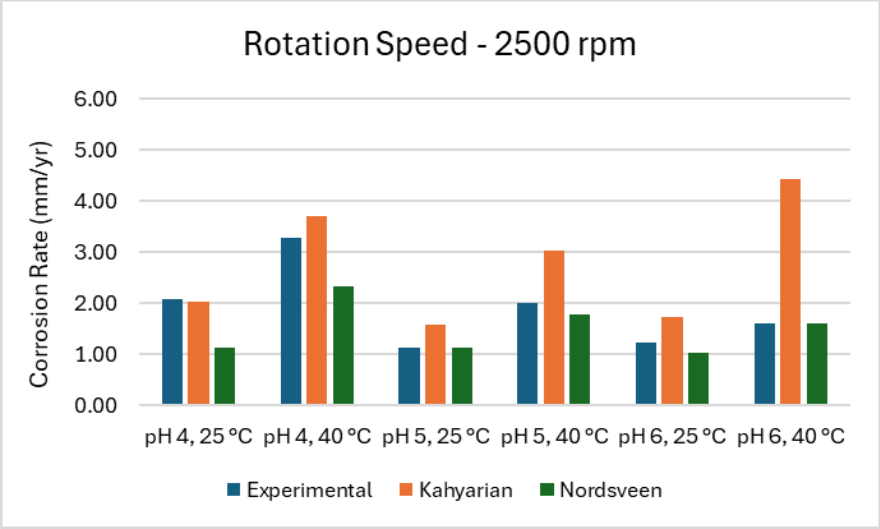

Figure 5-6 – Comparison of numerical models with experimental data for pHs 4, 5, and 6, and temperatures of 25 °C and 40 °C at RCE rotation rates of: (a) 500 rpm (b) 1000 rpm (c) 1500 rpm (d) 2000 rpm (e) 2500 rpm.

From the experimental corrosion rate data provided in Table 4.8 and presented in Figure 5-6, several general trends can be identified based on how the changing conditions influence the corrosion response:

- Increasing temperature increases the corrosion rate and has a greater influence at low pH and high rotation rates.
- Lowering the pH increases the corrosion rate and has a greater influence at high temperatures.

- Increasing rotation rate increases the corrosion rate across all tested conditions.

5.2.1 Prediction of Trends - Kahyarian Model

Looking firstly at the Kahyarian model it can be seen that an increase in temperature correlates with increase the corrosion rate across all conditions. Discounting the previously discussed issue with overprediction, particularly at 40 °C, pH 6, the model captures the experimental temperature dependency reasonably well. However, the relative increase in corrosion rates between 25 °C and 40 °C is greater than in the experimental data for all pH values and rotation rates. This indicated most clearly by the corrosion rate values at pH, where in each case the Kahyarian model slightly underpredicts at 25 °C, but slightly overpredicts at 40 °C. As this occurs at every rotation rate and pH, it is likely that this is not due to species transport within the model, but in the calculation of temperature dependency of the surface reactions. It may be possible to improve the accuracy of the model in this regard by adjusting the α values within the electrochemical reactions.

The corrosion rate change in response to the increase in pH at high temperature produces the biggest discrepancy when compared to the experimental data, however the reason for this has been covered previously in section 5.1, and so will not be discussed further here. However, even when focusing solely on the low temperature conditions, it can be seen that the lowest corrosion rates are seen at pH 5 in the Kahyarian model across all rotation velocities. Interestingly, this is reflected in the corrosion rate data at 2,000 rpm and 2,500 rpm, however as the corrosion rates are so low under these conditions this may be due to the accuracy of the test method. Small changes in the surface finish of the samples or the stability of the LPR measurements may introduce error which becomes more noticeable at low corrosion rates. However, the trend in the Kahyarian model is much more definite, with the corrosion rate consistently increasing at pH 6. This suggests that the previously discussed increase in the dissociation of H_2CO_3 has an impact whenever the Kahyarian model is under mass-transport controlled conditions.

Looking at the effect of increasing the rotation rate, it can be seen that the Kahyarian model captures this well. In general, the corrosion rate increases with the rotation rate, as is seen in the experimental data. However, it can be seen that the transition to the dependence upon the H_2CO_3 dissociation reaction has an effect here too, as turbulent mass-transport becomes less

influential within the model as pH increases. This is shown in Table 5.1, which shows the percentage difference in the corrosion rate between 500 rpm and 2500 rpm calculated as:

$$\text{Percentage Difference} = \frac{CR_{2500} - CR_{500}}{CR_{500}} \quad (5.1)$$

Table 5.1 – Comparison of predicted corrosion rates between 500 rpm and 2,500 rpm for experimental data and the Kahyarian model.

	Percentage Difference in CR between 500-2500 rpm	
Conditions	**Experimental**	**Kahyarian**
pH 4, 25 °C	34.6%	42.4%
pH 4, 40 °C	31.6%	40.1%
pH 5, 25 °C	28.0%	9.0%
pH 5, 40 °C	26.4%	7.1%
pH 6, 25 °C	56.9%	0.2%
pH 6, 40 °C	29.0%	-14.9%

From Table 5.1, it can be seen that the experimental data sees a consistent increase in corrosion rate as a function of rotation rate across all conditions. The Kahyarian model on the other hand sees a gradual reduction in the relative difference as the pH increases, indicating that the importance of mass-transport is not being accurately accounted for at higher pHs.

5.2.2 Prediction of Trends – Nordsveen Model

As previously discussed, the Nordsveen model tends to underpredict the corrosion rate when the conditions are more aggressive. However, looking past that, it does capture the change in the corrosion rate with respect to temperature with a high degree of accuracy. An increase in the corrosion rate with temperature is seen across all conditions, as was found experimentally. However, the relative increase in the corrosion rate between 25 °C and 40 °C was found to be 68% on average in the Nordsveen model, which is very close to the 67% increase seen in the experiment results. For comparison, the Kahyarian model predicted an average 116% increase across all conditions, which, even when adjusted to remove the significant overprediction at pH 6, only drops to 89%. This provides strong support to the accuracy of the temperature dependencies of the reactions provided in the Nordsveen model.

Although further testing would be required at higher temperatures to confirm whether these relationships hold beyond 40 °C.

Looking next at the influence of pH, the Nordsveen model once again follows the predicted experimental trend of lower corrosion rates at higher pHs. However, the relative change in the corrosion rate as function of pH is much lower than is seen experimentally. Between pH 6 and pH 4, the experimental results see an average increase in the corrosion rate of 0.88 mm/yr and 1.55 mm/yr at 25 °C and 40 °C respectively. Within the Nordsveen model these average values are only 0.02 mm/yr and 0.40 mm/yr, indicating that the model significantly underpredicts the influence of pH. This may be due to the inclusion of the direct reduction of H_2CO_3 as a secondary cathodic reaction. As shown in Figure 5-5, as the pH increases, the dominant reaction shifts further in favour of H_2CO_3 reduction. Both of the cathodic reactions within the Nordsveen model are defined via the same formula:

$$i_0 = i_{0,ref}\left(\frac{c_H^+}{c_{H^+,ref}}\right)^{a_1}\left(\frac{c_{CO_2}}{c_{CO_2,ref}}\right)^{a_2}\left(\frac{c_{H_2CO_3}}{c_{H_2CO_3,ref}}\right)^{a_3} e^{-\frac{\Delta H}{R}\left(\frac{1}{T}-\frac{1}{T_{ref}}\right)} \quad (5.2)$$

The influence of the local pH on each of the cathodic reactions is determined by the value of a_1, defined by Nordsveen *et al*.[26] as 0.5 and -0.5 for H^+ reduction and H_2CO_3 reduction respectively. These values were quoted by Nešić and Postlethwaite[113], based on experiments originally conducted by Bockris *et al*.[150] in 1961. However, in the original publication the pH dependence was determined based upon the dissolution kinetics of Fe, not the individual cathodic reactions. The experimental data collected here suggests a more accurate representation pH dependence using the direct reduction model may require some adjustment of the a_1 values.

The increased mass-transport rates due to higher rotation rates are also captured for most conditions by the Nordsveen model. Greater change is seen when the pH is low, as would be expected due to the increased bulk species concentrations, and this is reflected in the experimental data. However, at 25 °C and pH 4, a decrease is seen in the corrosion rate when increasing from 1,000 rpm (Figure 5-6(b)) to 1,500 rpm (Figure 5-6(c)), which goes against the general trend. Looking more closely at these conditions, it can be seen that the surface pH transitions from just above 5 to just below 5 at 1,500 rpm (Table 5.2). These values are therefore affected by the step change in the anodic kinetics, discussed in detail in Chapter 2. Due to this change being defined within the model as a piecewise function, rather than the continuous function described in the 1996 work by Nešić *et al*.[114], the accuracy of the model

around this point is significantly reduced. As seen here, this results in a predicted reduction in corrosion rate which is not seen in the experimental data.

Table 5.2 – Surface pH values for each rotation rate within the Nordsveen model at 25 °C and pH 4.

Rotation Rate (rpm)	Surface pH
500	5.81
1000	5.61
1500	4.91
2000	4.81
2500	4.73

5.3 Summary of Experimental vs Numerical Data

In this a new method for the determination of hydrodynamic parameters in the near-wall region has been explored. By utilising turbulent flow models, combined with the theoretical understanding of near-wall behaviour, simulated values of D_T and δ have been obtained. The approach has been extended to demonstrate applications beyond a standard straight pipe flow, to calculate flow properties within both a converging channel and an RCE.

A series of static RCE experiments have been conducted on samples of carbon steel within a CO_2 saturated solution. Electrochemical techniques have been employed to determine the corrosion currents of samples at pH 4, 5, and 6, and temperatures of 25 °C and 40 °C across rotation rates varying between 500 – 2500 rpm. Polarisation scans have then been conducted to determine the associated Tafel constants to convert the measured current densities into corrosion rates for each set of conditions.

Corrosion models by Nordsveen *et al*.[26] and Kahyarian *et al*.[12, 36] have been used in conjunction with simulated hydrodynamic data to generate predicted corrosion rates for the experimental conditions, in order to provide insight into the performance of each model. Each model was compared directly to the experimental results and both the overall performance and specific prediction of trends were assessed.

When compared to the experimental data, it was found that the Kahyarian model had a tendency to overpredict the corrosion rate. This was particularly

noticeable under high temperatures, high pH conditions where the surface concentration of H^+ is very low and the dissociation of H_2CO_3 becomes more prevalent. However, the model performed strongly under harsher conditions, in which the experimental corrosion rates were high. At pH 4, the model managed to capture the high corrosion rates across the entire range of rotation velocities.

The Nordsveen model on the other hand had a tendency to underpredict the corrosion rate, particularly under the harsher conditions for which the Kahyarian model performed well. However, at both pH 5 and pH 6, the Nordsveen model performed very strongly in accurately predicting both the corrosion rate and the impact of increasing temperatures. The influence of pH is slightly understated in the model however, likely due to the inclusion of direct H_2CO_3 reduction compensating for any significant changes in the H^+ concentration. The most significant inaccuracy identified within the Nordsveen model however was identified when the surface pH is approximately 5 due to a step change in the anodic kinetics.

Overall, both models were found to perform reasonably well and mirrored the experimental data in many respects. The Kahyarian model performed better under harsher conditions, and the Nordsveen model performed better at higher pHs. In both cases however, limitations have been identified, indicating the potential for improvement by combining the favourable aspects of each model.

5.4 Model Refinement

Throughout this thesis, an in-depth exploration of the current state-of-the-art mechanistic corrosion models has been conducted, providing valuable insight into how they function. As a result of this research, several areas for potential development and improvement of these models have been identified. Additionally, with both models fully functional within COMSOL Multiphysics®, there is the possibility to incorporate additional physicochemical effects in order to expand their applicability to a wider range of operating and environmental conditions.

In the following sections, the identified developmental areas are discussed in greater detail. In each instance, proposals are put forth for a potential modelling approach and the foreseen challenges are highlighted. Suggestions are also made for how the models could be further advanced to incorporate aspects of film formation and machine learning methods.

5.4.1 Leeds CO_2 Corrosion Model Proposal

In Chapters 2 and 3 the process through which CO_2 corrosion models produced by Nordsveen *et al*.[26] and Kahyarian *et al*.[12, 36] respectively were recreated within COMSOL Multiphysics® is outlined. The development process and associated troubleshooting steps required for both models clearly highlighted the various strengths and weaknesses of each approach. In some instances, the implementation of relevant physics in one model presented clear advantages over the other, either in accuracy or ease of implementation. In many areas, both models present reasonable and valid approaches, however there are also instances in which neither model presents an optimal modelling strategy. It is for this reason that a proposal for a new model for CO_2 corrosion is presented here. The intention is to combine the most beneficial aspects of existing models alongside additional improvements that have been identified during the development of the COMSOL models.

5.4.1.1 Surface Electrochemistry

When considering the numerical representation of the electrochemical surface reactions there are three primary considerations that have arisen:

1. Role of carbonic acid (H_2CO_3) in the corrosion behaviour.
2. Complexity of the anodic and cathodic kinetics.
3. Limitations of near-zero hydrogen ion (H^+) concentration.

The first of these, refers specifically to whether the H_2CO_3 in solution is assumed to be directly reduced at the metal surface, or it is assumed to dissociate rapidly at the surface, supplying ions H^+ which are subsequently reduced (known as the ‘buffering effect’). Since the publication of the original model by Nordsveen *et al*.[26], research conducted by Remita *et al*.[32] and Tran *et al*.[33] has provided strong evidence in favour of the buffering effect mechanism. However, as noted in the 2016 review paper by Kahyarian *et al*.[31], whilst the experiments conducted by Tran *et al*.[33] were more extensive, testing was conducted on stainless steel and it is uncertain whether the same behaviour can be assumed for mild steel. Although the consensus appears to be shifting towards acceptance of the buffering mechanism in recent years, researchers remain divided. The 2022 model published by Alsalem *et al*.[39], for example employs the buffering mechanism, whilst the 2018 model published by Hu *et al*.[151] opts for the older direct reduction model. It is clear that more research is needed in this area to be able to definitively determine the ‘correct’ mechanism. However, from the data

gathered within Chapter 4 of this thesis, the use of the buffering mechanism within the corrosion model appeared more capable of predicting the corrosion behaviour under more acidic conditions. Combined with the data from the currently available literature, the buffering mechanism is the preferred mechanism for a Leeds model.

However, despite the strong performance of the buffering mechanism within the Kahyarian model at the higher temperature and lower pH, poor performance was identified under other conditions which was particularly noticeable when the bulk pH was higher. The Nordsveen model performed much better in this regard, and as such it may be possible to integrate certain aspects of both models to improve overall performance. This shifts the focus to the second point listed, which considers the complexity of the equations which define the electrochemical surface reactions. Table 5.3 below summarises the equations used in both models.

Table 5.3 – Summary of the equations defining the electrochemical surface reactions within the Nordsveen and Kahyarian models.

	Electrochemical Equations
Generalised Current Density (Nordsveen)	$i_0 = i_{0,ref}\left(\frac{c_H^+}{c_{H^+,ref}}\right)^{a_1}\left(\frac{c_{CO_2}}{c_{CO_2,ref}}\right)^{a_2}\left(\frac{c_{H_2CO_3}}{c_{H_2CO_3,ref}}\right)^{a_3} e^{-\frac{\Delta H}{R}\left(\frac{1}{T}-\frac{1}{T_{ref}}\right)}$ $i_{loc} = \pm i_0 \times 10^{\frac{\eta}{b_a}}$
Anodic Current Density (Kahyarian)	$i_{a,j} = Fk_j \cdot \left(a_{H^+}^s\right)^{m_{H^+,j}} \cdot \left(a_{CO_2}^s\right)^{m_{CO_2,j}} \cdot e^{\left(\frac{\alpha_j F\eta}{RT_K}\right)}$ $\theta = \frac{K_\theta \cdot \left(a_{H^+}^s\right)^{m_{H^+,\theta}} \cdot \left(a_{CO_2}^s\right)^{m_{CO_2,\theta}} \cdot e^{\left(\frac{\alpha_\theta F\eta}{RT_K}\right)}}{1 + K_\theta \cdot \left(a_{H^+}^s\right)^{m_{H^+,\theta}} \cdot \left(a_{CO_2}^s\right)^{m_{CO_2,\theta}} \cdot e^{\left(\frac{\alpha_\theta F\eta}{RT_K}\right)}}$ $i_a = \frac{(1-\theta) i_{a,1} i_{a,2}}{i_{a,1} + i_{a,2}} + \theta i_{a,3}$
Cathodic Current Density (Kahyarian)	$i_c = -Fk_{H^+} \cdot \left(a_{H^+}^s\right)^{m_{H^+,c}} \cdot e^{\left(\frac{\alpha_{H^+} F\eta}{RT_K}\right)}$

Comparing the surface reaction equations used within the two models, it becomes clear that the anodic kinetics used within the Kahyarian model are far more complex than in the Nordsveen model. The purpose of the θ term and

the three individual current densities in these equations is to capture the actively corroding ($i_{a,1}$), transition ($i_{a,2}$), and pre-passivation ($i_{a,3}$) ranges. However, the highly complex nature of these equations makes it very difficult to identify the root cause of any poor predictive performance. As such, it would simplify the fine-tuning of the model to reduce these equations to a single current expression, as done by Nordsveen *et al*.[26] and Alsalem *et al*.[39]

In the Nordsveen model the different regimes are instead accounted for by varying the exponential terms as a function of pH. However, the primary issue noted with the current implementation of the Nordsveen current density equations is the step change observed when the surface pH reaches values of 4 or 5. The same problem is not found within the Kahyarian model due to the θ function providing a smooth transition between the current densities. The optimal aspects of both sets of electrochemical equations could therefore be combined by utilising a single equation, with the changes to the exponential terms being described by a continuous function, as opposed to a piecewise function. In the original paper by Nešić and Thevenot[114], cited as the source of the anodic kinetics by Nordsveen *et al*.[26], it is even stated that "*In reality there are of course no sharp changes at pH 4 or pH 5 but rather there is continuous transition that leads from one mechanism to another*".

The final consideration mentioned here relates to an issue associated with the buffering model, as identified in Chapter 3 of this thesis. When H^+ is the sole cathodic reaction, a high charge-transfer rate within the mass-transport region leads to significant depletion of ions close to the surface. As this tends towards zero, the computational limits of the model are reached, with the values becoming sufficiently small as to be assumed zero. As the anodic kinetics are directly linked to the H^+ concentration on the boundary node, this commonly results in solver errors. In reality, such high surface pH values are not seen[152, 153], indicating that this issue is related to the solver method itself. Due to the dissociation reactions not being computed on the boundary node, the massive depletion of H^+ is largely superficial and is correct on the adjacent node. Therefore, one possible solution to this problem is to implement a damping function on the surface node, which artificially limits the concentration of the surface node in relation to adjacent node. This would prevent the pH on the surface node from deviating too far from the fluid in the boundary, however it would introduce a small degree of manual interference with the mechanistic equations.

An alternative solution would be to implement the corrosion model utilising a finite volume method (FVM), as opposed to the finite element method (FEM) used currently. As FVM evaluates dependent variables at cell centres rather than at the nodes[90], this would bypass the current limitation. The downside of this approach however is that it is not currently possible within COMSOL Multiphysics®, and as such the model would need to be implemented using different modelling software, such as Ansys, which utilises FVM.

5.4.1.2 Hydrodynamic Incorporation

Within Chapter 4 of this thesis, a methodology is outlined which allows for the determination of the hydrodynamic properties of the boundary layer based upon the overall flow characteristics. The advantage of using turbulence models to calculate the hydrodynamic properties, as opposed to using empirical values found in the literature[28, 43, 124, 125], is that it expands the application of the corrosion model to include variations in the pipe geometry as well as non-uniform flows. By removing these assumptions associated with the empirical formulae, this provides greater flexibility to the model, which represents a crucial first step when considering the future progression of hydrodynamic modelling (see Section 5.4.2). Due to this, capacity to introduce hydrodynamic characteristics from an external turbulence model is an important feature in the development of a Leeds model.

However, it would be counterproductive to remove the ability to utilise the empirical formulae entirely. Whilst the use of turbulence models removes many of the limitations of these formulae, it must be acknowledged that it is a much more time-consuming process, requiring the entire flow field to be modelled. For the purposes of straight pipe flows, this is an unnecessary computational expense as the equations provided within the literature are a much more rapid method of obtaining the same (or at least similar) values. It is therefore proposed here that the empirical values are calculated regardless and stored in the parameter list of the model to be accessed and utilised for the prediction corrosion specifically within straight pipe flows.

In order to decide which set of empirical relationships are the most appropriate for this purpose, it is helpful to summarise the formulae used in both the model by Nordsveen *et al*.[26] and the model by Kahyarian *et al*.[12, 36] These formulae, alongside the values used within COMSOL to numerically calculate the hydrodynamic effects are shown in Table 5.4.

Table 5.4 – Summary of hydrodynamic values used in the Nordsveen, Kahyarian, and COMSOL models.

Model	Boundary Layer Thickness (δ)	Turbulent Diffusivity (D_T)
Nordsveen	$25Re^{-\frac{7}{8}} \cdot d$	$0.18\left(\frac{y}{\delta}\right)^3 \cdot \left(\frac{\mu}{\rho}\right)$
Kahyarian	$\frac{5\nu}{\left(\frac{\tau_\omega}{\rho}\right)^{\frac{1}{2}}}$	$\frac{0.0007(y^+)^3}{\sqrt{(1+0.00405(y^+)^2}}$
COMSOL	$\frac{\nu}{\mu_\tau} \cdot \min\{y^+ : y^+ \neq u^+\}$	$\frac{\mu_\tau}{\rho \cdot Sc_t}$

In the calculation of δ, there is one significant difference between the formulae used in the two models, in that the Kahyarian model uses a pre-defined y^+ value ($y^+ = 5$) to represent the end of the boundary layer, whilst the Nordsveen model doesn't. This allows flexibility in the Nordsveen model to calculate the boundary layer thickness purely as a function of the hydrodynamic properties. This aligns with the methodology used to calculate δ within the COMSOL model, and as such would represent greater internal consistency in the approach. It would therefore be sensible to use the formula used by Nordsveen *et al*.[26], as originally proposed by Davies[28], for the purposes of this work. It should be noted however, that the formula provided by Kahyarian *et al*.[12, 36] does provide the capacity to introduce surface roughness into the equation via the wall shear stress (τ_ω) and would be more beneficial if considering rough pipelines.

As for the calculation of D_T, Figure 5-7 shows a comparison between the empirical formulae used in the models and the values calculated using a turbulence model for a smooth straight pipe ($Sc_t = 0.71$).

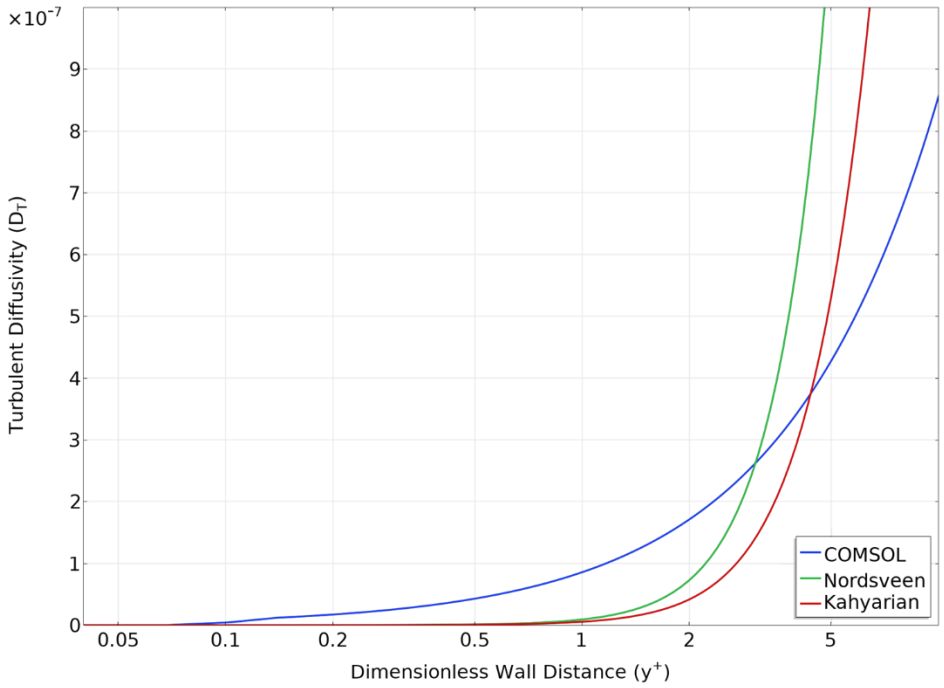

Figure 5-7 – Comparison of D_T values calculated using a turbulence model within COMSOL with values from the empirical formulae in the Nordsveen and Kahyarian models.

In each case, the calculated values for the boundary layer height D_T are very similar, with both empirical equations slightly below the numerical solution at low y^+ values, and above at larger y^+ values. When compared within the expected boundary layer region ($y^+ < 0$), the equation used in the Kahyarian model is much closer to the numerical values. The exponential growth of the equation used in the Nordsveen model occurs slightly sooner, leading to a significant difference to the numerical prediction at $y^+ = 5$. Combined with the relative simplicity of the equation, being solely a function of y^+, it is reasonable to conclude that the formula provided by Kahyarian *et al*.[12, 36] would be the most appropriate for this work.

5.4.1.3 Species Activity Calculations

As discussed in previous chapters, there is difference between the concentration of a species and the 'effective concentration' when considering solution chemistry. The difference between these two values is indicated by the activity coefficient (γ). The concept of species activity is used to approximate the real-world behaviour of a system and the deviation from the ideal state[29]. By calculating equilibrium constants and kinetic reaction rates based on species activity rather than concentration, as Kahyarian *et al*.[12, 36]

have done, the model is better able to predict corrosion responses at high ionic strengths.

The most complete description of species activities is given by the Pitzer equations[120], which account for the individual interactions of each of the species in solution[121]. However, the issue with this approach is that is becomes highly complex when multiple ions are included within the model, requiring large numbers of Pitzer parameters to be defined in order to account for the relative effects of all species. It is for this reason that the Debye-Hückel approximation is often used instead[123]. Instead of modelling every interaction, this approach calculates a single mean activity coefficient for each species, reducing the overall complexity.

As part of the validation between the COMSOL model and the publications by Kahyarian *et al*.[12, 36], a strong agreement between the two models found despite the use of the Debye-Hückel approximation in the calculation of the activity coefficients. This provides strong evidence that this approximation is sufficiently close to the values calculated via the Pitzer equations[120] that its use is justified for dilute solutions (I < 1 M). However, in 1974 Truesdell and Jones[154] proposed a modification to the extended Debye-Hückel to capture an effect seen in experimental data in which the activity coefficients begin to increase at high ionic strengths. The updated formula, given by Equation 5.3, simply adds an additional bI term to the existing formula:

$$\log \gamma_i = -\frac{Az_i^2\sqrt{I}}{1 + Ba_i\sqrt{I}} + bI \tag{5.3}$$

This small change extends the validity of the approximation to include solutions with ionic strengths of up to 2 M[29]. Beyond this, the full Pitzer equations would need to be implemented in order to accurately account for the effects of ionic strength. However, it is uncommon for low temperature solutions to reach such high salinity, with even the ionic strength of seawater only being around 0.7[29]. Therefore, for many applications of a CO_2 corrosion model, the much simpler Truesdell-Jones approximation can be used to provide a reasonable prediction of the behaviour.

5.4.2 Progression of Hydrodynamic Modelling

In Chapter 4, a method was proposed for integrating hydrodynamic data from turbulence models into the corrosion models detailed in Chapters 2 and 3. By initially solving for the flow field and the extracting hydrodynamic values in the near-wall region, a one-way coupling between the two models could be

introduced. The methodology proposed demonstrates the basic approach behind the future development of the prediction of corrosion in turbulent environments. However, the work discussed thus far does not represent a complete picture of the real-world scenario.

In this section, the known limitations of the current hydrodynamic method are highlighted, and the theory behind the progression of the approach going forwards is discussed. It is the belief of the author that the inclusion of the following phenomena would result in a robust and comprehensive representation of flow effects on corrosion behaviour.

5.4.2.1 Higher Dimensional Modelling

Perhaps the most evident limitation of the current methodology is that it considers the hydrodynamic profile along the surface as a series of independent 1-D cut-lines. As such there is an underlying assumption of uniform flow which means that the diffusion of species is only considered perpendicular from the surface. However, from the numerical explorations conducted throughout this work, it is known that, when under mass-transport control, the corrosion rate will vary as a function of the hydrodynamics. Hence, if the flow is non-uniform the electrochemical surface reactions produce and consume the electroactive species at different rates throughout the geometry. In turn, this shifts the charge balance of the system, altering the local pH and therefore the concentrations of all chemical species. With variations in local species concentrations parallel to the metal surfaces, concentration gradients would be introduced that initiate diffusion across the surface, referred to here as cross-flow.

The natural progression of the hydrodynamic methodology is to progress from 1-D into higher spatial dimensions. However, in order to do so, the cross-flow behaviour must be accounted for within the transport equations. This can be achieved by adding additional spatial gradients into the flux equation to represent the added degrees of freedom. In the current models, changes to the local species concentrations (c_j) are calculated using the Nernst-Planck equation:

$$\frac{\partial c_j}{\partial t} = -\frac{\partial N_j}{\partial x} + R_j \tag{5.4}$$

Where N_j is the species flux and R_j is a source/sink term describing the local change in species j.

In two-, or three-dimensional space, the flux equation would need to be modified to account for changes in the y and z directions:

$$\frac{\partial c_j}{\partial t} = -\nabla \cdot N + R_j \tag{5.5}$$

Where the generalised flux equation is also modified from the one-dimensional form to incorporate the additional spatial gradients:

$$N_j = -D_{M,j}\nabla c_j - z_j u_j F c_j \nabla \Phi + c_j \vec{v} \tag{5.6}$$

Where $D_{M,j}$ is the molecular diffusion coefficient, z_j is the valence, u_j is the mobility of species, F is the Faraday constant, Φ is the electrolyte potential, and v is the solution velocity.

Retaining the assumption that transport within the boundary layer is diffusion controlled, and that convection is negligible ($c_j \vec{v} \approx 0$), the flux equation becomes:

$$N_j = -(D_{M,j} + D_T)\nabla c_j - z_j u_j F c_j \nabla \Phi \tag{5.7}$$

5.4.2.2 Galvanic Interaction

Advancing the model to incorporate the effects of non-uniform flow does not solely introduce complexity in the diffusion of species, it would also have an effect on the electrochemical response of the system. As it stands, for a 1-D model, there is a boundary condition applied at the surface which states that total current exchange is zero. In effect this means that the anodic and cathodic currents are always equal:

$$\sum I_{anodic} + \sum I_{cathodic} = 0 \tag{5.8}$$

Where I_{anodic} and $I_{cathodic}$ are the anodic and cathodic currents respectively.

This boundary condition ensures the modelled system remains electroneutral at any given point. Under a uniform flow condition this is a valid assumption as the rates of reaction do not change as a function of position. However, once the reaction rates are no longer equal, galvanic effects must be considered.

Galvanic coupling refers to the concept of local anodes and local cathodes across a material. Often considered in relation to connected metallic components, galvanic effects can occur across a single material if the electrochemical behaviour varies significantly at different points along the

surface[5]. The local surface potential can shift the electrochemical response to favour either the anodic or cathodic branch of the corrosion reaction, depending on the rate of reaction and availability of ions. Electrons therefore may be consumed and produced at different points, meaning that isolated points along the surface are not necessarily electroneutral. However, as there is no external current exchange, it still remains true that the total current exchange in the system is zero. To account for this effect, the boundary condition given in Equation 5.8 would simply need to be updated to sum all anodic and cathodic currents across the entire surface:

$$I_{tot} = \int_A i_a \, dA + \int_A i_c \, dA = 0 \tag{5.9}$$

Where I_{tot} is the total current, i_a is the anodic current density, i_c is the cathodic current density, and A is the area of the corroding surface.

As modelling the galvanic interaction would require consideration of the movement of electrons, an additional transport term would need to be added on the surface. Accurately accounting for this would also mean introducing an additional material property, the conductivity of the metal (σ_s).

From Ohm's Law, it is known that:

$$E = I \cdot R \tag{5.10}$$

Where E is the potential, R is the resistance, and I is the current.

The current over a given area (A) can be calculated as a function of the current density through the metal (i_s):

$$I = i_s \cdot A \tag{5.11}$$

Additionally, the resistance can be defined in terms of σ_s and the characteristic length (L), which for a pipeline would be the thickness of the pipe wall:

$$R = \frac{\sigma_s \cdot L}{A} \tag{5.12}$$

Combining Equations 5.10-5.12 gives:

$$E = (i_s \cdot A) \cdot \left(\frac{\sigma_s \cdot L}{A}\right) = i_s \cdot \sigma_s \cdot L \tag{5.13}$$

Which can be rearranged to give:

$$i_s = \frac{E}{\sigma_S \cdot L} \tag{5.14}$$

Using Equation 5.14, the exchange current between the anodic and cathodic sites on the surface can be calculated. These currents can then be coupled with the electrochemical surface reactions to calculate the impact on the corrosion rate.

5.4.2.3 Transport of Species

Currently, there is an assumption within each of the models that the concentration of Fe^{2+} within the bulk is constant. Nominally this is set to 1 ppm_{Molar} in order to represent the accumulation of ions in the bulk. As there are ions being released from the surface and not being consumed elsewhere, it logically follows that the concentration within the bulk cannot be zero. It many cases the bulk concentration is sufficiently low as to be insignificant to the overall corrosion behaviour. However, if it were the case that the bulk concentration was unusually high, this would directly affect the diffusion of species through the boundary layer. A high concentration of Fe^{2+} in the bulk would reduce the rate of diffusion away from the surface due to the corresponding drop in the concentration gradients. This would increase the surface concentration, influencing the local charge balance, as well as contributing to the local saturation ratio (SR).

Instances in which this may be the case include flow cells with either low volumetric capacity or low flow rates, such as those used by Kahyarian and Nešić[12, 36] and Barker *et al*.[59]. As noted by Chen[155], the volumetric capacity of such cells can range from tens of mL down to µL scales. This may also apply to flow regimes in which regions of recirculation occur, such as may be found in geometries with rapid expansions (for example the backward-facing step shown in Figure 5-8).

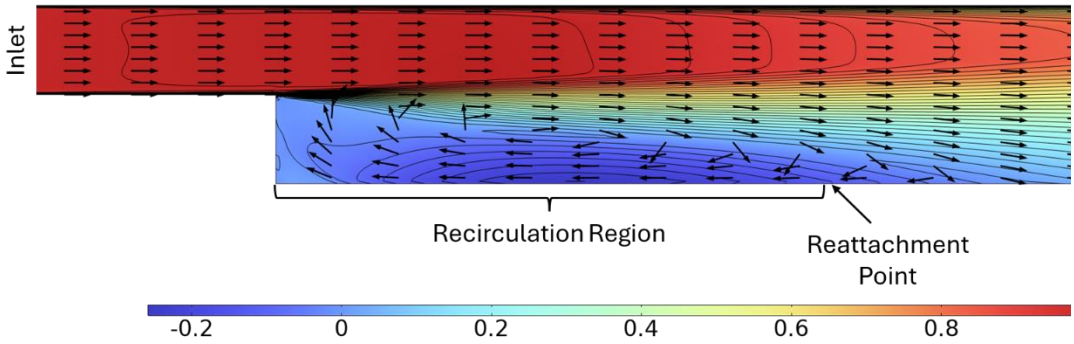

Figure 5-8 – Model of a backward-facing step scenario showing a recirculation region.

In such cases it may become necessary to account for the accumulation of Fe^{2+} within the bulk over time. In order to achieve this, a transportation of species mode would need to be introduced utilising the flow patterns from a turbulence model for the complete geometry. By introducing a flux of species at the corroding surfaces, based upon the outputs of the corrosion model, these ions could be introduced into flow model and evaluated over time. Such an approach was demonstrated in Owen *et al*.[96] in 2019 in which the transport of H^+ ions through a rapid pipe expansion was modelled. The local H^+ concentrations were then used in conjunction with a simple mass-transfer model to predict corrosion rates throughout the geometry.

5.4.2.4 Complex Flow Fields

The methodology for determining the hydrodynamic characteristics within the boundary layer, as discussed in Chapter 4, currently rely on the 'universal law of the wall' principle. By plotting the dimensionless velocity (u^+) against the dimensionless wall distance (y^+) and identifying the point at which the two are no longer equal, it is generally possible to determine the viscous sublayer height. However, despite its name, the universal law of the wall cannot be applied universally. In cases of swirling, impinging, or separating flows, or flows with steep pressure or temperature gradients[49], the velocity profile deviates from the generalised profile. The consequence of this is that the both the approach outlined with Chapter 4, as well as the empirical equations used in existing corrosion models become invalid.

In order to account for more complex flow fields, it becomes necessary to remove some of the simplifications previously made to the model. Firstly, it would be no longer reasonable to assume that the entire surface could be represented in one-dimension; the variations in hydrodynamics would alter the local corrosion response. Furthermore, the lack of a clear definition for the

value of δ under certain flow regimes, means that the domain cannot simply be discretized into a number of individual 1-D domains. Instead, the flow model would need to incorporate higher spatial dimensions, as discussed in section 5.4.2.1. Alongside this however, as there would be no clear transition between the boundary layer and the bulk flow, it would be necessary to define an extended near-wall region to ensure all local flow effects are captured. This would require that the flow profile is fully resolved down to the wall. Additionally, as this extended near-wall region may extend into the turbulent section of the flow, it would become necessary to re-integrate the convection term into the flux equation:

$$N_j = -(D_{M,j} + F_T D_T)\nabla c_j - z_j u_j F c_j \nabla \Phi + c_j \vec{v} \tag{5.15}$$

It should be noted that within Equation 5.15, D_T has been multiplied by an additional transition function (F_T). The purpose of this is to ensure that convective effects of the flow are not accounted for twice, once by the $D_T \nabla c_j$ term and then again by $c_j \vec{v}$ term. The function D_T would be a variable function between 1 and 0 defined based on the local flow velocity (v).

$$F_T = f(v) \tag{5.16}$$

5.4.3 Film Formation Models

Throughout the numerical exploration of mechanistic CO_2 corrosion models in this work, the potential for the precipitation of $FeCO_3$ has been discussed in detail. This is because it is known that in such systems, particularly under high temperature, high pH conditions[9], it is possible for $FeCO_3$ to out of solution and form protective layers (films) on the corroding surfaces. Under such conditions, CO_2 corrosion models which do not consider the formation of these films can no longer be considered accurate.

When $FeCO_3$ films form on a corroding surface they form a barrier between the electrolyte and the surface which impedes the diffusion of corrosive species from the bulk fluid and can block actively corroding sites[156]. If thick, dense $FeCO_3$ films are formed on the surface, this can reduce the rate of the surface reactions by over an order of magnitude[9]. As these effects are not captured by pure corrosion models, it can result in significant overprediction of the corrosion rate.

The following section discusses how the rate of $FeCO_3$ precipitation can be mathematically determined and integrated into the corrosion models.

5.4.3.1 Diffusion Barrier

Perhaps the simplest implementation of $FeCO_3$ scaling within a corrosion model is via the introduction of a diffusion barrier. $FeCO_3$ films are often porous[9] and as such do not completely prevent species from reaching the corroding surface. However, within these films the fluid is static and as such turbulent effects can be entirely ignored. Species transport therefore becomes primarily determined by the diffusion, determined by the properties of the surface film. By segmenting the one-dimensional domain into a film and a hydrodynamic boundary layer, it is possible to account for the effects of $FeCO_3$ precipitation by assigning different transport equations either side of the protective surface. Above the layer, the transport equations would remain unchanged from the current corrosion models. Within the layer however, the transport equation would be reduced to only include molecular diffusion and electromigration, with the diffusion term being determined by the properties of the film.

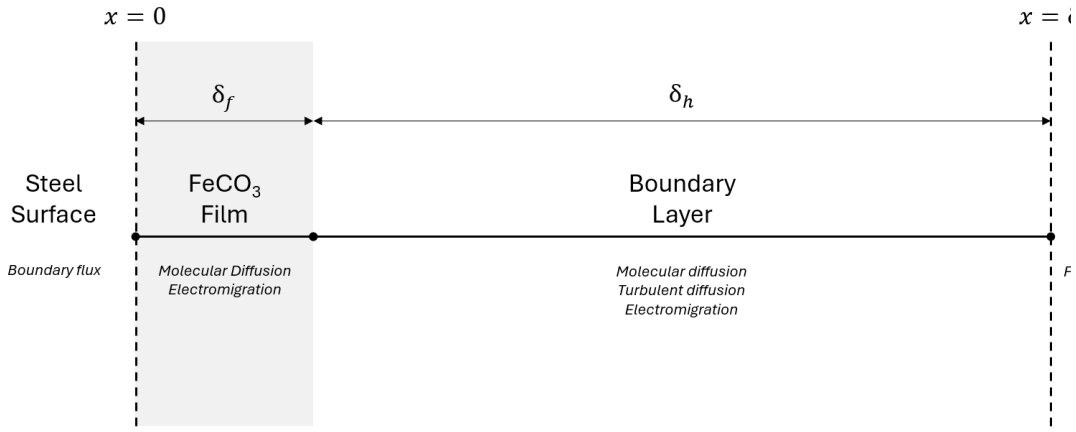

Figure 5-9 – Diagram of corrosion model including an $FeCO_3$ surface film summarising transport properties within each section of the domain.

The implementation of a diffusion barrier is clearly demonstrated in the papers by Nešić *et al*.[37], and Nešić and Lee[38] which formed parts 2 and 3 respectively of the original publication by Nordsveen *et al*.[26] In these papers, the properties of the boundary layer are defined by two important characteristics:

- Volumetric Porosity (ε_V) - A measure of the total void space within the layer.
- Tortuosity (τ) - A measure of the complexity of the flow path within the layer[157].

Both of these properties are necessary to consider when modelling transport within an $FeCO_3$ layer as combined they account for both the volume of free space as well as the freedom with which ions are able to move. A film with a low porosity forms a dense layer on the surface, preventing the transport of ions through it. However, even a film with a high porosity can significantly reduce the diffusive transport if the tortuosity is sufficiently high as to restrict movement between pores[158]. Transport due to diffusion within a $FeCO_3$ is therefore generally defined via an effective diffusion term (D_{eff}), which is a function of both ε and τ. In the Nordsveen works, D_{eff} is calculated as:

$$D_{eff} = \varepsilon^{1.5} \cdot (D_M + D_T) \tag{5.17}$$

Where D_M is the molecular diffusion coefficient, and D_T is the turbulent diffusivity (set to zero within the film). The exponent value of 1.5 is derived from the product of ε and τ, known as the permeability (κ_f):

$$\kappa_f = \varepsilon \cdot \tau \tag{5.18}$$

Where τ is defined as:

$$\tau = \varepsilon^{0.5} \tag{5.19}$$

A similar approach is taken in the 2023 work by Alsalem *et al.*[39] when modelling CO_2 corrosion of a rotating cylinder electrode. Their one-dimensional corrosion model accounted for the precipitation of an $FeCO_3$ film via an effective diffusivity, calculated from the surface porosity (θ), alongside the Bruggeman model of tortuosity[159]:

$$D_{eff} = \frac{\theta}{\tau} \cdot D_M \tag{5.20}$$

$$\tau = \theta^{-0.5} \tag{5.21}$$

The assumption made by Nordsveen *et al.*[26] is that $\varepsilon \approx \theta$, in which case formulae (Equations 5.17 and 5.20) can be rearranged to show that both models calculate the same value for D_{eff}.

5.4.3.2 Precipitation and Film Growth

For a simple diffusion barrier model, the height of the protective film δ_f can be manually defined based upon either real-world or experimentally derived values. However, it is possible to numerically determine an approximate thickness of the film based on the precipitation rate within the solution. The precipitation rate of $FeCO_3$ (P_{FeCO_3}), given in $mol \cdot m^{-3} \cdot s^{-1}$, is the rate at which

aqueous Fe^{2+} ions and CO_3^{2-} ions combined to form solid $FeCO_3$. A 2018 review by Barker *et al*.[9] identified a total of 4 precipitation models available within the literature, published by: Greenberg and Tomson[20], Johnson and Tomson[21], Van Hunnik *et al*.[22], and Sun and Nešić.[15]. These formulae are provided in Table 5.5 below.

Table 5.5 – Summary of models available in literature for the calculation of the precipitation rate of $FeCO_3$.

Model	P_{FeCO_3}	
Greenberg and Tomson	$A_0 e^{-\left(\frac{E_a}{RT}\right)} \left(\frac{A}{V}\right) K_{sp} \left(\sqrt{SR} - 1\right)^2$	(5.22)
Johnson and Tomson	$A_0 e^{-\left(\frac{E_a}{RT}\right)} \left(\frac{A}{V}\right) K_{sp} \left(\sqrt{SR} - 1\right)^2$	(5.23)
Van Hunnik, Pots, and Hendriksen	$A_0 e^{-\left(\frac{E_a}{RT}\right)} \left(\frac{A}{V}\right) K_{sp} (SR - 1) \left(1 - \frac{1}{SR}\right)$	(5.24)
Sun and Nešić	$A_0 e^{-\left(\frac{E_a}{RT}\right)} \left(\frac{A}{V}\right) K_{sp} (SR - 1)$	(5.25)

Where in each case A_0 is a pre-exponent factor, E_a is the activation energy (kJ·mol^{-1}), A is the surface area of the crystals (m^2), V is the volume of solution (m^3), K_{sp} is the solubility product (M^2), and SR is the saturation ratio.

The contributions of the local concentrations of both Fe^{2+} and CO_3^{2-} to the rate of precipitation are included in the calculation of SR, which is defined as:

$$SR = \frac{[\mathrm{Fe}^{2+}] \cdot [\mathrm{CO}_3^{2-}]}{K_{sp}} \tag{5.26}$$

Where $[\mathrm{Fe}^{2+}]$ and $[\mathrm{CO}_3^{2-}]$ are the molar concentrations of aqueous Fe^{2+} and CO_3^{2-} respectively.

As noted by Barker *et al*.[9] however, there is a fundamental flaw in directly utilising the precipitation rate to determine film thickness in that it assumes that all precipitated $FeCO_3$ contributes to the growth of the film. In reality this is not the case as $FeCO_3$ can precipitate elsewhere in the system, leading to overpredictions if assuming complete deposition on the steel surface. It is for this reason that Sun and Nešić[15]. proposed instead using the corrosion layer accumulation rate ($CLAR$), a concept initially introduced by Gulbrandsen, to differentiate between surface precipitation and total precipitation. $CLAR$ specifically defines the precipitation rate on the steel surface, taking the same

form as the equations provided in Table 5.5, but omitting the area to volume ratio:

$$CLAR = A_0 e^{-\left(\frac{E_a}{RT}\right)} K_{sp}(SR - 1) \tag{5.27}$$

As the corrosion behaviour is not influence by $FeCO_3$ precipitation elsewhere in the system, it seems logical to use $CLAR$ as opposed to P_{FeCO_3} when modelling surface films.

Regardless of the precipitation rate model that used however, another consideration that must be accounted for is the loss of ions within the solution. The formation of $FeCO_3$ is the result of chemical reactions between Fe^{2+} and CO_3^{2-} ions in solution:

$$\mathrm{Fe}^{2+}_{(\mathrm{aq})} + \mathrm{CO}_3^{2-}{}_{(\mathrm{aq})} \rightarrow \mathrm{FeCO}_{3(\mathrm{s})} \tag{5.28}$$

Therefore, within the boundary layer reactions, an additional kinetic equation must be specified which accounts for the depletion of ions:

$$r_7 = -CLAR \tag{5.29}$$

The reaction r_7 provided in Equation 5.29 would then need to be added to the ODEs defining the rate of production of both Fe^{2+} and CO_3^{2-} within the boundary layer.

5.4.3.3 Moving Boundary

The method of modelling of protective films discussed thus far focus on the effects of $FeCO_3$ as a stationary problem. The assumption is that the thickness of the film (δ_f) remains constant and is therefore pre-defined within the domain. However, as $FeCO_3$ layers are formed through a deposition process, it may be of interest to instead model the growth of these films over time. Due to the various complex mechanisms by which $FeCO_3$ crystals can nucleate and grow[9], it is unrealistic to expect that the specific characteristics of the film could be accurately captured with such a simple model. However, if the precipitated $FeCO_3$ is assumed to form a uniform layer across the surface, Equation 5.27 can be used to predict the growth rate at any given point based upon local species concentrations at the surface. Therefore, by converting the model to a time-dependent model rather than a stationary model, it is possible to evaluate the growth of the film over time.

The production of a boundary layer model which shows the gradual change in the size of the $FeCO_3$ film would require the inclusion of a moving boundary. Fortunately, the functionality to introduce a moving boundary is already

included within the COMSOL Multiphysics® software. The boundary, representing the interface between the surface of the film and the fluid ($x = \delta_f$, see Figure 5-9), would move with a velocity relative to $CLAR$. As the units for $CLAR$, as calculated via Equation 5.27, are mol·m^{-2}·s^{-1}, this can be converted to a velocity in m·s^{-1} via the following equation:

$$v_f = CLAR \cdot \frac{M_{w,FeCO_3}}{\rho_{film}} \tag{5.30}$$

Where v_f is the growth velocity of the film (m·s^{-1}), $M_{w,FeCO_3}$ is the molecular weight of $FeCO_3$ (kg·mol^{-1}), and ρ_{film} is the density of the film (kg·m^{-3}).

The size of the domain (δ) would then vary with the growth of the film:

$$\delta_f = v_f \cdot t \tag{5.31}$$

$$\delta = \delta_f + \delta_h \tag{5.32}$$

Where t is the time (s) and δ_h is the height of the hydrodynamic boundary layer.

Due to the very slow rate at which these processes occur, converting v_f into mm·yr^{-1} and utilising time steps with units of years is likely to be more convenient.

The same approach could also be used to incorporate the regression of the surface due to corrosion. In this case the velocity (v_s) would be equal to the negative of the corrosion rate (CR) and the change in δ_f would be dependent upon the difference between v_f and v_s.

$$v_s = -CR \tag{5.33}$$

$$\delta_f = (v_f - v_s) \cdot t \tag{5.34}$$

A visualisation of this approach and times $t = 0$ and $t = t_1$, where t_1 is an arbitrary time step greater than 0, is shown in Figure 5-10 below.

(a)

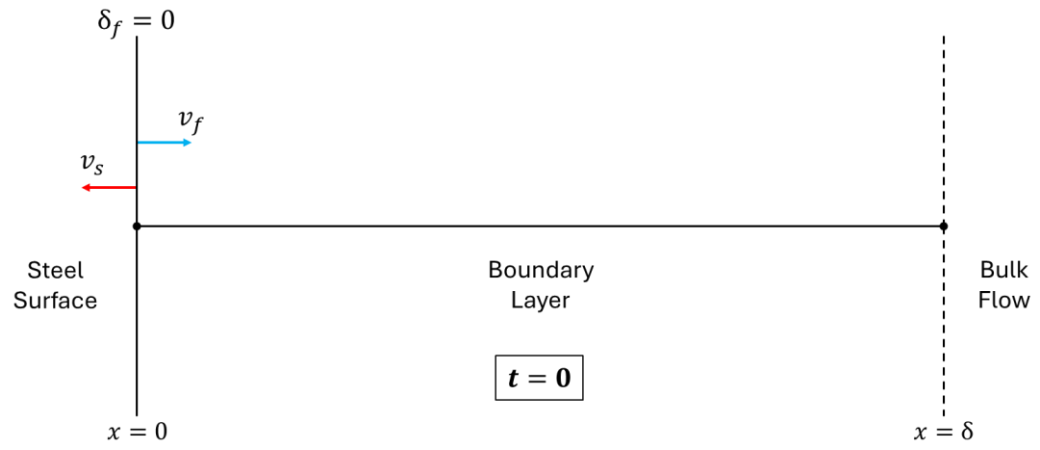

(b)

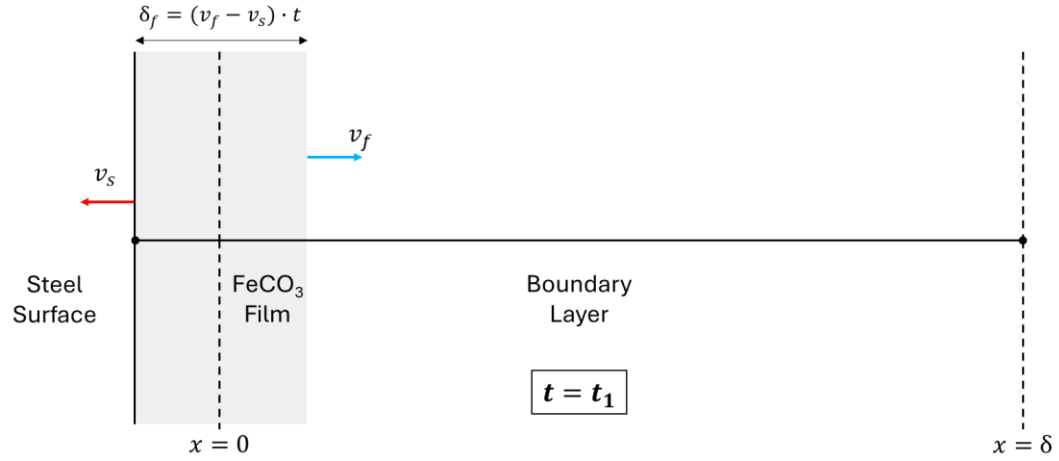

Figure 5-10 – Diagram of moving boundary at times (a) $t = 0$ and (b) $t = t_1$, showing the growth of an $FeCO_3$ film.

5.4.4 Prediction Models and Machine Learning

Many of the publications associated with the work detailed within this thesis have focused on the numerical exploration of the established corrosion models[131, 160-162]. In each of these works, thousands of data points were individually calculated via the use of parametric sweeps and iterative loops, with output values being stored in large matrices. Whilst these processes have been optimized as much as possible up to this point, solving the corrosion models for every individual combination of input conditions remains time-consuming and computationally expensive. The rise in process automation and machine learning in recent years offers a potential solution to the current limitations, however. By developing tools based upon data from the corrosion

models, it would become possible to rapidly evaluate a wide range of conditions without the need to run every set of conditions directly. The following section outlines several potential routes to achieve such a goal.

5.4.4.1 Multi-Dimensional Sampling

The first stage in the development of many prediction tools is to generate an initial data set on which to train the model. The data set needs to be sufficiently large as to allow the machine learning algorithm to capture the effects of the various inputs, without overtraining the model.

Throughout the development and testing of the corrosion models discussed in previous chapters, six controlling inputs have been identified which can have a significant effect on the outputs of the model, namely:

- Temperature
- Partial pressure of CO_2
- Bulk fluid pH
- Bulk fluid velocity
- Pipe diameter
- Ionic strength

Generating a complete training data set would therefore require that each of the above parameters are appropriately sampled to incorporate their respective influence. There are many different sampling methods which exist, each of isolate a portion of the data from which to extract outputs.

Perhaps the simplest technique, which is commonly used for Monte Carlo methods[163], is to just randomly sample the data. The benefit of such a technique is that it is generally easy to implement as it does not require any pre-treatment of the data. However, as the method is entirely random, it means that a large number of points are required to ensure the full data range is adequately represented. It is therefore not an appropriate technique to use for the purposes of this work as the objective is to reduce the computational expense.

A slightly more sophisticated technique, and the default sampling technique used within COMSOL Multiphysics® v6.2, is Latin Hypercube Sampling (LHS).[164] Fundamentally, LHS functions based on the concept of a Latin square, in which data within an n×n array is arranged such that is appears in each row and column exactly once.

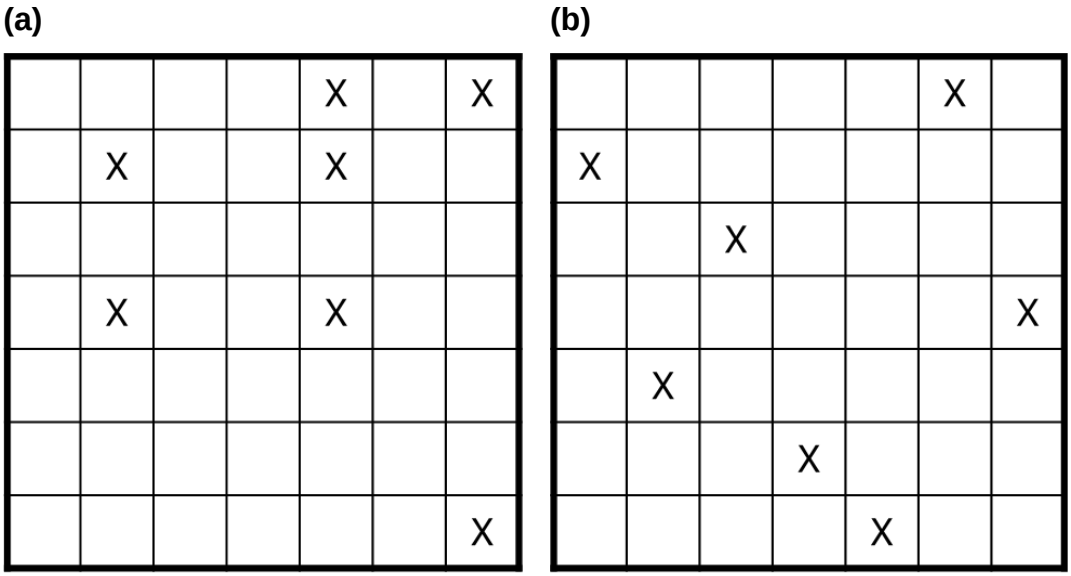

Figure 5-11 – Examples of data sampling in 2-D based on (a) random sampling and (b) LHS techniques.

A Latin hypercube extends this concept to higher dimensions and is the basis of LHS. In order to ensure that the final data selection follows the rules of a Latin hypercube, LHS implements memory to account for the previously selected data points. The subsequent data points are then randomly selected from the available locations within the hypercube. The result is an even distribution of data points across the entire domain, reducing the number of computations required compared to purely random sampling.

LHS would be a reasonable approach to use for the purposes generating data for training a corrosion model tool. However, there is one weakness in the approach in that it disproportionately favours data within the centre of the cube. As each variable is limited in the number of data points within its range, it is unlikely that the extreme values of all variable ranges will be selected. The result of this is that it causes LHS to miss these values, effectively cutting off the corners of the hypercube. This can be improved upon by introducing a probability density function to adjust the distribution of the data. For example, a β distribution using values of $\alpha = 0.5$ and $\beta = 0.5$ would skew the distribution to favour the ends of the data ranges[165].

5.4.4.2 'Black Box' Model

The benefits of accurate corrosion models for both industrial and research applications are clear. However, their use is often limited by their complex nature and the need for specialist knowledge in order to make them function

reliably. A potential solution to this problem is via the development of a ‘black box’ model which hides the underlying mathematics from the end user. These models operate by simply requiring the user to enter their specific input conditions and then providing a pre-selected list of relevant outputs based on the model’s calculations. In this instance, the user has little control over the model itself, which simplifies the experience significantly, allowing it to be used much more widely.

Black box models are very useful for industrial applications, as evidenced by the existence of models such as the NORSOK[98], Hydocor[166], Corpos[167], and Cassandra[168] models[169], each developed by various industrial companies. These models vary in complexity, both in terms of required inputs, as well as the outputs they produce, but they each allow for rapid evaluation of corrosion behaviour without a full understanding of the supporting mathematics being necessary.

There are many ways in which a black box model can be produced, two of the most relevant approaches are discussed here. The first relates to forming a series of equations which directly relate outputs to their inputs based on a large data set. The second relates to building a graphical user interface (GUI) within COMSOL, which allows the base model to be run directly from a simplified interface.

5.4.4.2.1 Multivariate Function

The process of curve fitting to a set of data is a well-established practice, and in fact forms the basis of many of the reaction rate equations used within the mechanistic models. Empirical models for corrosion prediction use this same technique, scaling mathematical functions via correction factors to fit experimental data[31]. However, such models are generally limited to a small range of conditions due to the difficulties with running large-scale multi-variable experiments. The lack of a theoretical foundation for the formulae also limits extrapolation beyond the range of parameters for which the model has been developed.

The limitation of experimentally derived empirical data could be avoided however by instead basing the formula of the outputs of a fully mechanistic model. As discussed previously, with a one-dimensional computational model, it is entirely possible to run a very large number of simulations across a wide range of input parameters. By first generating a large output data set from a representative selection of inputs, as discussed in Section 5.4.4.1, multivariate

polynomial regression techniques can then be used to define output values as functions of the inputs. For example, the corrosion rate could be defined as a function of the six inputs discussed previously:

$$CR = f\left(T, P_{CO_2}, pH, v, d, I\right) \tag{5.35}$$

There are various methods that can be used to perform the polynomial fitting, however, given the previous use of MATLAB LiveLink™ to perform parametric sweeps, an appropriate approach may be to use the 'polyfit' or 'polyfitn' functions within MATLAB. The polyfit function calculates the coefficients of n^{th} order polynomial which produce the best fit using a least-squares approach[170]. The corresponding R^2 value can then be used to determine whether or not an accurate polynomial fit could be achieved. If not, a more involved technique such as surrogate modelling, discussed in the following section, may be required.

5.4.4.2.2 Surrogate Modelling

Whilst an efficient and relatively simple approach, it may not always be possible to obtain a sufficiently strong data fit via polynomial regression. Therefore, a more robust approach would be to train a surrogate model which uses machine learning to train a model based on an existing dataset. As of version 6.2[171], the functionality to do exactly this have been introduced into COMSOL Multiphysics®.

The purpose of a surrogate model is to provide an approximation of a given output without needing to actually solve the primary model. In order to do this, COMSOL utilises a known data set to train the model via a deep neural network (DNN). The DNN attempts to replicate learning process of the brain to determine links between inputs and outputs

A number of layers and nodes within the DNN are specified based upon the complexity of the data, and then the known data is fed into the machine learning algorithm. The data is divided into training data, used to teach the model how the outputs relate to the inputs, and validation data used to check whether the model can accurately predict outputs[172]. It is important to ensure that sufficient data is used to train the model to accurately capture the relationships between the inputs and outputs. However, if too much data is provided to the model, the issue of overtraining may arise, in which the model effectively remembers results as opposed to predicting values, which may reduce accuracy[173]. Development of a strong surrogate model may require

some fine-tuning in regard to the structure and number of nodes and layers, as well as the size of the training data set. But, once a surrogate model is created which is able to accurately determine how a change in a given input affects the corresponding output, it becomes a powerful tool for rapid evaluation of corrosion behaviour. The removal of the need to run the full model reduces the solver time and can be combined with a COMSOL application to make it accessible to those unfamiliar with the software.

5.4.4.2.3 COMSOL Application

Within COMSOL Multiphysics®, there is in-built functionality to create applications via a tool known as the 'application builder'[174]. The applications built with this tool generally solve the same equations as the full model (although they can be used to run surrogate models), however the designer of the application is able to limit the parameters and variables that can be adjusted by the user. Additionally, the output plots and tables produced can be pre-defined to both allow for rapid evaluation of the results, and to hide any superfluous information. For example, an application built for the corrosion model discussed within this section could provide the 6 variables outlined in section 5.4.4.1 as inputs, with limits defining the maximum and minimum input values. The outputs may then include, for example, tables or plots of the corrosion rate, surface pH, bulk solution chemistry, velocity flow field, surface saturation index, or the surface potential.

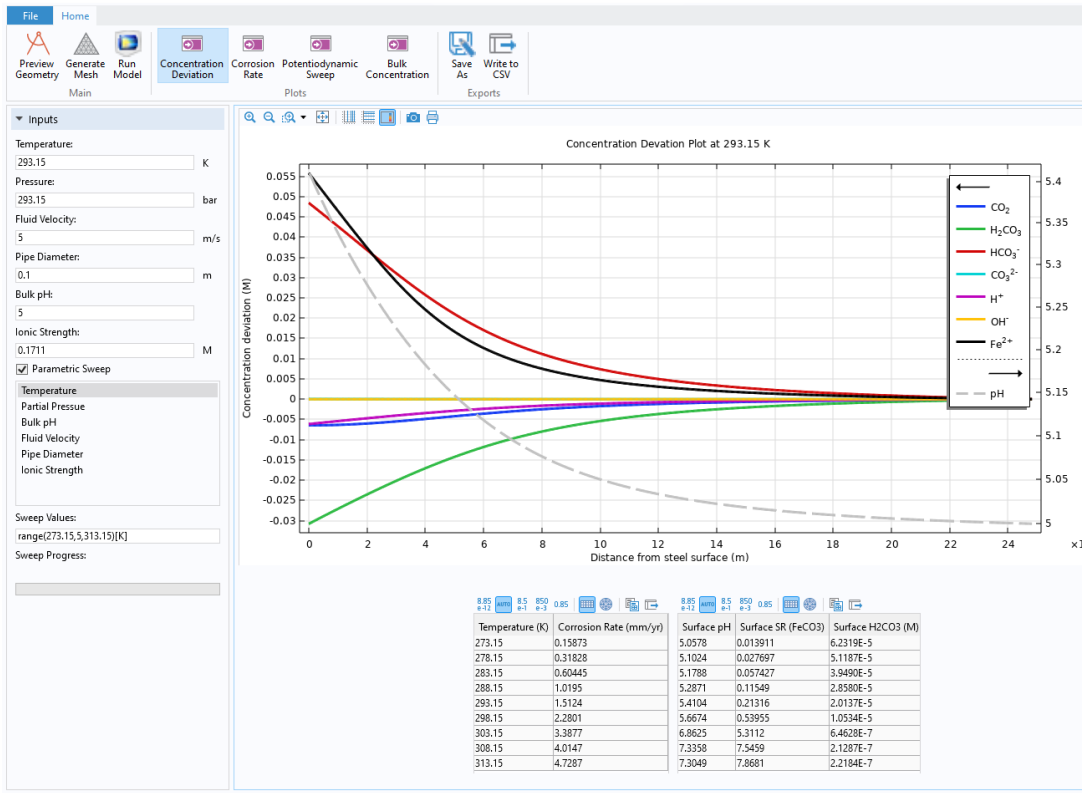

Temperature (K)	Corrosion Rate (mm/yr)
273.15	0.15873
278.15	0.31828
283.15	0.60445
288.15	1.0195
293.15	1.5124
298.15	2.2801
303.15	3.3877
308.15	4.0147
313.15	4.7287

Surface pH	Surface SR (FeCO3)	Surface H2CO3 (M)
5.0578	0.013911	6.2319E-5
5.1024	0.027697	5.1187E-5
5.1788	0.057427	3.9490E-5
5.2871	0.11549	2.8580E-5
5.4104	0.21316	2.0137E-5
5.6674	0.53955	1.0534E-5
6.8625	5.3112	6.4628E-7
7.3358	7.5459	2.1287E-7
7.3049	7.8681	2.2184E-7

Figure 5-12 – Example COMSOL application with showing input options, output plot options and data tables.

Functional applications can also be compiled into standalone executable files, which are useable without the need for a COMSOL license. Compiling an application allows for it to be shared with individuals who may not have the required software installed to evaluate the full model. Additional guidance and information can be provided to the user via the GUI in order to remove the necessity for specific training to use the application.

Chapter 6 - Conclusion

In this concluding chapter, an overview of the final state of the developed models is provided alongside a compiled summary of the main findings discussed throughout the preceding chapters of this thesis. The novelty of the completed work is reviewed and discussed in relation to the existing works in the field of CO_2 corrosion modelling. Finally, the applications of the completed work, both in relation to industrial applications, as well as the advancement of the academic field are discussed.

6.1 Final State of Developed Models

Two separate one-dimensional CO_2 corrosion models based on existing works have been re-created within the COMSOL Multiphysics® software. The first, based on the 2003 work by Nordsveen *et al*.[26], implements the direct reduction mechanism of CO_2 corrosion which comprises two cathodic reactions, H^+ reduction and H_2CO_3 reduction. The second, based on work by Kahyarian *et al*.[12, 36], implements the buffering mechanism of CO_2 corrosion, which utilises only one cathodic reaction, being H^+ reduction. Both corrosion models were validated against the respective literature to ensure that they accurately reflected the results used as the basis for each model's respective development. Regions of inaccuracy were identified in both models due to the limitations of the equations defining the electrode kinetics. Discontinuities were identified in the first model as a function of pH due to step changes in the kinetic variables. In the second model, the H^+ concentration on the surface node under mass-transport control region was found to be superficially low due to the solver method. In both cases, these issues have been highlighted and functional solutions have been proposed, via either the implementation of a continuous function in the first instance, or via 2nd node evaluation or a damping function in the second instance. Despite this, both models have been developed to a functional state, capable of performing rapid analysis under a range of conditions that allows for in-depth analysis.

Code has been written in MATLAB LiveLink™ which can be used to directly drive each of the COMSOL models. By using the linked software, an approach has been developed which is facilitates rapid generation and storage of large data sets representing a wide range of input conditions. In each case, these MATLAB scripts have been written to automatically record relevant output values, including corrosion rate, surface pH, surface $FeCO_3$ saturation ratio, and surface species concentrations.

A new methodology for integrating hydrodynamic effects via turbulence models has also been created. By solving both the turbulence model and the corrosion model, a one-way coupling has been established between the two, evaluating corrosion behaviour at specified positions along a geometry. The validity of this method was first established utilising a straight pipe model and subsequently provided the foundations for applying the corrosion model to different geometries, as demonstrated by a converging channel model. Following this validation and testing, a scale representation of an RCE was modelled within COMSOL. The hydrodynamic methodology was used to extract the characteristics of the flow near the rotating surface to ultimately produce a new RCE corrosion model. This model allowed for a more accurate representation of a standard experimental set-up to be used when comparing experimental and simulated results.

6.2 Main Findings

Numerical explorations of both corrosion models were conducted and compared to experimental data collected via an RCE. The model based on the work of Nordsveen *et al*.[26] predicted consistent increases in the corrosion rate with partial pressure and pH, as well as a general increasing trend with temperature. The complexities of the interactions within the model, in particular, the inclusion of the direction reduction of H_2CO_3 produced various contour shapes based upon the combined set of modelled conditions. Surface pH was found to increase at the surface across all conditions due to the loss of H^+, with the greatest change occurring at high temperature, low pressure when the surface reaction rates occur quickly but the bulk concentration of H_2CO_3 is low. Across the range of conditions tested, it was found invariably that the increased rate of species transport at higher temperature due to the thinner boundary layer and higher diffusion rates were not sufficient to overcome the increased surface consumption of H^+. This in turn shifted the ratio of the cathodic reactions in favour of the H_2CO_3 reduction reaction due to the relatively high surface concentration. In regard to $FeCO_3$ surface saturation, the saturation index predicted by the model was found to increase in a reasonably predictable manner with increasing pressure and temperature. At higher pHs the system was supersaturated at the surface across most of the evaluated conditions due to the increased CO_3^{2-} concentration in solution.

When compared to experimental data, the Nordsveen model performed strongly in predicting corrosion rates in less-aggressive environments. At pH 5 and 6 the model was able to accurately predict corrosion behaviour in

response to changing temperatures and hydrodynamic conditions. Under more-aggressive conditions however, at higher temperatures and low pH, the model was found to underpredict the corrosion rate. Further investigation of the model suggested that this underprediction may be due to a combination of H_2CO_3 reduction compensating for any significant drop in H^+ concentration, as well as a steps change in the anodic kinetics when the surface pH reached either 4 or 5.

From the numerical exploration of the model based on the work by Kahyarian *et al*.[12, 36] the primary finding was the identification of two distinct response patterns based upon the modelled conditions. The first region, occurring at low temperatures and high CO_2 partial pressures predicted corrosion rates that were independent of both changes in pressure and hydrodynamic conditions. Investigation of the model revealed this to be due to the system being under charge-transfer control at these conditions and therefore limited by the rate of the surface reactions. This was further supported by the small difference between the surface and bulk pHs, indicating a high surface H^+ concentration. Conversely, the second region, which was found to be under mass-transport control, was highly sensitive to changes in the pressure and fluid velocity. The high rate of consumption of H^+ ions relative to the supply resulted in very high surface pH values in this region, as well as an increased dependence on factors which increased the surface concentration. The temperature dependence was reduced in this region the system is insensitive to increased surface reaction rates, however the higher rates of species transport from the bulk did still produce an increase in the corrosion rate with temperature. The contrast of these two regimes produced a complex transition region when plotting the $FeCO_3$ SI as a function of P_{CO2} and temperature. In both regions a stable and predictable response was eventually reached, however the differences between the responses produced a region in which the saturation behaviour was highly unstable due to the competing influences.

When compared to the experimental data, the Kahyarian model performed strongly at low pH conditions, with strong correlation to the experimental data even at the higher temperatures. This indicated strong performance when the system was charge-transfer controlled. However, at higher pHs, the model had a tendency to significantly overpredict the corrosion rate, particularly at higher temperatures. Under these conditions, the surface H^+ concentration dropped very low, drastically increasing the rate of H_2CO_3 dissociation. The H^+ ions produced in this reaction were then immediately consumed, increasing the corrosion rate. In general, the Kahyarian model could predict the general

response of the system to increases in temperature, pH, and rotation speed (fluid velocity). However, the surface chemistry immediately adjacent to the corroding surface under harsh, mass-transport limited conditions was found to introduce a degree of unreliability.

In regard to the incorporation of CFD into the corrosion models, it was found that this could be achieved by combining the law of the wall theory with simulated data from a turbulence model in COMSOL. Data from a simulated pipe flow was found to strongly correlate with the empirical values used in both of the published corrosion models. When expanding to a converging channel, evaluation of δ and D_T along cut-lines across the surface allowed for the corrosion rate to be predicted as a function of the position along the surface. A slight complication was found when applying the approach to an RCE model, as the moving wall produced an off-set between the simulated and theoretical u^+ values. However, it was found that this could be resolved by relative gradients of the u^+ vs y^+ plots to determine the value of δ. By using this approach, a simulated model of an RCE could be developed and used to perform a more direct comparison between experimental and simulated data.

6.3 Industrial Relevance and Novelty

In an industrial context, accurate and reliable prediction of corrosion behaviour and factors such as the growth of surface films are important for economic and environmental reasons, as well as for safety. Knowing how, when and where a system might be vulnerable to the effects of corrosion can allow for preventative measures to be taken in order to avoid potential failure. The work conducted throughout this thesis is highly relevant in this regard. The numerical explorations of tens of thousands of input conditions into each of the corrosion models goes far beyond any currently available literature. By conducting such an extensive study, results can be published demonstrating how these models behave in response to a wide array of conditions that may be found in real-world applications. The hydrodynamic advancement also allows the application of the existing corrosion models to be expanded beyond the current 1-D straight pipe scenario. The flexibility of the generalised approach allows more complex geometry features, such as beds and changes in diameter to be evaluated to produce more refined models of specific systems. For industrial applications this means that bespoke corrosion models can be generated that much more accurately reflect the real-world environment.

The independent experimental evaluation of each of the models also provides useful insight into the accuracy of each of the corrosion models. By performing validation against a system that is completely separate from the environment in which the models were initially developed, the robustness of the models has been shown for general applications. The experimental work has also provided new insights as to the relative performance of the two models and the conditions in which each showed the strongest correlation with real-world data. This is vitally important information for industrial applications in choosing a corrosion model to adopt for a given system, as the simulation can be tailored to the application.

Lastly, the industrial relevance of constructing a comprehensive mechanistic model of CO_2 corrosion within multiphysics software such as COMSOL cannot be understated. As seen throughout this work, corrosion is a highly complicated topic with many influencing factors. It is not feasible to account for all physical phenomena in a general model of CO_2 corrosion, however the novelty of the models constructed here is the ease with which additional factors can be introduced. This has been demonstrated in this work through the integration of CFD, however further development could introduce specialised physics to refine the models further for specific applications. By building the models within COMSOL Multiphysics, a framework has been created that facilitates the rapid production of unique and highly specialised industrially-relevant models.

6.4 Contribution to Academic Advancement

It is the belief of the author that the outputs of this work have made a significant contribution to the academic field both within the University of Leeds and in the wider academic community. This is evidenced by the numerous publications in both conference proceedings and academic journals that have been the direct result of this work. The numerical explorations conducted offer a vast array of reference points for future academic works, both numerical and experimental. As well as this, the hydrodynamic methodology produced provides a pathway for the development of specialised corrosion models.

Additionally, as explored in detail in Chapter 5, the production of both corrosion models within COMSOL Multiphysics facilitates a range of further development opportunities. Expansion of the current equations into two- or three-dimensional space, combined with the hydrodynamic methodology detailed here, would allow for complete evaluation of complex surfaces. Combined with

the incorporation of galvanic effects, this would expand mechanistic modelling capabilities far beyond current models.

However, even in one dimension, the models produced throughout this work provide a basis for significant advancement in the modelling of surface films. A simple version of this can be achieved by incorporating a diffusion barrier of a fixed thickness within the existing, which would allow for examination of the effects of restricted ionic movement through a film. A more complex version could introduce factors such as the local depletion of ions and moving boundaries, both of the corroding surface and of the film itself. COMSOL's multiphysics capabilities even make it possible to account for local changes in the characteristics of the film. Each of these developments would constitute a highly useful advancement to the academic field and is possible to produce as an extension the fundamental work conducted throughout this thesis.

References

1. Koch, G., Varney, J., Thompson, N., Moghissi, O., Gould, M. and Payer, J. *International Measures of Prevention, Application, and Economics of Corrosion Technologies Study.* Houston, TX, 2016.
2. Karlsdóttir, S.N. *Corrosion, Scaling and Material Selection in Geothermal Power Production.* Amsterdam: Elsevier Ltd, 2012.
3. Revie, R.W. *UHLIG's corrosion handbook, third edition.* 3rd ed. ed. Hoboken, N.J: John Wiley & Sons, Inc., 2011.
4. McCafferty, E. *Introduction to corrosion science.* New York: Springer, 2010.
5. Robertson, J.O. and Chilingar, G.V. Corrosion. In: *Environmental Aspects of Oil and Gas Production*. first ed. United States: John Wiley & Sons, 2017, pp.269-328.
6. Guo, X., Gin, S., Lei, P., Yao, T., Liu, H., Schreiber, D.K., Ngo, D., Viswanathan, G., Li, T., Kim, S.H., Vienna, J.D., Ryan, J.V., Du, J., Lian, J. and Frankel, G.S. Self-Accelerated Corrosion of Nuclear Waste Forms at Material Interfaces. *Nature materials.* 2020, **19**(3), pp.310-316.
7. Nogara, J. and Zarrouk, S.J. Corrosion in geothermal environment: Part 1: Fluids and their impact. *Renewable & sustainable energy reviews.* 2018, **82**, pp.1333-1346.
8. Kaya, T. and Hoşhan, P. Corrosion and Material Selection for Geothermal Systems. In: *World Geothermal Congress*, *24-29 April 2005*, *Antalya, Turkey*. International Geothermal Assosciation, 2005, pp.1-5.
9. Barker, R., Burkle, D., Charpentier, T., Thompson, H. and Neville, A. A Review of Iron Carbonate ($FeCO_3$) Formation in the Oil and Gas Industry. *Corrosion Science.* 2018, **142**, pp.312-341.
10. Butler, J.N. *Carbon Dioxide Equilibria and Their Applications.* Florida: CRC Press, 1982.
11. Kern, D.M. The hydration of carbon dioxide. *Journal of Chemical Education.* 1960, **37**(1), p.14.
12. Kahyarian, A. and Nešić, S. On the Mechanism of Carbon Dioxide Corrosion of Mild Steel: Experimental Investigation and Mathematical Modeling at Elevated Pressures and Non-Ideal Solutions. *Corrosion Science.* 2020, **173**, pp.1-27.
13. Hernandez, J., Muñoz, A. and Genesca, J. Formation of iron-carbonate scale-layer and corrosion mechanism of API X70

pipeline steel in carbon dioxide-saturated 3% sodium chloride. *Afinidad.* 2013, **69**(560).
14. Barker, R., Al Shaaili, I., De Motte, R.A., Burkle, D., Charpentier, T., Vargas, S.M. and Neville, A. Iron carbonate formation kinetics onto corroding and pre-filmed carbon steel surfaces in carbon dioxide corrosion environments. 2019.
15. Sun, W. and Nešić, S. Kinetics of Corrosion Layer Formation. Part 1-Iron Carbonate Layers in Carbon Dioxide Corrosion. *Corrosion (Houston, Tex.).* 2008, **64**(4), pp.334-346.
16. Sun, W., Nešić, S. and Woollam, R.C. The effect of temperature and ionic strength on iron carbonate (FeCO 3) solubility limit. *Corrosion Science.* 2009, **51**(6), pp.1273-1276.
17. Dugstad, A. Fundamental Aspects of CO_2 Metal Loss Corrosion - Part 1: Mechanism. In: *Corrosion*, *March 2006*, *California*. U.S.A.: NACE International, 2006, pp.1-18.
18. Burkle, D.P. *Understanding the Formation of Protective FeCO3 on to Carbon Steel Pipelines during CO2 Corrosion*. PhD thesis, University of Leeds, 2017.
19. Lasaga, A.C. *Kinetic Theory in the Earth Sciences.* 1st ed. Princeton, N.J: Princeton University Press, 1998.
20. Greenberg, J. and Tomson, M. Precipitation and Dissolution Kinetics and Equilibria of Aqueous Ferrous Carbonate vs Temperature. *Applied Geochemistry.* 1992, **7**(2), pp.185-190.
21. Johnson, M.L. and Tomson, M.B. Ferrous Carbonate Precipitation Kinetics and Its Impact CO_2 Corrosion. In: *CORROSION 91*, *11-15 March 1991*, *Cincinnati, Ohio*. Texas, U.S.A.: NACE, 1991, pp.1-16.
22. Van Hunnik, E., Pots, B.F.M. and Hendriksen, E.L.J.A. The Formation of Protective $FeCO_3$ Corrosion Product Layers in CO_2 Corrosion. In: *CORROSION 96*, *Denver, Colorado*. U.S.A.: NACE International, 1996, pp.1-22.
23. Woollam, R.C., Yang, Y. and Nešić, S. *Evaluation of Models for Ferrous Carbonate (FeCO3) Precipitation Kinetics*. Unpublished,
24. Turgoose, S., Cottis, R.A. and Lawson, K. Modeling of Electrode Processes and Surface Chemistry in Carbon Dioxide Containing Solutions. In: Munn, R.S. ed. *Computer Modeling in Corrosion*. Philadelphia: ASTM International, 1992, pp.67-81.
25. Nešić, S., Nyborg, R., Stangeland, A. and Nordsveen, M. Mechanistic Modeling for CO_2 Corrosion with Protective Iron

Carbonate Films. In: *CORROSION 2001*, *11 March 2001*, *Texas*. U.S.A.: NACE International, 2001.
26. Nordsveen, M., Nešić, S., Nyborg, R. and Stangeland, A. A Mechanistic Model for Carbon Dioxide Corrosion of Mild Steel in the Presence of Protective Iron Carbonate Films - Part 1: Theory and Verification. *Corrosion.* 2003, **59**(5), pp.443-456.
27. Prabhakara, S. and Deshpande, M.D. The No-Slip Boundary Condition in Fluid Mechanics: 1. The Riddle of Fluid Sticking to the Wall in Flow. *Resonance.* 2004, **9**(4), pp.50-60.
28. Davies, J.T. *Turbulence Phenomena.* first ed. ed. New York, U.S.A.: Academic Press, Inc., 1972.
29. Misra, K.C. *Introduction to Geochemistry: Principles and Applications.* first ed. ed. Oxford: Wiley-Blackwell, 2011.
30. de Waard, C. and Milliams, D.E. Carbonic Acid Corrosion of Steel. *Corrosion.* 1975, **31**(5), pp.177-181.
31. Kahyarian, A., Singer, M. and Nešić, S. Modeling of Uniform CO_2 Corrosion of Mild Steel in Gas Transportation Systems: A Review. *Journal of Natural Gas Science and Engineering.* 2016, **29**, pp.530-549.
32. Remita, E., Tribollet, B., Sutter, E., Vivier, V., Ropital, F. and Kittel, J. Hydrogen Evolution in Aqueous Solutions Containing Dissolved CO_2: Quantitative Contribution of the Buffering Effect. *Corrosion Science.* 2008, **50**(5), pp.1433-1440.
33. Tran, T., Brown, B. and Nešić, S. Corrosion of Mild Steel in an Aqueous CO_2 Environment – Basic Electrochemical Mechanisms Revisited. In: *Corrosion*, *2015*, *Dallas, Texas*. NACE International, 2015, pp.1-11.
34. Linter, B.R. and Burstein, G.T. Reactions of Pipeline Steels in Carbon Dioxide Solutions. *Corrosion Science.* 1999, **41**(1), pp.117-139.
35. Song, F.M., Kirk, D.W., Graydon, J.W. and Cormack, D.E. Predicting Carbon Dioxide Corrosion of Bare Steel Under an Aqueous Boundary Layer. *Corrosion.* 2004, **60**(8), pp.736-748.
36. Kahyarian, A. and Nešić, S. A New Narrative for CO_2 Corrosion of Mild Steel. *Journal of the Electrochemical Society.* 2019, **166**(11), pp.C3048-C3063.
37. Nešić, S., Nordsveen, M., Nyborg, R. and Stangeland, A. A Mechanistic Model for Carbon Dioxide Corrosion of Mild Steel in the Presence of Protective Iron Carbonate Films -

Part 2: A Numerical Experiment. *Corrosion.* 2003, **59**(6), pp.489-497.
38. Nešić, S. and Lee, K.L.J. A Mechanistic Model for Carbon Dioxide Corrosion of Mild Steel in the Presence of Protective Iron Carbonate Films - Part 3: Film Growth Model. *Corrosion.* 2003, **59**(7), pp.616-628.
39. Alsalem, M.M., Ryan, M.P., Campbell, A.N. and Campbell, K.S. Modelling of CO_2 Corrosion and $FeCO_3$ Formation in NaCl Solutions. *Chemical Engineering Journal.* 2023, **451**(11), pp.1-19.
40. Schlichting, H. and Gersten, K. *Boundary-Layer Theory.* Ninth ed. Berlin, Germany: Springer, 2017.
41. Von Kármán, T. *Mechanical Similitude and Turbulence.* Washington D.C., 1931.
42. Coles, D. The law of the wake in the turbulent boundary layer. *Journal of fluid mechanics.* 1956, **1**(2), pp.191-226.
43. Notter, R.H. and Sleicher, C.A. The Eddy Diffusivity in the Turbulent Boundary Layer Near a Wall. *Chemical Engineering Science.* 1971, **26**(1), pp.161-171.
44. Ting, D.S.K. *Wall Turbulence.* first ed. ed. London: Academic Press, 2016.
45. Cebeci, T. General Behavior of Turbulent Boundary Layers. In: *Analysis of Turbulent Flows with Computer Programs*. 2nd ed. Amsterdam: Elsevier Science & Technology, 2004, pp.81-140.
46. Spalding, D.B. A Single Formula for the "Law of the Wall". *Journal of Applied Mechanics.* 1961, **28**(3), pp.455-458.
47. Laufer, J. *The Structure of Turbulence in Fully Developed Pipe Flow.* Washington D.C.: National Bureau of Standards, 1952.
48. Ali, S.Z. and Dey, S. The Law of the Wall: A New Perspective. *Physics of Fluids.* 2020, **32**(12).
49. Stanković, B., Stojanović, A.D., Sijerčić, M., Belošević, S. and Čantrak, S. Evaluation and limitations of standard wall functions in channel and step flow configurations. *Journal of the Serbian Society for Computational Mechanics.* 2014, **8**(1), pp.1-22.
50. Butler, J.A.V. The mechanism of overvoltage and its relation to the combination of hydrogen atoms at metal electrodes. *Transactions of the Faraday Society.* 1932, **28**, pp.379-382.
51. Butler, J.A.V. Studies in heterogeneous equilibria. Part II.—The kinetic interpretation of the nernst theory of electromotive

force. *Transactions of the Faraday Society.* 1924, **19**(March), pp.729-733.
52. Butler, J.A.V. Studies in heterogeneous equilibria. Part III. A kinetic theory of reversible oxidation potentials at inert electrodes. *Transactions of the Faraday Society.* 1924, **19**(March), p.734.
53. Erdey-Grúz, T. and Vomer, M. Zur Theorie der Wasserstoff Überspannung. *Zeitschrift für Physikalische Chemie.* 1930, **150A**(1), pp.203-213.
54. Dickinson, E.J.F. and Wain, A.J. The Butler-Volmer equation in electrochemical theory: Origins, value, and practical application. *Journal of electroanalytical chemistry (Lausanne, Switzerland).* 2020, **872**, p.114145.
55. Stern, M. and A.L.Geary. Electrochemical Polarization: I . A Theoretical Analysis of the Shape of Polarization Curves. *Journal of the Electrochemical Society.* 1957, **104**(1), pp.56-63.
56. Lazanas, A.C. and Prodromidis, M.I. Electrochemical Impedance Spectroscopy - A Tutorial. *ACS measurement science au.* 2023, **3**(3), pp.162-193.
57. Orazem, M.E. and Tribollet, B. A Tutorial on Electrochemical Impedance Spectroscopy. *ChemTexts (Cham).* 2020, **6**(2), pp.1-9.
58. Jacklin, R., Owen, J., Sykes, A., Burkle, D., Woollam, R.C. and Barker, R. An Electrochemical Study of Iron Carbonate Layers Formed on Carbon Steel During Corrosion in Elevated Pressure CO_2 Environments. *Corrosion Science.* 2024, **235**, pp.1-13.
59. Barker, R., Pickles, B., Kapur, N., Hughes, T., Barmatov, E. and Neville, A. Flow Cell Apparatus for Quantitative Evaluation of Carbon Steel Corrosion During Transitions in Fluid Composition: Application to Transition From Inhibited Hydrochloric Acid to Sodium Chloride Brine. *Corrosion Science.* 2018, **138**, pp.116-129.
60. Duan, Z. and Li, D. Coupled Phase and Aqueous Species Equilibrium of the H_2O–CO_2–NaCl–$CaCO_3$ System From 0 to 250°C, 1 to 1000 bar with NaCl Concentrations up to Saturation of Jalite. *Geochimica et Cosmochimica Acta.* 2008, **72**(20), pp.5128-5145.
61. Li, D. and Duan, Z. The Speciation Equilibrium Coupling with Phase Equilibrium in the H_2O–CO_2–NaCl System From 0 to 250 °C, from 0 to 1000 bar, and from 0 to 5 Molality of NaCl. *Chemical Geology.* 2007, **244**(3-4), pp.730-751.

62. Marshall, W.L. and Franck, E.U. Ion Product of Water Substance, 0–1000 °C, 1–10,000 bars New International Formulation and its Background. *Journal of Physical and Chemical Reference Data.* 1981, **10**(2), pp.295-304.
63. Palmer, D.A. and van Eldik, R. The chemistry of metal carbonato and carbon dioxide complexes. *Chemical reviews.* 1983, **83**(6), pp.651-731.
64. Bistafa, S.R. On the Development of the Navier-Stokes equation by Navier. *Revista Brasileira de Ensino de Física.* 2018, **40**(2), pp.1-12.
65. Hirsch, C. *Numerical computation of internal and external flows introduction to the fundamentals of CFD.* New edition. ed. Oxford: Butterworth-Heinemann, 2007.
66. McLean, D. Continuum Fluid Dynamics and the Navier-Stokes Equations. In: *Understanding Aerodynamics: Arguing from the Real Physics*. UK: Wiley, 2013, pp.13-78.
67. Lemarié-Rieusset, P.G. *The Navier-Stokes Problem in the 21st Century.* first ed. New York: CRC Press, 2016.
68. Garde, R.J. *Turbulent Flow.* third ed. London, UK: New Academic Science Ltd., 2010.
69. Alfonsi, G. Reynolds-Averaged Navier–Stokes Equations for Turbulence Modeling. *Applied mechanics reviews.* 2009, **62**(4).
70. Schmitt, F.G. About Boussinesq's turbulent viscosity hypothesis: historical remarks and a direct evaluation of its validity. *Comptes Rendus Mécanique.* 2007, **335**(9-10), pp.617-627.
71. Gorman, J., Bhattacharyya, S., Cheng, L. and Abraham, J.P. Turbulence Models Commonly Used in CFD. In: Bhattacharyya, S. ed. *Applications of Computational Fluid Dynamics Simulation and Modeling*. London, UK: IntechOpen, 2022, pp.11-30.
72. Marvin, J.G. and Huang, G.P. *Turbulence Modeling - Progress and Future Outlook.* Moffett Field, California: National Aeronautics and Space Administration, Ames Research Center, 1996.
73. Prandtl, L. Bericht über Untersuchungen zur ausgebildeten Turbulenz. *Journal of Applied Mathematics and Mechanics.* 1925, **5**(2), pp.136-139.
74. Smith, A.M. and Cebeci, T. *Numerical Solution of the Turbulent-Boundary-Layer Equations.* Long Beach, CA, U.S.A.: Douglas Aircraft Company, 1967.

75. Baldwin, B.S. and Lomax, H. Thin Layer Approximation and Algebraic Model for Separated Turbulent Flows. In: *AIAA 16th Aerospace Sciences Meeting*, *Huntsville, AL, U.S.A.*: American Institute of Aeronautics and Astronautics, 1978.
76. Spalart, P.R. and Allmaras, S.R. A One-Equation Turbulence Model for Aerodynamic Flows. *La Recherche Aérospatiale.* 1994, **1**, pp.5-21.
77. Baldwin, B.S. and Barth, T.J. *A One-Equation Turbulence Transport Model for High Reynolds Number Wall-Bounded Flows.* California, U.S.A.: NASA, 1990.
78. Ting, D.S.K. Turbulence Simulations and Modeling. In: *Basics of Engineering Turbulence*. London, UK: Elsevier Inc, 2016, pp.99-118.
79. COMSOL. *CFD Module User's Guide.* [Online]. Stockholm, Sweden: COMSOL, 2019. [Accessed 21/01/2021]. Available from: https://doc.comsol.com/5.5/doc/com.comsol.help.cfd/CFDModuleUsersGuide.pdf
80. Sip, J., Pokorny, J., Fiser, J., Lizal, F. and Jicha, M. New Ventilation Schemes of Car Cabin Evaluated by CFD Simulations. *EPJ Web of Conferences.* 2022, **269**, p.1056.
81. Xu, X., Wu, J., Weng, W. and Fu, M. Investigation of Inhalation and Exhalation Flow Pattern in a Realistic Human Upper Airway Model by PIV Experiments and CFD Simulations. *Biomechanics and modeling in mechanobiology.* 2020, **19**(5), pp.1679-1695.
82. Lin, C.H. and Ferng, Y.M. Predictions of Hydrodynamic Characteristics and Corrosion Rates Using CFD in the Piping Systems of Pressurized-Water Reactor Power Plant. *Annals of nuclear energy.* 2014, **65**, pp.214-222.
83. van der Laan, M.P., Sørensen, N.N., Réthoré, P.-E., Mann, J., Kelly, M.C., Troldborg, N., Schepers, J.G. and Machefaux, E. An Improved k- ϵ Model Applied to a Wind Turbine Wake in Atmospheric Turbulence. *Wind Energy.* 2014, **18**(5), pp.889-907.
84. Dhahri, M., Aouinet, H. and Mhamdi, N. CFD Analysis of the Effect of Uniformly Sheared Air Flow on Natural Ventilation in Building. *International journal of ambient energy.* 2022, **43**(1), pp.818-829.
85. Li, T., Qin, D. and Zhang, J. Effect of RANS Turbulence Model on Aerodynamic Behavior of Trains in Crosswind. *Chinese journal of mechanical engineering.* 2019, **32**(1), pp.1-12.

86. Heinz, S. A Review of Hybrid RANS-LES Methods for Turbulent Flows: Concepts and Applications. *Progress in aerospace sciences.* 2020, **114**(100597), pp.1-25.
87. Pan, Y. and Persson, P.O. High-order accurate finite difference discretisations on fully unstructured dual quadrilateral meshes. *Journal of computational physics.* 2022, **461**, pp.1-19.
88. Blazek, J. Chapter 3 - Principles of Solution of the Governing Equations. In: *Computational Fluid Dynamics: Principles and Applications*. second ed. Great Britain: Elsevier, 2005, pp.29-75.
89. Tu, J., Yeoh, G.H. and Liu, C. *Computational Fluid Dynamics a Practical Approach.* 1st ed. Amsterdam: Butterworth-Heinemann, 2008.
90. Yasuki, N. Computational Fluid Dynamics. In: Valutkevich, A. ed. *Introduction to Fluid Mechanics*. Second ed. Tokyo, Japan: Elsevier Ltd, 2018, pp.293-327.
91. Chung, T.J. Relationships Between Finite Differences and Finite Elements and Other Methods. In: *Computational Fluid Dynamics*. USA: Cambridge University Press, 2002, pp.509-530.
92. Veressm, Á. and Rohács, J. Application of Finite Volume Method in Fluid Dynamics and Inverse Design Based Optimization. In: Petrova, R. ed. *Finite Volume Method : Powerful Means of Engineering Design*. Rijeka, Croatia: IntechOpen, 2012, pp.3-34.
93. Chung, T.J. Introduction. In: *Computational Fluid Dynamics*. USA: Cambridge University Press, 2002, pp.3-28.
94. Obbink-Huizer, C. Implicit Vs Explicit Finite Element Analysis: When to Use Which? 2021. [Online]. Available from: https://simulation-blog.technia.com/simulation/implicit-vs-explicit-finite-element-analysis
95. COMSOL. Single-Phase Flow Interfaces. *CFD Module User's Guide 5.5.* [Online]. Stockholm, Sweden: COMSOL, 2019, pp.56-239. [Accessed 28/04/2021].
96. Owen, J., Godfrey, J., Ma, W., de Boer, G., Al-Khateeb, M., Thompson, H., Neville, A., Ramsey, C. and Barker, R. An Experimental and Numerical Investigation of CO_2 Corrosion in a Rapid Expansion Pipe Geometry. *Corrosion Science.* 2019, **165**.
97. Dana, M.M. and Javidi, M. Corrosion Simulation via Coupling Computational Fluid Dynamics and NORSOK CO_2 Corrosion Rate Prediction Model for an Outlet Header Piping of an Air-

Cooled Heat Exchanger. *Engineering failure analysis.* 2021, **122**, pp.1-17.
98. Norwegian Oil Industry Association and Federation of Norwegian Manufacturing Industries. *NORSOK Standard M-506.* Norway: Standards Norway, 2005.
99. Thorat, U., Jones, M., Woollam, R., Owen, J., Barker, R., Thompson, H. and de Boer, G. Computational Fluid Dynamics Driven Mass Transfer Model for the Prediction of CO_2 Corrosion in Pipelines. *Journal of Pipeline Science and Engineering.* 2023.
100. Nešić, S., Solvi, G.T. and Enerhaug, J. Comparison of the Rotating Cylinder and Pipe Flow Tests for Flow-Sensitive Carbon Dioxide Corrosion. *Corrosion.* 1995, **51**(10), pp.773-787.
101. Liu, X., Gong, C., Zhang, L., Jin, H. and Wang, C. Numerical Study of the Hydrodynamic Parameters Influencing Internal Corrosion in Pipelines for Different Elbow Flow Configurations. *Engineering applications of computational fluid mechanics.* 2019, **14**(1), pp.122-135.
102. Gnanavelu, A., Kapur, N., Neville, A., Flores, J.F. and Ghorbani, N. A Numerical Investigation of a Geometry Independent Integrated Method to Predict Erosion Rates in Slurry Erosion. *Wear.* 2011, **271**(5), pp.712-719.
103. Ige, O.O. and Umoru, L.E. Effects of Shear Stress on the Erosion-Corrosion Behaviour of X-65 Carbon Steel: A Combined Mass-Loss and Profilometry Study. *Tribology international.* 2016, **94**, pp.155-164.
104. Stack, M.M. and Abdelrahman, S.M. A CFD Model of Particle Concentration Effects on Erosion–Corrosion of Fe in Aqueous Conditions. *Wear.* 2011, **273**(1), pp.38-42.
105. Song, F.M. A comprehensive model for predicting CO2 corrosion rate in oil and gas production and transportation systems. *Electrochimica acta.* 2010, **55**(3), pp.689-700.
106. Lide, D.R. *CRC Handbook of Chemistry and Physics.* 75th ed ed. New York: CRC Press, 1994.
107. Oddo, J.E. and Tomson, M.B. Simplified Calculation of CACO3 Saturation at High Temperatures and Pressures in Brine Solutions. *Journal of petroleum technology.* 1982, **34**(7), pp.1583-1590.
108. Covington, A.K., Bates, R.G. and Durst, R.A. Definition of pH scales, standard reference values, measurement of pH and related terminology. *Pure and Applied Chemistry.* 1985, **57**(3), p.12.

109. Stephens, L.I. and Mauzeroll, J. Demystifying Mathematical Modeling of Electrochemical Systems. *Journal of Chemical Education.* 2019, **96**(10), pp.2217-2224.
110. Britz, D. and Strutwolf, J. *Digital Simulation in Electrochemistry.* fourth ed. ed. Switzerland: Springer International Publishing, 2016.
111. Battelle Memorial Institute. Steel -- Physical and Typical Mechanical Properties. In: Battelle Memorial Institute ed. *Metallic Materials Properties Development and Standardization (MMPDS)*. Ohio: Battelle Memorial Institute,, 2017, pp.1-12.
112. COMSOL. *Electrodeposition Module User's Guide.* sixth ed. ed. Stockholm, Sweden: COMSOL, 2022.
113. Nešić, S., Postlethwaite, J. and Olsen, S. An Electrochemical Model for Prediction of Corrosion of Mild Steel in Aqueous Carbon Dioxide Solutions. *Corrosion.* 1996, **52**(4), pp.280-294.
114. Nešić, S., Thevenot, N., Drazic, D. and Crolet, J.L. Electrochemical Properties of Iron Dissolution in the Presence of CO_2 - Basics Revisited. In: *CORROSION96*, *1996*, *Houston, Texas*. NACE, 1996.
115. Stumm, W. and Morgan, J.J. *Aquatic Chemistry : Chemical Equilibria and Rates in Natural Waters.* 3rd ed. New York: Wiley, 1996.
116. Hurlen, T., Gunvaldsen, S. and Blaker, F. Effects of buffers on hydrogen evolution at iron electrodes. *Electrochimica acta.* 1984, **29**(8), pp.1163-1164.
117. Hurlen, T., Gunvaldsen, S., Tunold, R., Blaker, F. and Lunde, P.G. Effects of carbon dioxide on reactions at iron electrodes in aqueous salt solutions. *Journal of electroanalytical chemistry and interfacial electrochemistry.* 1984, **180**(1), pp.511-526.
118. Pourbaix, M. *Atlas of Electrochemical Equilibria in Aqueous Solutions.* second ed. ed. Texas: NACE International, 1974.
119. Tanupabrungsun, T., Young, D., Brown, B. and Nesic, S. Construction and Verification of Pourbaix Diagrams for CO_2 Corrosion of Mild Steel Valid up to 250°C. In: International, N., ed. *Corrosion*, *Salt Lake City, UT*. NACE International, 2012, pp.1-16.
120. Pitzer, K.S. Thermodynamics of electrolytes. I. Theoretical basis and general equations. *Journal of Physical Chemistry.* 1973, **77**(2), pp.268-277.

121. Langmuir, D. *Aqueous environmental geochemistry.* 1st ed. Upper Saddle River, N.J: Prentice Hall, 1997.
122. Wissbrun, K.F., French, D.M. and Patterson, A. The True Ionization Constant of Carbonic Acid in Aqueous Solution from 5 to 45°. *Journal of Physical Chemistry.* 1954, **58**(9), pp.693-695.
123. Archer, D.G. and Wang, P. The Dielectric Constant of Water and Debye-Hückel Limiting Law Slopes. *Journal of Physical and Chemical Reference Data.* 1990, **19**(2), pp.371-411.
124. Aravinth, S. Prediction of Heat and Mass Transfer for Fully Developed Turbulent Fluid Flow Through Tubes. *International Journal of Heat and Mass Transfer.* 2000, **43**(8), pp.1399-1408.
125. Churchill, S.W. A Critique of Predictive and Correlative Models for Turbulent Flow and Convection. *Industrial & Engineering Chemistry Research.* 1996, **35**(9), pp.3122-3140.
126. Swamee, P.K. and Akalank, K.J. Explicit Equations for Pipe-Flow Problems. *Journal of the Hydraulics Division.* 1976, **102**(5), pp.657-665.
127. Nešić, S. Key Issues Related to Modelling of Internal Corrosion of Oil and Gas Pipelines – A Review. *Corrosion Science.* 2007, **49**(12), pp.4308-4338.
128. Pessu, F., Barker, R. and Neville, A. The Influence of pH on Localized Corrosion Behavior of X65 Carbon Steel in CO_2-Saturated Brines. *Corrosion.* 2015, **71**(12), pp.1452-1466.
129. Hinds, G. and Thomas, J.G.N. *The Electrochemistry of Corrosion.* [Online]: National Physical Laboratory, 2014.
130. Eisenberg, M., Tobias, C.W. and Wilke, C.R. Ionic Mass Transfer and Concentration Polarization at Rotating Electrodes. *Journal of the Electrochemical Society.* 1954, **101**(6), p.306.
131. Jones, M., Owen, J., de Boer, G., Woollam, R.C. and Barker, R. Numerical Exploration Of A Comprehensive Mechanistic CO_2 Corrosion Model Part II: Influence Of Hydrodynamics And Bulk pH. In: *AMPP Annual Conference + Expo 2023*, *Denver, Colorado*. AMPP, 2023, pp.1-9.
132. Granger Robert, A. Turbulent Pipe Flow. In: *Fluid Mechanics*. New York, U.S.A.: Dover Publications, 1995, pp.541-586.
133. Moin, P. and Mahesh, K. DIRECT NUMERICAL SIMULATION: A Tool in Turbulence Research. *Annual review of fluid mechanics.* 1998, **30**(1), pp.539-578.

134. Korson, L., Drost-Hansen, W. and Millero, F.J. Viscosity of Water at Various Temperatures. *The Journal of Physical Chemistry.* 1969, **73**(1), pp.34-39.
135. Wang, F. and Postlethwaite, J. Modelling of Aqueous CO_2 Corrosion of Iron in Turbulent Pipe Flow. In: *CORROSION 2001*, *Houston, Texas*. NACE International, 2001, pp.1-13.
136. Rivero, E.P., Granados, P., Rivera, F.F., Cruz, M. and González, I. Mass Transfer Modeling and Simulation at a Rotating Cylinder Electrode (RCE) Reactor Under Turbulent Flow for Copper Recovery. *Chemical Engineering Science.* 2010, **65**(10), pp.3042-3049.
137. Richard, D., Tom, M., Jang, J., Yun, S., Christofides, P.D. and Morales-Guio, C.G. Quantifying Transport and Electrocatalytic Reaction Processes in a Gastight Rotating Cylinder Electrode Reactor via Integration of Computational Fluid Dynamics Modeling and Experiments. *Electrochimica acta.* 2023, **440**, pp.1-17.
138. Rosales, M., Pérez, T. and Nava, J.L. Computational Fluid Dynamic Simulations of Turbulent Flow in a Rotating Cylinder Electrode Reactor in Continuous Mode of Operation. *Electrochimica acta.* 2016, **194**, pp.338-345.
139. Menter, F.R. Two-Equation Eddy-Viscosity Turbulence Models for Engineering Applications. *AIAA journal.* 1994, **32**(8), pp.1598-1605.
140. Tomboulides, A., Aithal, S.M., Fischer, P.F., Merzari, E., Obabko, A.V. and Shaver, D.R. A Novel Numerical Treatment of the Near-Wall Regions in the k−ω Class of RANS Models. *The International journal of heat and fluid flow.* 2018, **72**, pp.186-199.
141. Tominaga, Y. and Stathopoulos, T. Turbulent Schmidt numbers for CFD analysis with various types of flowfield. *Atmospheric environment (1994).* 2007, **41**(37), pp.8091-8099.
142. COMSOL. CFD Module User's Guide 5.5. [Online]. Stockholm, Sweden: COMSOL, 2019, pp.184-223. [Accessed 28/04/2021].
143. Paolinelli, L.D. and Nesic, S. Calculation of Mass Transfer Coefficients for Corrosion Prediction in Two-Phase Gas-Liquid Pipe Flow. *International Journal of Heat and Mass Transfer.* 2021, **165**, pp.1-11.
144. Abdar, P.S., Hariri, M.B., Kahyarian, A. and Nesic, S. A Revision of Mechanistic Modeling of Mild Steel Corrosion in

H_2S Environments. *Electrochimica acta.* 2021, **382**, p.138231.
145. Walsh, F.C., Kear, G., Nahlé, A.H., Wharton, J.A. and Arenas, L.F. The rotating cylinder electrode for studies of corrosion engineering and protection of metals—An illustrated review. *Corrosion Science.* 2017, **123**, pp.1-20.
146. Gabe, D.R. The rotating cylinder electrode. *Journal of applied electrochemistry.* 1974, **4**(2), pp.91-108.
147. Gabe, D.R. and Walsh, F.C. The rotating cylinder electrode: a review of development. *Journal of applied electrochemistry.* 1983, **13**(1), pp.3-21.
148. Gabe, D.R., Wilcox, G.D., Gonzalez-Garcia, J. and Walsh, F.C. The rotating cylinder electrode: its continued development and application. *Journal of applied electrochemistry.* 1998, **28**(8), pp.759-780.
149. De Motte, R., Basilico, E., Mingant, R., Kittel, J., Ropital, F., Combrade, P., Necib, S., Deydier, V., Crusset, D. and Marcelin, S. A Study by Electrochemical Impedance Spectroscopy and Surface Analysis of Corrosion Product Layers Formed During CO_2 Corrosion of Low Alloy Steel. *Corrosion Science.* 2020, **172**, p.108666.
150. Bockris, J.O.M., Drazic, D. and Despic, A.R. The Electrode Kinetics of the Deposition and Dissolution of Iron. *Electrochimica acta.* 1961, **4**(2-4), pp.325-361.
151. Hu, H., Xu, H., Huang, C., Chen, X., Li, X. and Li, Y. Numerical Predictions of Uniform CO_2 Corrosion in Complex Fluid Domains Using Low Reynolds Number Models. *Metals (Basel).* 2018, **8**(12), p.1001.
152. De Motte, R., Mingant, R., Kittel, J., Ropital, F., Combrade, P., Necib, S., Deydier, V. and Crusset, D. Near Surface pH Measurements in Aqueous CO_2 Corrosion. *Electrochimica acta.* 2018, **290**, pp.605-615.
153. Han, J., Brown, B.N., Young, D. and Nešić, S. Mesh-Capped Probe Design for Direct pH Measurements at an Actively Corroding Metal Surface. *Journal of applied electrochemistry.* 2010, **40**(3), pp.683-690.
154. Truesdell, A.H. and Jones, B.F. WATEQ, A Computer Program for Calculating Chemical Equilibria of Natural Waters. *Journal of Research of the U.S. Geological Survey.* 1974, **2**(2), pp.233-248.
155. Chen, T.Y., Moccari, A.A. and Macdonald, D.D. Development of Controlled Hydrodynamic Techniques for Corrosion Testing. *Corrosion.* 1992, **48**(3), pp.239-255.

156. De Motte, R.A., Barker, R., Burkle, D., Vargas, S.M. and Neville, A. The early stages of FeCO3 scale formation kinetics in CO2 corrosion. *Materials chemistry and physics.* 2018, **216**, pp.102-111.
157. Fu, J., Thomas, H.R. and Li, C. Tortuosity of porous media: Image analysis and physical simulation. *Earth-science reviews.* 2021, **212**(103439), pp.1-30.
158. da Silva, M.T.Q.S., do Rocio Cardoso, M., Veronese, C.M.P. and Mazer, W. Tortuosity: A Brief Review. *Materials Today: Proceedings.* 2022, **58**, pp.1344-1349.
159. Chung, D.-W., Ebner, M., Ely, D.R., Wood, V. and Edwin García, R. Validity of the Bruggeman Relation for Porous Electrodes. *Modelling and simulation in materials science and engineering.* 2013, **21**(7), pp.1-16.
160. Jones, M., de Boer, G., Woollam, R., Owen, J., Folena, M.C., Farhat, H. and Barker, R. Assessing Comprehensive Mechanistic CO_2 Corrosion Modeling Methods and their Impact on Predicted Corrosion Behavior. In: *AMPP*, *New Orleans, LA*. AMPP, 2024, pp.1-15.
161. Jones, M., Owen, J., de Boer, G., Woollam, R.C. and Barker, R. Numerical Exploration of a Comprehensive Mechanistic CO_2 Corrosion Model Part I: Influence of Temperature, Pressure and Bulk pH. In: *AMPP 2022*, *Denver, CO*. AMPP, 2023, pp.1-12.
162. Jones, M., Owen, J., de Boer, G., Woollam, R.C., Folena, M.C., Farhat, H. and Barker, R. Numerical Exploration of a Fully Mechanistic Mathematical Model of Aqueous CO_2 Corrosion in Steel Pipelines. *Corrosion Science.* 2024, **236**, pp.1-15.
163. Kalos, M.H. and Whitlock, P.A. *Monte Carlo Methods.* second ed. Weinheim, Germany: Wiley-Blackwell, 2008.
164. COMSOL. Introduction to Solvers and Studies. *COMSOL Multiphysics Reference Manual.* [Online]. Stockholm, Sweden: COMSOL, 2023, pp.1442-1460.
165. NIST/SEMATECH. Beta Distribution. *Engineering Statistics Handbook.* [Online]. 2006, pp.482-485.
166. Cenosco. *Hydrocor Corrosion Prediction Software.* [Online]. 2024. [Accessed 07/08/2024]. Available from: https://cenosco.com/products/hydrocor
167. Wigen, S.M. *Enhancing Pipeline Integrity Management with Advanced Inspection Technology.* [Online]. 2024. [Accessed 07/08/2024]. Available from:

https://forcetechnology.com/no/artikler/enhancing-pipeline-integrity-management-advanced-inspection-technology
168. McMahon, A.J. and Paisley, D.M.E. *Corrosion Prediction Modelling.* London, UK: BP, 1997.
169. Nyborg, R. CO_2 Corrosion Models for Oil and Gas Production Systems. In: *Corrosion*, *San Antonio, TX*. NACE International, 2010, pp.1-20.
170. MathWorks. *Polyfit.* [Online]. 2024. [Accessed 07/08/2024]. Available from: https://uk.mathworks.com/help/matlab/ref/polyfit.html
171. COMSOL. New and Updated Operators, Functions, and Definitions. *COMSOL Multiphysics 6.2 Release Notes.* [Online]. Stockholm, Sweden: COMSOL, 2023, pp.26-30.
172. COMSOL. Uncertainty Quantification Modeling. *Uncertainty Quantification Module User's Guide.* [Online]. Stockholm, Sweden: COMSOL, 2023, pp.38-68.
173. Berke, L. and Hajela, P. Applications of Artificial Neural Nets in Structural Mechanics. In: *Lecture Series on Shape and Layout Optimization of Structural Systems*, *Udine, Italy*. NASA, 1990, pp.1-20.
174. COMSOL. *Introduction to Application Builder.* [Online]. Stockholm, Sweden: COMSOL, 2023.